

AD-A214 730

INVESTIGATION OF LIQUID SLOSHING
IN SPIN-STABILIZED SATELLITES

Joseph R. Baumgarten
Donald R. Flugrad
Joseph M. Prusa

Department of Mechanical Engineering

August 31, 1989



**College of
Engineering
Iowa State University**

89 11 17 032

AFOSR-TR- 89 - 1312

FINAL REPORT

Grant #AFOSR-86-0080

INVESTIGATION OF LIQUID SLOSHING
IN SPIN-STABILIZED SATELLITES

Joseph K. Baumgarten
Donald R. Flugrad
Joseph M. Piusa

Department of Mechanical Engineering

August 31, 1989

This report has been prepared for the
Air Force Office of Scientific Research



engineering research institute

iowa state university

This is a preprint of a paper intended for publication in a journal or proceedings and should not be used for reproduction or distribution without the permission of the publisher.

ISU-ERI-Ames 90401
Project 1873

2

REPORT DOCUMENTATION PAGE

1a. REPORT SECURITY CLASSIFICATION Unclassified		1d. RESTRICTIVE MARKINGS None	
2a. SECURITY CLASSIFICATION AUTHORITY NOV 20 1989		3. DISTRIBUTION/AVAILABILITY OF REPORT Approved for public release; distribution unlimited.	
2b. DECLASSIFICATION/DOWNGRADING SCHEDULE None		5. MONITORING ORGANIZATION REPORT NUMBER AFOSR-TR-89-12	
4. PERFORMING ORGANIZATION REPORT NUMBER(S) ISU-ERI-Ames-90401 Project 1873		7a. NAME OF MONITORING ORGANIZATION Air Force Office of Scientific Research(AFOSR)	
6a. NAME OF PERFORMING ORGANIZATION Iowa State University Dept. of Mechanical Engineering	6b. OFFICE SYMBOL (If applicable) NA	7b. ADDRESS (City, State and ZIP Code) Air Force Office of Scientific Research Directorate of Aerospace Science (AFOSR/NA) Bolling AFB, DC 20332	
6c. ADDRESS (City, State and ZIP Code) Room 2025 Black Engineering Building Ames, IA 50011		9. PROCUREMENT INSTRUMENT IDENTIFICATION NUMBER Grant No. AFOSR-86-0080 Pur. Req. No. F08671-8700690	
8a. NAME OF FUNDING/SPONSORING ORGANIZATION AFOSR	8b. OFFICE SYMBOL (If applicable) NA	10. SOURCE OF FUNDING NOS.	
8c. ADDRESS (City, State and ZIP Code) Bldg. 410 Bolling AFB, DC 20332-6448		PROGRAM ELEMENT NO. 6100FE	PROJECT NO. 2302
		TASK NO. 2302/B1	WORK UNIT NO.
11. TITLE (Include Security Classification) Investigation of Liquid Sloshing in Spin-Stabilized Satellites (Unclassified)			
12. PERSONAL AUTHOR(S) Baumgarten, Joseph R.; Flugrad, Donald R.; Prusa, Joseph M.			
13a. TYPE OF REPORT Final Report	13b. TIME COVERED FROM 1/86 TO 8/31/89	14. DATE OF REPORT (Yr., Mo., Day) 1989 August 31	15. PAGE COUNT i-vi, 1-9, A1-A4, B1-B33, C1-C32, D1-D56, E1-E47, F1-F50, G1-G46
16. SUPPLEMENTARY NOTATION			
17. COSATI CODES		18. SUBJECT TERMS (Continue on reverse if necessary and identify by block number)	
FIELD	GROUP	SUB GR.	Coning of satellites, nutation due to sloshing fluid.
19. ABSTRACT (Continue on reverse if necessary and identify by block number)			
<p>Launching of several Star 48 Communication Satellites from the Space Shuttle have consistently resulted in a nutating motion of the spacecraft. Sloshing fluid stores have been suspected as the source of this dynamic instability. A mathematical model of the sloshing fluid motion coupled with the satellite dynamics was developed and the launch phase simulated. The flight simulation shows similar behavior when compared to the telemetered flight data. Additionally, a control law was developed using an equivalent mechanical model of the fluid motion, which results in a stable dynamic system. The control law may also be used for pointing maneuvers and is implemented by sensing only the main body angular rates and attitude.</p> <p style="text-align: right;">(continued on other side)</p>			
20. DISTRIBUTION/AVAILABILITY OF ABSTRACT UNCLASSIFIED/UNLIMITED <input checked="" type="checkbox"/> SAME AS RPT <input checked="" type="checkbox"/> DTIC USERS <input checked="" type="checkbox"/>		21. ABSTRACT SECURITY CLASSIFICATION Unclassified	
22a. NAME OF RESPONSIBLE INDIVIDUAL George K. Hakites II, (USA) (SM)		22b. TELEPHONE NUMBER (Include Area Code) 702-0463	22c. OFFICE SYMBOL NA

19. ABSTRACT (continued)

An experimental satellite-simulator test rig has been designed and built to study the interaction of the sloshing fluid and spinning structure. The test rig has been instrumented to monitor the motion of several rotating configurations. A mathematical model of the simulator has been developed and is presented here. Simulation of experimental results has been achieved. The computational fluid dynamic analysis has now developed a primitive variable numerical algorithm for a two-dimensional and three-dimensional sloshing problem. The key feature of the formulation is the use of a coordinate transformation that maps the fluid body into the fixed geometric shape of the containing rectangle or sphere. The formulation removes an initial singularity from the governing equations that would otherwise cause the numerical method to diverge.

CONTENTS

ABSTRACT	iii
I. INTRODUCTION	1
1.1 Research Objectives	2
1.2 Status of Research	3
1.3 Publications	4
1.4 List of Research Personnel, Thesis Titles and Degrees Awarded	6
1.5 Seminars, Papers, and Laboratory Visits	9
Appendix A - Spacecraft Dynamic Simulation	A1
Appendix B - Spacecraft Control	B1
Appendix C - Satellite Simulator Test Rig Design	C1
Appendix D - Satellite Simulator Test Rig Experiments	D1
Appendix E - Simulator Dynamic Response	E1
Appendix F - Two-Dimensional Viscous Slosh Analysis	F1
Appendix G - Three-Dimensional Viscous Slosh Analysis	G1

A-1	
Date	
by	
Checked	
Approved	
Title	
Author	
Subject	
Abstract	
Notes	
Remarks	

Approved for Release by NSA on 05-08-2014 pursuant to E.O. 13526
 100-12
 Information Division



I. INTRODUCTION

This final technical report presents a comprehensive summary of the research accomplishments supported by Grant #AFOSR-86-0080 over the period January 1, 1986 to August 31, 1989. The report reviews the objectives of the research in Section 1. The status of the research effort is reported in Section 2. Section 3 of Chapter 1 presents a chronological list of written publications resulting from this research effort. Manuscripts planned for imminent submission to technical journals are also listed. Following this, the report presents a recapitulation of the advanced degrees awarded, a list of thesis titles, and a history of the professional personnel associated with this grant. Seminars, presented papers, and advisory meetings with Air Force and other DOD laboratories are reviewed in Section 5.

Appendix A of the report summarizes the results of the dynamic simulation of the Star 48 spacecraft. The results of a control law analysis to stabilize the spacecraft are considered in Appendix B of this report.

The need for a convenient stationary bench model of a nutating spacecraft is outlined in the research objectives. This model was developed as the satellite simulator test rig and its design is described briefly in Appendix C. The development of the instrumentation which was used to measure the dynamic motion of the simulator is given in Appendix D. Appendix E is a discussion of the successful computer simulation of the test-rig dynamic response from a Lagrangian formulation of the equation of motion.

Appendices F and G summarize the results of the computational fluid dynamic analysis of 2-dimensional and 3-dimensional models of the sloshing fluid. The dynamics of a fluid in a rectangular space was analyzed and, more recently, the response of a free surface liquid in a spherical tank has been studied.

1.1 Research Objectives

The objectives of this research grant were to derive the equations of motion of a spacecraft containing liquid fuel stores; the modeling of the free-surface liquid was to be done by (a) equivalent two-dimensional pendulum representation and (b) by computational fluid dynamic modeling.

This project proposed to build an experimental test rig which simulated the spinning and coning motion of a spacecraft. The satellite simulator would contain symmetrically placed spherical tanks with adequate instrumentation to study the dynamic state of the free surface liquid as well as the instantaneous structural response. It was the stated objective of the project that the physical system modelling be continued and adapted until total agreement was achieved between the analytical response and the experimental data obtained from the satellite simulator.

It was the purpose of this research that it produce a mathematical model of the spacecraft capable of predicting the precession of the spin axis of a satellite that develops as the spacecraft responds to a sudden axial thrust.

1.2 Status of Research

The work of simulation of the Star 48 Communication Satellite flight dynamics, begun in June 1983 at AEDC-Arnold AFS, was completed and culminated in a published paper (see Appendix A). The analysis of a control law to provide dynamic flight stability to the satellite was completed. A technical publication abstracted from this work has been submitted for review (see Appendix B).

The analysis and design of the satellite simulator test-rig model was completed. A technical publication will be abstracted from this and submitted for review for publication in the literature (see Appendix C). Instrumentation of the spinning and nutating simulator was completed to provide measured dynamic response of the basic structural components as well as the fluid response. A technical publication abstracted from this work will be submitted for review for publication in the literature (see Appendix D). The equations of motion of the simulator were formulated from a Lagrangian analysis and were programmed for solution on the digital computer. The successful computer simulation of measured response of the test rig resulted. This work is abstracted for publication in Appendix E of this report.

The computational fluid dynamic analysis completed under this grant has produced a primitive variable simulation of two-dimensional fluid response (see Appendix F). The three-dimensional modeling of a free surface viscous fluid in a spherical container has now simulated the dynamic response to basic centrifugal disturbance and is presented in Appendix G in abstract for review for publication.

1.3 Publications

Listed below are the technical publications resulting from this work which have been previously submitted to the Air Force Office of Scientific Research.

Hill, D. E., Baumgarten, J. R., and Miller, J. T., "Dynamic Simulation of Spin-Stabilized Spacecraft with Sloshing Fluid Stores," Technical Report No. ISU-ERI-Ames-86451, Dec. 1986.

Hill, D. E. and Baumgarten, J. R., "Control of Spin-Stabilized Spacecraft with Sloshing Fluid Stores," Technical Report No. ISU-ERI-Ames 86452, Dec. 1986.

Baumgarten, J. R., Prusa, J. M., and Flugrad, D. R., "An Investigation of Liquid Sloshing in Spin-Stabilized Satellites," Technical Report No. ISU-ERI-Ames 88175, Jan. 31, 1988.

Hill, D. E., Baumgarten, J. R., and Miller, J. T., "Dynamic Simulation of Spin-Stabilized Spacecraft with Sloshing Fluid Stores," AIAA Journal of Guidance, Control, and Dynamics, Vol. 11, No. 6, Nov-Dec 1988, pp. 597-599.

Listed in the following are technical publications resulting from this work which are currently under review and which will be submitted for publication.

Hill, D. E., and Baumgarten, J. R., "Control of Spin-Stabilized Spacecraft with Sloshing Fluid Stores," under review for the Proceedings of the 1990 American Control Conference.

Prusa, J. M., and Kassinos, A. C., "Numerical Solution of 2-D Viscous Sloshing in Rectangular Containers of Finite Aspect Ratio," to be submitted to Journal of Computational Physics.

Kassinos, A. C. and Prusa, J. M., "Study of 3-D Viscous Sloshing in Spherical Containers," to be submitted to Journal of Computational Physics.

Flugrad, D. R., Anderson, M. D. and Cowles, D. S., "A Test Rig to Simulate Liquid Sloshing in Spin-Stabilized Satellites - Part One: Design and Instrumentation," to be submitted to AIAA Journal of Guidance, Control, and Dynamics.

Flugrad, D. R. and Anderson, M. D., "A Test Rig to Simulate Liquid Sloshing in Spin-Stabilized Satellites - Part Two: Experimental Results," to be submitted to AIAA Journal of Guidance, Control, and Dynamics.

Flugrad, D. R., and Obermaier, L. A., "Computer Simulation of a Test Rig to Model Liquid Sloshing in Spin-Stabilized Satellites," to be submitted to ASME Journal of Dynamic Systems and Control.

1. List of Research Personnel, Thesis Titles, and Degrees Awarded

- (A) This research was initiated in June 1983 by D. E. Hill and J. R. Baumgarten during an AFOSR summer faculty appointment to AEDC Engine Test Facility at Arnold Air Force Station, Tennessee. As indicated in Appendix A, AEDC had tested a typical PAM rocket motor and had found no instabilities that could explain the coning motion of spinning communication satellites. A forerunner to this present grant, AFOSR Research Initiation Grant, Subcontract No. 83RIP33 allowed Hill to initiate the study of the dynamic response of sloshing fuel stores as a possible contributor to spacecraft coning motion. Dr. Hill received the Ph.D. degree in December 1985 and the present grant supported publication of this thesis titled:

Hill, D. E., "Dynamics and Control of Spin-Stabilized Spacecraft with Sloshing Fluid Stores," Ph.D. Thesis, Iowa State University, Ames, IA, 1985.

- (B) The desire to have a bench test device to duplicate the relative fluid motion in a spinning-rotating structure motivated the study of D. S. Cowles. Under direction of D. R. Flugrad, Cowles designed and built the first working version of the satellite simulator described and pictured in Appendix C. Douglas S. Cowles received the M.S. in Mechanical Engineering Degree in December 1987. His thesis was titled:

Cowles, D. S. "Design of a Spin-Stabilized Spacecraft Simulator with Liquid Fuel Stores," M.S. Thesis, Iowa State University, Ames, IA, 1987.

(C) The need for measured response of the sloshing fluid and the nutating structure prompted the instrumentation effort of M. D. Anderson. Working under the direction of D. R. Flugrad, Anderson reconfigured the simulator, instrumented the fluid tanks, the two degree of freedom universal joint, and set up a data collection system as outlined in Appendix C. Michael D. Anderson received the M.S. Degree in Mechanical Engineering in August 1988 and his thesis was titled:

Anderson, M. D., "Instrumentation of a Spin-Stabilized Spacecraft Simulator with Liquid Fuel Stores," M. S. Thesis, Iowa State University, Ames, IA, 1988.

(D) Having a working bench model of the spin stabilized satellite, it was now desired to complete the dynamic modeling of the simulator. Under direction of D. R. Flugrad, Lisa Ann Obermaier completed the formulation of the test-rig equations of motion. Her successful computer simulation of the test rig allowed the study of many response parameters and will be a valuable tool in subsequent work. She received the M.S. Degree in Mechanical Engineering in December 1988 and her thesis was titled:

Obermaier, L. A., "Computer Simulation of a Spin-Stabilized Spacecraft Simulator with Liquid Fuel Stores," M.S. Thesis, Iowa State University, Ames, IA, 1988.

(E) The need to replace the pendulum model of the sloshing liquid in its spherical tank with a computational fluid dynamic modeling of the free-surface liquid motivated the work of A. C. Kassinos. Directed by

J. M. Prusa, Kassinos has formulated a primitive variable computer program for analysis of the dynamic fluid response. Adonis C. Kassinos expects to receive his Ph.D. degree in December 1989 and his thesis will be titled:

Kassinos, A. C., "Study of 3-D Viscous Sloshing in Moving Containers,"
Ph.D. Thesis, Iowa State University, Ames, IA, 1989.

- (F) The desire to study the fluid and structure interaction during the sloshing and nutating phase of the simulator motion prompted Janet L. Meyer to instrument the upper arm assembly of the simulator. Under direction of J. R. Baumgarten, Meyer made strain gage measurements of structural deflection of the spinning simulator. Lt. Janet Meyer's graduate study program was interrupted after one year by her orders to report to her first U. S. Air Force duty station at the Los Angeles Aerospace Command. It will be necessary for her to complete her M.S. dissertation in absentia. Her thesis is tentatively titled:

Meyer, J. L., "Correlation of Liquid Motion and Structural Deflection in the Spacecraft Simulator Response," no date of graduation is committed.

1.5 Seminars, Papers, and Laboratory Visits

J. R. Baumgarten visited Dr. Anthony Amos at AFOSR Bolling AFB in March 1986 and at Wright Patterson AFB in March 1988. These visits coordinated the work of various technical personnel with the interests of the Air Force during the term of this grant. Dr. Amos visited the Mechanical Engineering Department, Iowa State University in August, 1987 to review research progress.

J. R. Baumgarten visited the Naval Research Laboratory on March 7, 1986 to study the construction of the Gyrodynamic Motion Simulator. Mr. Samuel Hollander, Head of Control Systems, Space Systems Division was his host. Baumgarten presented the seminar "Sloshing Fuel Stores in Spinning Spacecraft" to the Landing Dynamics Branch, NASA Langley Research Center, March 10, 1988. Mr. John Tanner, Branch Manager, was the host. Baumgarten visited the Engine Test Facility, AEDC, Arnold AFS, on March 9, 1989 to discuss research results with Mr. J. R. Smith, Section Manager. The seminar "Tumbling Satellites" was conducted for the Society of American Military Engineers at Iowa State University, on April 3, 1989.

APPENDIX A

SPACECRAFT DYNAMIC SIMULATION

**Dynamic Simulation of Spin-Stabilized
Spacecraft with Sloshing Fluid Stores**
D. E. Hill, J. R. Baumgarten, J. T. Miller

Reprinted from



Journal of Guidance, Control, and Dynamics

Volume 11, Number 6, November-December 1988, Pages 597-599
AMERICAN INSTITUTE OF AERONAUTICS AND ASTRONAUTICS, INC.
370 L'ENFANT PROMENADE, SW • WASHINGTON, DC 20024

Dynamic Simulation of Spin-Stabilized Spacecraft with Sloshing Fluid Stores

Daniel E. Hill* and Joseph R. Baumgartent
Iowa State University, Ames, Iowa

and

John T. Millert†
*Arnold Engineering Development Center,
Tullahoma, Tennessee*

Introduction

LAUNCHINGS of several communications satellites have consistently resulted in a nutating motion of the spacecraft. Flight data from the roll, pitch, and yaw axis rate gyros indicated a constant-frequency, equal-amplitude, sinusoidal oscillation about the pitch and yaw axis. The vector combination of these two components of oscillation resulted in a coning motion of the satellite about the roll axis. The vehicle was spin-stabilized at launch about the minor axis, having a one revolution per second (rps) roll angular velocity imparted to it.

After launching from the carrier vehicle in the perigee phase of its orbit, the satellite's perigee assist module (PAM) fired its thruster to establish a geosynchronous Earth orbit. It is this axial thrust that gives rise to the coning that predominates after PAM motor burnout. Consistently, flight data from rate gyros indicated the steady-state one-half cycle per second (cps) coning frequency and a one-half cycle cps small-amplitude disturbance superimposed on the 1 rps roll angular velocity.

Combustion instabilities in the PAM rocket motor were suspected to be the source of a side force that would induce the coning motion. In order to investigate the presence of any such combustion instabilities, a PAM rocket motor was fired at the Engine Test Facility, Arnold Engineering Development Center, Arnold Air Force Station. A test fixture having lateral and axial load cells was utilized, allowing the PAM to be spun at 1 rps during firing. A spectral analysis was completed of the resulting load cell records obtained during firing. The test results indicated no forces at the required frequency (one-half cps), and it was concluded that combustion instabilities were not the source of moments causing coning motion.

A preliminary analysis of the payload (communication satellite) was completed indicating that sloshing fluid stores may induce the coning motion. It was suspected that sloshing motion of the liquid stores in the vehicle, excited by the axial thrust, was the mechanism for creating the nutation of the spacecraft.

The modeling of fluid slosh is extensive and has been used by researchers to study its effect on space vehicle motion.^{1,3} Michelini et al.⁴ outlined a procedure for developing the equations of motion of a spinning satellite containing fluid stores. The equations of motion were not presented, but the study supplied the analytical background for the experimental identification of the dynamic model. Experimental results showed that small-amplitude free surface wave motion does not cause instabilities in the vehicle. Instabilities were found to be generated by the fundamental mode of fluid slosh, which is not excited by small-amplitude free surface wave motion. The consequence of the first-mode natural frequency causing instability in the vehicle justifies the use of an equivalent spherical pendulum model of fluid slosh.

Received May 15, 1987; revision received Nov. 3, 1987. Copyright © 1987 by Daniel E. Hill. Published by the American Institute of Aeronautics and Astronautics, Inc., with permission.

*Graduate Student, currently Senior Engineer, Martin Marietta.

†Professor of Mechanical Engineering.

‡Research Engineer.

The equivalent spherical pendulum model, which is based on experimental results, is a means of simplifying the extremely complicated problem of modeling the free surface fluid behavior coupled to the vehicle dynamics. The problem would normally consist of solving a boundary value problem and an initial value problem. The simplified equivalent mechanical model reduces the complexity to an initial value problem, which is handled with much more ease mathematically. This study uses the experimental results of previous researchers to develop a simplified mathematical model that describes the interaction between the fluid mass and main vehicle body.

Numerical Simulation of the Equations of Motion

The equations that define the motion of the system shown in Fig 1 are a set of nonlinear coupled ordinary differential equations.^{5,7} The equations must be solved by numerical methods because an analytical solution is not available.

Numerical values for the vehicle geometry and fuel tank configuration were obtained from test data. The vehicle main body mass varies from 6400 to 2000 lbm during the 85.3-s PAM burn while the roll axis moment of inertia varies from 18869 to 10240 lbm-ft² and the transverse axis inertia from 67652 to 19513 lbm-ft². Sloshing fluid stores were modeled to

have a pendulous mass of 5 lbm and a length of 7.2 in. with the centers of the four tanks positioned symmetrically 25 in. along and 18 in. radially from the main body centerline. Fluid damping was estimated to have a 0.01 dimensionless damping ratio. The dimensionless damping ratio is determined from a single degree of freedom slosh analysis based on fluid type, mass, level, and tank geometry. The damping coefficient used in the model is then determined from the classical vibration relationships between the dimensionless damping ratio, pendulum geometry, and pendulum natural frequency. Symmetry of the tank geometry allows the same damping coefficient to be used with respect to both of the pendulum degrees of freedom.

The flight simulation was made with the vehicle spin-stabilized about the minor axis. Initial conditions on the vehicle were simple spin about the minor axis, with the main body fixed axis aligned with the inertial frame, an altitude of 200 miles and a 1.5-h orbital period. Figure 2 shows the body fixed angular rates vs time with instability occurring near the PAM burnout at 85.3 s. It is reasoned that the instability is caused by increasing torque on the main body resulting from the mass expulsion coupled with the fluid sloshing mass motion. Expulsion of mass not only produces time-varying inertia but also generates what may be interpreted as external torque on the main body even if the exit velocity vector is aligned with the spin axis. The torque is zero if there is no coning motion, but any small disturbance, i.e., fluid sloshing mass motion, perturbs the main body, causing it to cone more which, in turn, excites the sloshing mass motion. The torque and sloshing mass motion effects will be diminished if the main body is gyroscopically stiff enough. Before PAM burnout, the motion of the vehicle is still relatively stable because the system is gyroscopically stiff and has a transverse to roll axis inertia ratio of 3.6. After PAM burnout, the inertia is constant while the transverse to roll axis inertia ratio is reduced to 1.9 and there is a step

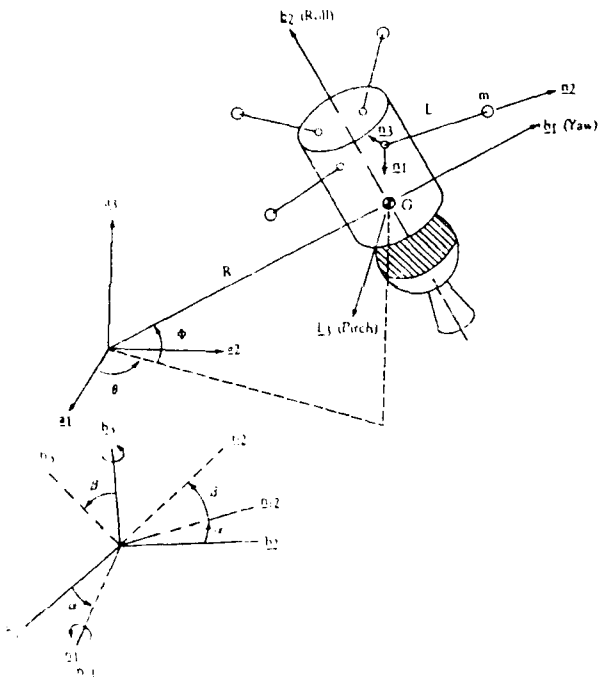


Fig. 1 Model of spacecraft with spherical pendulum.

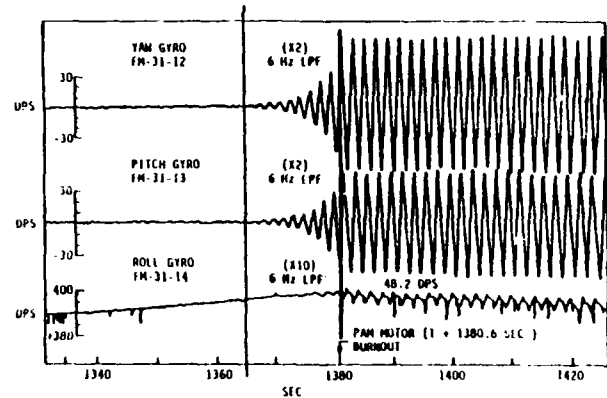


Fig. 3 Body fixed angular rates vs time- RCA-C1.

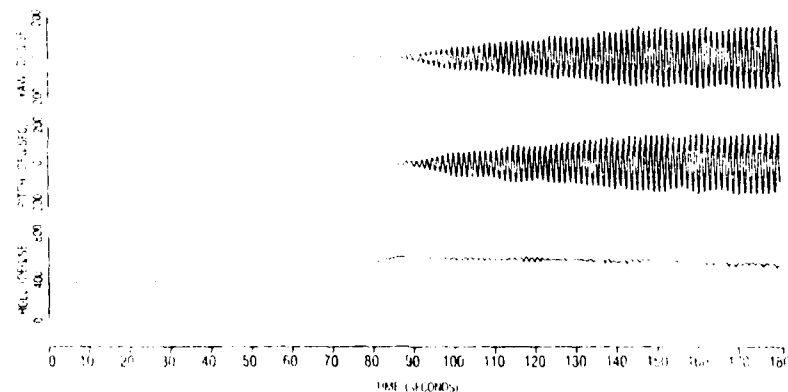


Fig. 2 Body fixed angular rates vs time with powered flight.

change in the main body acceleration. The step change in acceleration excites the sloshing mass motion which, when coupled with the main body decreased inertia ratio, produces an unstable oscillation.

Figure 3 shows telemetered flight data from a previous mission. The pitch and yaw rate gyro data show approximately equal amplitude with 90-deg phase shift, indicating a coning response. Comparison of Figs. 2 and 3 shows that the growth of the coning motion is substantially different, indicating that sloshing mass motion is not the mechanism causing the anomaly.

Conclusions and Recommendations

This study has shown that powered flight of a spacecraft carrying fluid stores within the main rigid body can be a source of dynamic instability.

The major conclusions and recommendations drawn from this study are:

- 1) Explicit dynamic response equations for this complex system were derived using both Kane's method and Lagrange's equation, with the fluid modeled as an equivalent spherical pendulum.
- 2) Sloshing fluid stores are not the source of dynamic instability seen in the launchings of STAR 48 rocket-motor-equipped spacecraft that carried the fluid stores.

Acknowledgments

This study was completed under partial support of Contract AFOSR-86-0080 and Subcontract 83RIP33, U.S. Air Force. The authors wish to acknowledge the support of Iowa State University in accomplishing the lengthy digital computer simulation required in this study.

References

- ¹Sumner, I. E., "Experimentally Determined Pendulum Analogy of Liquid Sloshing in Spherical and Oblate-Spherical Tanks," NASA TN D-1991, Dec. 1963.
- ²Sumner, I. E. and Stefan, A. J., "An Experimental Investigation of the Viscous Damping of Liquid Sloshing in Spherical Tanks," NASA TN D-1991, Dec. 1963.
- ³Sayar, B. A. and Baumgarten, J. R., "Linear and Nonlinear Analysis of Fluid Slosh Dampers," *AIAA Journal*, Vol. 20, Nov. 1982, pp. 1534-1538.
- ⁴Michelini, R. C., Lucifredi, A., and Dini, D., "The Dynamics of a Non-Rigid Spinning Satellite Containing Oscillating Liquids," *Proceedings of the Third International Conference on Automatic Control in Space*, France, 1970.
- ⁵Hill, D. E., "Dynamics and Control of Spin-Stabilized Spacecraft with Sloshing Fluid Stores," Thesis, Iowa State Univ., Ames, IA, 1985.
- ⁶Kane, T. R., *Dynamics*, Stanford Univ. Press, Stanford, CA, 1972.
- ⁷Kane, T. R., Likins, P. W., and Levinson, D. A., *Spacecraft Dynamics*, McGraw-Hill, New York, 1983.

APPENDIX B

SPACECRAFT CONTROL

Control of Spin-stabilized Spacecraft with Sloshing Fluid Stores

Daniel E. Hill, Senior Engineer, Martin Marietta Astronautics Group
Joseph R. Baumgarten, Professor of Mechanical Engr., Iowa State University

Abstract

Spin-stabilized spacecraft with sloshing fluid stores are known to be a source of dynamic instability for certain spacecraft configurations. A control law was developed, using an equivalent mechanical model of the fluid motion, which results in a stable dynamic system. The control law may also be used for pointing maneuvers and is implemented by sensing only the main body angular rates and attitude.

Introduction

Spin-stabilized spacecraft carrying fluid stores are known to be dynamically unstable for certain spacecraft configurations [1,2]. Spacecraft design constraints cause many vehicles to have the unstable configuration. The excitation of the fluid motion may be constrained by baffle systems but any added weight is costly in terms of payload reduction. Equivalent mechanical models have been developed by various investigators to approximate the complex free surface sloshing fluid behavior [3,4,5]. The control law development in this study is based on an equivalent pendulum model of the fluid motion coupled with the main body dynamics [6].

The dynamic system using the equivalent mechanical model is highly nonlinear and coupled which complicates the control system analysis. Many nonlinear systems may be linearized about a nominal operating point and linear optimal control theory can then be applied to construct a closed loop controller [7]. Stability of the nonlinear system with the linear controller cannot be guaranteed but simulation of the system within the region of operation can be used as a check on the design.

The goal of this study was the development of a closed loop control law which may be applied to a spin-stabilized spacecraft with sloshing fluid stores without baffling or changing the design of the spacecraft. The closed loop feedback control law developed stabilizes the spacecraft and may also be used for pointing maneuvers. A closed loop control system tries to maintain a prescribed relationship of one system variable to another by comparing functions of these variables and using the difference as a means of control [8]. The method of closed loop control

used in this application consists of external torque reaction jets which are normally used on spin-stabilized spacecraft. Spacecraft angular rate and attitude are measured and compared to a reference state as input to the controller for command of the reaction jets.

Control System Analysis

The model of the spacecraft system is shown in Figure 1 and was used as the basis for control law development. Figure 2 shows the spherical pendulum relative to the body fixed reference frame. The dynamic system is highly nonlinear (see Appendix A) which complicates the control analysis. In many cases a nonlinear system may be linearized about a nominal operating point and a feedback control law developed using linear control theory to control the nonlinear system. Linear control theory was used in this study to obtain a control which when applied to the nonlinear system, brings the system to the desired angular rate and attitude.

The linearized equations [6] are time varying because the Euler parameters are periodic if the vehicle is spin-stabilized. Euler parameters are an efficient method of defining the orientation of a body [9]. Assumptions made in the analysis were,

1. The rocket motor has burned out and the inertia of the main body remains constant.
2. The mass of the fluid, therefore the equivalent pendulum length, does not change as fuel is expelled for control.

The problem to be solved in this study is known as the Linear Quadratic Regulator Problem (LQRP). This consists of minimizing the functional,

$$J = \frac{1}{2} [\bar{y}(t_f) - \bar{r}(t_f)]^T H(t_f) [\bar{y}(t_f) - \bar{r}(t_f)]$$

$$+ \frac{1}{2} \int_{t_0}^{t_f} \left[\bar{y}(t) - \bar{r}(t) \right]^T Q(t) \left[\bar{y}(t) - \bar{r}(t) \right] + \bar{u}^T(t) R(t) \bar{u}(t) \right] dt \quad (1)$$

subject to,

$$\dot{\bar{y}}(t) = A(t) \bar{y}(t) + B(t) \bar{u}(t), \quad (2)$$

which is the linearized system of the equations of motion.

The variables in the functional are defined as,

$H(t), Q(t) \equiv$ Positive semidefinite weighting arrays

$\bar{r}(t) \equiv$ Reference state vector

$R(t) \equiv$ Positive definite weighting array

$t \equiv$ Time

$t_0 \equiv$ Initial time

$t_f \equiv$ Final time

$\bar{u}(t) \equiv$ Control vector

$\bar{y}(t) \equiv$ State vector

Kirk [10] derived the necessary conditions for optimality which results in the following matrix differential equations;

$$\dot{P}(t) = -P(t) A(t) - A^T(t) P(t) - Q(t) + P(t) B(t) R^{-1}(t) B^T(t) P(t) \quad (3)$$

$$\dot{\bar{s}}(t) = \left[A^T(t) - P(t) B(t) R^{-1}(t) B^T(t) \right] \bar{s}(t) + Q(t) \bar{r}(t) \quad (4)$$

with boundary conditions,

$$P(t_f) = H(t_f) \quad (5)$$

$$\bar{s}(t_f) = -H(t_f) \bar{r}(t_f) \quad (6)$$

Equation 3 is known as the matrix Riccati equation. $P(t)$ is symmetric and consists of $n(n+1)/2$ independent equations where n is the dimension of the system. $S(t)$ is an n vector. If the solutions to equations 3-6 are found, then the linear optimal control law is given by,

$$\begin{aligned}\bar{u}(t) &= -R^{-1}(t) B^T P(t) \bar{y}(t) - R^{-1}(t) B^T(t) \bar{s}(t) \\ &\equiv F(t) \bar{y}(t) + \bar{v}(t)\end{aligned}\tag{7}$$

The linear optimal control law may be found by integrating the $[n(n+1)/2] + n$ system of equations backward in time and storing the values of $F(t)$ and $v(t)$.

Control System Simulation

Equations 3-7 were solved by numerical methods and the feedback gain matrix, $F(t)$, and command vector, $v(t)$, were stored. The control law was then applied to the nonlinear system of equations. An initial coning state was given by setting the roll, pitch, and yaw rates to 360, 0, and 35 degrees per second with the pitch and yaw angles set to 15 and 0 degrees, respectively. The vehicle was spin-stabilized about the minor axis. Simulation of the nonlinear controlled system showed that the linear feedback control law stabilized and reoriented the vehicle to the desired attitude. The feedback gains shown in Figures 3 and 4 reflect the time varying nature of the Euler parameters as each gain is associated with its respective Euler parameter. Figures 5 and 6 show the gains associated with the roll, pitch, and yaw angular rate states while Figures 7-10 are the gains with respect to the pendulum relative angular velocity and position states.

The linear feedback control law simulated requires that the entire state vector be measured. Measurement of the fluid relative angular velocity and position would be impossible. Techniques of estimating states have been developed with the Kalman-Bucy filter being very popular. A controller that would neither have to measure or estimate the pendulum (fluid) states would be the most practical to implement. Simulation of a reduced order controller consisting of only main body fixed angular rates and attitude measurements showed virtually identical response to the system with the entire state vector measured.

The assumption that the mass of the fluid remains constant as fluid is expelled for spacecraft control was also checked, i.e. robustness. A control law was computed for seventy percent full fluid tanks and the nonlinear response of the system with ninety percent full fluid tanks was computed. Figures 11-13 show the body fixed angular rates, orientation angles, and thrust forces, respectively. The only state variables which were assumed measurable were the main body fixed angular rates and attitude parameters. The simulation shows that the control law in equation 15, using a reduced order controller, can stabilize the vehicle.

A pointing maneuver was also simulated by applying the reduced order controller to orient the spinning vehicle so that the pitch angle was ten degrees while maintaining the yaw angle near zero. Figures 14 and 15 show the body fixed angular rates and orientation angles which indicate the final desired orientation is approached. Figures 16 and 17 show the thrust and command forces required to perform the maneuver. The command forces correspond to components v_1 and v_2 of the $v(t)$ vector in equation 7.

Conclusions

This study has shown that the dynamic instability caused by sloshing fluid stores carried in the main rigid body of a spacecraft may be controlled by use of a linear optimal feedback control system with the fluid modeled as an equivalent spherical pendulum and only the first mode of fluid oscillation included.

The control system presented here uses easily measured state variables (only main body fixed angular rates and attitude) and was shown to be stable for a wide variation in fluid level. It was shown that sensing the dynamic state of the fluid was not necessary for this specific spacecraft under study. A pointing maneuver was also successfully accomplished by this control system.

Acknowledgements

This study was completed under partial support of contract no. AFOSR - 86 - 0080 and subcontract 83RIP33, U.S. Air Force. The authors wish to acknowledge the support of Iowa State University in accomplishing the lengthy digital computer simulation required in this study.

References

1. Kaplan, Marshall H. Modern Spacecraft Dynamics and Control. New York: John Wiley and Sons, Inc., 1976.
2. Agrawal, B. N. "Stability of Spinning Spacecraft with Liquid-Filled Tanks." American Institute of Aeronautics and Astronautics, Aerospace Sciences Meeting, 19th, St. Louis, MO, January 1981.
3. Sumner, Irving E. "Experimentally Determined Pendulum Analogy of Liquid Sloshing in Spherical and Oblate-Spherical Tanks." Technical Note TN D-1991, NASA, December 1963.
4. Sayar, B.A.; and Baumgarten, J.R. "Linear and Nonlinear Analysis of Fluid Slosh Dampers." AIAA Journal, 20, No. 11, November 1982, 1534-1538.
5. Michelini, R.C.; Lucifredi, A; and Dini, D. "The Dynamics of a Non Rigid Spinning Satellite Containing Oscillating Liquids." Proceedings of the Third International Conference on Automatic Control in Space, France, 1970.
6. Hill, D.E. "Dynamics and Control of Spin-Stabilized Spacecraft with Sloshing Fluid Stores." Iowa State University, 1985.
7. Kwakernaak, Huibert, and Sivan, Raphael. Linear Optimal Control Systems. New York: Wiley-Interscience, 1972.
8. Dorf, Richard C. Modern Control Systems. Menlo Park, California: Addison-Wesley Publishing Company, 1980.
9. Morton, H. S., Junkins, J. L., and Blanton, J. N. "Analytical Solutions for Euler Parameters." Celestial Mechanics, 19, 1974, 287-301.
10. Kirk, D. E. Optimal Control Theory. Englewood Cliffs, New Jersey: Prentice-Hall, Inc., 1970.

Appendix A

The equations of motion may be written as,

$$\sum_{l=1}^n \sum_{k=1}^5 \sum_{i=1}^3 [-m_l u_{(i+(3j-3))} u_{(i+(3k-3))}] \begin{bmatrix} \dot{Y}_k \text{ for } k \leq 3 \\ \dot{Y}_{k+2(l-1)} \text{ for } k > 3 \end{bmatrix} - I_j \dot{Y}_j$$

$$+ \sum_{l=1}^n \sum_{i=1}^3 [-m_l u_{(i+(3j-3))} B_i] + C_j + [-RF_j] = 0 \text{ for } j=1, \dots, 3.$$

$$\sum_{k=1}^5 \sum_{i=1}^3 [-m_l u_{(i+(3j-3))} u_{(i+(3k-3))}] \begin{bmatrix} \dot{Y}_k \text{ for } k \leq 3 \\ \dot{Y}_{k+2(l-1)} \text{ for } k > 3 \end{bmatrix}$$

$$+ \sum_{l=1}^n \sum_{i=1}^3 [-m_l u_{(i+(3j-3))} B_i] - D_{\beta_l} Y_{3+2n-1} - D_{\alpha_l} Y_{3+2n} = 0 \text{ for } j=4,5 \text{ and } l=1, \dots, n.$$

The equations relating the main body angular rates to the Euler parameters are given by,

$$\dot{\epsilon}_1 = \frac{1}{2} [\epsilon_4 \omega_1 - \epsilon_3 \omega_2 + \epsilon_2 \omega_3]$$

$$\dot{\epsilon}_2 = \frac{1}{2} [\epsilon_3 \omega_1 + \epsilon_4 \omega_2 - \epsilon_1 \omega_3]$$

$$\dot{\epsilon}_3 = \frac{1}{2} [-\epsilon_2 \omega_1 + \epsilon_1 \omega_2 + \epsilon_4 \omega_3]$$

$$\dot{\epsilon}_4 = \frac{1}{2} [-\epsilon_1 \omega_1 - \epsilon_2 \omega_2 - \epsilon_3 \omega_3]$$

The coefficients and parameters in the equations of motion are defined as,

$$B_1 = (\dot{\beta}_1(\omega_3 + \dot{\alpha}_1) \text{cs}\alpha_1 - \dot{\alpha}_1 \omega_1) L_3 - (\dot{\beta}_1(\omega_1 \text{sn}\alpha_1 - \omega_2 \text{cs}\alpha_1)) L_2$$

$$+ \omega_1 \omega_2 r_2 - r_1(\omega_2^2 + \omega_3^2) + \omega_1 \omega_3 r_3$$

$$+ ((\omega_1 + \dot{\beta}_1 \text{cs}\alpha_1)(\omega_2 + \dot{\beta}_1 \text{sn}\alpha_1) L_2 - ((\omega_2 + \dot{\beta}_1 \text{sn}\alpha_1)^2 + (\omega_3 + \dot{\alpha}_1)^2) L_1$$

$$+ (\omega_1 + \dot{\beta}_1 \text{cs}\alpha_1)(\omega_3 + \dot{\alpha}_1) L_3$$

$$B_2 = (\dot{\beta}_1(\omega_1 \text{sn}\alpha_1 - \omega_2 \text{cs}\alpha_1) L_1 - (\dot{\beta}_1(-\omega_3 - \dot{\alpha}_1) \text{sn}\alpha_1 + \dot{\alpha}_1 \omega_2) L_3$$

$$+ \omega_2 \omega_3 r_3 - r_2(\omega_1^2 + \omega_3^2) + \omega_1 \omega_2 r_1$$

$$+ ((\omega_2 + \dot{\beta}_1 \sin \alpha_1)(\omega_3 + \dot{\alpha}_1) L_3 - ((\omega_1 + \dot{\beta}_1 \cos \alpha_1)^2 + (\omega_3 + \dot{\alpha}_1)^2) L_2$$

$$+ (\omega_1 + \dot{\beta}_1 \cos \alpha_1)(\omega_2 + \dot{\beta}_1 \sin \alpha_1) L_1$$

$$B_3 = (\dot{\beta}_1(-\omega_3 - \dot{\alpha}_1) \sin \alpha_1 + \dot{\alpha}_1 \omega_2) L_2 - (\dot{\beta}_1(\omega_3 + \dot{\alpha}_1) \cos \alpha_1 - \dot{\alpha}_1 \omega_1) L_1$$

$$+ \omega_1 \omega_3 r_1 - r_3(\omega_1^2 + \omega_2^2) + \omega_2 \omega_3 r_2$$

$$+ ((\omega_1 + \dot{\beta}_1 \cos \alpha_1)(\omega_3 + \dot{\alpha}_1) L_1 - ((\omega_1 + \dot{\beta}_1 \cos \alpha_1)^2 + (\omega_2 + \dot{\beta}_1 \sin \alpha_1)^2) L_3$$

$$+ (\omega_2 + \dot{\beta}_1 \sin \alpha_1)(\omega_3 + \dot{\alpha}_1) L_2$$

$$C_1 = (I_2 - I_3) \omega_2 \omega_3$$

$$C_2 = (I_3 - I_1) \omega_1 \omega_3$$

$$C_3 = (I_1 - I_2) \omega_1 \omega_2$$

$$D_{\beta_l} = \text{Damping coefficient wrt } \beta \text{ angle} \quad \begin{array}{l} = 0.35 \text{ ft-lb}_f\text{-sec} \\ = 0 \end{array} \quad \begin{array}{l} \text{for } j=4 \text{ and } l=1, \dots, n \\ j <> 4 \end{array}$$

$$D_{\alpha_l} = \text{Damping coefficient wrt } \alpha \text{ angle} \quad \begin{array}{l} = 0.35 \text{ ft-lb}_f\text{-sec} \\ = 0 \end{array} \quad \begin{array}{l} \text{for } j=5 \text{ and } l=1, \dots, n \\ j <> 5 \end{array}$$

$$F_j = \text{Control thrust} \quad \begin{array}{l} \\ = 0 \end{array} \quad \begin{array}{l} \text{for } j=1, 3 \\ j=2 \end{array}$$

$$I_1, I_3 = \text{Transverse axis inertia} \quad = 19513 \text{ lb}_m\text{-ft}^2$$

$$I_2 = \text{Roll axis inertia} \quad = 10240 \text{ lb}_m\text{-ft}^2$$

$$L = \text{Pendulum length} \quad = 7.2 \text{ inches}$$

$$L_1 = -L \sin \alpha_l \cos \beta_l \quad \text{for } l=1, \dots, n$$

$$L_2 = L \cos \alpha_l \cos \beta_l \quad \text{for } l=1, \dots, n$$

$$L_3 = L \sin \beta_l \quad \text{for } l=1, \dots, n$$

$$\begin{aligned}
m_l &= \text{Pendulum mass} & = 5 \text{ lb}_m & \text{for } l=1, \dots, n \\
n &= \text{Number of pendulums} & = 2 & \\
r_1 &= -18 \cos\left(\frac{\pi}{2}\right)(l-1) \text{ inches} & & \text{for } l=1, \dots, n \\
r_2 &= 25 \text{ inches} & & \\
r_3 &= 18 \sin\left(\frac{\pi}{2}\right)(l-1) \text{ inches} & & \text{for } l=1, \dots, n \\
R &= \text{Thruster moment arm} & = 6 \text{ ft} & \\
u_1 &= 0 & & \\
u_2 &= -(r_3 + L_3) & & \\
u_3 &= r_2 + L_2 & & \\
u_4 &= r_3 + L_3 & & \\
u_5 &= 0 & & \\
u_6 &= -(r_1 + L_1) & & \\
u_7 &= -(r_2 + L_2) & & \\
u_8 &= r_1 + L_1 & & \\
u_9 &= 0 & & \\
u_{10} &= L_3 \sin \alpha_1 & & \\
u_{11} &= -L_3 \cos \alpha_1 & & \\
u_{12} &= L_2 \cos \alpha_1 - L_1 \sin \alpha_1 & & \\
u_{13} &= -L_2 & & \\
u_{14} &= L_1 & & \\
u_{15} &= 0 & &
\end{aligned}$$

The state variables for numerical solution of the equations are defined as,

Y_1	= Angular velocity of main body along b_1 direction wrt main body fixed frame	= ω_1
Y_2	= Angular velocity of main body along b_2 direction wrt main body fixed frame	= ω_2
Y_3	= Angular velocity of main body along b_3 direction wrt main body fixed frame	= ω_3
Y_4	= Angular velocity component of pendulum about β_1 degree of freedom relating the pendulum relative angular velocity wrt the main body fixed frame	= $\dot{\beta}_1$
Y_5	= Angular velocity component of pendulum about α_1 degree of freedom relating the pendulum relative angular velocity wrt the main body fixed frame	= $\dot{\alpha}_1$
.		
.		
.		
Y_{3+2n-1}		= $\dot{\beta}_n$
Y_{3+2n}		= $\dot{\alpha}_n$
Y_{4+2n}	= Angular position component of pendulum about β_1 degree of freedom relating the pendulum position wrt the main body fixed frame	= β_1
Y_{5+2n}	= Angular position component of pendulum about α_1 degree of freedom relating the pendulum position wrt the main body fixed frame	= α_1
.		
.		
.		
Y_{2+4n}		= β_n
Y_{3+4n}		= α_n
Y_{4+4n}	Euler parameter 1 relating orientation of main body fixed frame to inertial frame	= ϵ_1
Y_{5+4n}	Euler parameter 2 relating orientation of main body	= ϵ_2

fixed frame to inertial frame

Y_{6+4n} Euler parameter 3 relating orientation of main body
fixed frame to inertial frame = ϵ_3

Y_{7+4n} Euler parameter 4 relating orientation of main body
fixed frame to inertial frame = ϵ_4

List of Figures

1. Model of spacecraft with spherical pendulum
2. Pendulum fixed and body fixed reference frame orientation
3. Euler parameter gains vs. time for thruster 1
4. Euler parameter gains vs. time for thruster 2
5. Body fixed angular rate gains vs. time for thruster 1
6. Body fixed angular rate gains vs. time for thruster 2
7. Pendulum angular rate gains vs. time for thruster 1
8. Pendulum angular rate gains vs. time for thruster 2
9. Pendulum angular position gains vs. time for thruster 1
10. Pendulum angular position gains vs. time for thruster 2
11. Body fixed angular rates vs. time for stabilization maneuver without fluid state observation
12. Main body orientation angles vs. time for stabilization maneuver without fluid state observation
13. Thrust forces vs. time for stabilization maneuver without fluid state observation
14. Body fixed angular rates vs. time for pointing maneuver without fluid state observation
15. Main body orientation angles vs. time for pointing maneuver without fluid state observation
16. Thrust forces vs. time for pointing maneuver without fluid state observation
17. Command forces vs. time for pointing maneuver without fluid state observation

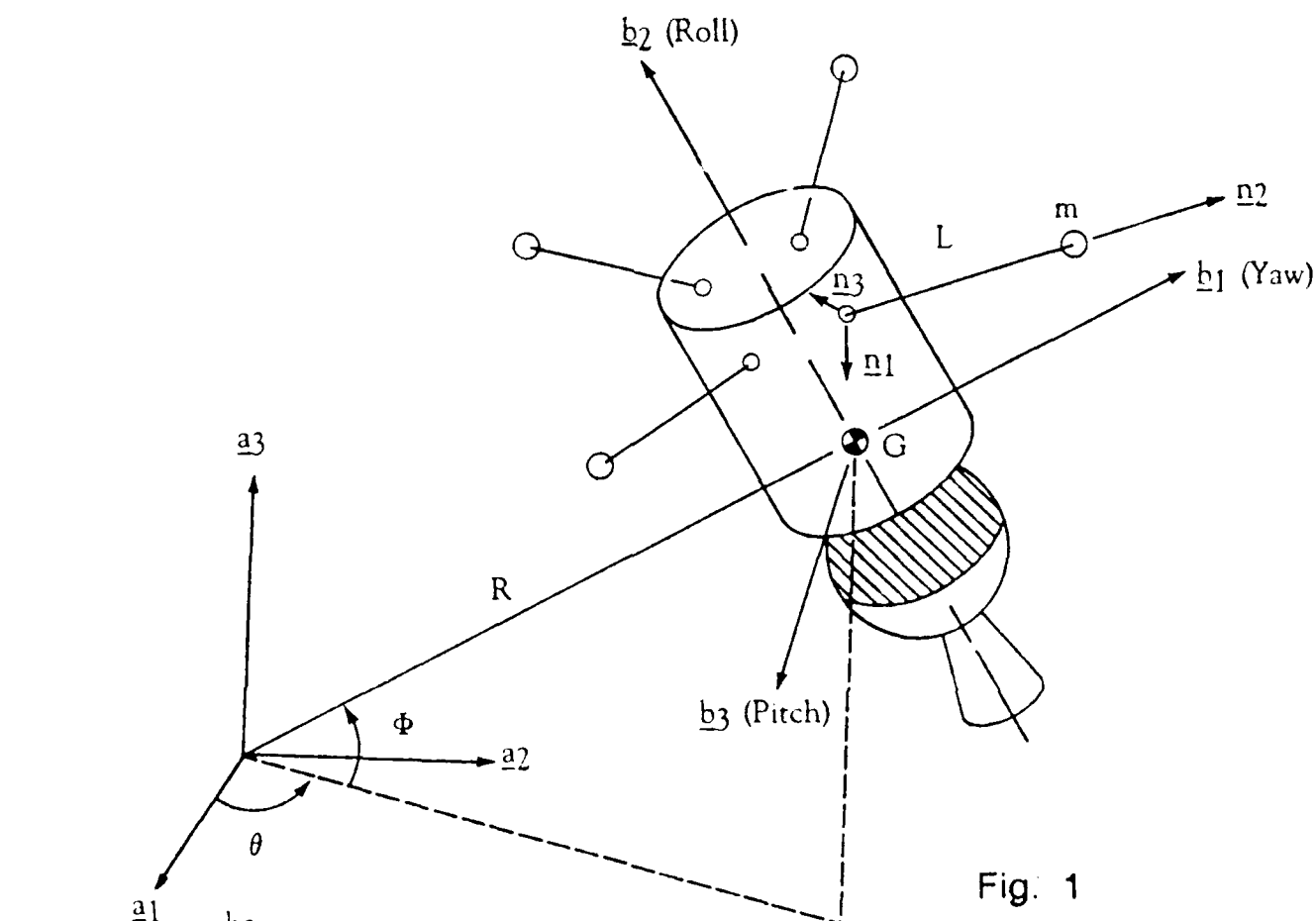


Fig. 1

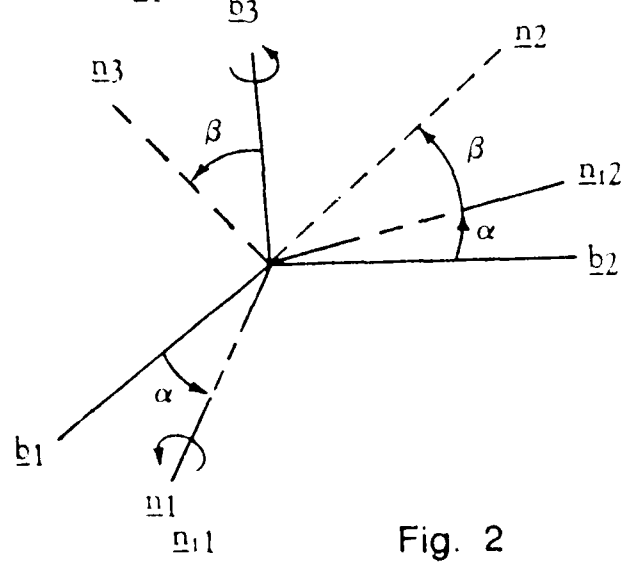


Fig. 2

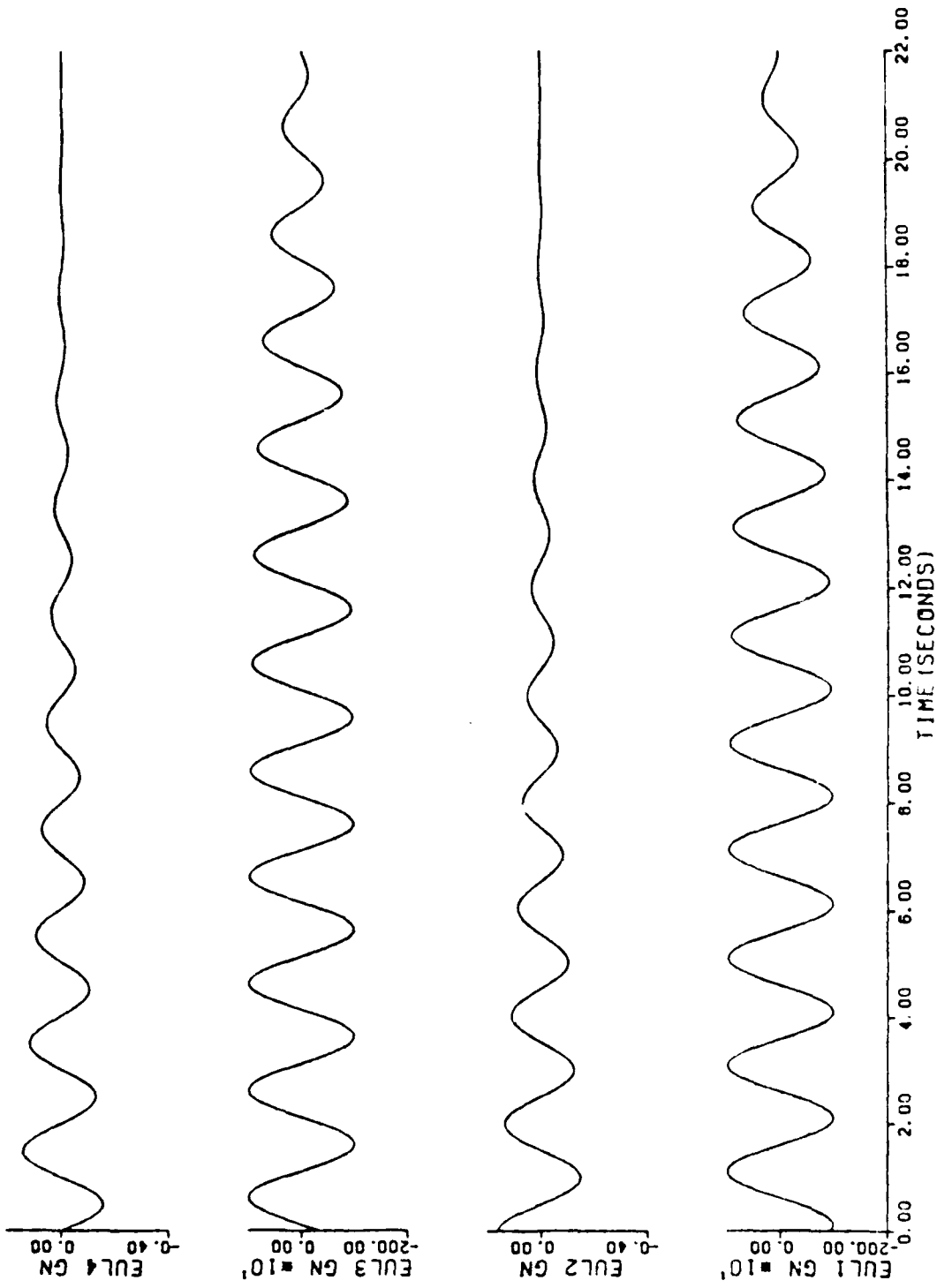


Fig. 3

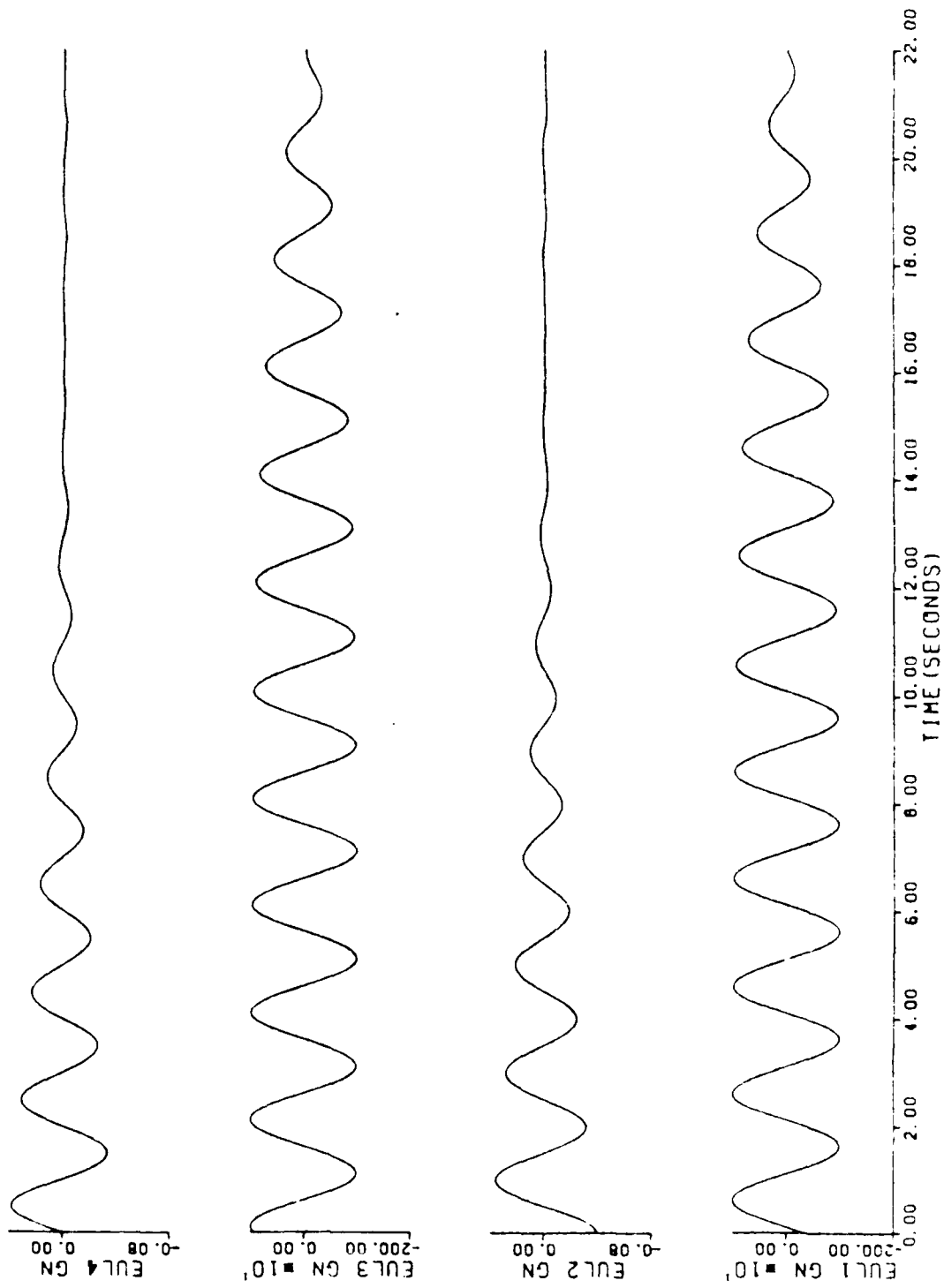


Fig. 4

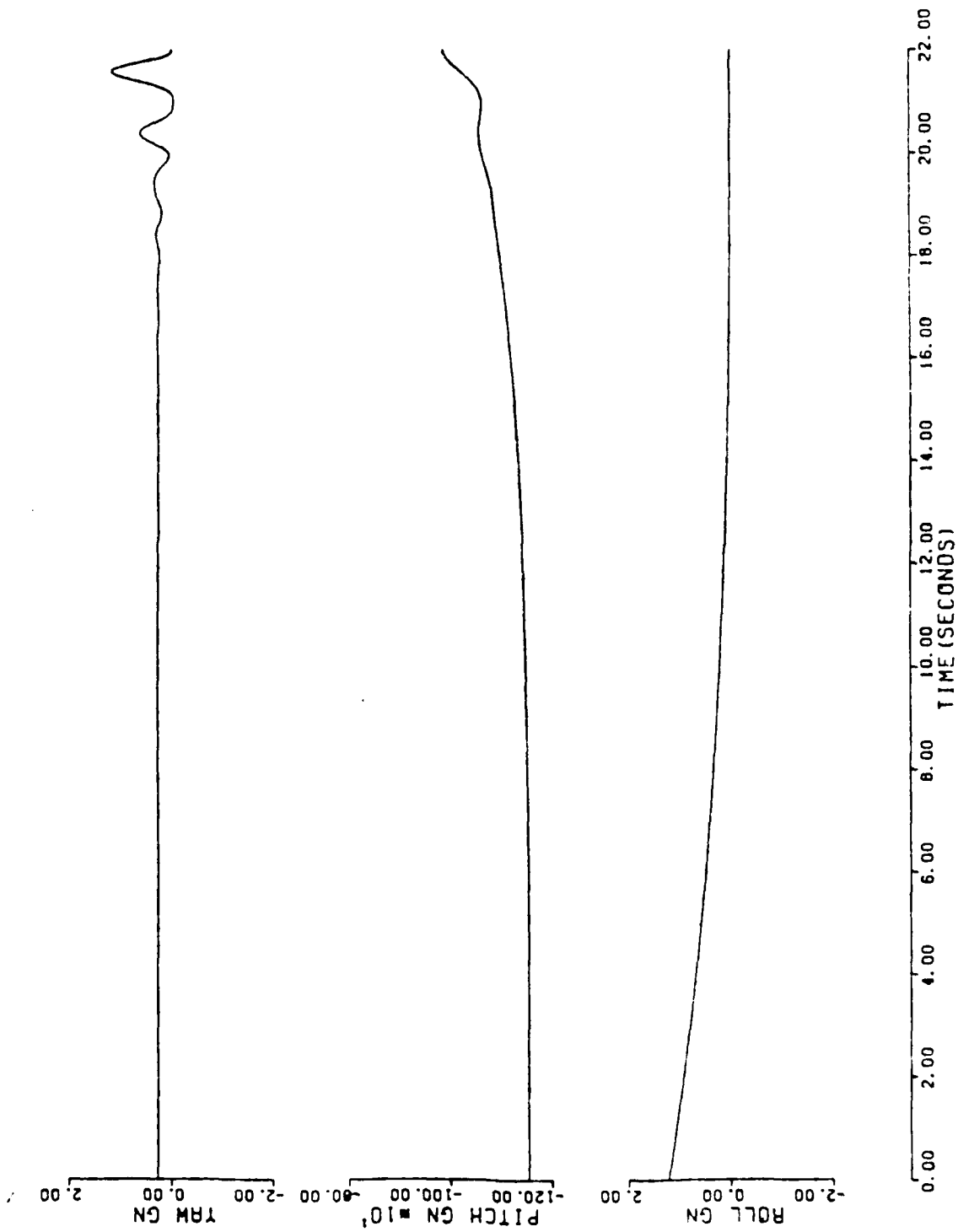


Fig. 5

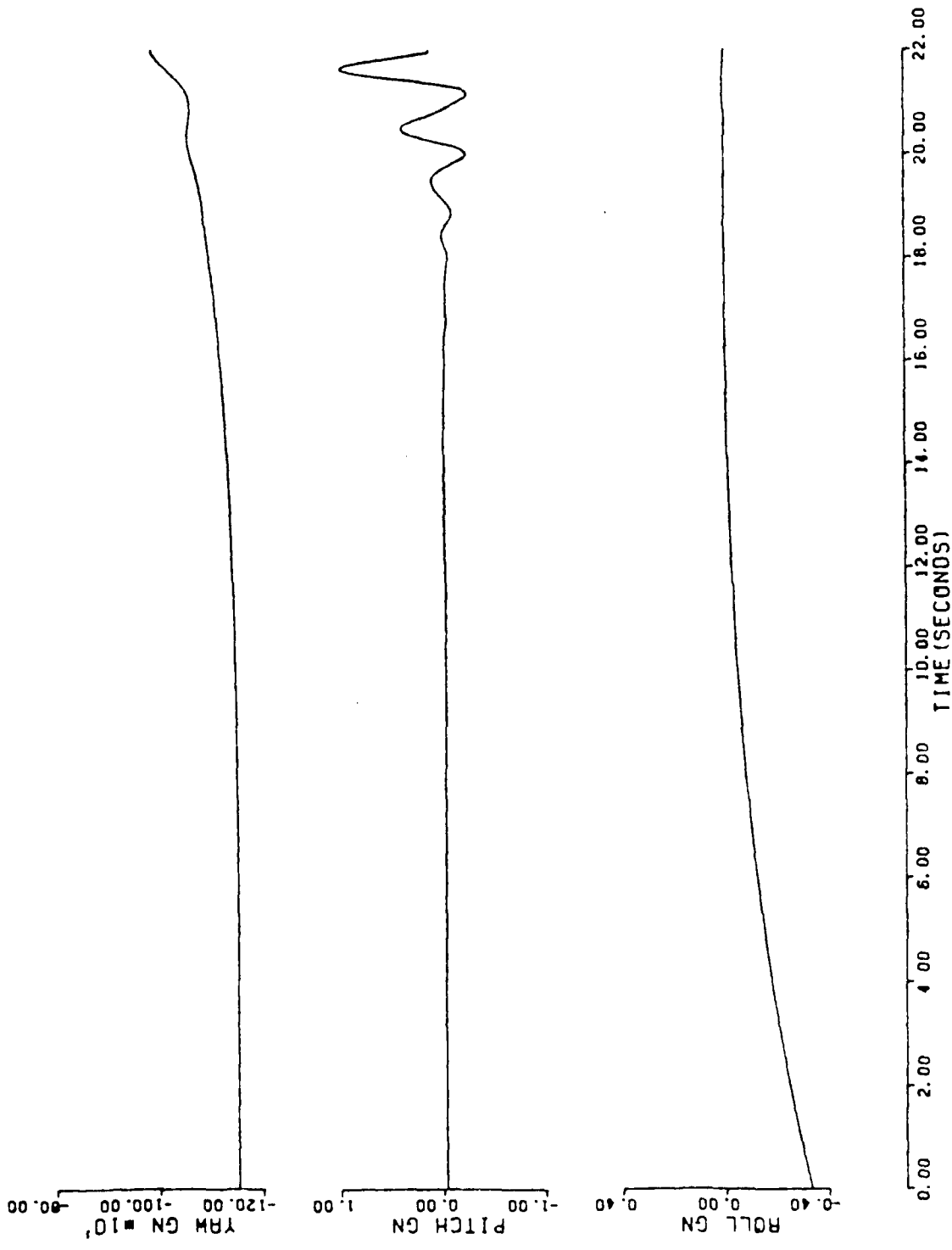


Fig. 6

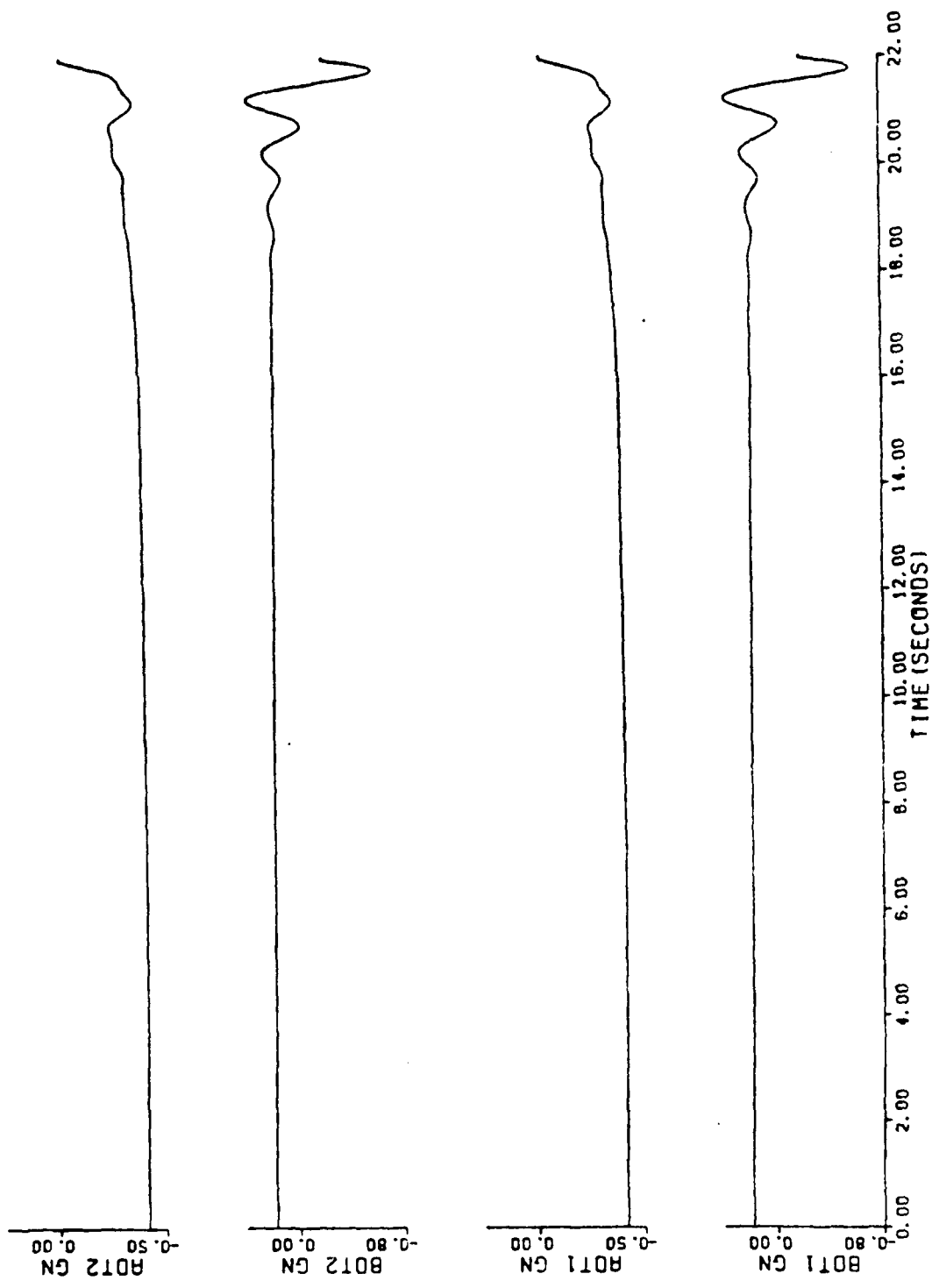


Fig. 7

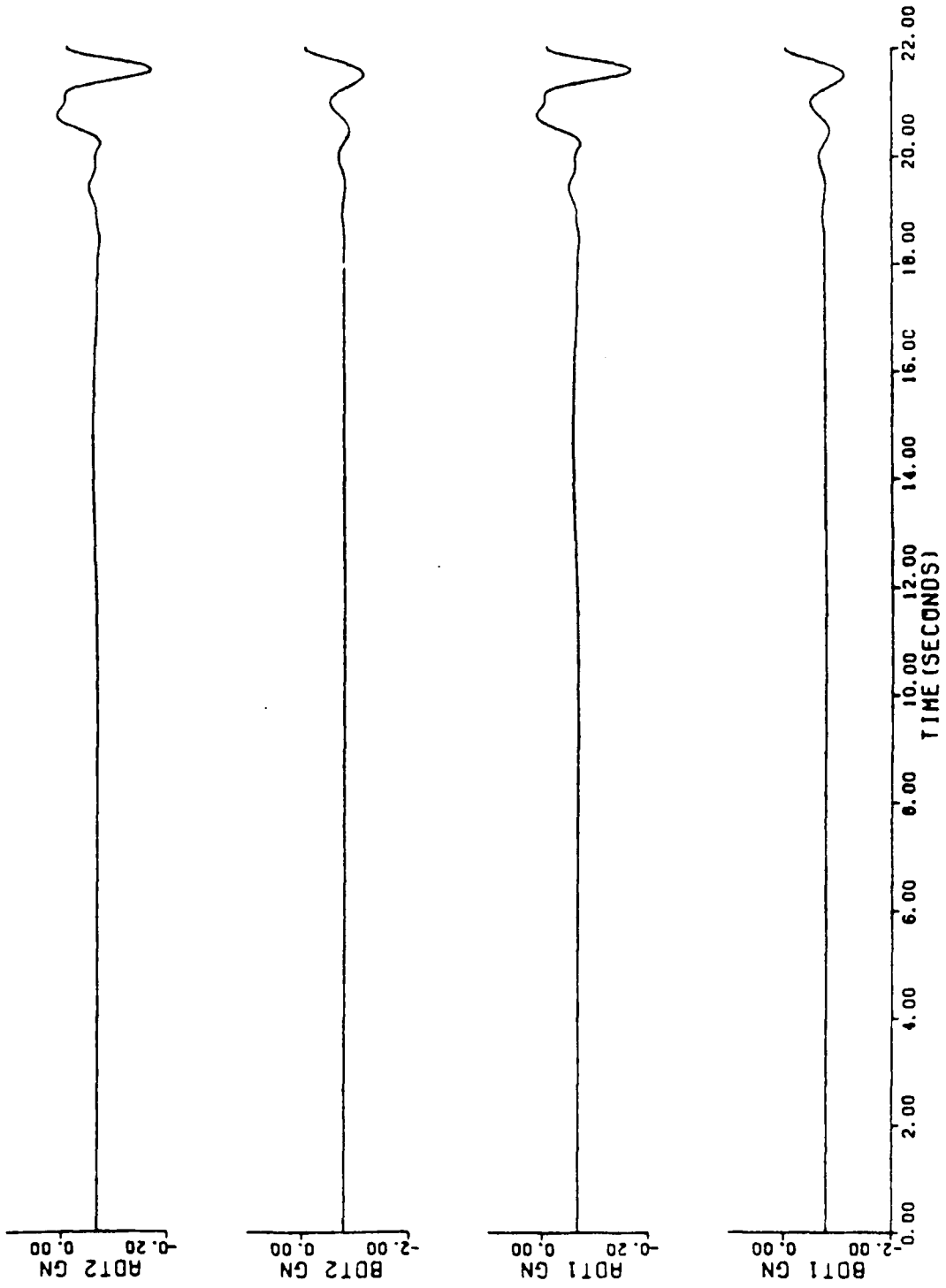


Fig. 8

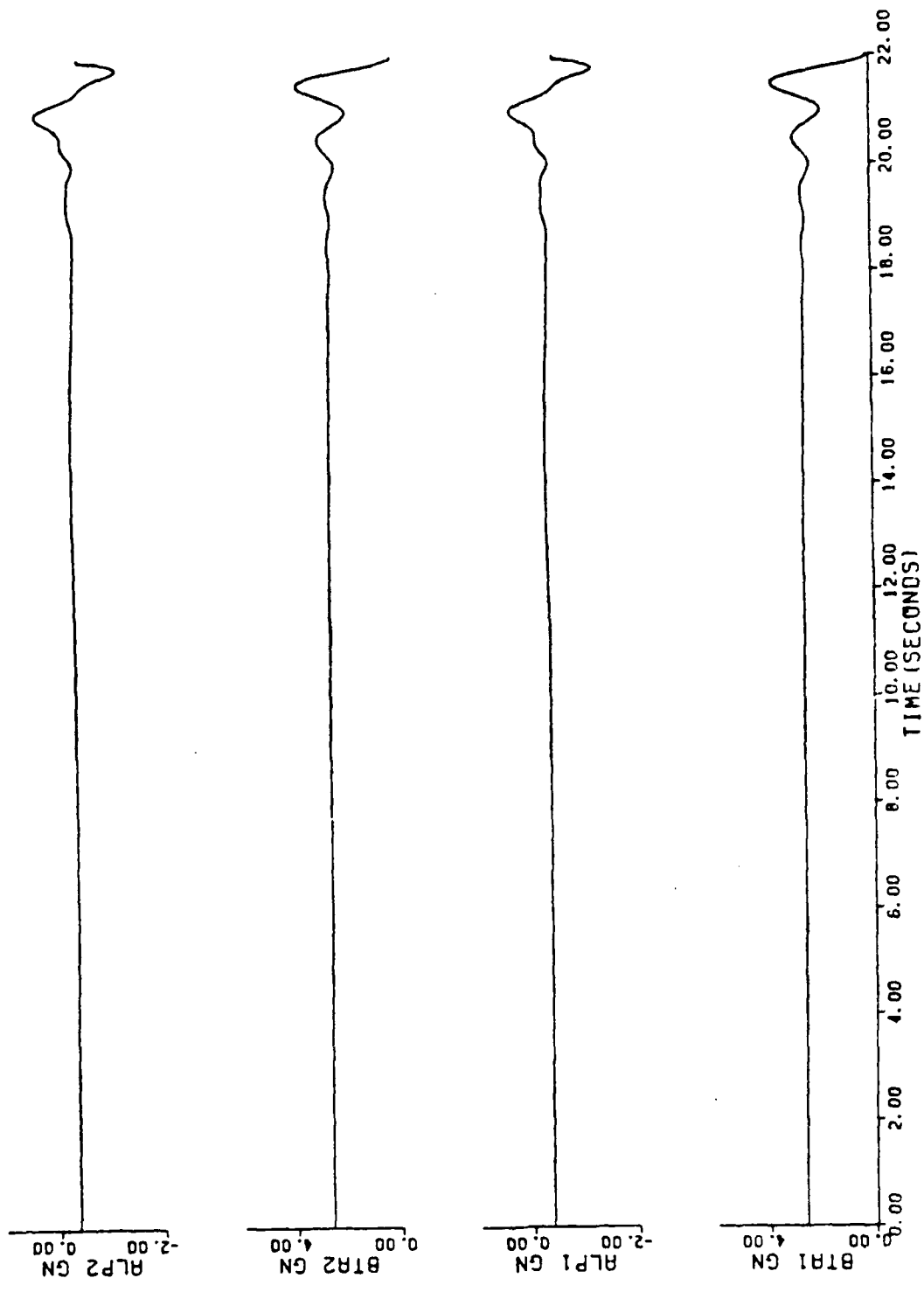


Fig. 9

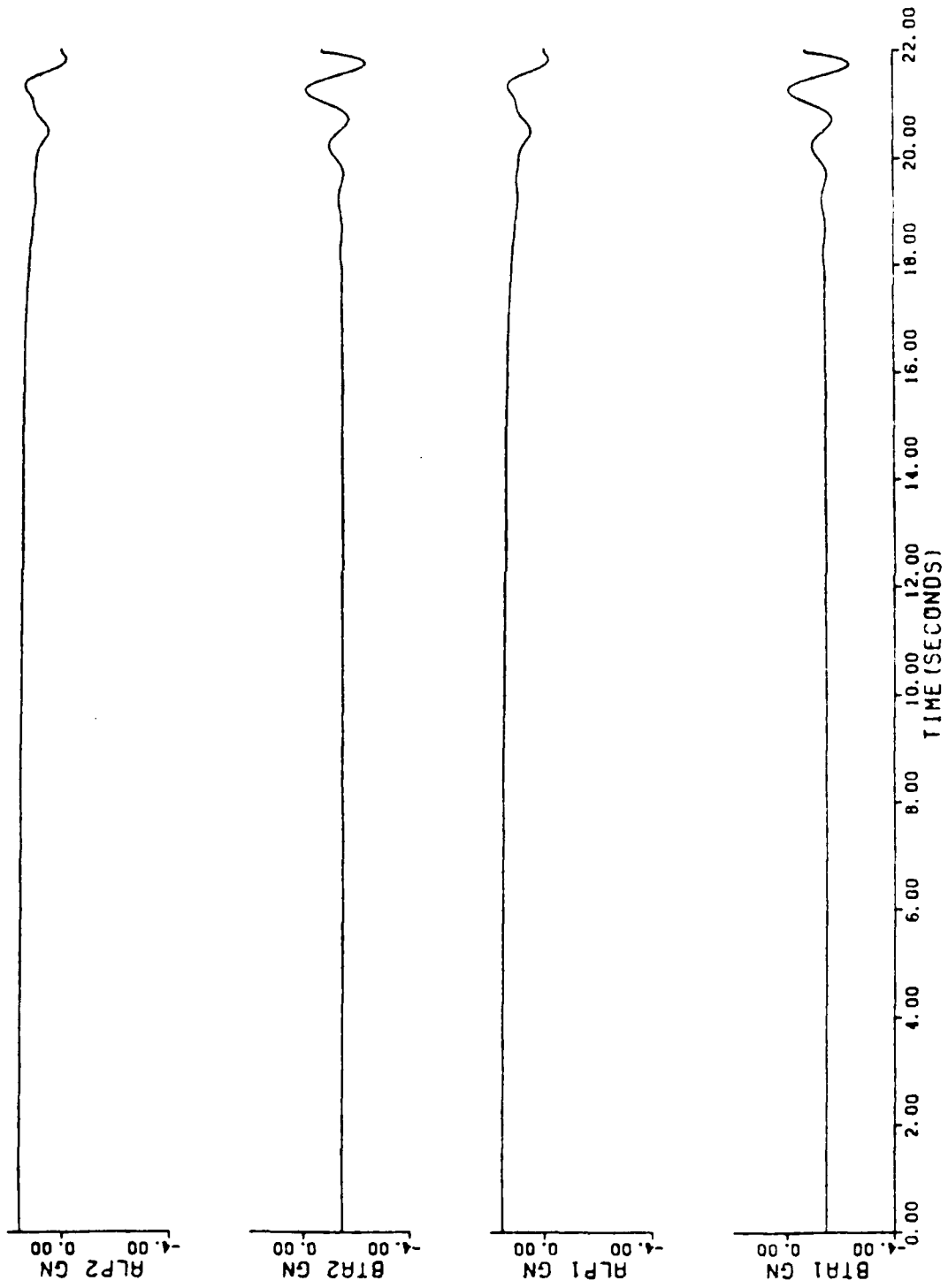


Fig. 10

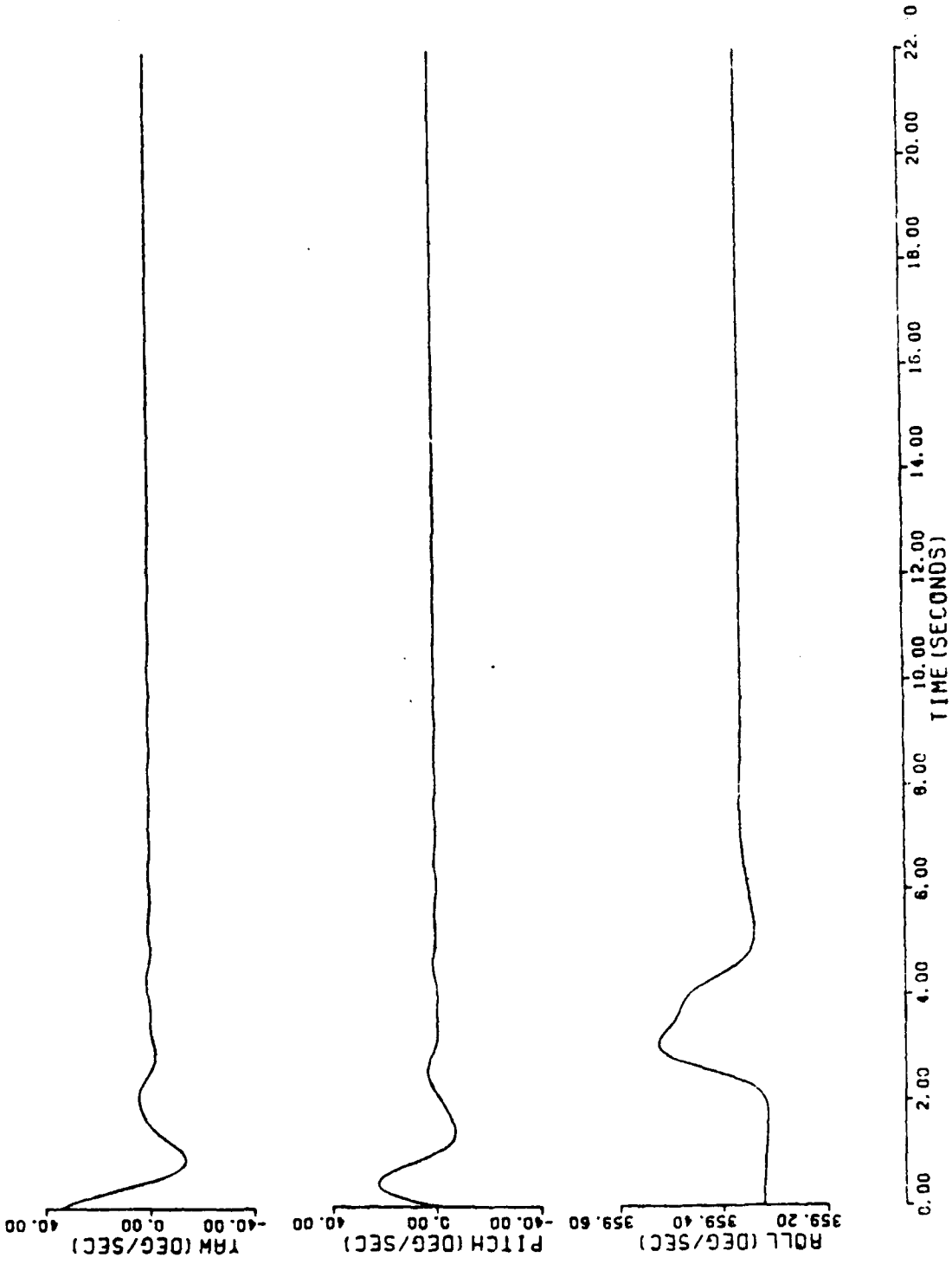


Fig. 11

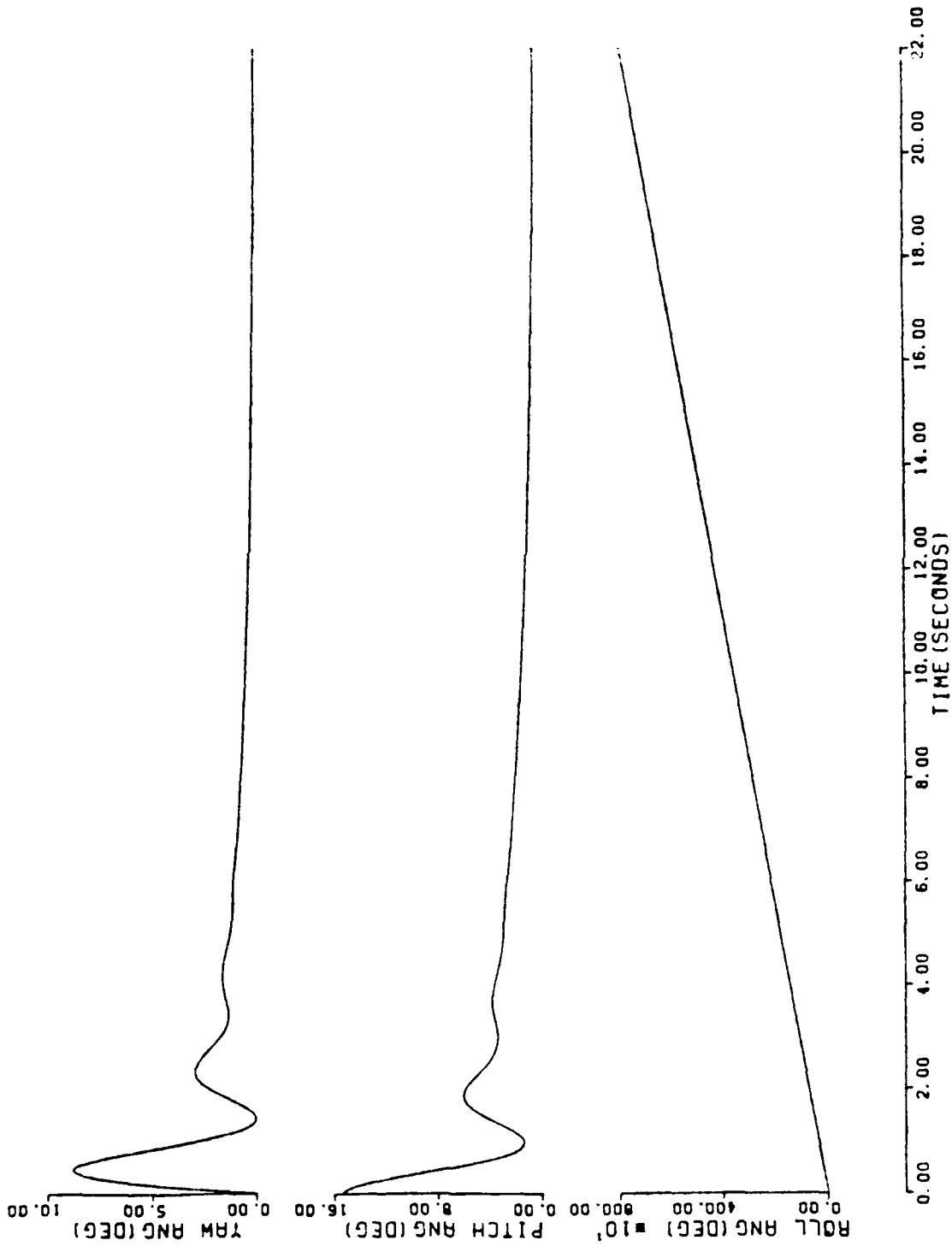


Fig. 12

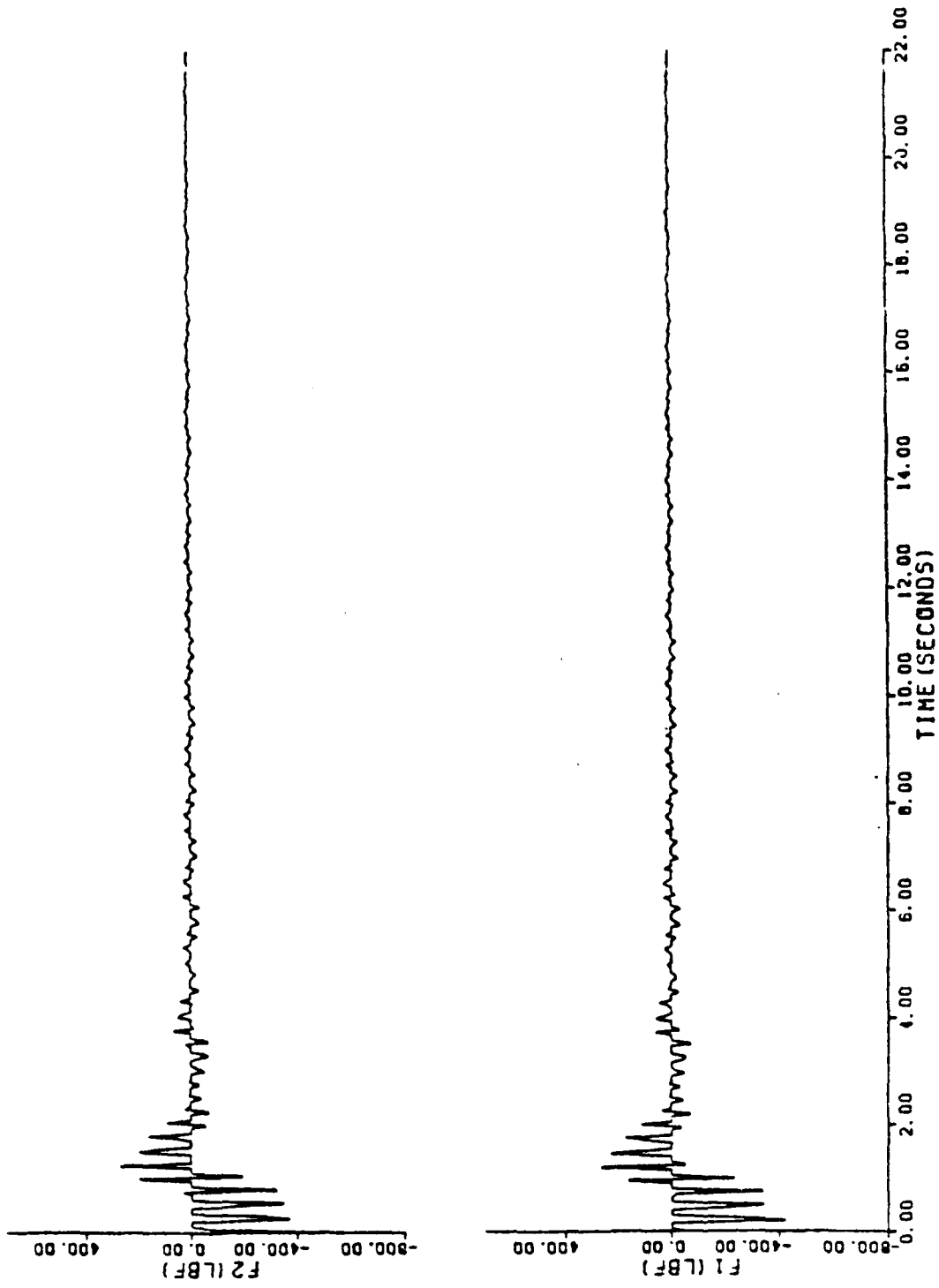


Fig. 13

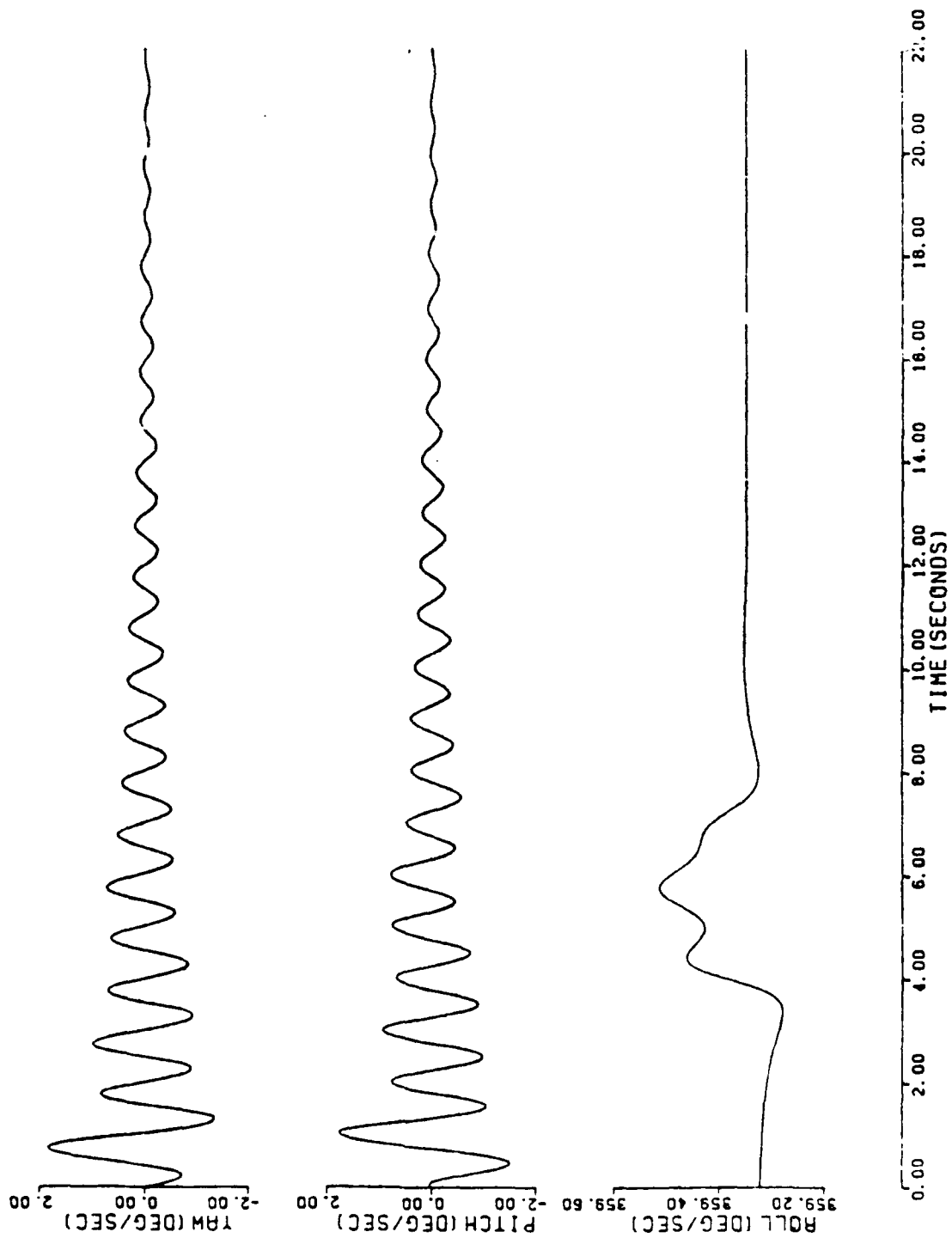


Fig. 14

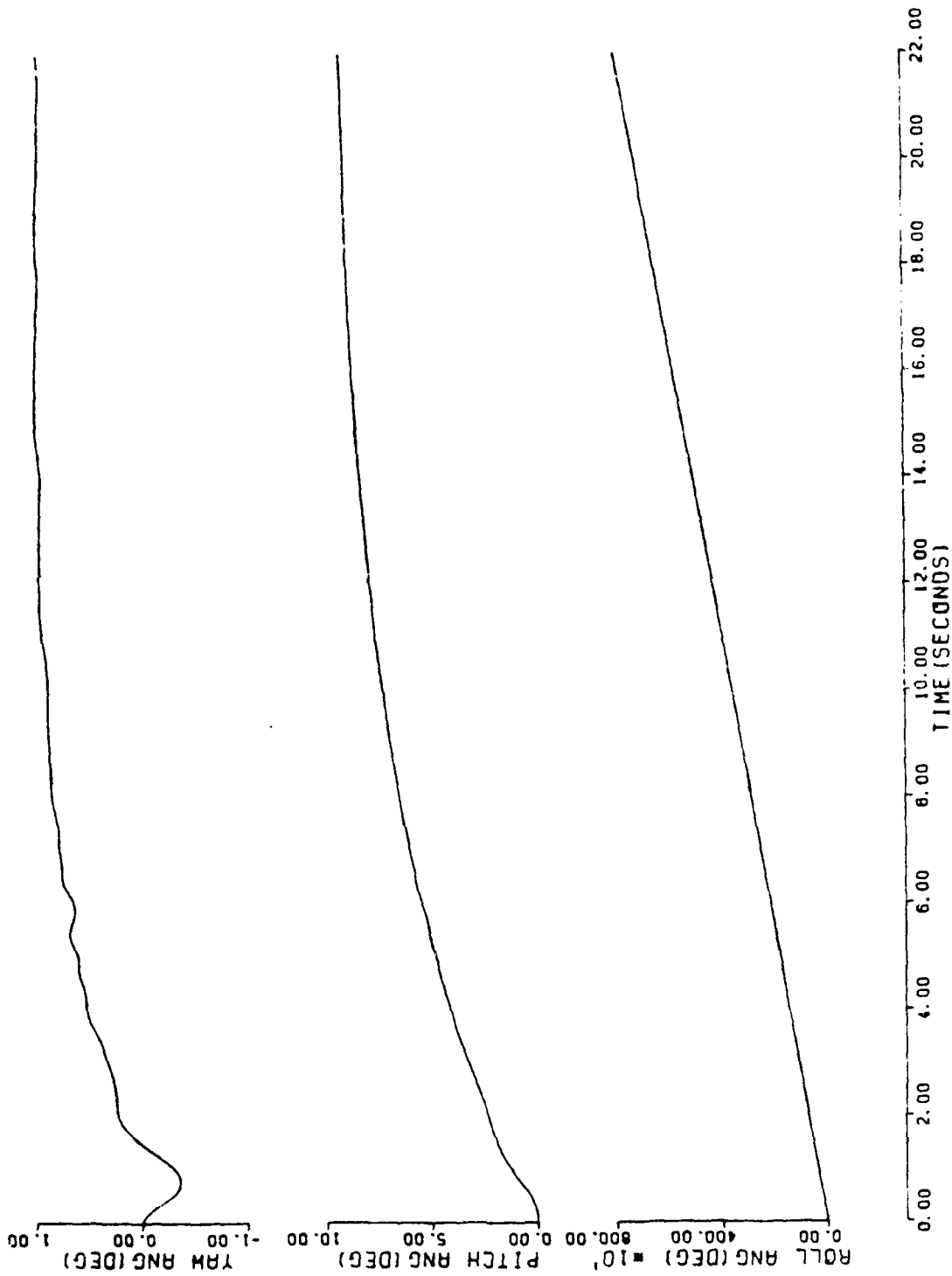


Fig. 15

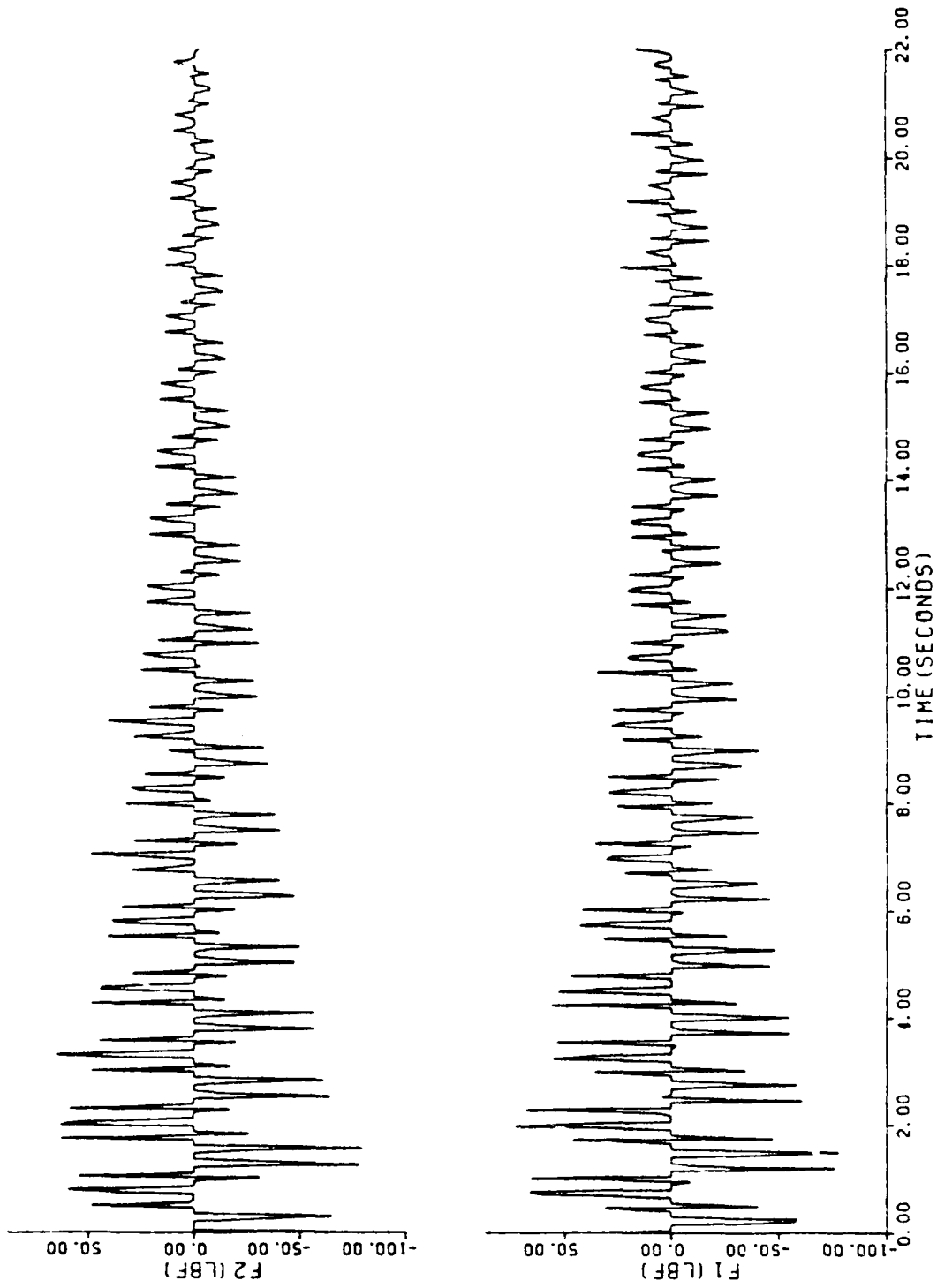


Fig. 16

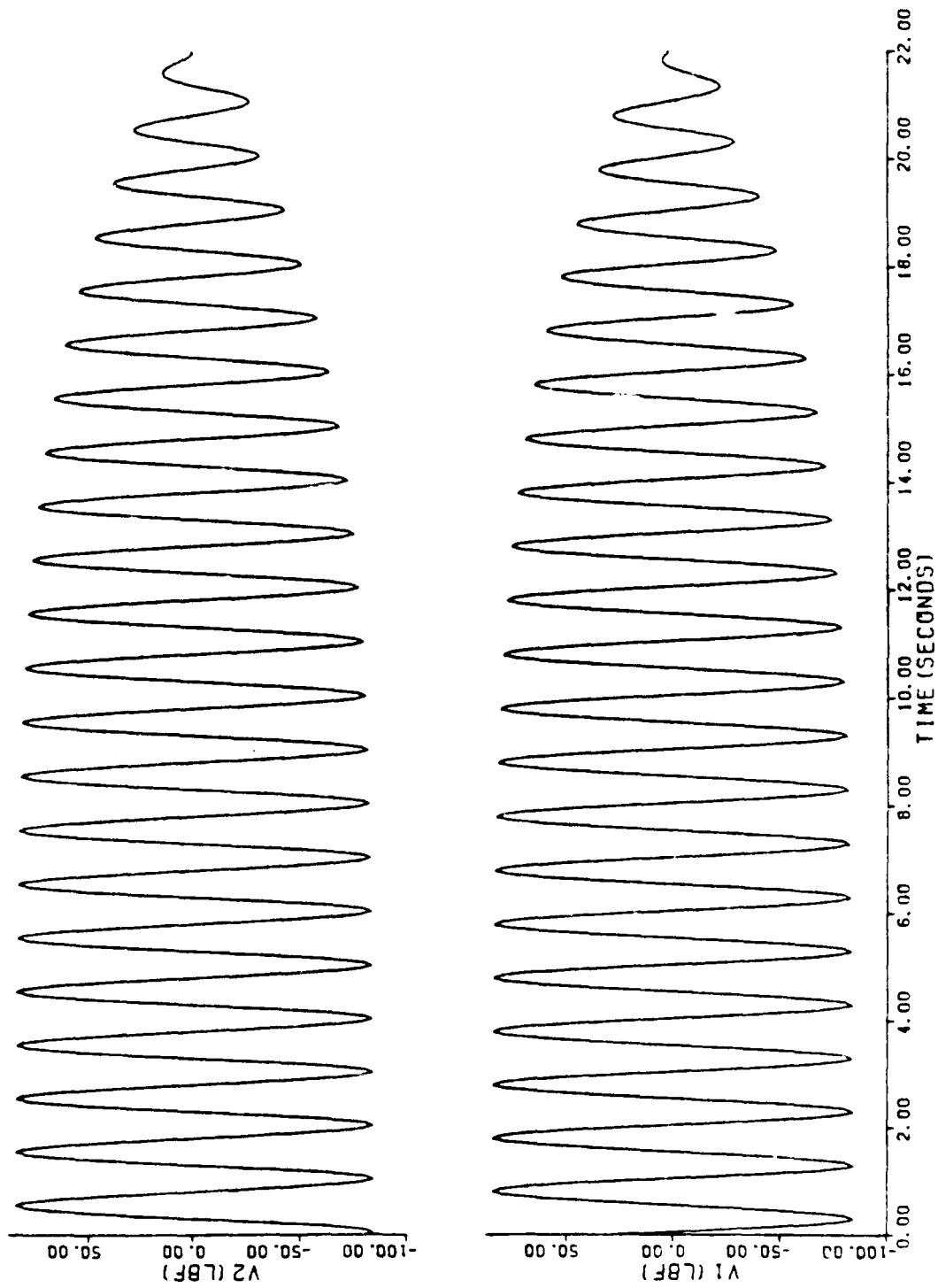


Fig. 17

APPENDIX C

SATELLITE SIMULATOR
TEST RIG DESIGN

A TEST FIG TO SIMULATE LIQUID SLOSHING
IN SPIN-STABILIZED SATELLITES -- PART I: DESIGN AND INSTRUMENTATION

D. R. Flugrad
M. D. Anderson
D. S. Cowles
Iowa State University
Ames, Iowa

ABSTRACT

Several communication satellites with liquid stores on board have experienced an undesirable coning motion when boosted into a geosynchronous orbit about the earth. These spin-stabilized satellites carry tanks filled with liquid for station tending and attitude adjustment of the spinning structure. If a significant amount is used to eliminate an initial nutational motion, the useful life of the satellite is correspondingly decreased. On the other hand, sloshing of the liquid is believed to be the cause of the problem. A test rig was built to study the interaction between the rotating body and the sloshing liquid. The design and instrumentation of the rig is described in this paper with experimental results presented in the companion paper, Part II. The spinning assembly, which is mounted atop a universal joint to allow coning, includes two liquid-filled tanks. Instrumentation monitors the spin speed of the rig, the rigid body orientation of the assembly, and the motion of the liquid.

INTRODUCTION

Launchings of several of the STAR 48 communications satellites from the space shuttle have resulted in an unstable, nutating motion of the satellite. Flight data from roll, pitch, and yaw axis rate gyros have indicated a constant frequency, equal amplitude, sinusoidal oscillation of the spacecraft about its pitch and yaw axes. The pitch and yaw oscillations have been 90° out of phase. The vector combination of these two components of vibration are consistent with a coning motion of the satellite spin axis. This nutation occurs even though the spacecraft is spin-stabilized at launch with a one revolution per second roll velocity.

After launch from the shuttle in the perigee phase of its orbit, the satellite's power assist module (PAM) is fired to establish a geosynchronous earth orbit. At first it was theorized that the axial thrust gives rise to the coning motion which predominates after PAM motor burnout. Combustion instabilities in the PAM rocket motor were thought to be the source of a side force that could induce the coning motion [1]. But an investigation performed at Arnold Engineering Development Center's Engine Test Facility indicated that no significant forces at the required frequency (one-half cycle per second) were present. Therefore, it was concluded that combustion instabilities were not the source of moments about the principal axes of the spacecraft causing coning motion.

It was then proposed that the sloshing motion of the liquid fuel stores in the vehicle was the mechanism for inducing the nutational motion. If a perfectly rigid body spins about its axis of maximum moment of inertia or about its axis of minimum moment of inertia with no external forces acting on the body, then the resulting motion is stable [2]. If, however, there is any

internal energy dissipation, then the only stable spin is about the axis of maximum moment of inertia. This axis provides a minimum rotational energy state for a given constant angular momentum. Spin about the intermediate axis of inertia is an unstable motion.

Although spin-stabilization of a body about its axis of maximum moment of inertia produces a stable spin, this is subject to some constraints with regard to the design of flexible spacecraft with liquid-filled tanks. Agrawal [3] presented stability conditions for a flexible spinning spacecraft by a Liapunov method. Various techniques have been developed to determine the effects of liquid propellant motion on the spacecraft's moments of inertia. The stability conditions require that the spin to transverse moment of inertia ratio be greater than $(1+C)$, where C is a positive definite function of spacecraft parameters, such as propellant density, tank size and location relative to the spacecraft center of mass, and spacecraft inertias.

The STAR 48, and many other spacecraft, are prolate spinners -- spin-stabilized about their axes of minimum moment of inertia. This is the maximum energy state for a given angular momentum. Therefore, if there is any internal dissipation of energy, the spacecraft will attempt to conserve its angular momentum, and it will begin to reorient its spin about an axis associated with a lower energy state. This is commonly referred to as "coning" since the spin axis generates a cone with its vertex located at the center of mass of the spacecraft. If this coning motion is not controlled, the spacecraft will eventually enter a flat spin--a spin about the axis of maximum moment of inertia (the minimum energy state for a given angular momentum). Since the STAR 48 and many other spacecraft contain a large liquid propellant mass fraction, it seems probable to consider sloshing fluid stores as a major source of internal kinetic energy dissipation, hence a mechanism

for the destabilization of a prolate spinner.

Many investigators have studied the basic characteristics associated with sloshing liquids. This has formed a basis for researchers interested in the sloshing effect on space vehicle dynamics. The motion of a spinning spacecraft with liquid propellant is described by very complex mathematical equations for the rigid spacecraft dynamics and partial differential equations for the liquid in the tanks, including appropriate initial and boundary conditions.

In order to simplify fluid slosh studies, researchers have sought a mechanical model to represent the fundamental mode of fluid slosh. Sumner [4] conducted an experimental investigation to determine the general liquid sloshing characteristics (fundamental frequencies, horizontal or side slosh forces, and damping ratios) as well as quantities for a pendulum analogy that would effectively represent the fundamental mode of liquid sloshing in unbaffled oblate-spheroid and spherical tanks over a range of liquid depths. Although the fundamental slosh damping was measured by the log decrement method, the pendulum model he used didn't allow for any viscous damping.

Hill [1] coupled the pendulum model of Sumner [4] to a set of nonlinear ordinary differential equations for the rigid spacecraft dynamics and simulated the system on a digital computer. The pendulum model was also augmented by adding viscous dashpots to represent the viscous damping of the fundamental slosh mode. Results were compared to actual telemetered flight data with good correlation. A control scheme was presented and implemented in the simulation, also with good results.

Zedd and Dodge [5] devised a mechanical model composed of a pendulum, a rotor, and viscous dashpots. The pendulum represented the free surface modes of oscillation (sloshing) and the rotor represented the inertial wave modes of

oscillation--circulatory or to-and-fro motions in the liquid interior. In this model the rotor was connected to the tank by a dashpot to simulate the forcing of inertial waves by the boundary layer shear at the tank wall. Other dashpots were used to simulate the viscous damping of the fundamental and inertial modes of fluid oscillation. The model was used to simulate liquid forces and moments; to predict liquid resonances and energy dissipation rates; and to scale-up test results to flight conditions. A forced-motion spin table was used to estimate the numerical values for the model parameters.

Using the principles of similitude, Garg, Furumoto, and Vanyo [6] directly scaled test data from a forced motion test apparatus to predict energy dissipation rates. Results were compared to previous drop test data and to actual flight data.

This present study involves the design and instrumentation of a physical test rig to demonstrate the dynamic characteristics of a spin-stabilized system with sloshing liquid stores. A vertical spin axis was chosen for a horizontal beam that supports two six inch diameter plastic spheres located at an equal radial distance from the spin axis. A two degree-of-freedom Hooke's type universal joint was located just below the horizontal beam in the vertical shaft to allow the spin axis of the beam structure to cone. A yoked sleeve, actuated by a straight-line motion four-bar mechanism, was utilized to cover the universal joint to give initial stability and rigidity to the system during spin-up.

The initial design configuration resulted in a spin about the axis of intermediate moment of inertia. This was a very unstable mode of operation. The second configuration involved the addition of another crossbar, perpendicular to the main horizontal beam, to act as an inertial counterbalance. This resulted in a spin about the axis of maximum moment of

inertia. This system configuration was very stable and any perturbation to induce coning quickly disappeared (within 2-3 seconds). The third configuration, attained after considerable design modification, allowed spin about the axis of minimum moment of inertia. This proved to be unstable.

Also described in this paper are the transducers and instrumentation system used to monitor the motions of the rotating structure and the sloshing liquid. It was decided that the most important factors to observe were the driving spin rate, the oscillations of the spinning test rig assembly, and the liquid motion in the spheres. A computer based data acquisition system was employed to rapidly record data and to perform quantitative analysis of large data files. The test rig was redesigned to incorporate the instrumentation. Simultaneously, the rig was modified so the weight could be redistributed to achieve a static balance condition with the center of mass located near or slightly below the supporting joint.

TEST RIG DESIGN

The test rig design had to allow modification of most major dimensions to allow testing of various sizes of tanks and geometric configurations. It was decided that a minimum of instrumentation would be implemented until the operation of the system was better understood and decisions could be made about which parameters to instrument.

A physical system was designed, consisting of a vertical spin shaft with a horizontal crossbar. Figs. 1 and 2 show assembly views of the test rig design. Two plastic spheres were supported by the horizontal bar at equal radial distances from the vertical spin axis. A two degree-of-freedom Hooke's type universal joint was located just below the horizontal beam in the

vertical shaft to allow the spin axis of the horizontal beam structure to cone. A yoked sleeve, hand-actuated by a straight-line motion four-bar mechanism was utilized to cover the universal joint to give initial stability and rigidity to the system during spin-up. A 1/4 hp electric d.c. motor was selected to drive the system.

Six inch diameter spheres were used. A fill height of approximately 3.9 inches produced a beam load on each end of about five pounds. The length of the steel horizontal beam for the first design was 27.32 inches. It was 0.625 inches wide, and 0.25 inches thick. The overall crossbar length was 54.64 inches.

A 10:1 right angle gear reducer was inserted between the motor and vertical drive shaft to utilize the more efficient upper speed range of the motor. Since the STAR 48 satellites are spin-stabilized at one revolution per second, this was chosen as the nominal operating speed, although speeds up to three times this were possible with the motor and gear reducer system.

Test Rig Operation and Analysis

Operation of the initial design of the completed test rig, as shown in Fig. 3, resulted in a very unstable motion. As soon as the supporting sleeve was lowered, the upper assembly would instantly drop over, rotating about an axis parallel to the main horizontal beam.

An analysis of the system inertias indicated that the spin axis was the axis of intermediate inertia. The transverse inertias were 0.02 and 2.37 slug-ft², and the inertia about the spin axis was 2.36 slug-ft². From Greenwood [2], spin of a torque-free, rigid body about its axis of intermediate moment of inertia is an unstable motion. Although the test rig is not absolutely rigid, it is assumed to be nearly so, and it is further

assumed to be torque-free since the system center of mass is approximately located at the intersection of the universal joint axes.

For the second design configuration a shorter main support beam of 35.2 inches was chosen (compared to 54.6 inches for the initial design). A 54.6 inch inertial counterbalance beam was added normal to the main beam to produce a maximum moment of inertia about the spin axis. The inertias were 0.13 and 2.38 slug-ft² about the transverse axes and 2.46 slug-ft² about the spin axis.

Operation of the second configuration pictured in Fig. 4 proved to be very stable. Any perturbation disappeared within one or two seconds. It was impossible to determine visually whether or not any significant fluid slosh was present and whether or not there was any interaction between the fluid and the physical structure.

It was decided that a spin about the minimum axis of inertia--a spin that is stable only if there is no internal energy dissipation--would best demonstrate the destabilizing effects of sloshing liquid fuel on a spin-stabilized vehicle.

Test Rig Modifications

The major change in the rig structure to allow for instrumentation of additional configurations involved lengthening the main vertical shaft by 15 inches to provide additional clearance between the universal joint and the bearing supports. This clearance allowed the spheres to be mounted low enough to place the center of mass at or below the universal joint, even when the assembly was spun about an axis of minimum moment of inertia. Decreasing the radial distance from the main shaft to the sphere centers while raising the cross-beams higher above the universal joint provided the key to achieving spin about the minimum axis of inertia. The only other obvious way to produce

a spin about the minimum axis of inertia would have required a substantial addition of weight concentrated near the spin axis. The new design allowed investigation of a wide variety of inertia ratios both greater than and less than one by changing cross beams or by raising and lowering the spheres.

A new upper collar was designed to restrict the cone angle and to prevent damage to the unit under unstable operating conditions while providing the ability to restabilize the rig during spin. This can be seen in Fig. 5. The collar is free to slide vertically along the length of the spinning shaft and allows the operator to stabilize the rig while bringing it up to speed. The top of the collar has an oversized inner diameter to restrict the half-cone angle to a maximum of 10° . If the collar didn't have this feature, the nutational motion could produce an interference between the lower shaft and spheres. The oversized diameter affords clearance necessary for the universal joint to pivot within the collar, and it contacts the shaft about one inch above the pivot to allow sufficient leverage to restabilize the rig.

Providing a fixed reference on which to mount the rotational potentiometers, while maintaining the features of the collar described above, proved to be a significant instrumentation challenge. It was determined that the upper collar could be slotted to allow it to slide vertically with the potentiometer mounting pins extending through the slots. The potentiometers were mounted on two threaded rods which pass through the lower shaft to provide a rigid reference. A small brass tube was placed around the protruding threads to provide a bearing surface between the rods and the slots in the upper collar. The two sets of threaded rods together maintain alignment and reduce binding of the collar.

The slip rings were mounted below the collar arrangement on the lower shaft. Therefore, the redesign required machining a groove in the lower shaft

to allow the instrumentation wires to pass through the inside of the shaft to avoid contact with the fork of the linkage. Because the upper collar was already restrained from rotating relative to the shaft, it seemed logical to slot the collar and pass the wires through the slot. The wires exit the lower shaft in an intermediate collar section to avoid disturbing the natural motion of the rig.

INSTRUMENTATION

Instrumentation was developed to study the effects of liquid motion on the test rig dynamics. It was anticipated that the important quantities would be liquid position, test rig rotation rate and orientation. One obstacle to instrumentation was the collection of transducer signals from the rotating assembly. Slip rings were chosen based on cost and anticipated ease of use. It was decided to track the position of the liquid by monitoring the free surface profile. A d.c. tachometer was chosen to sense the input rotational speed. The rig orientation was monitored with two rotational potentiometers used to sense rotation of the test rig about perpendicular axes through the universal joint. The tachometer and potentiometers were sufficient to allow comparison of experimental data with satellite parameters from the literature such as half-cone angle, precession rate and relative spin rate. A computer data acquisition system was utilized because of its analysis capability and its ability to handle large quantities of data.

Slip Ring Selection

Transmission of transducer signals from the rotating structure to a stationary data recording system was an important objective in the

instrumentation of the satellite test rig. Slip rings were selected over alternatives such as telemetry based on cost, anticipated reliability, and simplicity of use. A through ring design was chosen to mount on the supported portion of the lower shaft. After selection of all transducers, a slip ring assembly was picked based on satisfactory noise level, current capacity, and an acceptable design suited to the work envelope provided by the test rig.

A fourteen ring assembly was chosen to supply 10 volt d.c. power to the sensors and to receive up to ten signals. An external brush block design was specified based on its ample performance specifications at reasonable cost. This slip ring set was used to receive readings from two rotational potentiometers and six light sensitive photopotentiometers. The signals were of sufficient magnitude so that any noise associated with the slip rings was negligible. The assembly has additional capacity to handle future addition of strain gauges on the rotating structure. Amplification of the strain gauge bridge signal prior to transmission through the rings is expected to produce satisfactory results.

Measurement of Tilt, Nutation and Precession

The important parameters for tracking the rig orientation include the tilt angle from vertical (the half-cone angle), the nutation rate (the time rate of change of the half-cone angle), and the precession rate. The precession rate is specified as the angular velocity of the main axis of the spinning test rig about a ground fixed vertical axis. To determine these quantities, the instrumentation was designed to sense rotations about the axis of each pin of the universal joint. This approach provided information about the rig orientation relative to the lower input shaft.

Two inexpensive rotational potentiometers were selected for this task. A

light weight spring was designed to overcome the friction of the rotational potentiometer and maintain tension on the pulley string. Thirty pound monofilament fishing line was selected over a variety of other possibilities for resisting stretch, and for closely conforming to the pulley radius with little tension.

During the design phase, it was anticipated that each of the rotational potentiometers would be insensitive to rotation about the axis on which it was mounted. However, trial calibrations showed that this was not the case. One cause was found to be a slight misalignment between the beams of the test rig and the axes of the potentiometers. Because of the complexity of the geometry, it was decided that the nonlinear equations describing the system with its misalignment should be developed and solved rather than have the parts remachined. The orientation of the rig at any time can be determined by first rotating through an angle, λ_3 , about the vertical \bar{k}_2 -axis; by then rotating about the \bar{j}'_2 -axis through an angle λ_1 ; and finally by rotating through an angle $\bar{\lambda}_2$ about the \bar{i}_4 -axis. This sequence is illustrated in Fig. 6. The equations that describe the system are a combination of six equations from two vector loops and four equations relating the extension of the pulley strings and the rotation of the potentiometers. Development of the equations is presented in the appendix. The construction error of the rig associated with the misalignment of the cross beams was determined by using a computer program to first solve for a theoretical rotational potentiometer position for known rig rotations. Voltage readings were experimentally determined at positions located by measuring the tilt of the cross bars with a carpenter's level and adjustable triangle. The theoretical voltages were determined by interpolating between the experimental voltages corresponding to $+8^\circ$ and -8° of rotation about each axis for the theoretical potentiometer positions.

Construction angle, λ_3 , was then determined as the value that minimized the sum of the absolute differences between the experimental and calculated voltages.

To ensure accuracy of the data, it was decided that the calibration procedure should be carried out before and after each set of trials. After initial practice to gain familiarity with the system, this procedure proved quite workable.

Once the set of fourteen nonlinear equations describing the geometry of the rig and potentiometer were solved, the two axis rotations were used to derive more information regarding the motion. For instance, the two rotations alone were used to solve for the half-cone angle and nutation rate. In addition, the projection of a vertical, body-fixed unit vector was located in a horizontal plane fixed to rotate with the input shaft. Furthermore, once the rig input speed was known, the precession rate was determined relative to a stationary reference frame.

Input Speed Measurement

Measurement of the driving rig speed is important because of the associated centrifugal acceleration. Furthermore, the input speed is used in the determination of the precession rate as discussed previously. A d.c. tachometer that produces a voltage proportional to rotational speed was used to provide a continuous reading of the instantaneous angular velocity.

For greater sensitivity, this tachometer was mounted on the high side of the 10:1 gear reducer that drives the rig. For calibration, the HP-85 data collection computer was used to average 15 voltage readings at each of several spin speeds. Simultaneously, the rig rotations were visually counted for a period ranging from 45 to 60 seconds to determine the average rotation rate.

This calibration was completed just once for the entire set of runs. The performance of the tachometer was characterized by a linear least squares fit technique.

Sensing The Liquid Sloshing Motion

The decision was made to instrument both spheres for liquid movement to allow determination of any interaction between the sloshing liquid on the two sides. It was assumed that the water would not break away from the free liquid surface. A photosensitive device which could give quantitative output based on light blockage by the moving liquid surface seemed ideal.

A light sensitive photopotentiometer was located with a working range of 3.4 inches. The operation of this device is similar to common wirewound potentiometers with the exception that the resistance and hence the voltage output is proportional to both intensity of incident light and sensor area exposed to light. The device was tested with various dyes introduced into the water in the spheres to block the transmission of light through the liquid. Blue dye #2 was selected for its high opacity. Yet it is highly soluble in water which prevents permanent discoloration of the spheres. Plans called for six photopotentiometers--two sensors on each sphere to measure oscillations in a radial direction and a third sensor mounted on each sphere to measure oscillations in the circumferential direction. See Fig. 7 for mounting locations.

The two radial sensing photopotentiometers were mounted at a 45° tilt angle based on estimates of the water position for half-filled spheres at expected spin speeds. The circumferential sensor was mounted perpendicular to the 45° tilt for maximum sensitivity. Since the photopotentiometers are rigid, they were encased in receptacles to ensure that their output would

depend only on light passing through the sphere. The current design of the structure holding the spheres doesn't allow for easy repositioning of these sensors. Thus, both radial sensors were nominally located for runs made with the spheres half filled. In the case of one-quarter volume fill, the lower inside sensor was inactive because it was uncovered at most experimental run speeds. Similarly, only one sensor was active at three-quarter fill since the upper, outside sensor was completely covered for this case.

During initial test runs the photopotentiometers exhibited erratic output with variations of nearly one volt. Similar variations were encountered even with the collar restraining the rig from nutating. The primary root of the problem was determined to be the uneven lighting provided by parallel rows of fluorescent lights in the laboratory. The variation in output was greatly reduced by repositioning the test rig midway between parallel rows of lights and by constructing a large six foot diameter "lampshade" from translucent material. With the shade in place over the rig, the signal noise measured during steady rotation was found to lie between 0.10 and 0.15 volts. Although not perfect, this level of noise was relatively small compared to the expected output signal.

Initially the photopotentiometers were calibrated statically to relate voltage output to an equivalent water angle. This calibration assumed that the liquid surface would remain flat and that tilting the sphere statically to a known angle would produce the same output as the water being spun outward during operation of the test rig. Reduced experimental data showed liquid oscillations of roughly 10° - 15° . The data indicated roughly the same magnitude of radial slosh from the radial sensors on each sphere, but the difference between the absolute water angles for the radial transducers on each individual sphere was too large to be ignored.

So that the sensors would better agree, the static calibration was replaced by a dynamic calibration technique using the HP-85 computer. This procedure related the voltage output of the photopotentiometers to an equivalent pendulum angle with the help of the following expression [4]:

$$\tan \gamma_0 = g/\Omega^2 (X_0 + \cos \gamma_0) \quad (1)$$

In Eq. (1)

γ_0 = the angle between a horizontal reference and the
equivalent pendulum arm

g = gravitational acceleration

Ω = the drive spin rate

X_0 = the radial distance from shaft center to the pivot
of the equivalent pendulum

The computer was used to average ten readings of each photopotentiometer while the spin speed was determined by the tachometer. A calibration curve of calculated angle vs. voltage output was developed by a polynomial curve fitting routine. The results of this calibration showed good agreement between the radial sensors on each respective sphere. However, the output of the lower inside sensor was slightly clipped when the liquid sloshed outward from the center. It is believed that this phenomenon was observed because the outer sensor saw the liquid advancing toward a previously clean portion of the sphere surface, while the inner sensor detected a sheeting action of the retreating liquid. Because the radial housing photopotentiometers were mounted at a 45° angle, the output for the half full spheres exhibited a near

linear relationship between tilt angle and voltage. The calibration curves for both one-quarter and three-quarter fill was better described by a cubic expression.

Data Collection System

The goal of the data acquisition system was to sample all measurements at a rate at least ten times the signal frequency to accurately record the quantity. The schematic diagram of the instrumentation and data collection system is shown in Fig. 8. Based on its ease of use, the Hewlett-Packard HP-85 computer was used to record up to 200 readings per second. To achieve this sample rate, the computer was used in the voltmeter complete mode, data were taken in binary coded decimal format, and both the filter and display were turned off.

The sample rate used for most runs was approximately 65 readings per second because a compromise had to be made between high sample rate and length of the data file created. This means each of the nine transducers was sampled seven times per second. This sample rate proved to be sufficient for most runs. For a few cases, such as runs with the spheres empty or runs that were physically perturbed, the sample rate was doubled to provide sufficient accuracy. The data were ultimately transferred from the HP-85 computer to a VAX 11-785 computer system for greater computing and plotting capabilities.

SUMMARY

The test rig described in this paper makes it possible to study the interaction between the dynamics of a rotating structure such as a spin-stabilized satellite and the sloshing motion of onboard liquid stores.

The rig was designed to allow different crossbeam configurations to be mounted on the supporting universal joint. In addition, the tanks can be repositioned vertically to adjust the location of the center of mass of the spinning assembly.

Instrumentation has been provided to monitor the input speed for the rig, the angular orientation of the rotating body and the motion of the liquid contained in the two spherical tanks. Slip rings are used to transfer the transducer signals from the rotating assembly to an automated computer data collection system. Additional rings are available to add strain gages to the system to measure the deflection of the rods on which the tanks are mounted. The data collected during test runs have been transferred to a VAX 11-785 computer which is used to calculate specific quantities of interest and to plot the results.

In the companion paper, Part II, several experimental runs are described in which such things as the inertias, tank fill heights and input speeds were varied to determine the effects these factors have on the overall stability of the motion. Many additional test cases are planned for the future.

ACKNOWLEDGMENT

This study was accomplished with the support of the Air Force Office of Scientific Research under grant AFOSR-86-0080.

REFERENCES

1. Hill, Daniel E. "Dynamics and control of spin-stabilized spacecraft with sloshing fluid stores." Ph.D. dissertation, Iowa State University, Ames, Iowa, 1985.
2. Greenwood, Donald T., Principles of Dynamics, Prentice Hall, Inc., Englewood Cliffs, New Jersey, 1965.
3. Agrawal, B. N., "Stability of Spinning Spacecraft with Liquid-Filled Tanks." American Institute of Aeronautics and Astronautics, 19th Aerospace Sciences Meeting, St. Louis, Missouri, January 1981.
4. Sumner, Irving E., "Experimentally Determined Pendulum Analogy of Liquid Sloshing in Spherical and Oblate-Spheroidal Tanks," Technical Note TN D-2737, National Aeronautics and Space Administration, April 1965.
5. Zedd, Michael, and Dodge, Franklin T., "Energy Dissipation of Liquids in Nutating Spherical Tanks Measured by a Forced Motion-Spin Table," NRL Report 8932, Naval Research Laboratory, Washington, D.C., October 1985.
6. Garg, S.C., Furumoto, N., and Vanyo, J. P., "Spacecraft Nutational Instability Prediction by Energy-Dissipation Measurements," American Institute of Aeronautics and Astronautics, Journal of Guidance, Vol. 9, May-June 1986.

APPENDIX

The equations for the rotational potentiometers are based on the quantities shown in Fig. 6. The rig orientation with cross beams parallel to the rotational potentiometer shafts can be determined by a rotation λ_3 about the \bar{k}_2 axis, followed by a rotation λ_1 about the \bar{j}_2' axis and finally by a rotation λ_2 about the \bar{i}_4 axis. The rig orientation expressed in coordinates of the lower shaft is described by the concatenation of the following transformations:

$$\bar{x}_3' = \bar{x}_4 \quad (2)$$

$$\bar{y}_3' = \cos \lambda_2 \bar{y}_4 - \sin \lambda_2 \bar{z}_4$$

$$\bar{z}_3' = \sin \lambda_2 \bar{y}_4 + \cos \lambda_2 \bar{z}_4$$

$$\bar{x}_3 = \cos \lambda_1 \bar{x}_3' + \sin \lambda_1 \bar{z}_3' \quad (3)$$

$$\bar{y}_3 = \bar{y}_3'$$

$$\bar{z}_3 = -\sin \lambda_1 \bar{x}_3' + \cos \lambda_1 \bar{z}_3'$$

$$\bar{x}_2 = \cos \lambda_3 \bar{x}_3 - \sin \lambda_3 \bar{y}_3 \quad (4)$$

$$\bar{y}_2 = \sin \lambda_3 \bar{x}_3 + \cos \lambda_3 \bar{y}_3$$

$$\bar{z}_2 = \bar{z}_3$$

A loop closure equation for the rig shaft, cross-beam, pulley string, and the potentiometer mount dimensions can be written for the x-axis potentiometer as follows:

$$\bar{z}_4 + \bar{x}_4 - S_2' - \bar{r}_p - \bar{H}_x - \bar{V}_x = 0 \quad (5)$$

where,

\bar{H}_x = horizontal distance and direction from lower shaft center
to pulley center

\bar{V}_x = vertical distance and direction from potentiometer shaft
to universal joint pins

\bar{r}_p = pulley radius directed to tangent point

Eq. (5) is then separated into three scalar component equations:

$$\frac{4}{2}x_2 - S_2' - Hx = 0 \quad (6)$$

$$\frac{4}{2}y_2 - S_2'y - r_p \cos \theta_2 = 0 \quad (7)$$

$$\frac{4}{2}z_2 - S_2'z - r_p \sin \theta_2 + V_{x2} = 0 \quad (8)$$

where,

$\frac{4}{2}x_2, \frac{4}{2}y_2, \frac{4}{2}z_2$ = rig components projected into the
{2} reference frame

S_2' = free length of the pulley string

$S_2'x, S_2'y, S_2'z$ = components of \bar{S}_2' in {2}

θ_2 = pulley rotation from horizontal to the line
tangent point (positive CW)

An additional required equation can be derived by applying the Pythagorean theorem to triangle $\bar{S}_2 \bar{S}_2' \bar{r}_p$. Neglecting the slight misalignment between \bar{r}_p and the actual pulley string attachment point, the expression may be written as

$$S_2^2 = S_2'^2 + r_p^2 \quad (9)$$

with,

S_2 = distance from the potentiometer shaft center to the line
attachment point on the test rig beam

If distance S_2 is expressed in terms of rig dimensions in the $x_2y_2z_2$ -coordinate system, then Eq. (9) yields

$$S_2'^2 + (r_p)^2 - ((\frac{4}{2}x_2 - Hx)^2 + (\frac{4}{2}y_2)^2 + (\frac{4}{2}z_2 + V_x)^2) = 0 \quad (10)$$

The quantity $S_2'^2$ can be written as the sum of the squares of the components

$$S_2'^2 = S_{2x}'^2 + S_{2y}'^2 + S_{2z}'^2 \quad (11)$$

The voltage drop measured for the potentiometer is proportional to the overall rotation, ϕ_2 . This rotation is the sum of the rotations due to the elongation of S_2' and the rotation of S_2 in space:

$$\phi_2 = \psi_2 + \theta_2 \quad (12)$$

where,

ϕ_2 = total rotation of x-axis potentiometer

ψ_2 = rotation due to elongation of S_2'

θ_2 = potentiometer rotation due to rotation of \bar{S}_2

The rotation, ψ_2 , due to elongation is determined from

$$S_2' - S_{20}' - r_p \psi_2 = 0 \quad (13)$$

with,

S_{20}' = arbitrary initial length of S_2'

Similarly, the equations for the potentiometer on the y-axis are:

$$\frac{4}{2}X_1 - S_{1x}' - r_p \cos \theta_1 = 0 \quad (14)$$

$$\frac{4}{2}Y_1 - S_{1y}' - H_y = 0 \quad (15)$$

$$\frac{4}{2}Z_1 - S_{1z}' - r_p \sin \theta_1 + V_y = 0 \quad (16)$$

$$S_1'^2 - \left(\frac{4}{2}X_1\right)^2 - \left(\frac{4}{2}Y_1 - H_y\right)^2 - \left(\frac{4}{2}Z_1 + V_y\right)^2 + (r_p)^2 = 0 \quad (17)$$

$$S_1'^2 - S_{1x}'^2 - S_{1y}'^2 - S_{1z}'^2 = 0 \quad (18)$$

$$\phi_1 - \psi_1 - \theta_1 = 0 \quad (19)$$

$$S_1' - S_{10}' - r_p \psi_1 = 0 \quad (20)$$

From the above development, Eqs. (8-20) and (10-20) fully describe the rig position. These 14 equations contain 14 quantities - λ_1, λ_2 .

S'_{1x} , S'_{1y} , S'_{1z} , S'_1 , S'_{2x} , S'_{2y} , S'_{2z} , S'_2 , θ_1 , θ_2 , ψ_1 , ψ_2 , ϕ_1 , and ϕ_2 . The rotational potentiometer voltage drops are utilized to experimentally determine ϕ_1 and ϕ_2 . A Newton-Raphson iterative technique can then be used to solve the equations for the 14 remaining entities. At the start, values are calculated for an orientation of $\lambda_1 = \lambda_2 = 0$ to establish estimates of the unknowns to be used in initiating the iterative technique. The initial guesses are then updated to the values from the previous solution for each successive position. The data reduction was carried out after the data had been transferred to the VAX computer. With the sampling rate used in this study, the scheme has proved to be quite satisfactory.

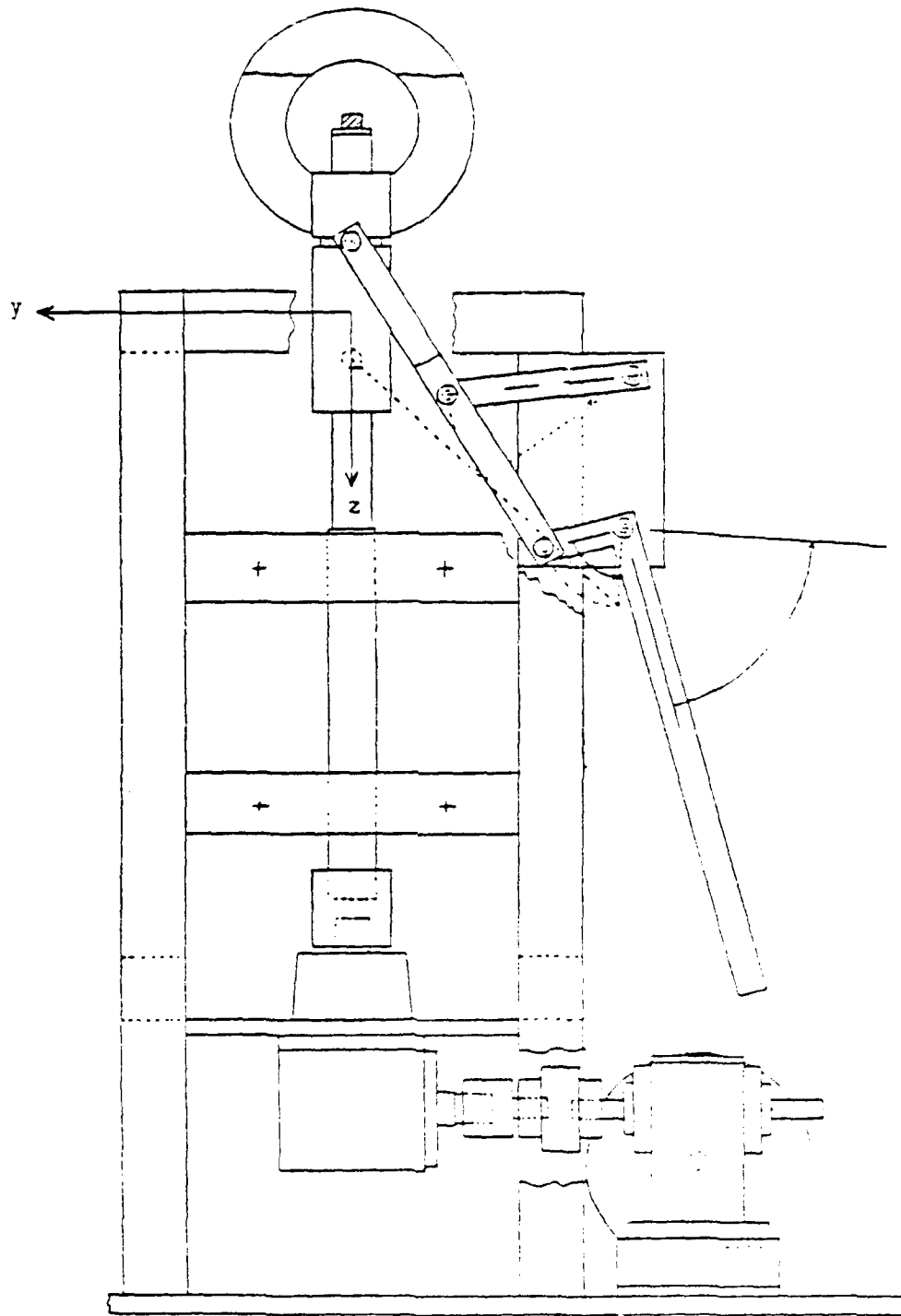


FIGURE 1. Test rig assembly, front view, initial design

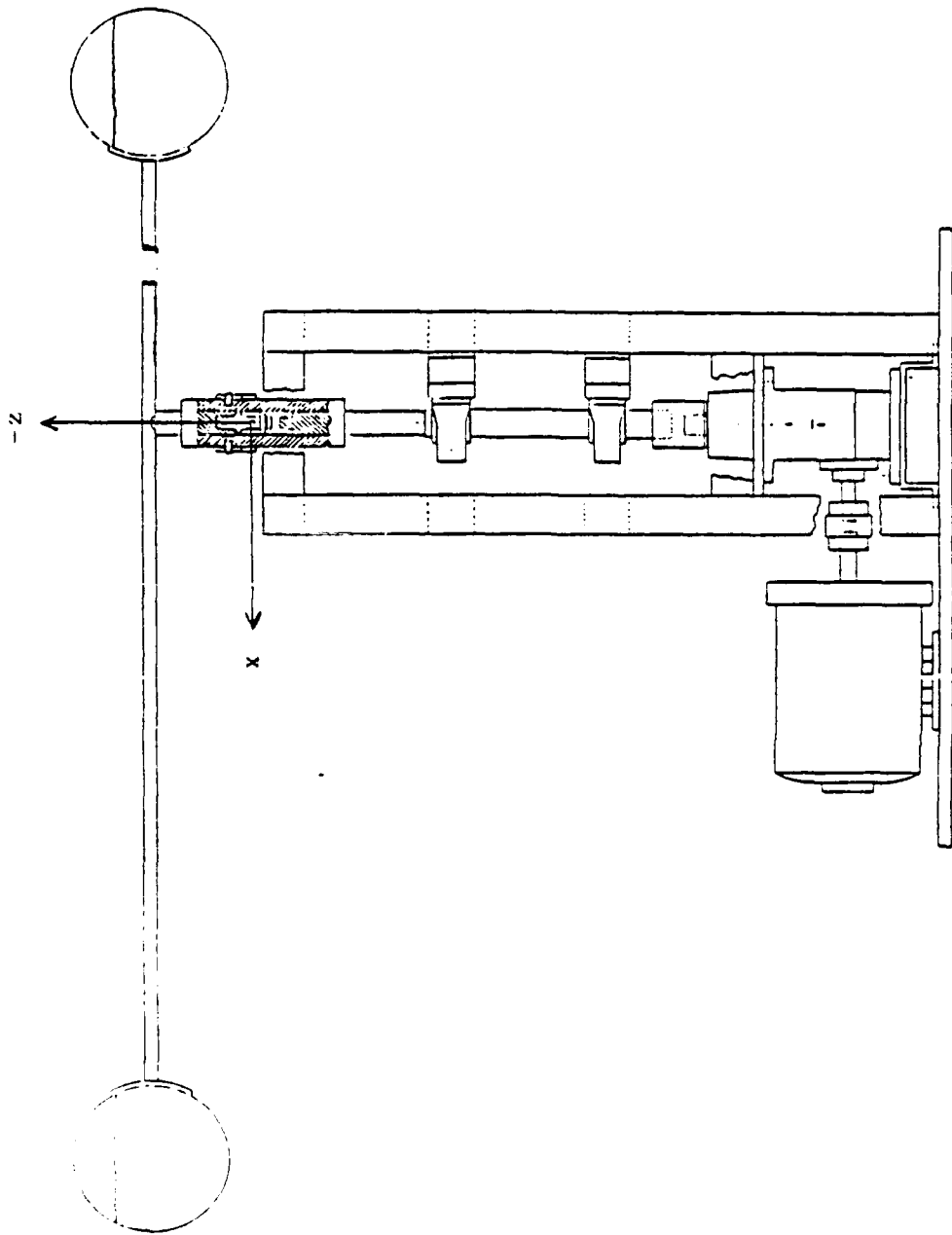


FIGURE 2. Test rig assembly, side view, initial design

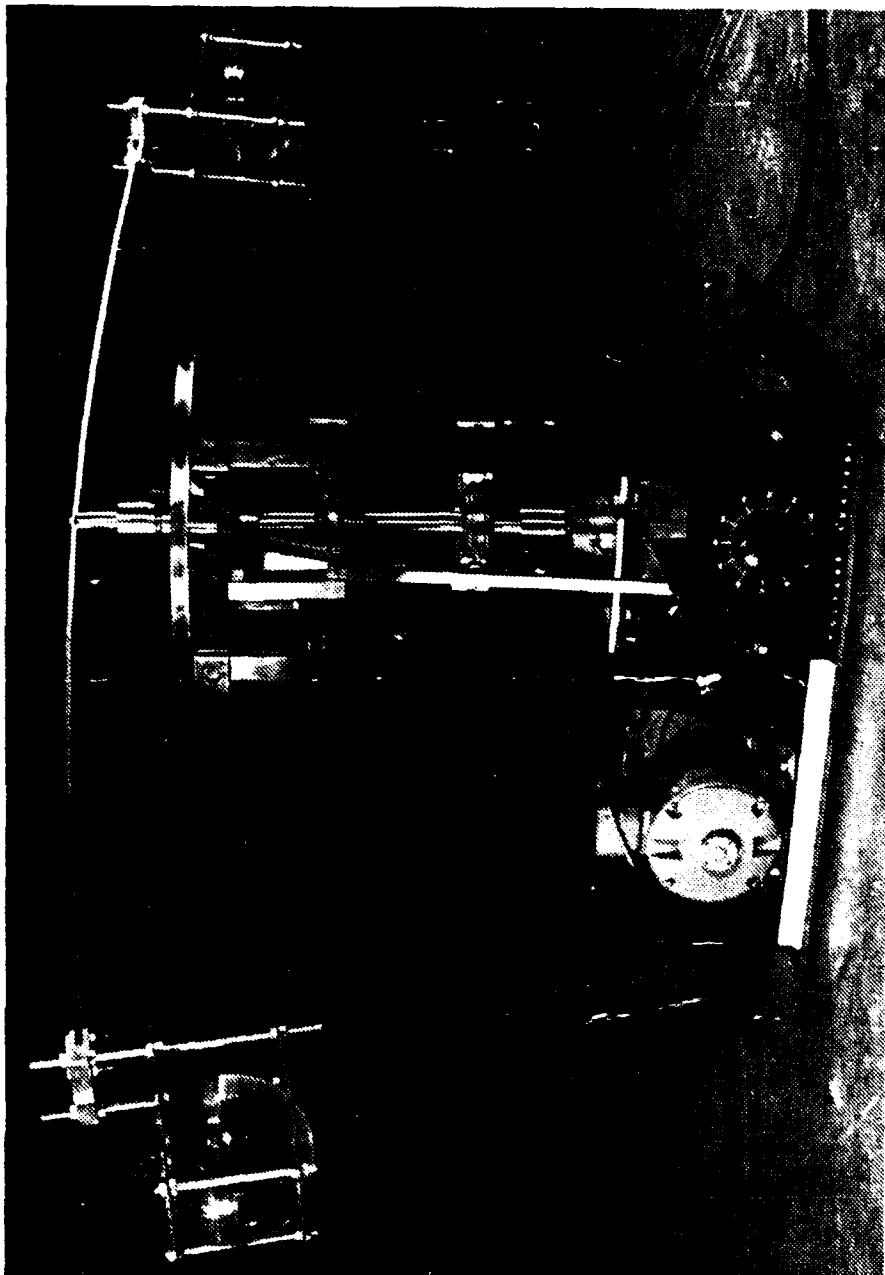


FIGURE 3. Initial rig design, spin about axis of intermediate inertia

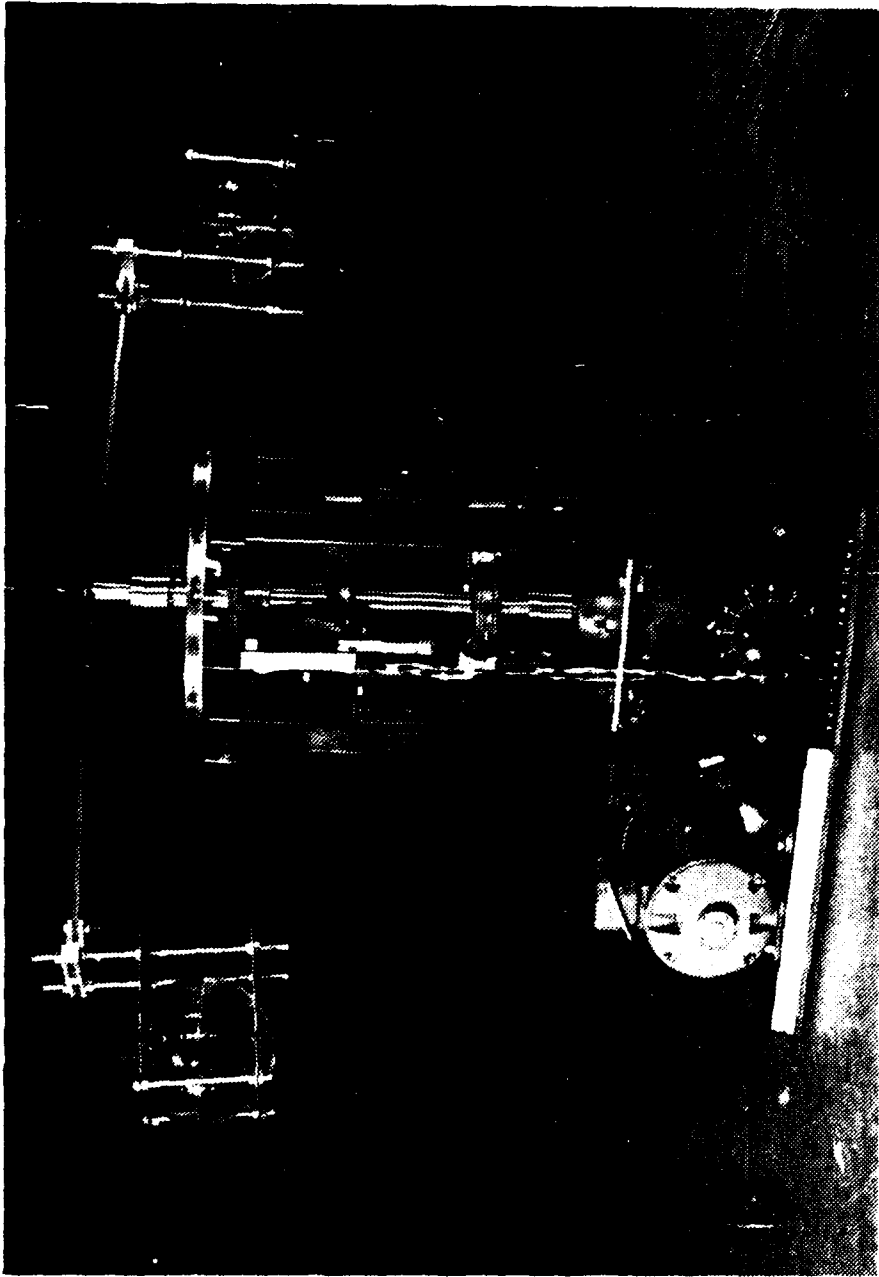


FIGURE 4. Initial rig design. spin about axis of maximum inertia

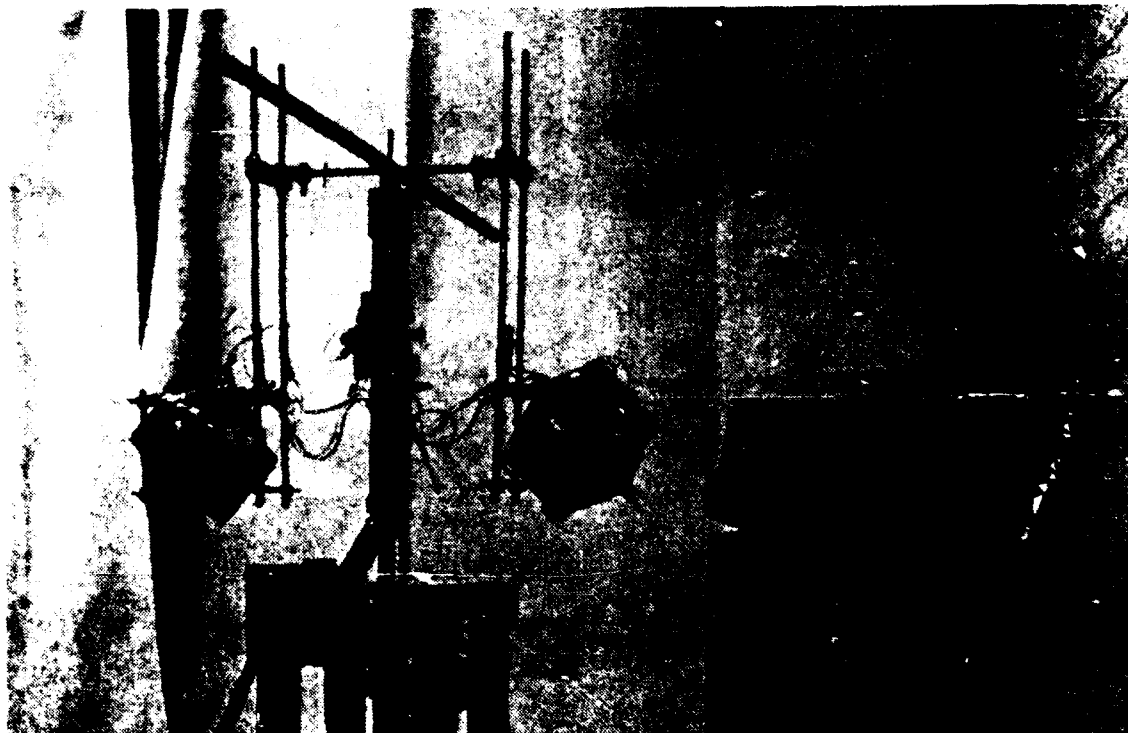


FIGURE 5. Modified test rig design

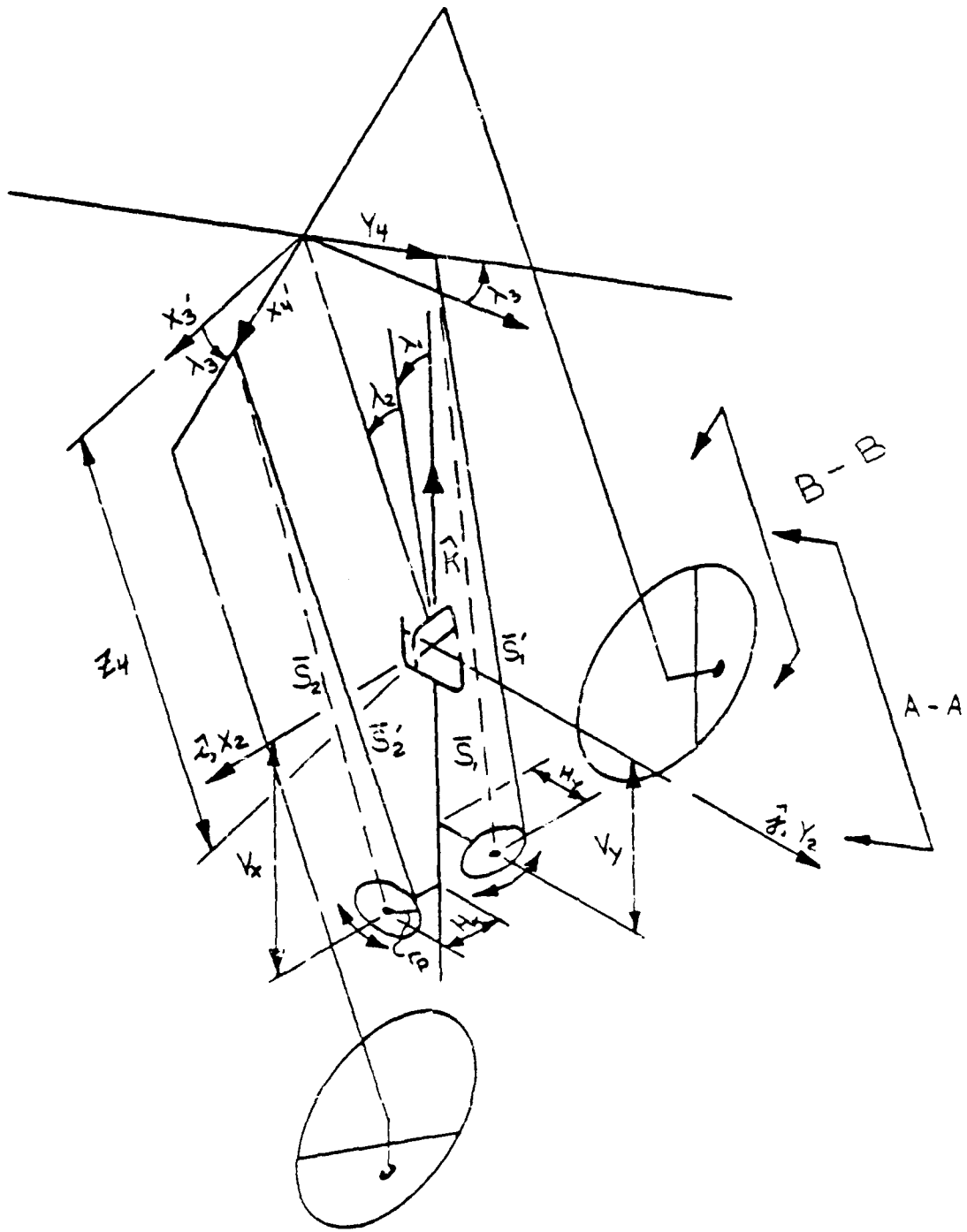


FIGURE 6. Schematic showing coordinates associated with tilted rig orientation

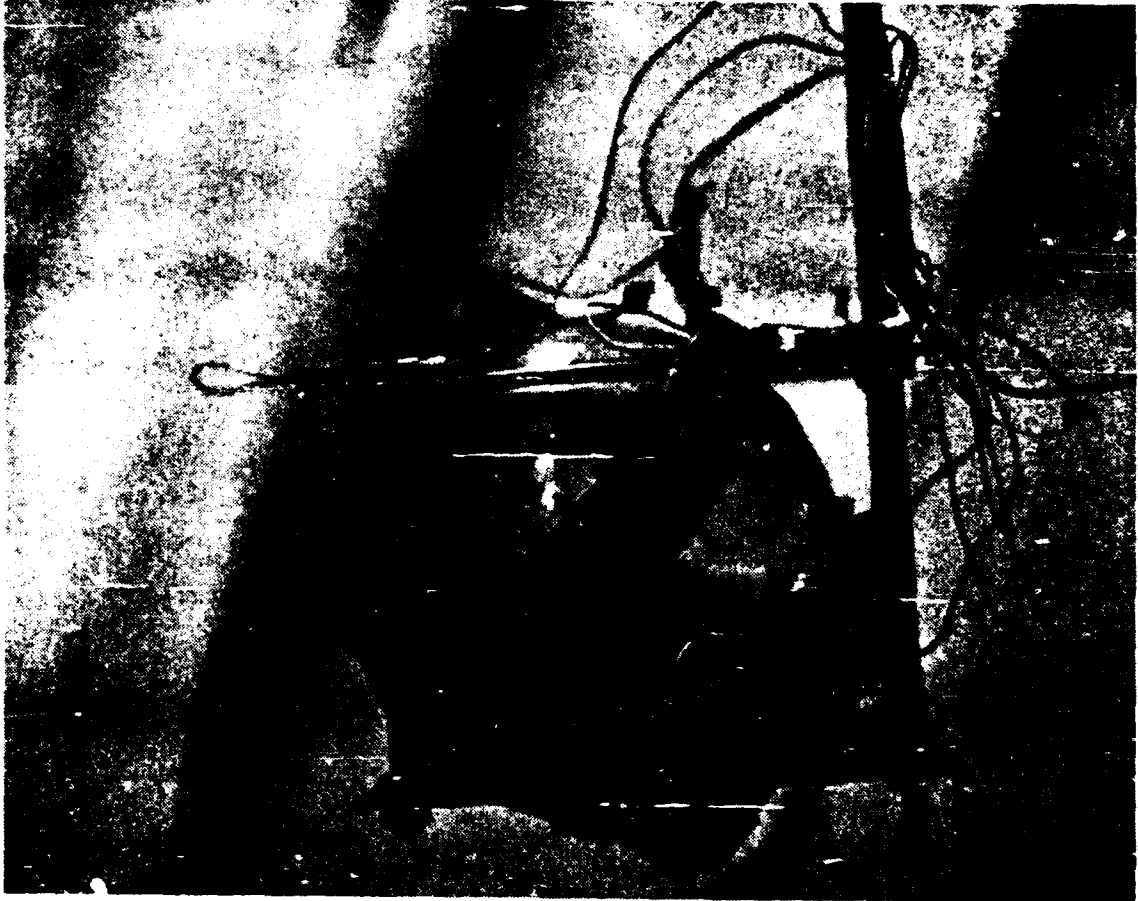


FIGURE 7. Photopotentiometer mounting location.

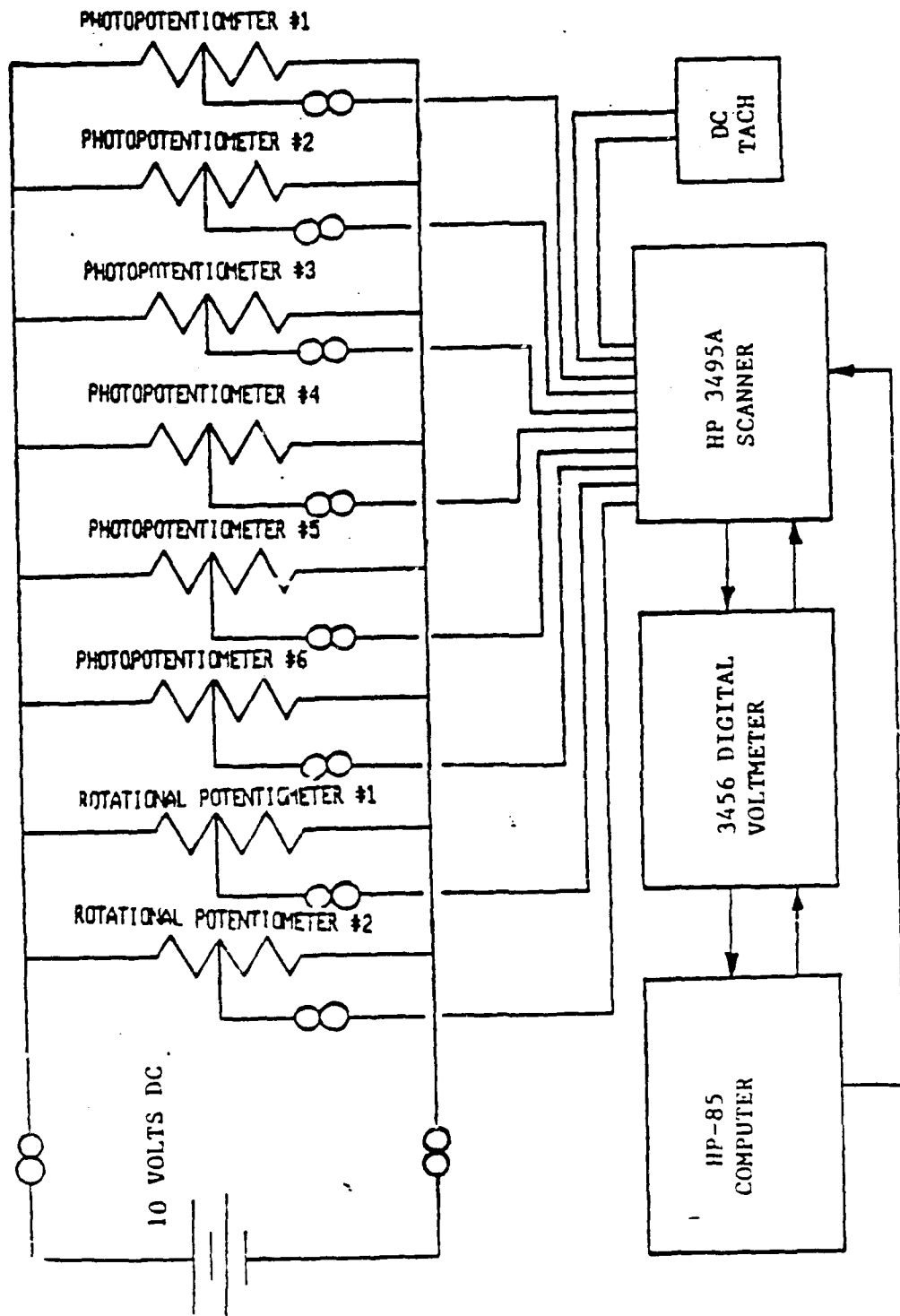


FIGURE 8. Data collection and instrumentation schematic

APPENDIX D

SATELLITE SIMULATOR
TEST RIG EXPERIMENTS

A TEST RIG TO SIMULATE LIQUID SLOSHING
IN SPIN-STABILIZED SATELLITES -- PART II: EXPERIMENTAL RESULTS

D. R. Flugrad
M. D. Anderson
Iowa State University
Ames, Iowa

ABSTRACT

Certain spin-stabilized satellites have exhibited an undesirable nutating motion when transferred to a geosynchronous orbit about the earth. It is believed that sloshing liquid stores on board the satellite are responsible for the nutation. A test rig was constructed to study the interaction between the spinning structure and the sloshing liquid. Its design and instrumentation were discussed in the companion paper, Part I. Experimental results are reported in this paper for spin about minimum and maximum axes of inertia. All runs for spin about an axis of minimum moment of inertia were found to be unstable and those for spin about an axis of maximum moment of inertia were stable. Results were generally found to be consistent with the findings of other investigators.

INTRODUCTION

Sloshing liquid stores onboard spacecraft have caused stability problems throughout the brief history of space travel. A rigid body, for example a rifle bullet, may be spin-stabilized about its axis of minimum moment of inertia. However, instability has been observed when attempting to spin-stabilize bodies containing a significant liquid mass fraction such as the XM761, which is a 155-mm cylindrical shaped artillery projectile [1], the INTELSAT IV satellite [2], and the STAR 48 communications satellite [3].

The STAR 48 communications satellites have consistently exhibited nutational motion in flight, despite being spin-stabilized at one revolution per second. Following launch from the space shuttle, the STAR 48's power assist module (PAM) is fired to thrust the satellite into a geosynchronous orbit about the earth. Coning motion about the spin axis predominates following the PAM motor burnout. Constant frequency, equal amplitude, sinusoidal oscillations about the pitch and yaw axes have been noted from flight data sensed by roll, pitch, and yaw axis rate gyros [3]. The liquid stores within the tanks of the satellite are intended for restabilization and directional pointing maneuvers.

It was initially hypothesized that combustion instabilities in the PAM rocket motor could produce a transverse thrust component which would induce the coning motion. The Engine Test Facility personnel at Arnold Engineering Development Center, Arnold Air Force Station, tested a STAR 48 motor for such forces [3]. The test stand was instrumented with axial and transverse load cells, and it had the ability to spin the PAM motor at one revolution per second during firing. The test results discounted this theory since no significant forces at the required frequency (one-half cycle per second) were

found [3].

Currently, the sloshing motion of the liquid stores is suspected of causing the unstable coning. Spin about the minimum axis of inertia, which is characteristic of a prolate spinner, corresponds to the maximum energy state, and spin about the maximum axis of inertia for an oblate spinner corresponds to the minimum energy state. The damping effect of liquid motion in a nutating spacecraft tends to reduce the kinetic energy which results in an increase in the nutational motion of the prolate spinner. If unrestrained, the satellite will seek a minimum energy state, resulting in spin about the axis of maximum moment of inertia. This is known as a flat spin.

Several researchers have attempted to model the fluid analytically to gain insight into the phenomenon of instability with liquid fluid stores present [4, 5, et al.]. The second order differential equations of motion for a mechanical analogy such as an equivalent pendulum model are usually selected over the more direct fluid equations because they are easier to solve in carrying out a computer simulation.

Sumner [5] conducted an experimental investigation on general liquid-sloshing characteristics and determined an experimental based pendulum analogy to represent the fundamental mode of liquid sloshing in unbaffled oblate-spheroidal and spherical tanks. His results were presented in terms of dimensionless parameters that are generally independent of tank size, imposed lateral acceleration, and density and viscosity of the contained liquid. The liquid tank was modeled as a combination of a stationary fixed mass and a fictitious pendulum mass to represent the sloshing liquid. Only the fundamental mode of liquid sloshing was simulated since the higher frequency modes are generally much higher than observed frequencies, and the side forces produced are small. The pendulum model of liquid sloshing is adequately

described by the pendulum mass, the pendulum arm length, the maximum angles through which the pendulum can oscillate, the fixed mass, and the centroid location of the fixed mass. Additional liquid slosh characteristics determined by Sumner were the fundamental frequencies, horizontal or side forces and damping ratios. All tests were performed using water as the liquid.

Zedd and Dodge [4] developed an equivalent mechanical model consisting of a pendulum, rotor and viscous dashpot to simulate the liquid motion. They also built an experimental test rig to create forced nutational motion of liquid-filled spherical tanks. This was used to measure the energy dissipation associated with the liquid motion. Their objectives were to determine all liquid resonant frequencies, and to relate oscillating liquid forces and moments to spin rate, nutation rate, coning angle and liquid fill height. In addition, the test results were used to observe and quantify liquid phenomena that could adversely affect prolate spacecraft under the control of spin-stabilization. The Zedd and Dodge model can be used to simulate liquid forces and moments, and to predict liquid slosh resonances and energy dissipation rates. Results can be scaled-up to actual flight conditions.

Slabinski [2] studied instability of the INTELSAT IV satellite due to liquid stores. He was able to supplement ground testing with in-orbit testing of the INTELSAT IV dual-spin satellite. The work of Slabinski is particularly relevant to this research because favorable comparisons can be made between the actual flight data presented by Slabinski and experimental results to be presented later in this work. One of the significant findings of Slabinski is the presence of a liquid slosh frequency in orbit that is approximately one-third of the predicted fundamental frequency based on ground testing.

Also, he found that products of inertia had a significant effect on stability.

Hill [3] developed a computer simulation to model a spacecraft with liquid fluid stores through the use of an equivalent spherical pendulum. The equivalent spherical pendulum models the liquid sloshing by matching the fundamental slosh modes. A closed loop feedback control law was derived for earth pointing maneuvers and stability correction of the spacecraft. Hill also outlined a means of implementing the control scheme.

This paper describes the results of an experimental investigation of the dynamic motion of a test rig built to simulate the interaction of a satellite with onboard sloshing fluid stores. Details of the design and instrumentation of the system were presented in the companion paper by Anderson, Cowles and Flugrad. The prolate spinner with a minimum inertia spin axis, and the oblate spinner with rotational motion about the axis of maximum moment of inertia were both tested, and the results compared with those of other researchers.

MINIMUM AXIS SPIN

Tests run during the first phase of the investigation involved configurations spun about the principal axis associated with the minimum moment of inertia. It is well known from classical dynamics that a perfectly rigid torque-free body will be stable when spun about either the minimum or maximum axis of inertia, but unstable when rotated about the intermediate axis of inertia. Because of the liquid in the spheres and the long length of unsupported rods, the test rig built for this study cannot be considered rigid. Many researchers working with spin stability have concluded that a non-rigid body, in the absence of an active stabilization mechanism, can only have a stable spin about the maximum principal axis. If a non-rigid body is

spun about the axis of minimum inertia, any internal damping present causes the system to move towards its minimum energy state, which requires spin about the maximum axis of inertia.

The previous work of Cowles [6] showed spinning the test rig about the maximum axis of inertia was indeed very stable with rapid dissipation of any perturbation imparted to the system.

Experimental Test Conditions

Location of the center of gravity at the center of the universal joint was necessary to allow instrumentation for spin about the axis of minimum inertia. Test runs were made with empty, one-quarter, half and three-quarter filled spheres by volume. The structure was statically balanced before each run, and experimental data were collected at constant input speeds between 70 and 100 rpm.

Test runs were made at three different speeds for each fill volume. For brevity, one run was selected to represent the results, but the parameters for all minimum inertia spin test runs are listed in Table 1. The inertias were estimated for the test rig to account for the nominal liquid position.

Large deflections were noted in the rods supporting the liquid spheres due to centripetal acceleration of the liquid mass. Consequently, monofilament line was tied between the rods on opposite sides of the rig to restrain the radial deflections of the spheres. The resulting coning motion exhibited a higher frequency of oscillation when the rods were tied together.

Results for a Specific Test Condition

Figs. 1-7 show experimental data collected for test run 2 of Table 1. Fig. 1 shows the oscillations of the rotating assembly about the x and y axes

in degrees. The collar was dropped at approximately 1.5 seconds, and the oscillations began immediately. Roughly 12.5 seconds later, the upper shaft made contact with the lowered collar, ending the oscillatory motion. The motion of the rig is perhaps best visualized by viewing a plot of the tip of a unit vector aligned along the center of the upper shaft. The projection of the tip onto a horizontal plane fixed to rotate with the lower shaft is shown in Fig. 2. The small diamonds indicate discrete data points. The rig started in the center and spiraled outward until the upper shaft came to rest on the collar. Fig. 3 shows the time history of the half-cone angle measured from vertical and the nutation rate. The nutation rate considered in this study is defined as the time rate of change of the half-cone angle. The precession rate, shown in Fig. 4, is defined as the time rate of change of the rotational position of the upper shaft about the vertical axis. These figures together show that the rig oscillated radially from vertical as it precessed. Thus a unit vector along the upper shaft traces out an oblong shape when projected onto the horizontal plane.

The angle γ_r , which locates the water surface in a radial plane, is zero for the static position and is defined to be positive as the water moves outward from the center shaft. The plot of the equivalent radial water angle vs. time for the half-filled case is shown in Fig. 5. The solid line represents the photopotentiometer located nearest the vertical input shaft on the inside of the sphere. The dashed line is the data recorded for the photopotentiometer located farthest from the shaft. It was expected that both devices should record identical signals. However, the signal of the photopotentiometer mounted nearest the shaft did not perfectly match the signal of the photopotentiometer mounted farthest from the shaft. Fig. 6 shows the opposite sphere with the same oscillation magnitude. The convention

for measuring the pendulum angle is such that when the oscillations are in phase the pendulum angle for one of the spheres decreases as the other increases. Thus, Figs. 5 and 6 show that the liquid sloshing is in phase. For half-filled spheres, the radial slosh amplitude is approximately 10-15 deg. The magnitude of the circumferential oscillations recorded is of the same order of magnitude as the expected noise in the signal as shown in Fig. 7. The circumferential photopotentiometers were calibrated statically, so the measured angle should be considered on a relative rather than an absolute basis.

General Results for Minimum Axis Spin

The experimental data for rig oscillations and cone angles for empty, one-quarter and three-quarter filled spheres appear in Figs. 8-13. Three runs were made at different spin rates for each fill volume, but only one run speed is shown at each fill volume for brevity. For all fill heights with spin about the minimum axis of inertia, the instrumentation recorded oscillations that increased rapidly until restricted by the collar. It took less than 15 seconds to reach the outer motion limit for all test conditions. The half-cone angle was found to oscillate about an increasing amplitude.

Precession and Relative Spin Rate Analysis

For this research, precession is defined as the angular rotational rate of the axis of the upper shaft relative to ground about a vertical reference. When the upper shaft made contact with the collar, the precession rate increased until there was no relative motion between the collar, which was rotating with the drive shaft, and the upper shaft. The precession rate was visually observed to be slower than the drive speed. The precession rate was

calculated in terms of the drive spin rate of the body, the body inertias, and the center of gravity location by the following equation:

$$\dot{\psi} = \frac{I_s \Omega \pm \{I_s^2 \Omega^2 - 4(I_t \cos \theta) W r_{cg}\}^{1/2}}{2I_t \cos \theta} \quad (1)$$

Where,

- Ω = the drive spin rate of the test rig
- r_{cg} = the distance from the universal joint pivot to the rig center of gravity (positive for center of mass above the pivot)
- I_s = the moment of inertia for the spin axis
- I_t = the moment of inertia for the transverse axis
- W = the weight of the rig supported by the universal joint
- θ = the half-cone angle

Since differences were noted in the literature regarding nomenclature of precession and nutation, the development of Eq. (1) is provided in the appendix. Eq. (1) can be simplified by approximating $\cos \theta = 1$ with no greater than 1.5% error for all possible cone angles of the rig. This equation assumes a body symmetrical about the z-axis, a constant input spin rate, and no torques except that due to gravity. Figs. 14-17 show the predicted precession rates, from Eq. (1), superimposed on the experimental data. For all runs, the observed root corresponded to the larger of the two solutions from Eq. (1). It must be noted that for the test rig to be truly axisymmetric, a different crossbeam would be required for every fill volume and spin speed combination. Therefore, a compromise was decided upon to use a crossbeam that provided nearly axisymmetric conditions for three-quarter filled spheres. Figs. 14-17 show that the predicted precession rate based on either I_x or I_y is near the average precession rate for the test runs. The predicted precession rates for the empty and one-quarter filled spheres both

appear reasonable, even though these two cases have markedly different transverse inertias.

The literature frequently refers to the relative spin rate, which is defined as spin rate of the test rig about its upper shaft independent of precession. It can be calculated based on the weight, center of mass location, body inertias, and drive spin rate as:

$$\dot{\phi} = \frac{(2I_t - I_s)\Omega \pm \{\Omega^2 I_s^2 - 4I_t W r_{cg} \cos \theta\}^{1/2}}{2I_t} \quad (2)$$

The development of Eq. (2) is also presented in the appendix. The predicted spin rate has been superimposed on the experimental data presented in Figs. 14-17. Both transverse inertias were used, and either choice yields good results for all runs. The smaller of the two roots of the quadratic of Eq. (2) was observed for all runs. For all runs made with water in the spheres, the predicted relative spin rates were near the average experimental relative spin rate. Fig. 14 shows a slightly different result since the predicted relative spin rates are approximately positioned at the extreme values of the observed relative spin rate. However, this case also had the most dissimilar transverse inertias. The empty spheres case shown in Fig. 14 was also slightly different in that the predicted relative spin rates based on the two different inertias form bounds for the majority of the data.

Analysis of Liquid Slosh for Minimum Axis Spin

It was anticipated that the instability of the test rig would be affected by the sloshing liquid. It was hypothesized that the force driving the oscillations was associated with the nutational motion. The frequency of the liquid oscillations was determined from the photopotentiometer data. The results of hand data reduction consistently showed the experimental liquid

slosh frequency at a value much lower than the predicted natural modes based on the research of Zedd and Dodge [4] or Sumner [5]. The results of frequency analysis for all minimum inertia spin runs are presented in Table 2.

Static Frequency Determination

The fundamental frequency of oscillation for the liquid in the test rig tanks in the static case can be found by perturbing the tank and timing the oscillations. Ten oscillations were counted for increased accuracy and three trials were made at each fill height. The stationary natural frequency of the six inch diameter tanks was determined to be 2.3 Hz, 2.55 Hz, and 2.65 Hz at one-quarter, half and three-quarter fill volumes respectively. The natural frequency of the stationary tank is much greater than the radial or circumferential liquid oscillations determined by hand reduction, as shown in Fig. 18. This observation that liquid sloshing occurred during dynamic testing at a much lower frequency than observed in the stationary tank was not expected. The work of Slabinski [2], however, agrees with this study as he found the liquid slosh frequency from dynamic testing on earth and in orbit to be roughly one-third of the expected value based on stationary tank resonance.

Sumner's Slosh Frequency Parameter Method

During an experimental test run, the spheres were subjected to an effective gravity that is the vector sum of the earth gravitational force plus the force due to centripetal acceleration. The method of Sumner [5], which relates the spherical tank to an "equivalent cylindrical tank", was used to estimate the fundamental slosh frequency for the tank. Sumner has related the ratio of tank fill height over the tank diameter to a fundamental frequency parameter which can be used to estimate the fundamental frequency for a

spherical tank. No distinction is made regarding radial or circumferential modes. The calculations demonstrate that increasing the rotational speed will cause the fundamental frequency to increase due to gravitational effects. This can be seen in Table 2.

Analysis of Forced Liquid Oscillations

The variation of the half-cone angle was investigated as a possible forcing function. The time history of the half-cone angle varied irregularly, so the cycles were estimated based on the highest peaks. In Figs. 14-17, the frequency of the water and half-cone angle calculated in cycles/min are in reasonable agreement for any given input speed and fill height. Slabinski [2] defined a driving frequency ratio as follows:

$$\rho = f_d / \omega_{rz} \quad (3)$$

where

f_d is the liquid driving frequency

ω_{rz} is the total rotor spin rate about the bearing axis
of the satellite

For a simple spinner, that is, a spacecraft rotating as a single integral unit about a principal axis, is determined by the mass properties according to [2]

$$\rho = |I_{rz} / I_t - 1| \quad (4)$$

Slabinski's liquid driving frequency based on Eqs. (3) and (4) corresponds to observed coning and liquid oscillations. For the test rig to have equal transverse inertias would require a unique beam for every fill height and spin rate combination. Therefore, practicality suggested a compromise beam that would yield nearly equal transverse axis inertias for the three-quarter fill volume. The transverse axis inertias remained close for half filled

conditions but were markedly different for one-quarter filled spheres, Fig. 19. For half and three-quarter filled volumes, the predicted frequencies were 4 to 35 percent too high as shown in Figs. 20 and 21. The relation of Slabinski correctly predicted the nonlinear increase in nutational driving frequency with increased spin rate.

For the one-quarter fill volume case Figs. 19-21 show the experimental slosh frequencies between the high and low values predicted by Slabinski's relationship. The wider range of predicted frequencies was due to the greater difference between the two transverse axis inertias.

By use of the driving frequency parameter, the calculations showed that the relationship between spin rate and nutational frequency depends on a product involving the spin rate and inertias of the body. The inertias of the rig were calculated as accurately as possible. This included an attempt to account for the liquid mass at a nominal position dependent upon the input speed. However, the fact that the inertias are actually variable during spin was not accounted for.

Although the numerical values don't match exactly, the work of Slabinski correctly predicted a nonlinear relationship between spin rate and liquid slosh frequency dependent on the inertias of the body. Table 2 shows that the driving frequency ratio was between 0.3 and 0.9 for all minimum inertia spin configurations tested. Therefore, to excite the tank resonance would require a spin rate of at least 190 rpm for the given inertia properties. This speed could not be achieved with the present test rig design. Based on system frequency response theory, it is anticipated that violent oscillations of the test rig would occur if the nutational motion, acting as a forcing function, were to have the same frequency as the fundamental slosh frequency of the liquid in the spheres.

Zedd and Dodge Equivalent Pendulum Method

The third method of determining the fundamental slosh frequency is based on the pendulum model of Zedd and Dodge [4]. The derivation involves summing moments about the hinge point of the pendulum. These calculations continued to exhibit the trend of increased fundamental frequency with increased rotational speed, as shown in Table 2. At one-quarter fill, the fundamental frequency of radial slosh was determined to be 2.289 Hz and 2.915 Hz at 82 and 101 rpm respectively.

The test rig was unable to directly excite the fundamental frequency of the tanks since all the primary observed nutational frequencies were less than 0.5 Hz, and the estimated fundamental frequencies of the liquid were all greater than 2 Hz. An increase in the drive speed had the general effect of increasing the nutational frequency, however it also increased the liquid natural frequency.

Experimental Work of Slabinski

The work of Slabinski based on the INTELSAT IV flight data concurs with the experimental results of this investigation and also concurs with the conclusion that the liquid sloshing is excited by the nutational motion. Under the sponsorship of the International Telecommunications Satellite Organization, Slabinski [2] found that the nutational frequency for dynamic testing is about one-third of the liquid slosh frequency determined by stationary ground testing. Since ground testing of spinning systems produced the same nutation frequencies, he concluded that this does not correspond to a simple resonance of the liquid. The work described in this study has already detailed an observed correlation between nutation and liquid sloshing. In addition, the slosh frequencies observed during testing were roughly one-third

the resonance of the static tank frequencies as shown in Fig. 18. Slabinski stated that the reason for lower natural frequencies is not understood, but consideration should be given to possible swirl oscillations of the liquid. The present instrumentation was not able to detect swirl motion.

MAXIMUM AXIS SPIN

The second area investigated in this research involved spin about an axis of maximum inertia. Cowles [6] demonstrated that the test rig was very stable for spin about the axis of maximum inertia and perturbations damped out very rapidly for this system. This is in good agreement with the work of many researchers who state that in the absence of an active stabilizing mechanism, the only stable spin for a body with flexible elements will occur about the maximum axis of inertia. However, Agrawal [7] developed a more stringent stability criterion for non-rigid, torque-free spinning bodies. He stated that the ratio of spin axis inertia to transverse axis inertia must be greater than $(1 + C)$ for a stable configuration, where C is a positive constant that depends on certain specific parameters.

The configurations tested in this work had inertia ratios ranging from 1 to 1.5, and the center of mass was located at or below the universal joint. The important parameters for all maximum inertia spin configurations are shown in Table 3. The motive behind testing spin to transverse inertia ratios only slightly greater than one was to determine if a spin about the maximum axis of inertia could be unstable as suggested by Agrawal. The upper shaft was shortened, and the spheres were moved farther away from the center drive shaft to achieve these goals. A maximum inertia ratio of approximately 1.4-1.5, depending on fill height, was achieved by decreasing the vertical distance

from the universal joint to the sphere center. By lowering the spheres until they just cleared the supporting structure, the inertia ratio was decreased to approximately unity.

Typical Results for Spin About the Maximum Spin Axis

Figs. 22-28 show experimental results for the half-filled spheres spun about the maximum axis of inertia. This is analogous to the data presented for the minimum spin configuration in Figs. 1-7. The conditions for run F shown in Figs. 22-28 include $I_x = 0.289$, $I_y = 0.289$, and $I_z = 0.325$ slug-ft². The center of gravity was determined to be 2.69 inches below the universal joint for the input spin rate of 75 rpm counterclockwise. Fig. 22 shows that after the collar was dropped at roughly 2.5 seconds, the rig immediately sought a steady orientation. Approximately 6 seconds later, the rig exhibited only a small oscillatory motion about the steady orientation. In Fig. 23, which shows the trace of the tip of a unit vector embedded in the upper shaft projected onto a horizontal plane fixed to spin with the lower shaft, it can be seen that the rotating assembly was approximating the motion of a rigid body. That is, there was very little movement of the upper shaft relative to the lower shaft. The half-cone angle and nutation rate are shown in Fig. 24. This figure confirms that the rig precesses with the upper shaft slightly off vertical. The experimental data presented in Fig. 25 show that the test rig had almost pure precession since the relative spin rate of the body about the upper shaft had only small oscillations about zero. The precession rate is shown to have a small oscillatory component about the driving input spin rate. The spike in both relative spin rate and precession at roughly 2.5 seconds was caused by interaction between the upper shaft and upper collar when the collar was lowered. Similar results were observed when dropping the collar for spin

about the minimum axis of inertia.

The radial liquid slosh data presented in Fig. 26 and Fig. 27 show small oscillations about a steady value. Only photopotentiometers 2 and 5, mounted farthest from the shaft, produced a clean signal of the radial liquid oscillations. This was attributed to liquid sheeting and orientation of the liquid relative to the spheres. The frequencies of the half-cone angle variation and of the liquid slosh in the radial direction were found by hand reduction of information in Figs. 24 and 26 to be 1.12 Hz and 1.15 Hz respectively. The circumferential liquid slosh was also seen to have nearly the same frequency as the half-cone frequency and the radial liquid frequency. Similar agreement between the half-cone and radial and circumferential liquid slosh modes is presented for all test cases in Table 4.

Stability Analysis for Maximum Axis Spin

The unexpected result noted during spin about the maximum axis of inertia was that the test rig did not seek a true vertical orientation. The collar was dropped, and the rig was allowed to seek its equilibrium position before the data collection began. To verify stability, the rig was struck with a hammer handle while spinning, and it was observed that the oscillations rapidly dissipated as the rig returned to its nonvertical equilibrium position as shown in Figs. 29-31.

The test cases considered were unable to verify the $(1 + C)$ stability criterion suggested by Agrawal. The rig exhibited stable motion for all inertia ratios and operating speeds attempted. One possible explanation is the fact that the test rig did not meet the torque-free requirement. To achieve an inertia ratio of nearly one, the half-filled spheres were lowered 8 inches below the universal joint, moving the center of gravity 2.85 inches

below the joint for the stationary configuration. Gravitation had a significant stabilizing effect under these conditions.

Analysis of Half-Cone Angle for Maximum Axis Spin

As noted before, when spun about the maximum inertia axis, the rig tilted to one side and rotated as a rigid body with the lower shaft. It returned to this position when perturbed for all fill heights, as shown in Figs. 29-31. When the spin rate was increased, the half-cone angle also increased. Initially, it was thought that due to friction in the universal joint the rig might be statically balanced in a vertical position without being dynamically balanced. The rotational potentiometers were disconnected since they apply a slight force on the test rig, but the same tilting effect was observed. Another hypothesis suggested that the center of gravity might not be located exactly at the center of the shaft with the centripetal acceleration causing an increased half-cone angle with an increase in speed. The center of mass can be moved along the y-axis by tightening both rods that support the spheres on one side of the x-axis. More tests were run with different static balance points to attempt to create a stable spin with the upper shaft spinning vertically. Because small tilt angles had little effect, the sphere support rods were tightened on one side until the static half-cone angle was 10 deg. Under these conditions at moderate speed, the rig lifted up off the collar, and the half-cone angle continued to decrease with increased speed up to the rig limit of approximately 100 rpm.

The fact that the rig would right itself when initially unbalanced triggered further evaluation of the spinning motion. Ultimately, it was discovered that small products of inertia could explain the behavior of the test rig. Numerical simulation results were similar to experimental motions

when small non-zero products of inertia were introduced.

Precession and Spin Rate Analysis

The results for spin about the axis of maximum moment of inertia show that the precession rate oscillated about a constant value for all fill heights. In addition, Fig. 25 illustrates that the spin component of the body about the upper shaft exhibited a small amplitude oscillation about zero. The spike apparent in the data several seconds into the run was caused by dropping the collar. The oscillations were of constant amplitude and did not appear to damp out. Therefore, the motion can be characterized primarily as precession with an average relative spin rate of zero. In this case, the rig speed was nearly identical to the precession rate. This is in sharp contrast with the minimum inertia spin configuration results which demonstrated both non-zero precession and relative spin rates.

Analysis of Liquid Slosh for Maximum Axis Spin

The photopotentiometer data from configurations spun about the maximum axis of inertia were markedly different from the minimum inertia axis spin case. For stability, it was anticipated that the liquid must act as a rigid body so there would be no liquid motion relative to the test rig [7]. The reason for initially holding the restraining collar in the up position for several seconds was to estimate the magnitude of noise present. For the case depicted in Fig. 22, the rotational potentiometer was seen to give a very clean signal during the collar up portion of the run. The significance of the photopotentiometer data was almost overlooked because the signal during the test run was very nearly the same as for the collar up portion as seen in Figs. 32-35.

Originally, no liquid oscillations were anticipated for a spin-stabilized motion. However, small slosh amplitudes were present as observed in Figs. 26-28 and 32-35. For one-quarter and three-quarter filled spheres, there was only one active radial liquid slosh sensor. Therefore, the radial liquid slosh results for both spheres are shown on the same graphs of Figs. 32 and 34. There were two active sensors on each sphere at half-filled conditions. Therefore, the data for each sphere are shown separately in Figs. 26 and 27. Figs. 32-35 show that the radial liquid oscillations were in phase for all sphere fill heights.

Frequency Analysis Based on Anticipated Driving Forces

Slabinski [2] related the liquid driving frequency to the spin rate of a simple spinner as:

$$\rho = f_d/\Omega = |I_s/I_t - 1| \quad (5)$$

Where f_d is the liquid driving frequency. This same relation was used in the analysis for spin about an axis of minimum moment of inertia. For unequal transverse axis inertias Eq. (5) was used to predict two values based on the two different inertias. The frequency analysis of the half-cone angle showed that the mode with the largest amplitude at all fill heights was consistent with the liquid driving frequency parameter.

Results and Observations for Maximum Axis Spin Tests

Table 4 shows all experimental half-cone, radial liquid slosh, and circumferential liquid slosh frequencies as determined by MATRIX_x, a software package with FFT capability. In Table 4, 'STATIC NAT. FREQ' refers to the characteristic slosh frequency of the tank as determined by perturbing the stationary tank. The quantities 'DYN. CONE', 'DYN. RADIAL SLOSH', and 'DYN.

CIRCUM. SLOSH' refer to the experimental frequencies detected through the use of the FFT capability of MATRIX_x. 'SLAB' refers to the driving frequency parameter of Slabinski given by Eq. (5). 'PEND. RADIAL SLOSH' and 'PEND. CIRCUM SLOSH' refer to the slosh modes predicted by the pendulum model of Zedd and Dodge. In addition, the precession rate was determined by Eq. (24) of the appendix. Run designations that include a 'P', such as run 'AP', refer to cases in which the rotating assembly was physically perturbed by a hammer blow during testing.

For the perturbed runs tested, the table shows that the driving frequency of Slabinski was still detected in both liquid slosh modes and the half-cone angle. All experimental half-cone angle and liquid slosh data exhibited a major frequency near the value predicted according to Slabinski [2]. In addition, the experimental radial and circumferential oscillations showed a major frequency component near each mode predicted by the pendulum model of Zedd and Dodge [4]. Both liquid traces showed a significant frequency near the value of precession or total spin rate. The exact cause of this frequency is unknown since both the precession and total spin were approximately equal for all maximum inertia spin axis configurations tested.

The frequency analysis indicated that the frequencies associated with Slabinski, Zedd and Dodge, and the total spin rate or precession are roughly of the same magnitude for either mode of liquid oscillation. The results for the minimum inertia spin case differed in that the only significant radial liquid slosh frequency to be observed was associated with Slabinski. Other observed modes were of much lower amplitude.

CONCLUSIONS AND RECOMMENDATIONS

Experimental data were in good agreement with the prediction of

precession rate based on the relative spin rate developed in the appendix [4, 8,9]. Instability was observed for all minimum inertia axis spin configurations tested, despite the fact that those configurations were statically balanced. The radial liquid slosh frequency observed during dynamic testing was less than a third of the natural slosh mode anticipated from ground testing in agreement with actual satellite data [2]. The coning motion of the test rig appeared to have the effect of a driving frequency, judging by the agreement between the coning frequency and the radial liquid slosh.

Experimental investigation of spin about the maximum axis of inertia revealed stability for all test cases. This study was unsuccessful in verifying the work of Agrawal [7], which states that the ratio of spin axis inertia to transverse axis inertia for a torque-free body must be greater than $(1 + C)$ for stability. This is more stringent than classical rigid body theory which holds simply that a torque-free body is stable for spin about its maximum inertia axis. Perhaps the test rig did not adequately meet the torque-free criterion. Future work should include testing configurations whose spin axis inertia is slightly maximum with a center of gravity closer to the center point of the universal joint.

The motion of the maximum axis configuration is nearly pure precession, as the spin rate of the body about the upper shaft has a very small value which oscillates about zero. Forced oscillations were identified based on the liquid driving frequency parameter of Slabinski [2]. This frequency was present in the time history of the half-cone angle. The natural radial and circumferential liquid slosh modes were also extracted from the photopotentiometer data.

It was found that small products of inertia can have a strong influence

on the dynamics of the test rig. Products of inertia much smaller than the body inertias cannot be neglected as they will cause the test rig to spin off vertical center, and the tilt increases with speed.

There are a number of areas related to this work that should be studied further. Among them are the following:

- the effect of flexible structural elements of the test rig on the dynamic motion.
- the effect of products of inertia on the system motion.
- the time history of the inertia variation due to rig tilt and liquid motion.
- the effect of forcing frequencies on the natural slosh modes as input speed, inertia ratios, sphere size, and liquid fill fraction are varied.
- the system stability associated with spin about an axis having a principal inertia only slightly greater than the transverse inertias with the center of mass located near the universal joint.
- the effect of fluids with different viscosities on the dynamic motion of the test rig.

ACKNOWLEDGMENT

This study was accomplished with the support of the Air Force Office of Scientific Research under grant AFOSR-86-0080.

REFERENCES

1. Miller, Miles C. "Flight Instabilities of Spinning Projectiles Having Nonrigid Payloads." *Journal of Guidance and Control*, 5, No. 2 (March-April 1982):151-157.
2. Slabinski, V. J. "INTELSAT IV In-orbit Liquid Slosh Tests and Problems in the Theoretical Analysis of the Data." *COMSAT Technical Review*, 8, No. 1 (Spring 1978):1-39.
3. Hill, Daniel E. "Dynamics and Control of Spin-stabilized Spacecraft with Sloshing Fluid Stores." Ph.D. dissertation, Iowa State University, Ames, Iowa, 1985.
4. Zedd, Michael F.; and Dodge, Franklin T. "Energy Dissipation of Liquids in Nutating Spherical Tanks Measured by a Forced Motion-Spin Table." NRL Report 8932. Washington, D.C.: Naval Research Laboratory, October 1985.
5. Sumner, Irving E. "Experimentally Determined Pendulum Analogy of Liquid Sloshing in Spherical and Oblate-Spheroidal Tanks." Technical Note TN D-2737. National Aeronautics and Space Administration, April 1965.
6. Cowles, Doug S. "Design of a Spin-Stabilized Spacecraft Simulator with Liquid Fuel Stores." M.S. thesis, Iowa State University, Ames, Iowa, 1987.
7. Agrawal, Brij N. "Stability of Spinning Spacecraft with Partially Liquid-Filled Tanks." American Institute of Aeronautics and Astronautics, 19th Aerospace Sciences Meeting, St. Louis, Missouri, January 1981.
8. Greenwood, Donald T. Principles of Dynamics. Englewood Cliffs, New Jersey: Prentice Hall, Inc., 1965.
9. Smith, Gerald M. and Downey, Glenn L. Advanced Engineering Dynamics. Scranton, Pennsylvania: International Textbook Company, 1968.

APPENDIX

The literature frequently cites expressions relating precession, total spin, and relative spin rate, but often the coordinates and quantities used are not clearly specified. Based on a review of available literature, it was decided to derive these relationships for the system of Euler angles shown in Fig. 36. These equations may be derived by solving the moment equations for the rigid body. The angular rotations associated with the universal joint of the test rig are not the same as the traditionally defined Euler angles. Therefore, the position and velocity vector for an equivalent orientation were derived in both systems and equated. The result provided expressions for the precession and relative spin rates in terms of the experimental data.

The orientation of the body in terms of Fig. 36 is described by first aligning the body with the ground-fixed XYZ coordinates. The body is then rotated through an angle, ψ , about the vertical \bar{Z} -axis. Next the body is rotated by an angle, θ , about the \bar{x} -axis, and finally, through the angle, ϕ , about the \bar{z}' -axis. The quantity $\dot{\psi}$ is known as the precession rate, and the quantity $\dot{\phi}$ is the relative spin rate.

The relative spin and precession rates can be determined by writing the moment equation about the xyz-axes. The moment equation is of the form [9]:

$$\bar{M}_o = (d\bar{H}_o/dt) + \bar{\omega}_c \times \bar{H}_o \quad (6)$$

where,

$\bar{\omega}_c$ = angular velocity of the xyz-coordinate system

\bar{H}_o = angular momentum vector of the body about o

The components of the angular momentum of the body are given by:

$$H_x = I_x \omega_{bx} - I_{xy} \omega_{by} - I_{xz} \omega_{bz} \quad (7)$$

$$H_y = I_y \omega_{by} - I_{yx} \omega_{bx} - I_{yz} \omega_{bz}$$

$$H_z = I_z \omega_{bz} - I_{zx} \omega_{bx} - I_{zy} \omega_{by}$$

with,

$$\bar{\omega}_b = \text{angular velocity of the body}$$

The angular velocity of the body may be written as

$$\bar{\omega}_b = \dot{\theta} \bar{x} + \dot{\phi} \bar{z}' + \dot{\psi} \bar{z} \quad (8)$$

It may also be expressed in terms of the xyz-coordinate system by use of the following expressions:

$$\bar{z} = \sin \theta \bar{y} + \cos \theta \bar{z} \quad (9)$$

$$\bar{z}' = \bar{z} \quad (10)$$

where,

$$\bar{z}, \bar{x}, \bar{y}, \bar{z} = \text{unit vectors}$$

Therefore, it follows that the angular velocity is

$$\bar{\omega}_b = \dot{\theta} \bar{x} + \dot{\psi} \sin \theta \bar{y} + (\dot{\psi} \cos \theta + \dot{\phi}) \bar{z} \quad (11)$$

The angular velocity components, ω_{bx} , ω_{by} , and ω_{bz} in the xyz system can then be obtained by inspection of Eq. (11). If we assume a symmetrical body so that all products of inertia are zero and $I_x = I_y = I_t$, Eqs. (7) become

$$H_x = I_t \omega_{bx} = I_t \dot{\theta} \quad (12)$$

$$H_y = I_t \omega_{by} = I_t \dot{\psi} \sin \theta$$

$$H_z = I_s \omega_{bz} = I_s (\dot{\phi} + \dot{\psi} \cos \theta)$$

where I_s is the mass moment of inertia about the body-fixed spin axis.

Therefore,

$$\dot{H}_x = I_t \ddot{\theta} \quad (13)$$

$$\dot{H}_y = I_t (\ddot{\psi} \sin \theta + \dot{\psi} \dot{\theta} \cos \theta)$$

$$\dot{H}_z = I_s (\ddot{\phi} + \ddot{\psi} \cos \theta - \dot{\psi} \dot{\theta} \sin \theta)$$

The angular velocity of the xyz-coordinate system is

$$\bar{\omega}_c = \dot{\theta} \bar{x} + \dot{\psi} \bar{z} = \dot{\theta} \bar{x} + \dot{\psi} \sin \theta \bar{y} + \dot{\psi} \cos \theta \bar{z} \quad (14)$$

Thus,

$$\bar{\omega}_c \times \bar{H}_o = \begin{vmatrix} & i & j & k \\ \dot{\theta} & \dot{\psi} \sin \theta & \dot{\psi} \cos \theta & \\ I_t \dot{\theta} & I_t \dot{\psi} \sin \theta & I_s (\dot{\phi} + \dot{\psi} \cos \theta) & \end{vmatrix}$$

Expansion of the determinant of Eq. (15) and substitution into Eq. (6) yields the following moment equations

$$\begin{aligned} M_x &= I_t \ddot{\theta} - I_t (\dot{\psi})^2 \sin \theta \cos \theta + I_s (\dot{\phi} + \dot{\psi} \cos \theta) \dot{\psi} \sin \theta \\ M_y &= 2I_t \dot{\theta} \dot{\psi} \cos \theta + I_t \ddot{\psi} \sin \theta - I_t \dot{\theta} (\dot{\phi} + \dot{\psi} \cos \theta) \\ M_z &= I_t (\ddot{\phi} + \ddot{\psi} \cos \theta - \dot{\psi} \dot{\theta} \sin \theta) \end{aligned} \quad (16)$$

The expressions of Eqs. (16) are the general equations of motion for a symmetric body in terms of Euler angles. The solution may be simplified by assuming steady precession due to a constant moment. Then, the only external moment acting on the body is due to the effect of gravity. This may be expressed as

$$\bar{M} = r_{cg} \bar{z}' \times -mg\bar{z} \quad (17)$$

Substitution of Eqs. (9) and (10) into Eq. (17) yields

$$M_x = W r_{cg} \sin \theta \quad (18)$$

The steady precession rate assumption reduces the number of terms in Eq. (16) since $\dot{\theta} = \ddot{\theta} = \ddot{\phi} = \ddot{\psi} = 0$ and $M_y = M_z = 0$. Therefore, equating the moment components, one arrives at the following:

$$M_x = W r_{cg} \sin \theta = (I_s - I_t) \dot{\psi}^2 \sin \theta \cos \theta + I_s \dot{\phi} \dot{\psi} \sin \theta \quad (19)$$

$$M_y = 0 \quad (20)$$

$$M_z = 0 \quad (21)$$

From Eq. (11), the input spin rate, Ω , of the test rig is

$$\Omega = \omega_z = \dot{\phi} + \dot{\psi} \cos \theta \quad (22)$$

Substitution of Eq. (22) into Eq. (19) to eliminate $\dot{\phi}$ yields

$$(I_s - I_t) \dot{\psi}^2 \cos \theta + I_s \dot{\psi} (\Omega - \dot{\psi} \cos \theta) - W r_{cg} = 0 \quad (23)$$

Application of the quadratic formula to Eq. (23) produces an expression for $\dot{\psi}$:

$$\dot{\psi} = \frac{I_s \Omega \pm \{I_s^2 \Omega^2 - 4(I_t \cos \theta) W_{r_{cg}}\}^{1/2}}{2I_t \cos \theta} \quad (24)$$

Then, substitution of Eq. (22) into Eq. (19) to eliminate $\dot{\psi}$ yields

$$(I_s - I_t) \left(\frac{\Omega - \dot{\phi}}{\cos \theta} \right)^2 \cos \theta + I_s \dot{\phi} \left(\frac{\Omega - \dot{\phi}}{\cos \theta} \right) - W_{r_{cg}} = 0 \quad (25)$$

A final application of the quadratic formula to Eq. (25) produces

$$\dot{\phi} = \frac{(2I_t - I_s) \Omega \pm \{\Omega^2 I_s^2 - 4I_t W_{r_{cg}} \cos \theta\}^{1/2}}{2I_t} \quad (26)$$

Relative motion of the universal joint of the test rig does not involve the same angular coordinates as defined for the system of Euler angles shown in Figs. 36 and 37. The precession and relative spin rates must be expressed in terms of rig coordinates to apply Eqs. (24) and (26) to the instrumentation data. To accomplish this, the direction and velocity components for an arbitrary orientation in the Euler and rig coordinate systems are equated.

The angular velocity in terms of the Euler angles was given previously in Eq. (8). The angular velocity of the system can be transformed to the XYZ ground fixed coordinate system by

$$\bar{x} = \cos \psi \bar{X} + \sin \psi \bar{Y} \quad (27)$$

Substitution of Eqs. (14.5) and (14.22) into Eq. (14.3) yields

$$\begin{aligned} \bar{\omega}_b = & (\dot{\theta} \cos \psi + \dot{\phi} \sin \theta \sin \psi) \bar{X} \\ & + (\dot{\theta} \sin \psi - \dot{\phi} \sin \theta \cos \psi) \bar{Y} \\ & + (\dot{\phi} \cos \theta + \dot{\psi}) \bar{Z} \end{aligned} \quad (28)$$

From Fig. 36 the rig orientation may be expressed in terms of the XYZ ground fixed coordinates by a sequence of transformations. First, transform the body fixed coordinates $x_o y_o z_o$ into the $x' y' z'$ system by the following expressions:

$$\bar{x}' = \cos \phi \bar{x}_o - \sin \phi \bar{y}_o \quad (29)$$

$$\bar{y}' = \sin \phi \bar{x}_0 + \cos \phi \bar{y}_0$$

$$\bar{z}' = \bar{z}_0$$

The $x'y'z'$ -coordinates may then be transformed into the xyz-coordinate system:

$$\bar{x} = \bar{x}' \quad (30)$$

$$\bar{y} = \cos \theta \bar{y}' - \sin \theta \bar{z}'$$

$$\bar{z} = \sin \theta \bar{y}' + \cos \theta \bar{z}'$$

The XYZ-coordinate system is subsequently expressed in terms of the xyz-coordinates by

$$\bar{X} = \cos \psi \bar{x} - \sin \psi \bar{y} \quad (31)$$

$$\bar{Y} = \sin \psi \bar{x} + \cos \psi \bar{y}$$

$$\bar{Z} = \bar{z}$$

The orientation of the test rig may now be written in terms of body fixed coordinates by the concatenation of Eqs. (29-31) as follows:

$$\bar{X} = (\cos \psi \cos \phi - \cos \theta \sin \phi \sin \psi) \bar{x}_0 \quad (32)$$

$$- (\cos \psi \sin \phi + \cos \theta \cos \phi \sin \psi) \bar{y}_0$$

$$+ \sin \theta \sin \psi \bar{z}_0$$

$$\bar{Y} = (\sin \psi \cos \phi + \cos \theta \sin \psi \sin \phi) \bar{x}_0 \quad (33)$$

$$+ (\cos \theta \cos \psi \cos \phi - \sin \psi \sin \phi) \bar{y}_0$$

$$- \cos \psi \sin \theta \bar{z}_0$$

$$\bar{Z} = \sin \theta \sin \phi \bar{x}_0 + \sin \theta \cos \phi \bar{y}_0 + \cos \theta \bar{z}_0 \quad (34)$$

The operation of the universal joint restricts direct spin about the upper shaft. Consequently, the instrumentation is set up to measure the coordinates as shown in Fig. 37. The motion of the actual test rig is fully described by a rotation through the angle λ about the z_2 -axis followed by a rotation λ_1 about the λ_2 -axis and finally by a rotation λ_2 about the x_3' -axis. The rig position

and angular velocity will once again be written in terms of the ground fixed system.

The position of the test rig in the $x_3y_3z_3$ -coordinates can be written in terms of the body-fixed $x_0y_0z_0$ -coordinates as

$$\bar{x}_3 = \bar{x}_0 \quad (35)$$

$$\bar{y}_3 = \cos \lambda_2 \bar{y}_0 - \sin \lambda_2 \bar{z}_0$$

$$\bar{z}_3 = \sin \lambda_2 \bar{y}_0 + \cos \lambda_2 \bar{z}_0$$

The $x_3y_3z_3$ -components of Eqs. (35) are transformed to the $x_2y_2z_2$ -system as follows:

$$\bar{x}_2 = \cos \lambda_1 \bar{x}_3 + \sin \lambda_1 \bar{z}_3 \quad (36)$$

$$\bar{y}_2 = \bar{y}_3$$

$$\bar{z}_2 = -\sin \lambda_1 \bar{x}_3 + \cos \lambda_1 \bar{z}_3$$

Then, the $x_2y_2z_2$ -components of Eqs. (36) are used to express the ground fixed XYZ-coordinate system vectors as:

$$\bar{X} = \cos \lambda \bar{x}_2 - \sin \lambda \bar{y}_2 \quad (37)$$

$$\bar{Y} = \sin \lambda \bar{x}_2 + \cos \lambda \bar{y}_2$$

$$\bar{Z} = \bar{z}_2$$

By combining Eqs. (35-37) one can express the position of the rig in the XYZ-coordinate system by use of

$$\bar{X} = \cos \lambda \cos \lambda_1 \bar{x}_0 \quad (38)$$

$$+ (\cos \lambda \sin \lambda_1 \sin \lambda_2 - \sin \lambda \cos \lambda_2) \bar{y}_0$$

$$+ (\sin \lambda \sin \lambda_2 + \cos \lambda \sin \lambda_1 \cos \lambda_2) \bar{z}_0$$

$$\bar{Y} = \sin \lambda \cos \lambda_1 \bar{x}_0 \quad (39)$$

$$+ (\sin \lambda \sin \lambda_1 \sin \lambda_2 + \cos \lambda \cos \lambda_2) \bar{y}_0$$

$$+ (\sin \lambda \sin \lambda_1 \cos \lambda_2 - \cos \lambda \sin \lambda_2) \bar{z}_0$$

$$\bar{Z} = \sin \lambda_1 \bar{x}_0 + \cos \lambda_1 \sin \lambda_2 \bar{y}_0 + \cos \lambda_1 \cos \lambda_2 \bar{z}_0 \quad (40)$$

From Fig. 21 the angular velocity of the test rig may be written as

$$\bar{\omega}_b = \Omega \bar{Z} + \dot{\lambda}_1 \bar{y}_2 + \dot{\lambda}_2 \bar{x}_3 \quad (41)$$

where, $\Omega = \dot{\lambda}$

It may also be written in terms of the XYZ-coordinate system by use of

$$\bar{y}_2 = -\sin \lambda \bar{X} + \cos \lambda \bar{Y} \quad (42)$$

$$\bar{x}_3 = \cos \lambda_1 \bar{x}_2 - \sin \lambda_1 \bar{z}_2$$

$$\bar{x}_2 = \cos \lambda \bar{X} + \sin \lambda \bar{Y}$$

$$\bar{z}_2 = \bar{Z}$$

Substitution of Eqs. (42) into Eq. (41) then yields

$$\begin{aligned} \bar{\omega}_b = & (-\dot{\lambda}_1 \sin \lambda + \dot{\lambda}_2 \cos \lambda_1 \cos \lambda) \bar{X} + (\dot{\lambda}_1 \cos \lambda + \dot{\lambda}_2 \cos \lambda_1 \sin \lambda) \bar{Y} \\ & + (\Omega - \dot{\lambda}_2 \sin \lambda_1) \bar{Z} \end{aligned} \quad (43)$$

The quantities λ , λ_1 , and λ_2 are determined from the instrumentation.

Therefore, the Euler angles may be calculated by equating the components of Eqs. (32-34) and those of Eqs. (38-40). If a unit vector along the upper shaft ($x_o = 0$, $y_o = 0$, $z_o = 1$) is considered, the directional components simplify to:

$$\sin \psi \sin \theta = \sin \lambda \sin \lambda_2 + \cos \lambda \sin \lambda_1 \cos \lambda_2 \quad (44)$$

$$-\cos \psi \sin \theta = \sin \lambda \sin \lambda_1 \cos \lambda_2 - \cos \lambda \sin \lambda_2 \quad (45)$$

$$\cos \theta = \cos \lambda_1 \cos \lambda_2 \quad (46)$$

The cosine of the half-cone angle is given by Eq. (46). The trigonometric identity, $\sin^2 \theta + \cos^2 \theta = 1$, can be used to express the sine of the half-cone angle as

$$\sin \theta = \{1 - (\cos \lambda_1 \cos \lambda_2)^2\}^{1/2} \quad (47)$$

Substitution of the expression for $\sin \theta$ into Eqs. (44) and (45) yields

$$\sin \psi = \frac{(\sin \lambda \sin \lambda_2 + \cos \lambda \sin \lambda_1 \cos \lambda_2)}{\{1 - (\cos \lambda_1 \cos \lambda_2)^2\}^{1/2}} \quad (48)$$

$$\cos \psi = \frac{(\cos \lambda \sin \lambda_2 - \sin \lambda \sin \lambda_1 \cos \lambda_2)}{\{1 - (\cos \lambda_1 \cos \lambda_2)^2\}^{1/2}} \quad (49)$$

The expressions of Eqs. (48) and (49) are necessary for calculating the precession and spin rates. The next step is to equate the components of angular velocity in Euler coordinates to the coordinates of the rig. Equating the xyz-components of Eqs. (28) and (43), one finds

$$\dot{\theta} \cos \psi + \dot{\phi} \sin \theta \sin \psi = \dot{\lambda}_2 \cos \lambda_1 \cos \lambda - \dot{\lambda}_1 \sin \lambda \quad (50)$$

$$\dot{\theta} \sin \psi - \dot{\phi} \sin \theta \cos \psi = \dot{\lambda}_1 \cos \lambda + \dot{\lambda}_2 \cos \lambda_1 \sin \theta \quad (51)$$

$$\dot{\theta} \cos \theta + \dot{\psi} = \Omega - \dot{\lambda}_2 \sin \lambda_1 \quad (52)$$

From Eqs. (50) and (51), it is possible to isolate the unknowns $\dot{\theta}$ and $\dot{\psi}$. The unknown $\dot{\psi}$ can be eliminated by multiplying Eq. (50) by $\cos \psi$ and Eq. (51) by $\sin \psi$. The results are then added together and simplified to produce

$$\begin{aligned} \dot{\theta} = \cos \psi (\dot{\lambda}_2 \cos \lambda_1 \cos \lambda - \dot{\lambda}_1 \sin \lambda) \\ + \sin \psi (\dot{\lambda}_1 \cos \lambda + \dot{\lambda}_2 \cos \lambda_1 \sin \lambda) \end{aligned} \quad (53)$$

Similarly, the relative spin rate, $\dot{\phi}$, can be found by adding the results after multiplying Eq. (50) by $\sin \psi$ and Eq. (51) by $-\cos \psi$, to yield

$$\begin{aligned} \dot{\phi} \sin \theta = \sin \psi (\dot{\lambda}_2 \cos \lambda_1 \cos \lambda - \dot{\lambda}_1 \sin \lambda) \\ - \cos \psi (\dot{\lambda}_1 \cos \lambda + \dot{\lambda}_2 \cos \lambda_1 \sin \lambda) \end{aligned} \quad (54)$$

Eq. (54) defines the relative spin rate in terms of quantities available from experimental data. The relative spin rate must be known before calculating the precession rate. Substitution of Eq. (46) into Eq. (52)

to eliminate the half-cone angle results in a precession rate given by

$$\dot{\psi} = \Omega - \dot{\lambda}_2 \sin \lambda_1 - \dot{\phi} \cos \lambda_1 \cos \lambda_2 \quad (55)$$

The first derivatives of λ_1 and λ_2 may be approximated by the incremental angle change divided by the time step between data points. The relative spin rate and precession rates may then be determined from the experimental measurements of λ , λ_1 , and λ_2 .

TABLE 1. Minimum inertia axis spin test conditions

RUN	VOL	Ω	I_x	I_y	I_z	W	r_{cg}
	frac.	RPM	slug-ft ²			lbs.	ft.
1	.25	100	.339	.290	.209	14.54	.003
2	.50	100	.371	.349	.239	16.32	-.080
3	.75	90	.358	.357	.263	18.09	-.033
4	.75	90	.358	.357	.263	18.09	-.033
5	.75	100	.358	.356	.263	18.09	-.034
6	.0	112	.291	.203	.168	12.62	.156
7	.25	80	.341	.291	.208	14.54	.002
8	.25	90	.340	.290	.208	14.54	.002
9	.50	70	.376	.351	.237	16.32	-.080
10	.50	83	.374	.350	.238	16.32	-.080
11	.75	72	.361	.357	.262	18.09	-.033
12	.0	130	.291	.203	.168	12.62	.156

TABLE 2. Frequency analysis of all minimum inertia spin configurations

RUN	STATIC NAT. FREQ.	DYN. CONE SLOSH	DYN. RADIAL SLOSH	DYN. CIRCUM. SLOSH	SLABINSKI	PEND. RADIAL MODE	PEND. CIRCUM MODE	SUMNER	↓
1	2.30	0.10 0.60 1.12	0.10 0.60 2.50	0.25 0.60 1.60 3.20	0.47 0.64	2.85	4.00	3.66	1.02 1.20
2	2.55	0.50 3.15	0.50 3.15	0.50 2.50 3.15	0.53 0.60	3.13	4.30	3.86	1.15 1.22
3	(flexible elements, thus not analyzed)								
4	2.65	0.15	0.35	0.35 2.90	0.40 0.40	3.17	4.46	3.90	1.14
5	2.65	0.10 0.35	0.35 1.60 3.15	0.35 3.15	0.44 0.44	3.56	4.77	4.27	1.26 1.27
6		0.20 0.70 1.50			0.78				0.09 1.27

7	2.30	0.10	0.10	0.10	0.38	2.20	3.52	3.00	0.81
		0.45	0.45	0.45	0.50				0.95
				1.25					
				2.10					
				2.60					
8	2.30	0.12	0.45	1.45	0.42	2.52	3.75	3.31	0.92
		0.45	2.80	2.80	0.58				1.07
		0.90		3.40					
9	2.55	0.10	0.30	0.35	0.38	2.11	3.51	2.89	0.84
		0.35		1.15	0.43				0.90
10	2.55		0.35	2.60	0.44	2.51	3.82	3.28	0.97
					0.50				1.04
11	2.65	0.15	0.25	0.25	0.32	2.53	3.96	3.28	0.92
				2.25	0.33				0.93
12	2.65	0.20			0.37				1.09
		0.60			0.91				1.57

TABLE 3. Maximum inertia axis spin test conditions

RUN	VOL	Ω	I_x	I_y	I_z	W	r_{cg}
	frac.	RPM		slug-ft ²		lbs.	ft.
A	.25	80	.249	.212	.257	13.79	-.733
B	.25	118	.217	.211	.258	13.79	-.731
C	.25	90	.243	.236	.258	13.79	-.121
D	.25	75	.244	.236	.257	13.79	-.122
E	.25	80	.249	.212	.257	13.79	-.733
F	.50	70	.280	.289	.324	13.88	-.237
GP	.50	70	.280	.289	.324	13.88	-.237
H	.50	105	.272	.307	.303	15.57	0.194
I	.50	75	.301	.312	.322	13.88	-.274
JP	.50	70	.242	.275	.301	15.57	-.125
K	.50	90	.294	.306	.323	13.88	-.273
L	.75	90	.288	.333	.362	15.65	-.253
MP	.75	90	.220	.265	.362	15.65	-.063
N	.75	50	.292	.333	.358	15.65	-.254

TABLE 4. Frequency analysis results for all maximum inertia spin tests

RUN	STATIC NAT. FREQ.	DYN. CONE	DYN. RADIAL SLOSH	DYN. RADIAL SLOSH	DYN. CIRCUM. SLOSH	SLABINSKI	PEND. RADIAL MODE	PEND. CIRCUM MODE	SUMNER	$\dot{\psi}=\Omega$
AP	2.30	0.30	0.08	0.08	0.08	0.04	2.78	3.80	3.24	1.33
			0.25	0.22	0.28					
			3.45	0.32						
B	2.30	0.05	0.15	0.05	0.05	0.37	3.89	4.78	4.64	1.97
			1.75	1.75	.44					
			3.50	3.50						
C	2.30	0.10	0.20	0.10	0.10	0.10	2.42	4.19	3.76	1.50
			1.55	1.56	0.14					
			3.12	3.15						
D	2.30	0.10	0.15	0.10	0.10	0.10	2.32	3.49	3.06	1.25
			1.18	1.10	0.11					
			2.30	2.30						
E	2.30	0.05	1.18	1.18	1.18	0.28	2.78	3.80	3.24	1.43
				2.30	0.04					
				2.60						
F	2.55	0.20	0.25	1.15	1.15	0.12	2.39	3.63	3.26	1.17
			1.15	1.12	2.25	0.13				
			2.25	2.70	2.70					
			2.70	3.40	3.40					

GP	2.55	0.05	0.05	0.05	0.05	0.14	2.31	3.63	3.26	1.17
		0.25	3.40	2.65		0.18				
		1.60	3.70							
H	2.55	0.08	0.05	0.10	0.02	3.55	4.85	4.40	1.75	
			3.40	3.40	0.20					
			2.00	1.75						
			2.20	2.15						
I	2.55	0.15	0.10	1.15	0.04	2.60	3.75	3.28	1.25	
		1.18	1.15	2.30						
			2.30	3.40	0.09					
JP	2.55	0.05	0.05	0.10	0.11	2.39	3.63	3.26	1.17	
		0.15	0.20	1.20	0.28					
		1.62		1.50						
				2.75						
K	2.55	0.05	0.05	0.05	0.08	3.17	4.23	3.82	1.50	
			0.15		0.15					
			1.45							
			2.95							
L	2.68	0.05	0.05	1.45	0.13	3.61	4.71	4.23	1.50	
			1.45	2.95	0.39					
			2.95							
MP	2.68	0.07	0.10	0.20	0.57	3.73	4.87	4.36	1.55	
		1.50	0.35	0.30	1.00					
			1.70	5.80						
N	2.68	0.05	0.05	0.10	0.06	2.19	3.51	2.86	0.83	
		0.30	0.80	0.80	1.19					
		0.80	1.60	1.60						
			2.35	2.35						
			3.20	3.15						

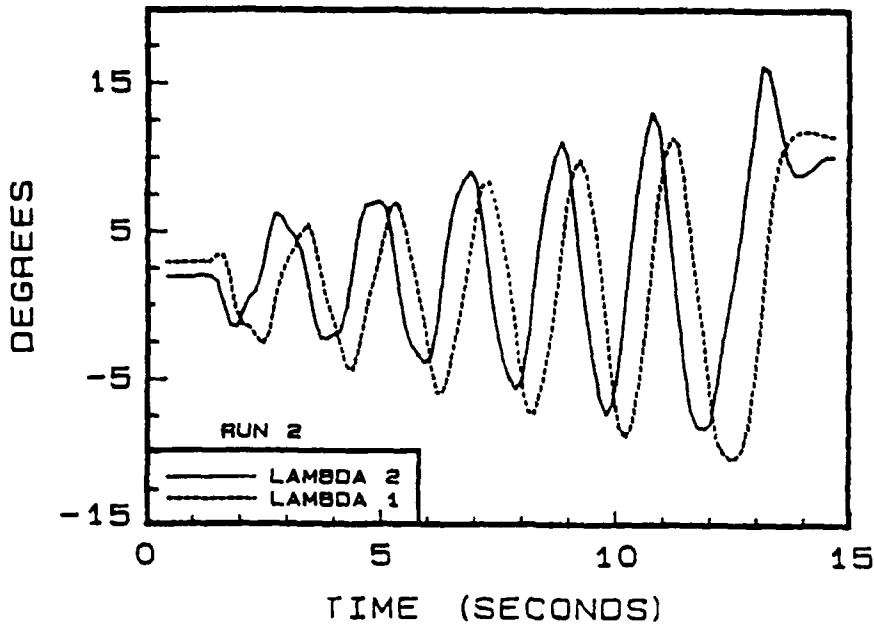


FIGURE 1. Test rig oscillations.

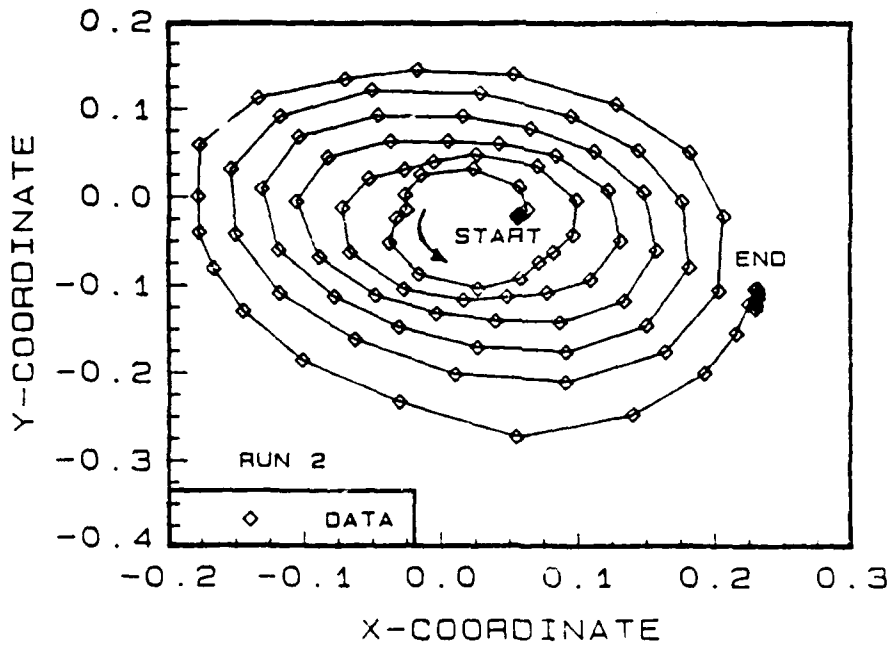


FIGURE 2. Trace of the tip of a unit vector imbedded in the upper shaft and projected onto the xy plane of the lower shaft, minimum inertia spin axis.

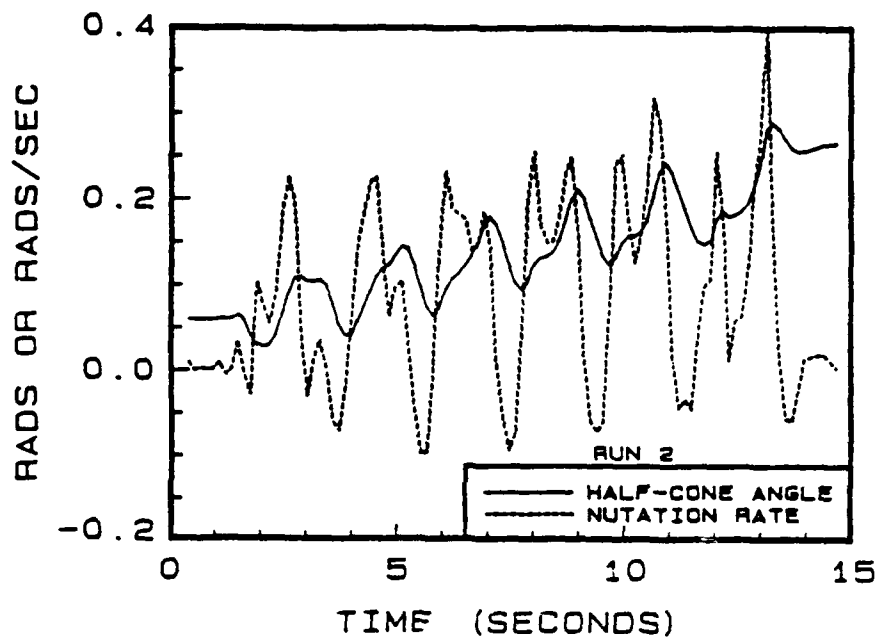


FIGURE 3. Half-cone angle and nutation rate

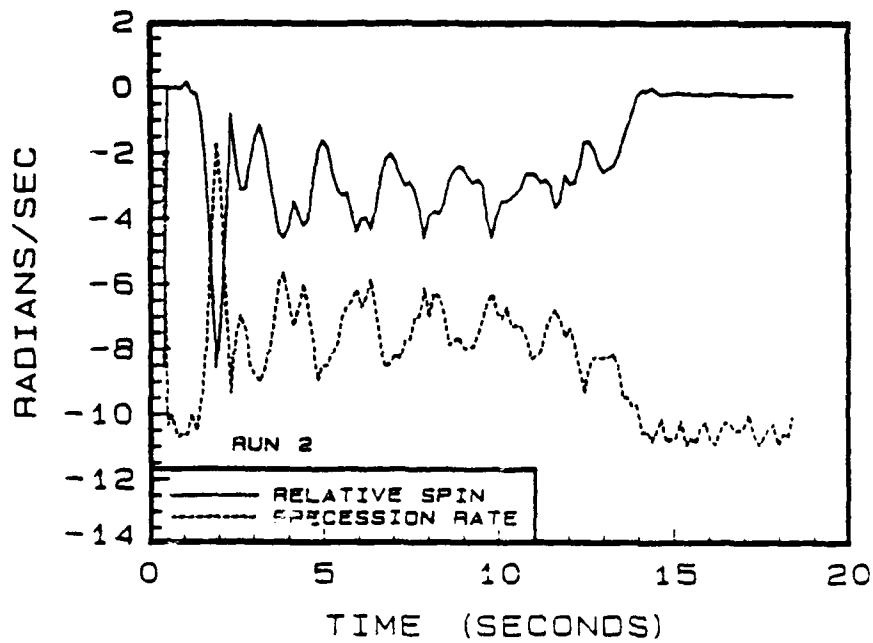


FIGURE 4. Precession rate and relative spin rate

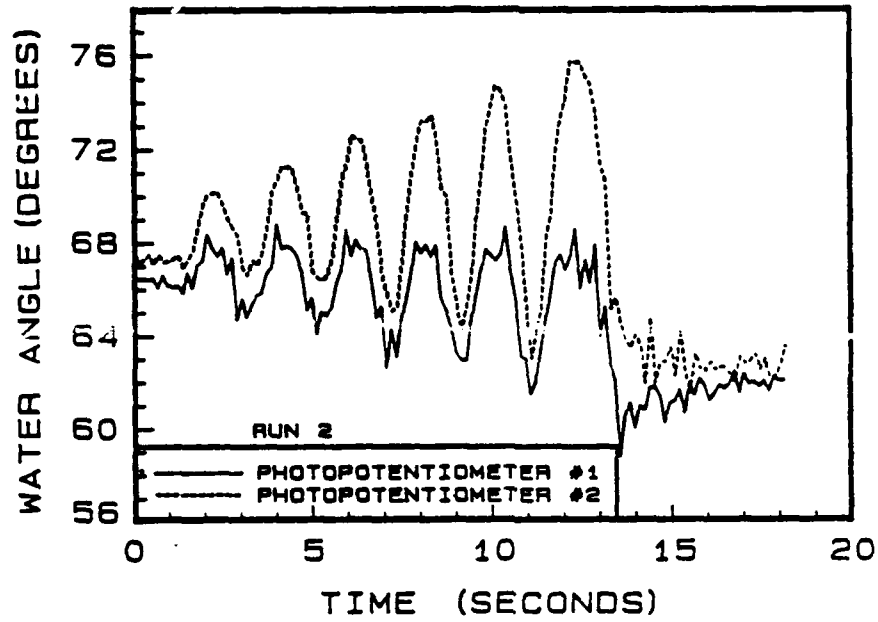


FIGURE 5. Radial pendulum oscillations measured by photopotentiometers 1 and 2

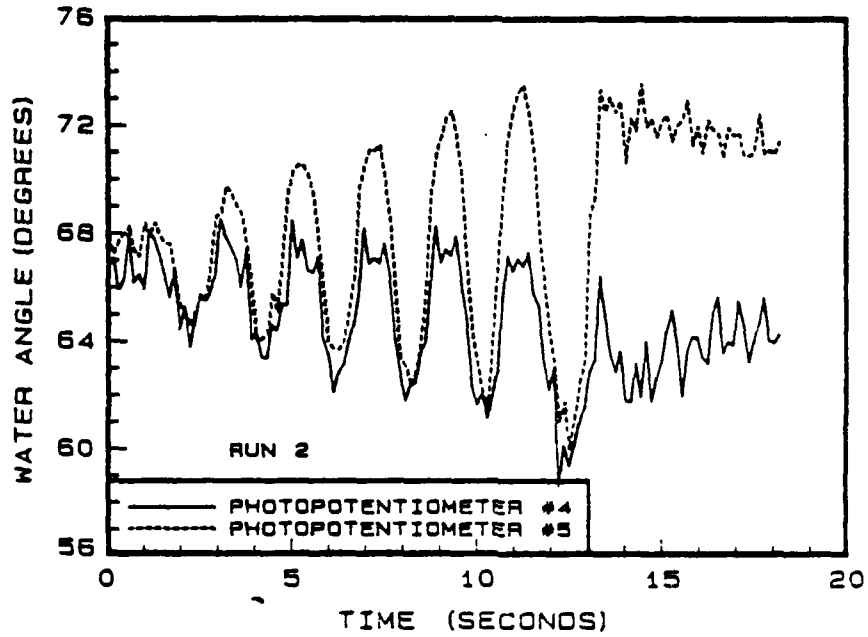


FIGURE 6. Radial pendulum oscillations measured by photopotentiometers 4 and 5

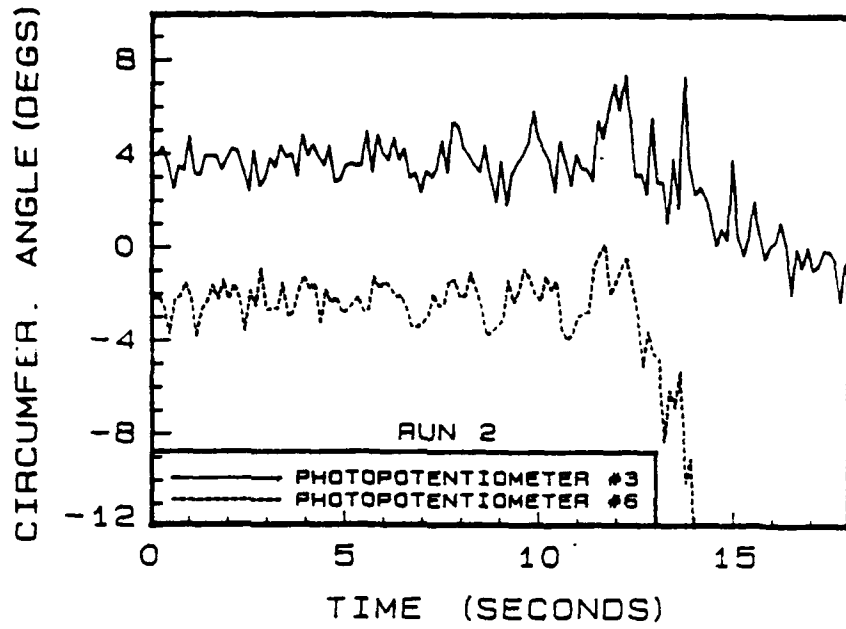


FIGURE 7. Circumferential liquid oscillations for both spheres

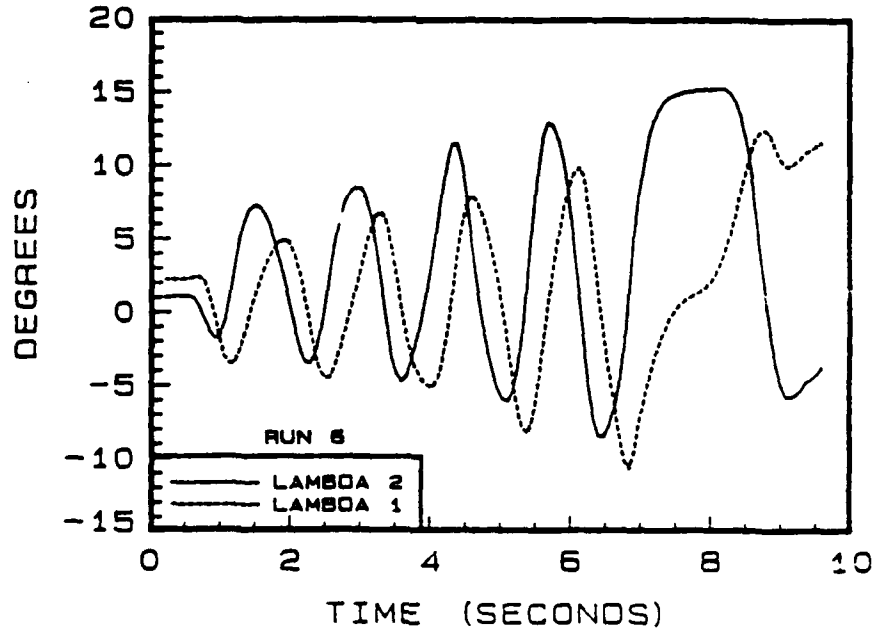


FIGURE 8. Rigid body oscillations of test rig for empty spheres

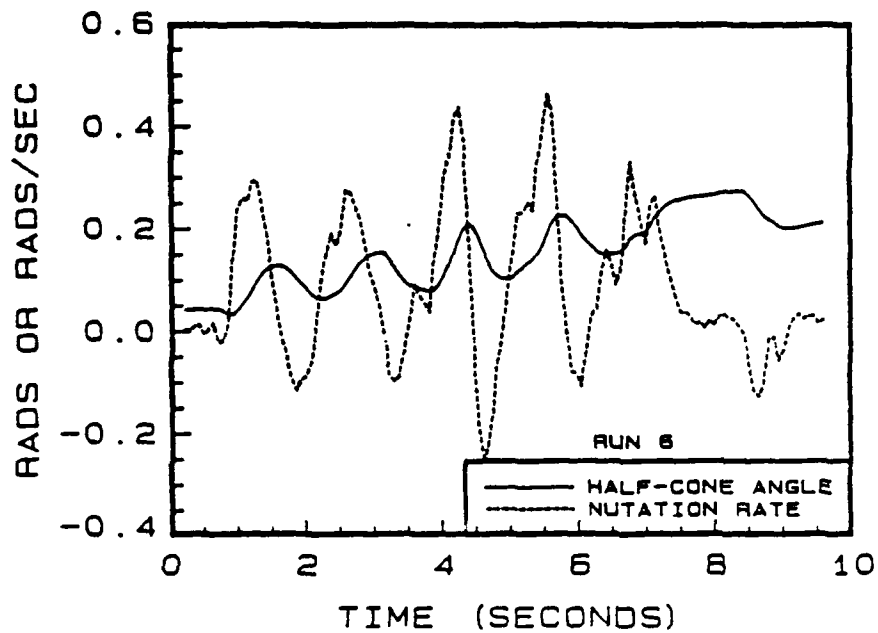


FIGURE 9. Half-cone and nutation rate for empty spheres

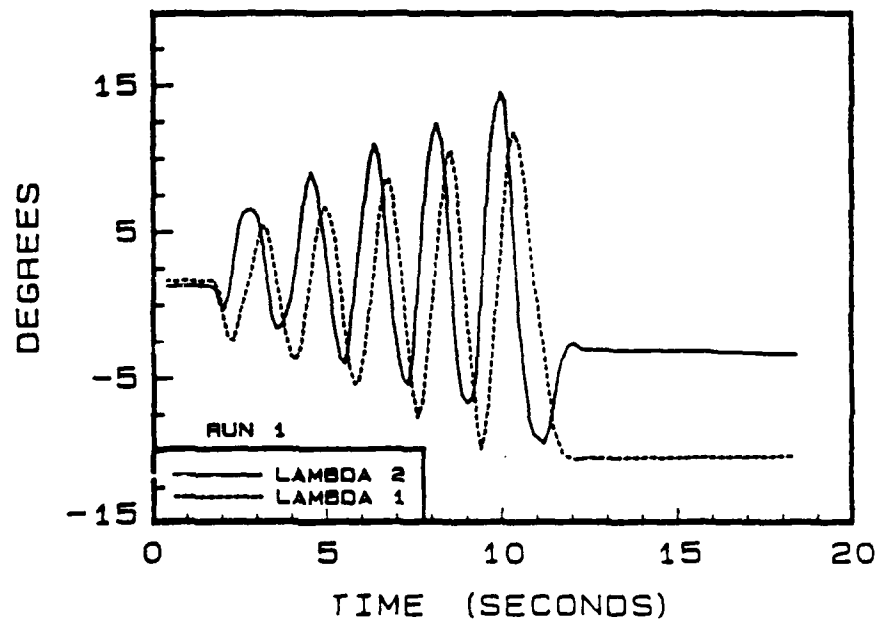


FIGURE 10. Rigid body oscillations of test rig for one-quarter filled spheres

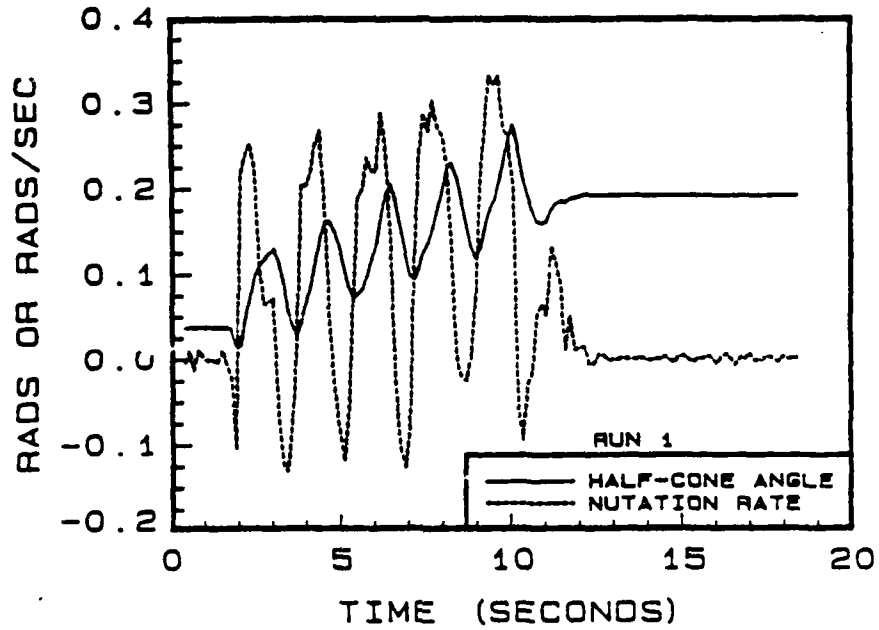


FIGURE 11. Half-cone angle and nutation rate for one-quarter filled spheres

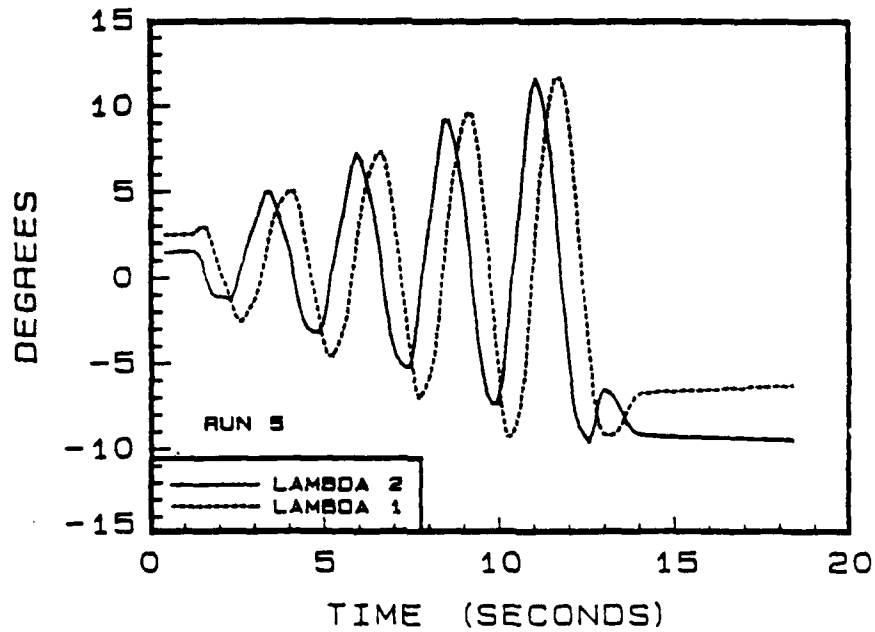


FIGURE 12. Rigid body oscillations of test rig for three-quarter filled spheres

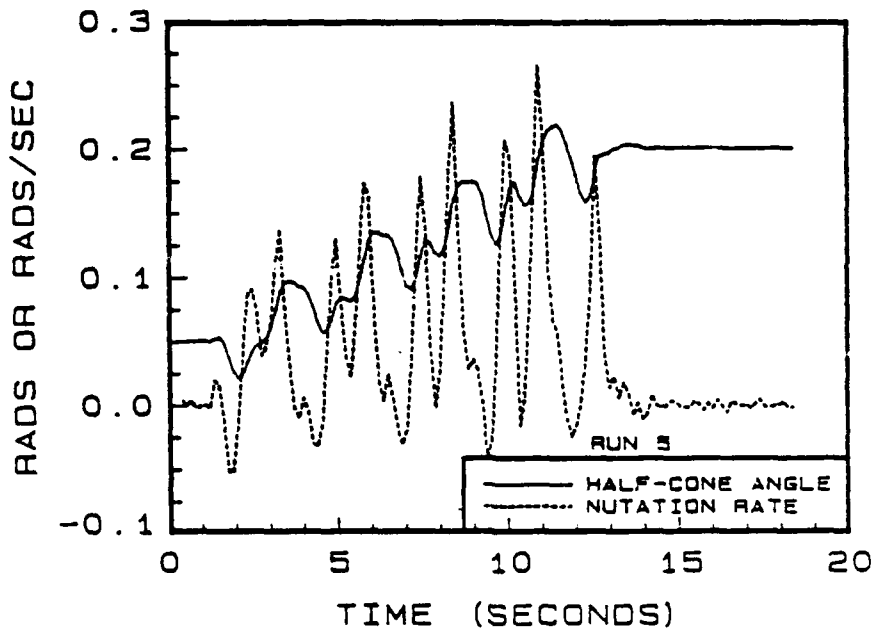


FIGURE 13. Half-cone angle and nutation rate for three-quarter filled spheres

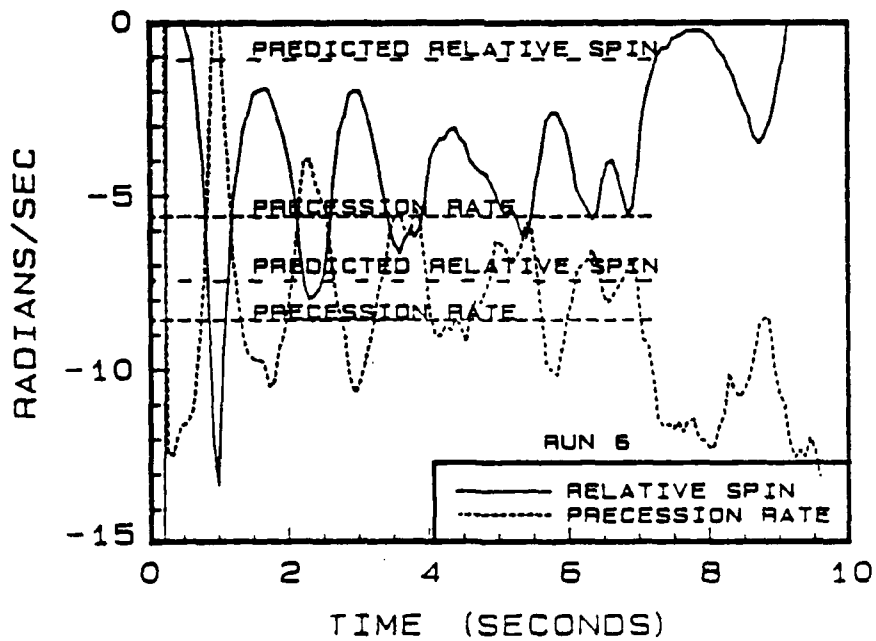


FIGURE 14. Predicted precession rate, relative spin rate and experimental results for empty spheres

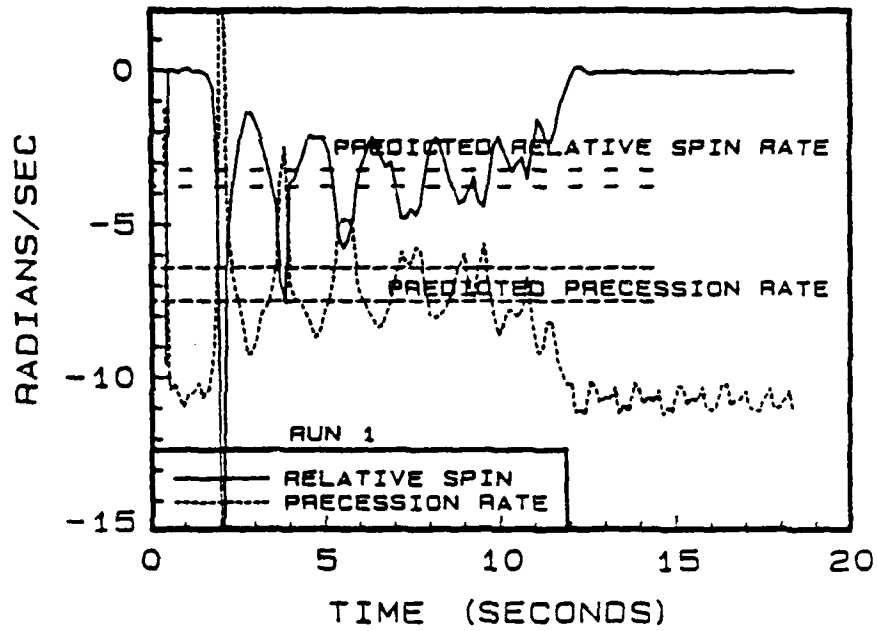


FIGURE 15. Predicted precession rate, relative spin rate and experimental results for one-quarter filled spheres

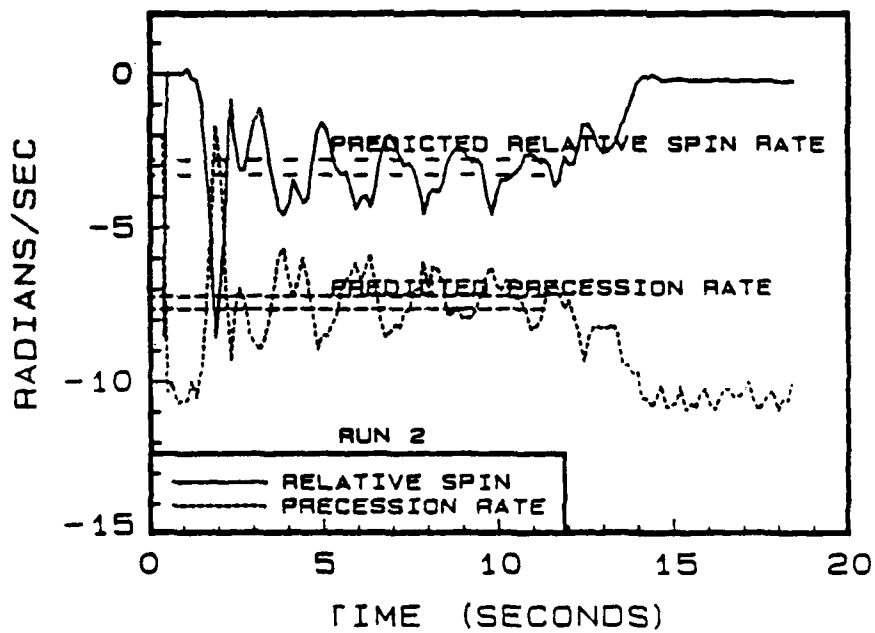


FIGURE 16. Predicted precession rate, relative spin rate and experimental results for half filled spheres

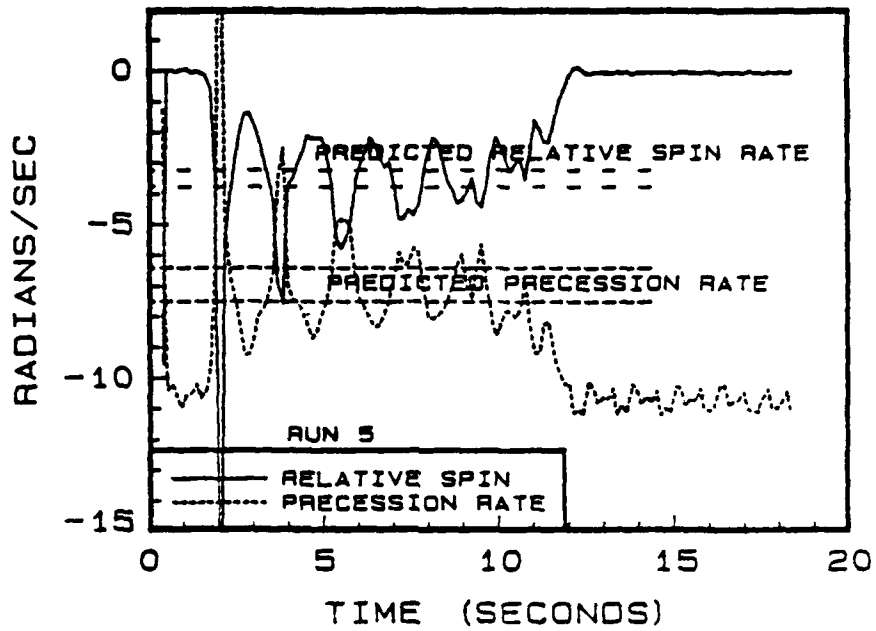


FIGURE 17. Predicted precession rate, relative spin rate and experimental results for three-quarter filled spheres

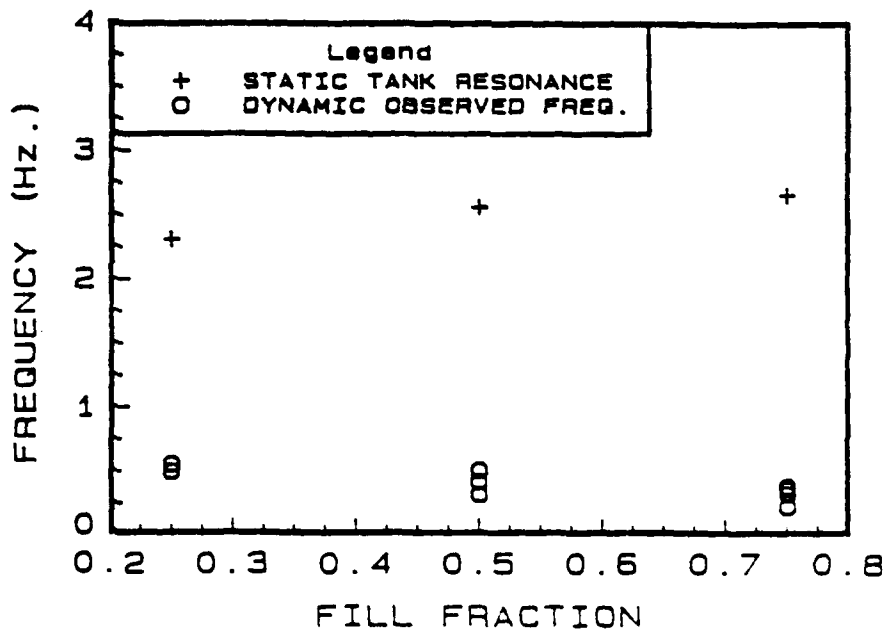


FIGURE 18. Experimental test slosh data and static tank resonance

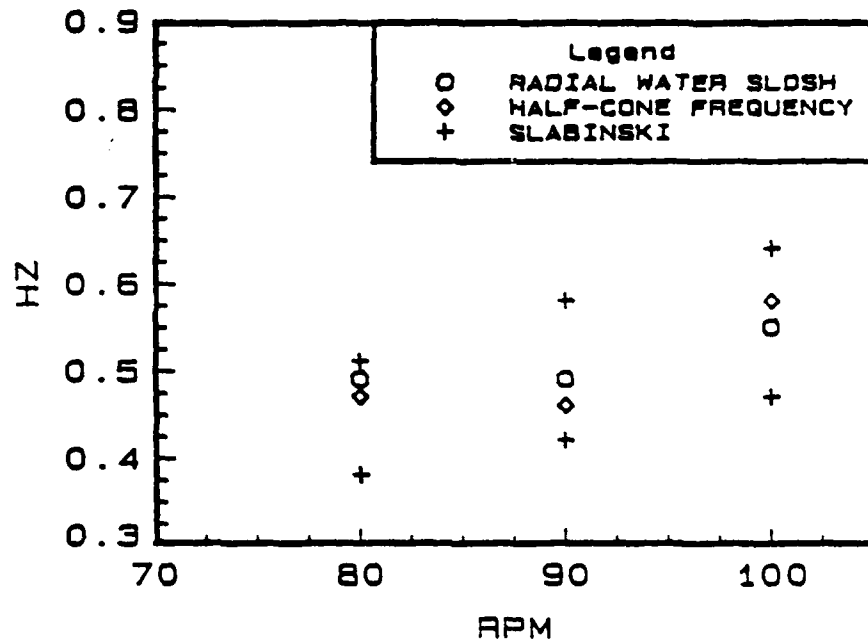


FIGURE 19. Experimental correlation with driving frequency of Slabinski for one-quarter filled spheres

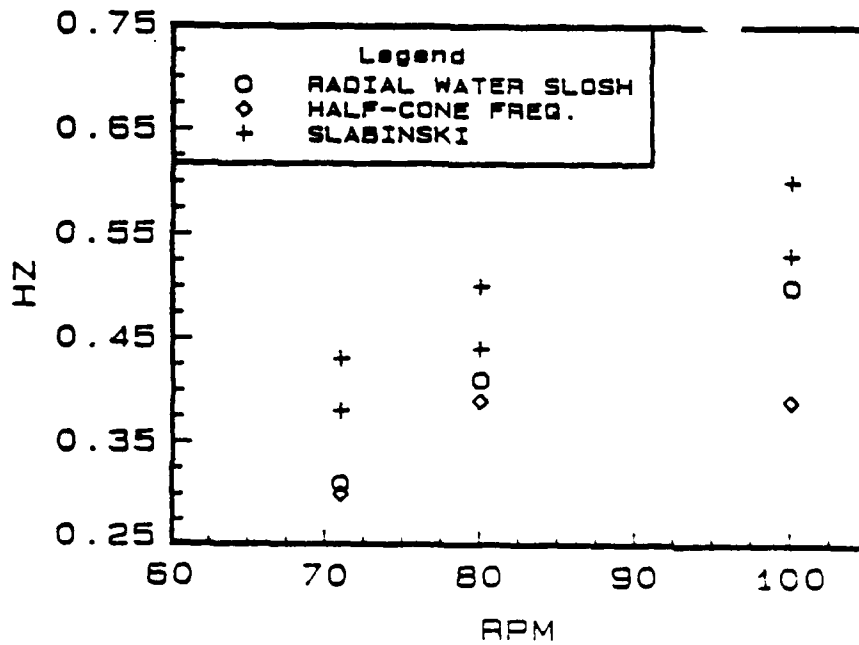


FIGURE 20. Experimental correlation with driving frequency of Slabinski for half filled spheres

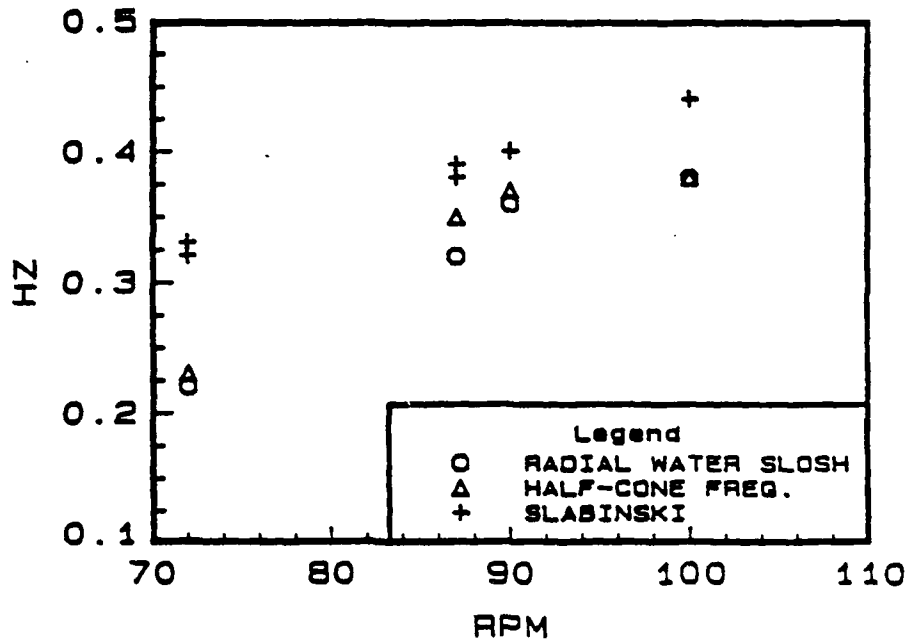


FIGURE 21. Experimental correlation with driving frequency of Slabinski for three-quarter filled spheres

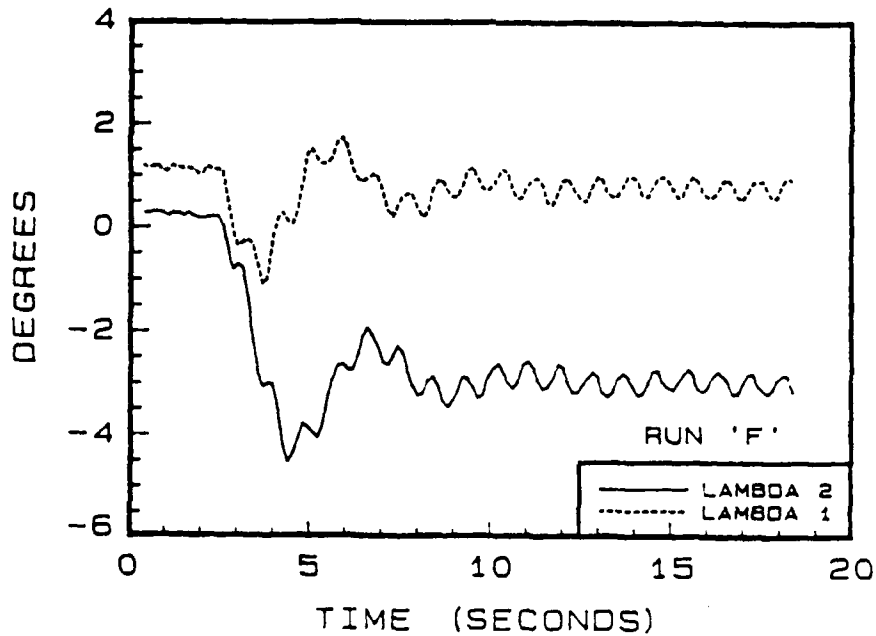


FIGURE 22. Oscillations of the test rig with half filled spheres for maximum inertia spin axis

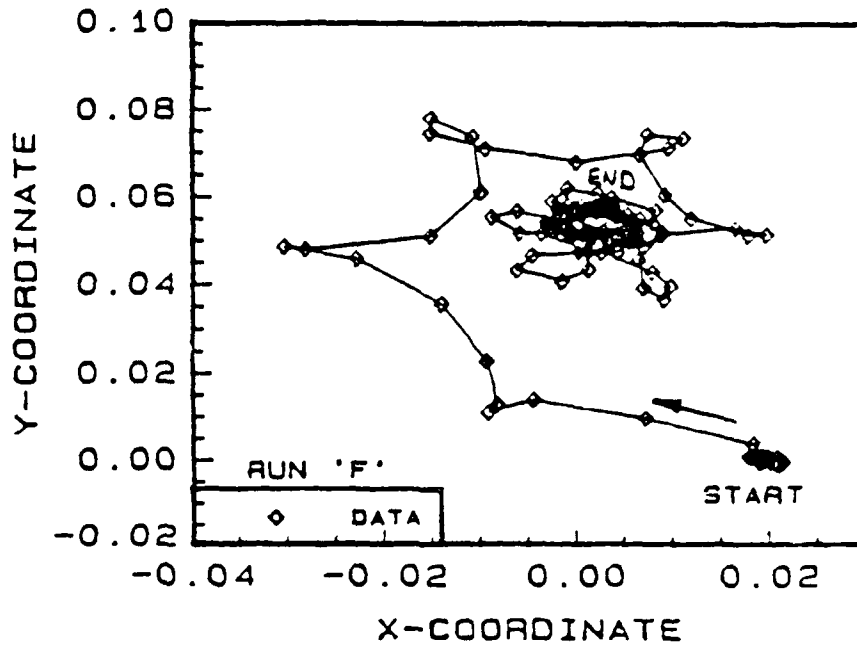


FIGURE 23. Trace of the tip of a unit vector imbedded in the upper shaft and projected onto the xy plane of the lower shaft for maximum inertia spin axis

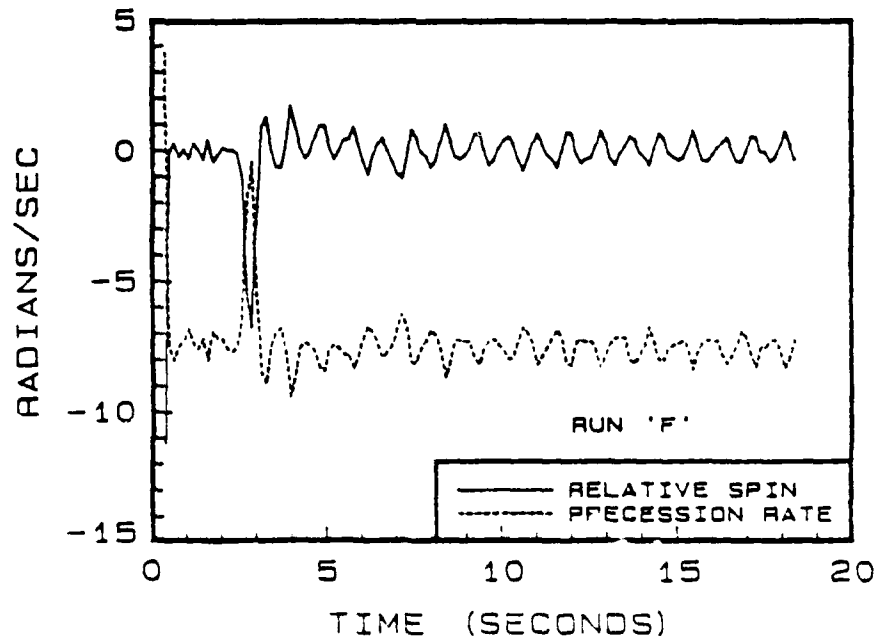


FIGURE 24. Half-cone angle and nutation rate for maximum inertia spin axis

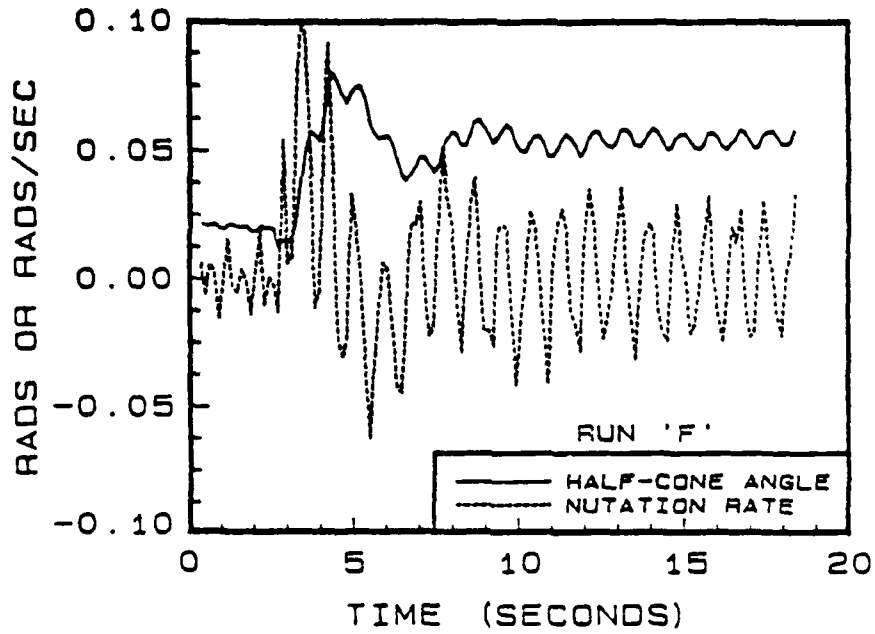


FIGURE 25. Precession and relative spin rate for maximum inertia spin axis

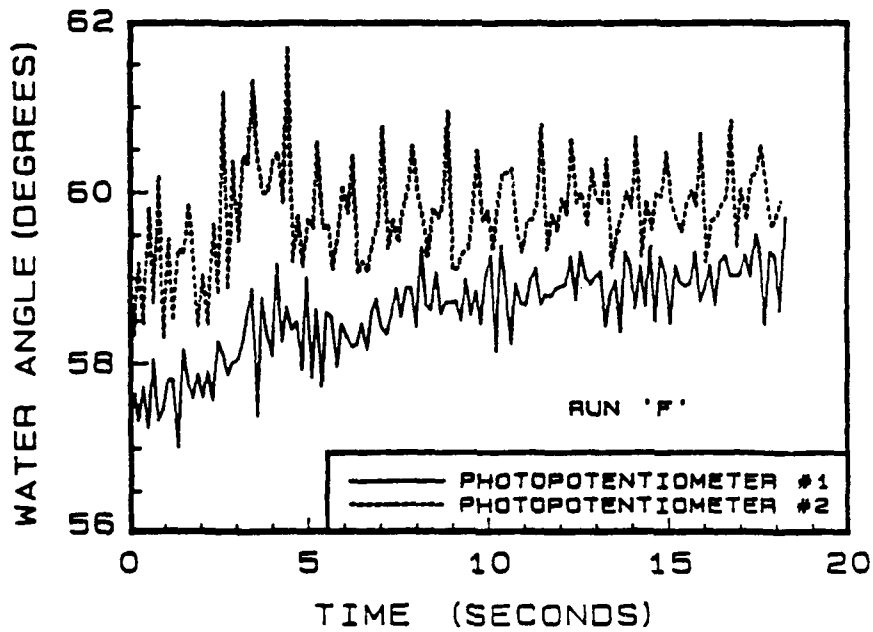


FIGURE 26. Radial liquid oscillations sensed by photopotentiometers 1 and 2 for maximum inertia spin axis

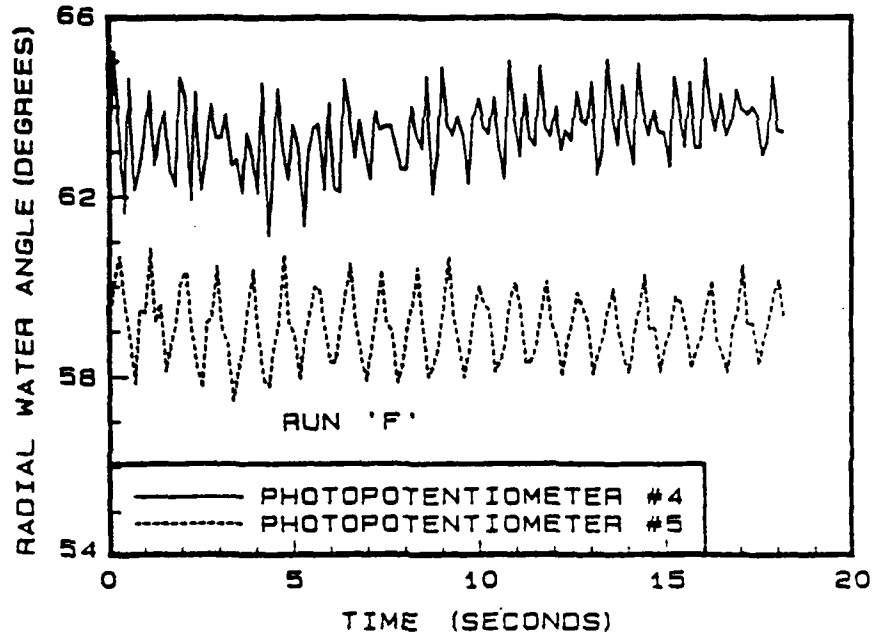


FIGURE 27. Radial liquid oscillations sensed by photopotentiometers 4 and 5 for maximum inertia spin axis

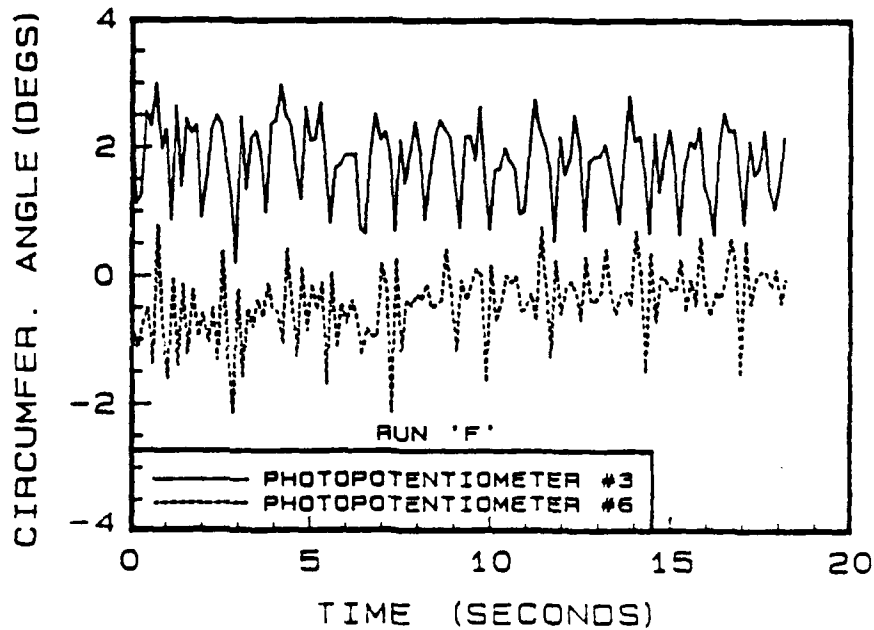


FIGURE 28. Circumferential liquid slosh oscillations sensed by photopotentiometers 3 and 6 for maximum inertia spin axis

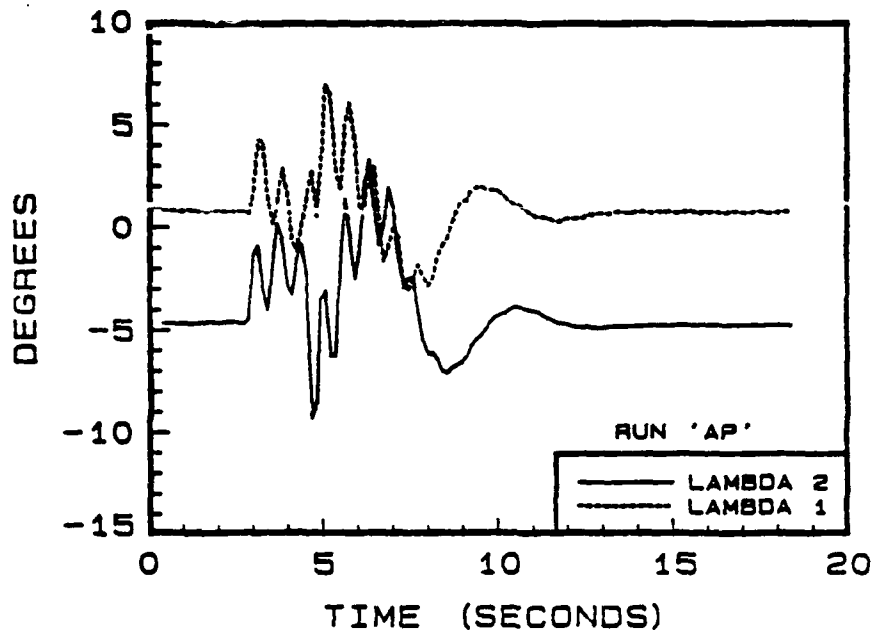


FIGURE 29. Stability verification for one-quarter filled spheres

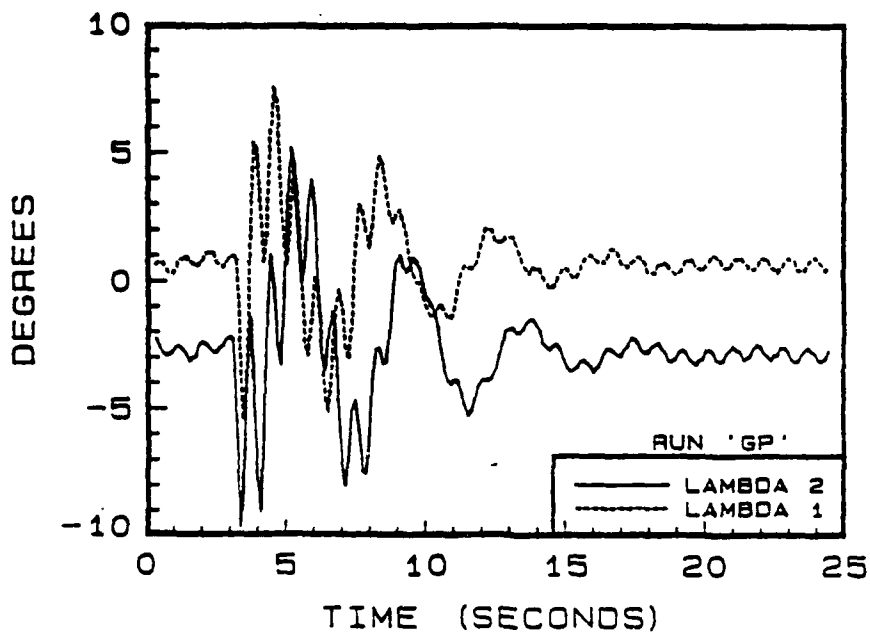


FIGURE 30. Stability verification for half filled spheres

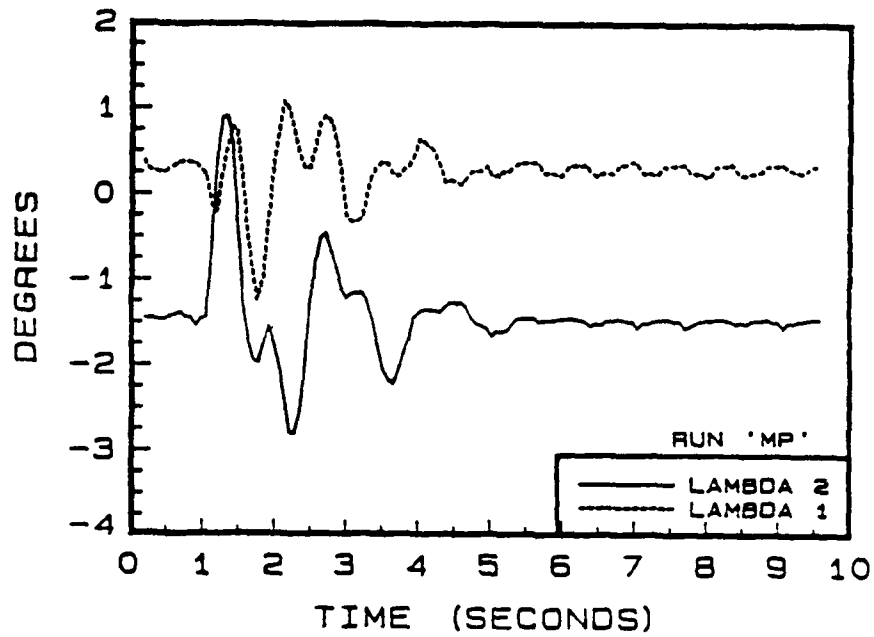


FIGURE 31. Stability verification for three-quarter filled spheres

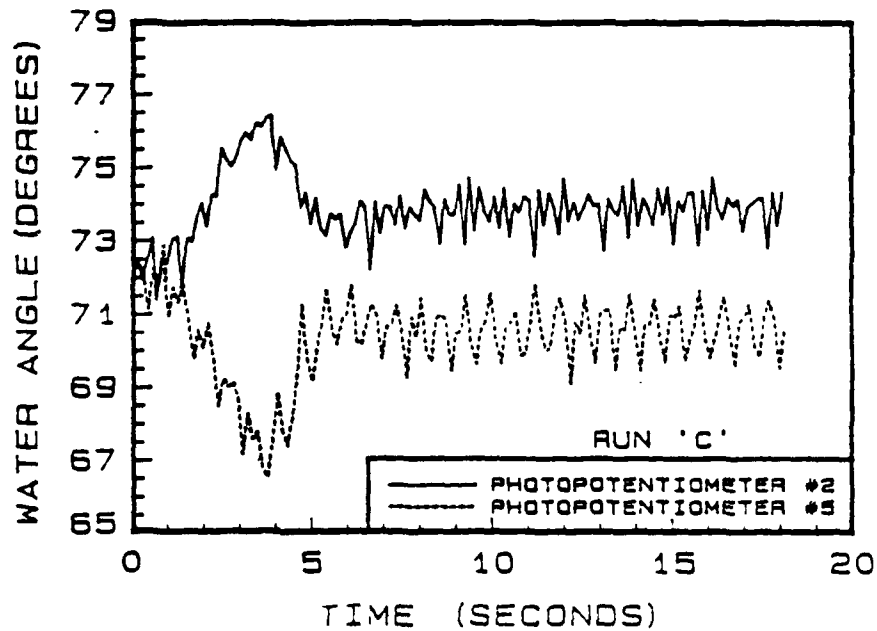


FIGURE 32. Radial liquid oscillations for one-quarter filled spheres

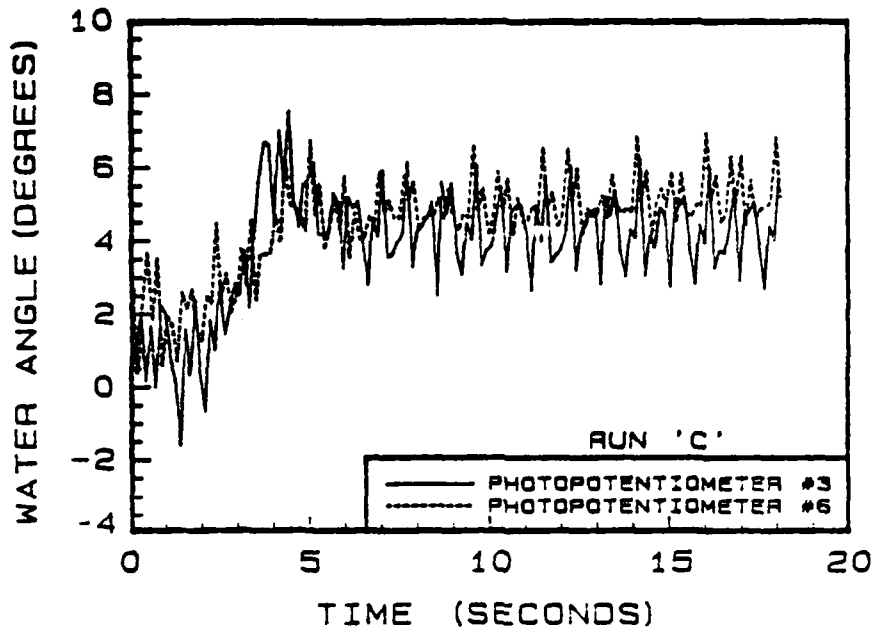


FIGURE 33. Circumferential liquid oscillations for one-quarter filled spheres

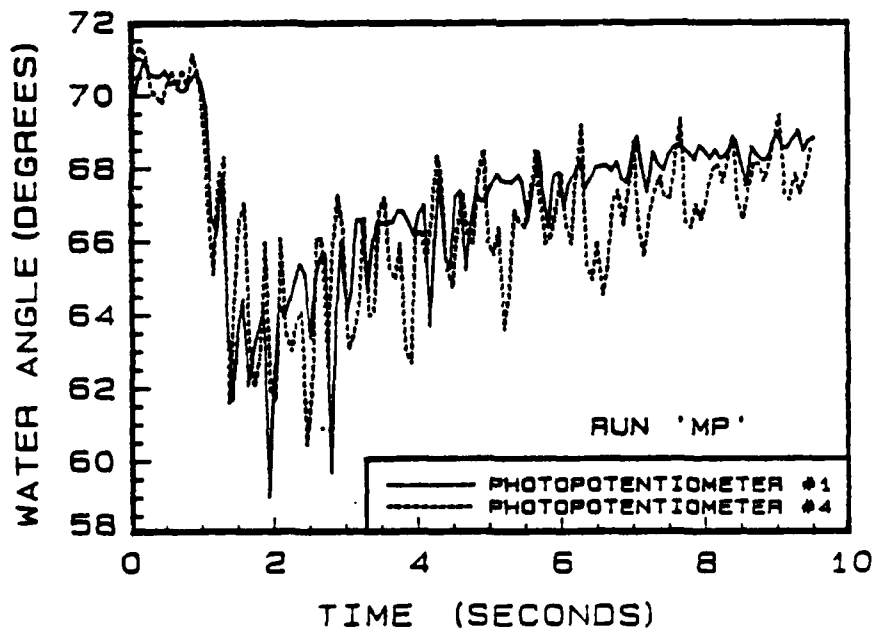


FIGURE 34. Radial oscillations for three-quarter filled spheres

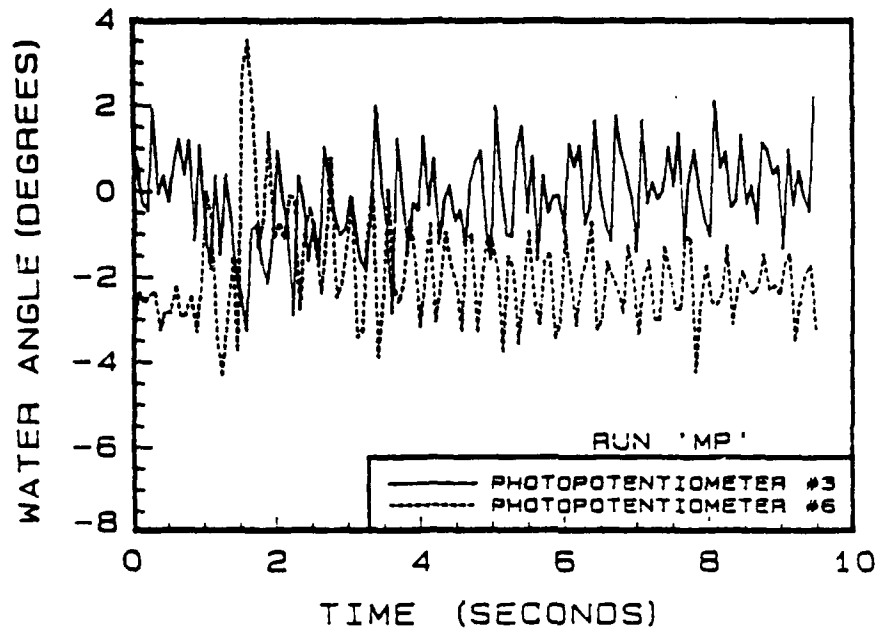


FIGURE 35. Circumferential liquid oscillations for three-quarter filled spheres

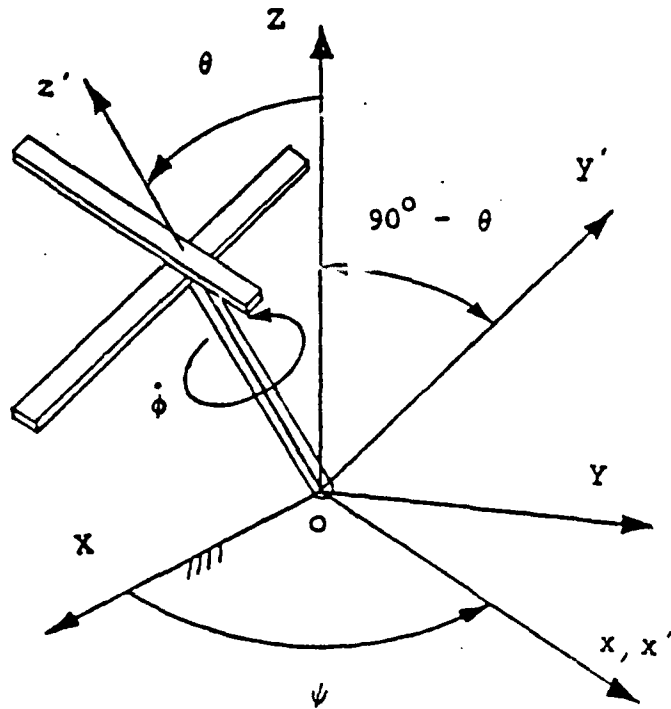


FIGURE 36. Typical precession and spin coordinates

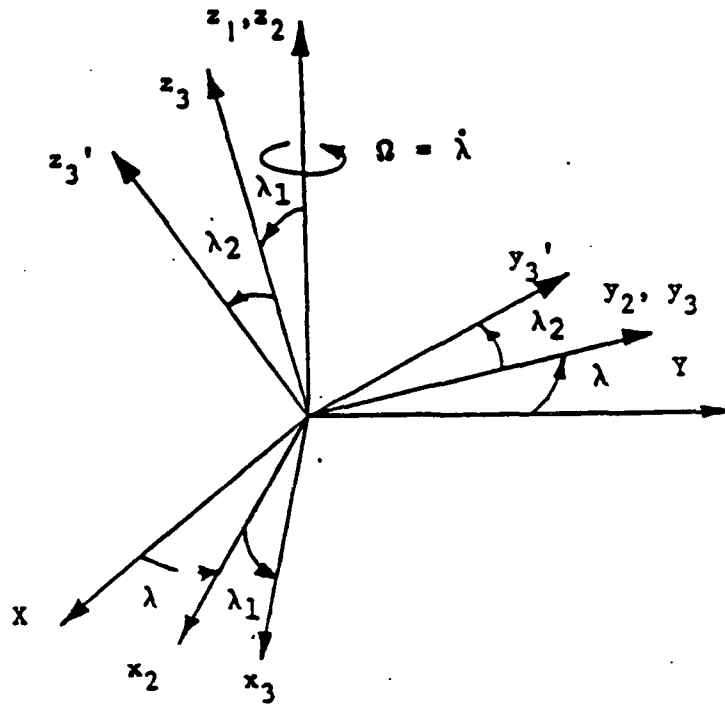


FIGURE 37. Angular coordinates for the test rig universal joint

APPENDIX E

SIMULATOR DYNAMIC RESPONSE

COMPUTER SIMULATION OF A TEST RIG TO MODEL
LIQUID SLOSHING IN SPIN-STABILIZED SATELLITES

D. R. Flugrad
L. A. Obermaier
Iowa State University
Ames, Iowa

ABSTRACT

Certain communications satellites carry liquid stores on board for station tending and attitude adjustment. However, sloshing of the liquid can cause an undesirable nutational motion of the spin-stabilized vehicle. In previous work a test rig was designed, built and instrumented to study the interaction between the rotating structure and liquid. To augment that experimental project, a computer model of the test rig has been developed to simulate the dynamic motion of the system for various parameter values. The sloshing liquid was replaced by a two degree-of-freedom pendulum in the mathematical model. Simulation results from this software are compared with those obtained from a general multibody dynamics program and with experimental output obtained from the test rig.

INTRODUCTION

Extensive research, both analytical and experimental, has been conducted on the stability of spacecraft having liquid fuel stores. A rigid body can be stabilized by spinning about an axis of either maximum or minimum moment of inertia. Common examples of spin stabilization about an axis of minimum moment of inertia include a spinning top or a football. However, systems containing a significant amount of liquid mass, such as the INTELSAT IV [1,2] and the STAR 48 [3] communications satellites, as well as the XM761 artillery projectile [4], have experienced instability when spun about an axis of minimum moment of inertia. Sloshing of liquid payloads has been suspected of causing instability of the spin-stabilized bodies.

Viscous dissipation resulting from relative movement between a liquid and its container tends to reduce the kinetic energy of a system. The body, attempting to conserve angular momentum, is then forced to seek a lower energy state. For a given amount of angular momentum, spin about an axis of maximum moment of inertia represents the minimum energy state possible. If a body spun about its axis of minimum moment of inertia experiences energy dissipation, it will seek the lower energy state and will end up spinning about its axis of maximum moment of inertia if unrestrained. This is known as a flat spin.

Agrawal [5] states that for a body with flexible elements, the ratio of the moment of inertia of the spin axis to that of the transverse axis must be greater than one for stability. Thus, to be stable, a body containing liquid must be spun about an axis of maximum moment of inertia.

Several launchings of the STAR 48 communications satellites resulted in a coning motion of the spacecraft. Hill [3] used an equivalent mechanical

pendulum model, along with a mass representing the main body and rocket motor to approximate the STAR 48 system. He developed control laws using linearized equations of motion.

The INTELSAT IV communications satellite also experienced instability once launched. Slabinski [1] conducted in-orbit testing of the satellite, as well as a theoretical analysis, to study the sloshing phenomenon inside the tanks containing liquid propellant. He developed relationships between driving frequencies and nutation frequencies. Martin [2] experimented with tanks of liquid propellant on earth. Martin, through his experimental investigations, found that when a spinning tank is subjected to angular oscillations about an axis which is not parallel to an axis of symmetry of the tank, turbulent fluid motion is excited. However, when the tank is accelerated rectilinearly, the motion of its contents is relatively calm, like that of a rigid body. Because a sphere is axisymmetric, liquid in a sphere did not experience the turbulent motion that it did in differently shaped tanks. In the spherical tanks, the liquid behaved like a pendulous rigid body.

Many analytical attempts to quantify the movement of liquids in tanks have used a pendulum analogy. Such an analogy assumes that the liquid inside the tank moves as a spherical pendulum would under the same conditions. Sumner [6] developed relations to describe a pendulum representing the liquid in spherical and oblate spheroidal nonrotating tanks as a function of tank geometry and fill fraction. The mass of the pendulum is not equal to the mass of the liquid in the tank. A nonsloshing mass is fixed at approximately the center of the tank. The sum of the nonslosh mass and the pendulum mass is equal to the total liquid mass. Sayar and Baumgarten [7] included a rotational damper and a cubic spring in their pendulum analogy to improve

Sumner's model in the nonlinear range.

Zedd and Dodge [8] examined the energy dissipated by liquids in rotating spherical tanks using a pendulum analogy. Their model included a pendulum, a rotor, and a viscous dashpot. Through this analogy, they developed equations for natural frequencies of the pendulum as functions of tank location, tank fill fraction, and the spin rate of the tank.

Cowles [9] built a test rig to model a satellite containing liquid fuel stores. His model consisted of a motor driven shaft which supported a semi-rigid assembly. The assembly was connected to the vertical input shaft by a Hooke's type universal joint. The assembly held two tanks which were partially filled with water. By altering the location of the tanks and the dimensions of the assembly, Cowles was able to achieve a variety of test conditions, including spin about axes of maximum, intermediate, and minimum moments of inertia. When spun about an axis of maximum moment of inertia, the assembly was extremely stable, even when perturbed. The assembly, however, fell immediately into a flat spin when spun about an axis of intermediate moment of inertia. Though a configuration was designed and built for spin about an axis of minimum moment of inertia, tests were never completed because it was felt the assembly might be damaged in a collision with the supporting structure if it attempted to go into a flat spin.

Anderson [10] redesigned the mechanical assembly built by Cowles. Anderson's assembly included a restricting collar so that even an unstable test assembly could not damage itself or the supporting structure. The redesign included instrumentation in order to acquire quantitative measurements of the motion of the assembly and the liquid contained in it. Just as predicted, Anderson found the case of spin about an axis of minimum moment of inertia to be unstable.

The work described in this study develops the equations of motion for the test rig designed and constructed by Cowles and Anderson. Equations of motion were derived using Lagrange's equations. State variables were chosen to best match the quantities being measured by Anderson's instrumentation. The equations of motion were then numerically integrated. Results of the numerical simulation were compared with those from an existing rigid body dynamic analysis program to verify the validity of the numerical simulation. Simulation results were also compared with Anderson's experimental results.

DEVELOPMENT OF EQUATIONS

A schematic drawing of the mechanical system modeled is shown in Fig. 1. The model contains four rigid bodies. A lower shaft which rotates in pillow block bearings supports the structure. The upper assembly is connected to the lower shaft by a Hooke's type universal joint. Two pendula, representing the sloshing liquid in the tanks, are then symmetrically attached to the upper assembly by Hooke's type universal joints. The pendula are assumed to be point masses suspended from the upper assembly by rigid, massless rods. Fig. 2 shows the positioning of a pendulum with respect to the mechanical model.

A note of clarification is perhaps necessary to define terminology of bodies in the system. The "test rig" is defined as the structure that encloses the liquid and its associated supports, as well as the contained fluid. This basically includes everything supported by the universal joint on the mechanical assembly. The "upper assembly" is associated with the mathematical model and does not have a direct physical representation. The upper assembly is defined as the test rig minus the enclosed liquid plus the

nonslough masses.

To develop the equations of motion for the system, a Lagrangian formulation was used. Through the use of coordinate transformations, position vectors were determined for each of the bodies. The position vectors were then differentiated with respect to time to determine velocities for the bodies. The kinetic and potential energies of the bodies were then developed. Once the equations of motion were determined according to Lagrange's equations, they were numerically integrated using a double precision version of DIFFEQ, a numerical integration program.

Coordinate Transformations and Body Positions

The positions of the bodies were determined through simple coordinate transformations consisting of rotations and translations of Cartesian coordinates. All coordinate systems used were defined to be right-handed.

The $\hat{x}_1-\hat{y}_1-\hat{z}_1$ coordinate system is stationary and is positioned at the center of the universal joint. The \hat{z}_1 axis is directed vertically upward. Positioning of the \hat{x}_1 and \hat{y}_1 axes is arbitrary.

Transformation to the $\hat{x}_2-\hat{y}_2-\hat{z}_2$ coordinate system is achieved by a right hand rotation about the \hat{z}_1 axis. The $\hat{x}_2-\hat{y}_2-\hat{z}_2$ coordinate system is attached to the lower shaft of the test rig and its origin is at the center of the universal joint. The $\hat{x}_2-\hat{y}_2-\hat{z}_2$ axes are fixed in such a way that when the \hat{z}_1 and \hat{z}_2 axes are aligned, the \hat{y}_2 components of the position vectors of the pendulum supports are zero. Generally, the matrix $[A_{ij}]$ is defined such that

$$\begin{Bmatrix} \hat{x}_i \\ \hat{y}_i \\ \hat{z}_i \\ 1 \end{Bmatrix} = [A_{ij}] \begin{Bmatrix} \hat{x}_j \\ \hat{y}_j \\ \hat{z}_j \\ 1 \end{Bmatrix} \quad (1)$$

The transformation matrix from the $\hat{x}_2-\hat{y}_2-\hat{z}_2$ coordinate system to the $\hat{x}_1-\hat{y}_1-\hat{z}_1$ coordinate system, $[A_{12}]$, is given in the appendix.

The rotation of the upper assembly relative to the lower shaft is defined by the two rotation angles, λ . First, a rotation by an amount λ_1 about the \hat{y}_2 axis defines the transformation to the $\hat{x}_3-\hat{y}_3-\hat{z}_3$ coordinate system. Then the coordinate system is rotated through an angle λ_2 about the \hat{x}_3 axis to arrive at the $\hat{x}_4-\hat{y}_4-\hat{z}_4$ system.

The $\hat{x}_4-\hat{y}_4-\hat{z}_4$ coordinate system is fixed to the upper assembly in such a way that the \hat{y}_4 components of the position vectors from the universal joint to the pendulum supports is zero. The origins of the $\hat{x}_3-\hat{y}_3-\hat{z}_3$ and $\hat{x}_4-\hat{y}_4-\hat{z}_4$ systems are located at the center of the universal joint. The rotations between the 2, 3 and 4 coordinate systems are shown in Fig. 3.

Because the body is assumed to be axisymmetric, the position vector of the upper assembly is given by

$$\vec{r}_{ua} = \rho \hat{z}_4 \quad (2)$$

where ρ is defined to be the height of the center of gravity of the upper assembly above the universal joint when λ_1 and λ_2 are equal to zero.

The pendula, which represent the water in the spherical tanks, are displaced from the universal joint. The physical constants r and (cg) are defined such that the position vector of the support of pendulum 1 is

$rx_4 + (cg)z_4$. Consequently, the origin of the $\hat{x}_5-\hat{y}_5-\hat{z}_5$ system is defined to be at $rx_4 + (cg)z_4$. This is the location of the hinge point of pendulum 1, and also the location of one of the nonslough masses of the upper assembly. Similarly, the origin of the $\hat{x}_8-\hat{y}_8-\hat{z}_8$ system is located at $-rx_4 + (cg)z_4$, which is the location of the hinge point of the second pendulum, as well as the second nonslough mass. There are no relative rotations for the $\hat{x}_4-\hat{y}_4-\hat{z}_4$, $\hat{x}_5-\hat{y}_5-\hat{z}_5$, and $\hat{x}_8-\hat{y}_8-\hat{z}_8$ coordinate systems.

The radial rotation of the pendula are defined by the angles, θ . The angle θ_1 is defined by right hand rotation of the $\hat{x}_6-\hat{y}_6-\hat{z}_6$ system about the \hat{y}_5 axis. In a parallel fashion, the angle θ_2 is defined by right hand rotation of the $\hat{x}_9-\hat{y}_9-\hat{z}_9$ system about the \hat{y}_8 axis. Note that if both pendula are flared outward from the universal joint by an amount θ , then $\theta_1 = -\theta$ while $\theta_2 = +\theta$.

Circumferential (or tangential) rotations of the pendula are described by the ϕ angles. The $\hat{x}_7-\hat{y}_7-\hat{z}_7$ axes are rotated through the angle ϕ_1 about the \hat{x}_6 axis. The $\hat{x}_7-\hat{y}_7-\hat{z}_7$ coordinate system is fixed to pendulum 1. Similarly, the $\hat{x}_{10}-\hat{y}_{10}-\hat{z}_{10}$ axes, which are fixed to pendulum 2, are rotated through an angle ϕ_2 about the \hat{x}_9 axis. Rotations of the pendula relative to the upper assembly are shown in Figs. 4 and 5.

The local position vectors of the pendula, \vec{r}_{p1} and \vec{r}_{p2} are easily defined as

$$\vec{r}_{p1} = -l\hat{z}_7 \quad (3)$$

and

$$\vec{r}_{p2} = -l\hat{z}_{10} \quad (4)$$

where l is the length of the pendulum. This length is a function of tank size, tank shape, and fill height [1].

By direct substitution, the position vectors of the bodies can be expressed in terms of world coordinates. Thus,

$$\begin{Bmatrix} \hat{x}_1 \\ \hat{y}_1 \\ \hat{z}_1 \\ 1 \end{Bmatrix} = [A_{12}][A_{23}][A_{34}] \begin{Bmatrix} \hat{x}_4 \\ \hat{y}_4 \\ \hat{z}_4 \\ 1 \end{Bmatrix} \quad (5)$$

The overall transformation matrix, $[A_{14}]$, is simply the product given by $[A_{12}][A_{23}][A_{34}]$. Since $\vec{r}_{ua} = \rho \hat{z}_4$, it can be expressed as

$$\begin{aligned} \vec{r}_{ua} &= \rho (\cos \psi \sin \lambda_1 \cos \lambda_2 + \sin \psi \sin \lambda_2) \hat{x}_1 \\ &\quad + \rho (\sin \psi \sin \lambda_1 \cos \lambda_2 - \cos \psi \sin \lambda_2) \hat{y}_1 \\ &\quad + \rho \cos \lambda_1 \cos \lambda_2 \hat{z}_1 \end{aligned} \quad (6)$$

In similar fashion,

$$\begin{Bmatrix} \hat{x}_1 \\ \hat{y}_1 \\ \hat{z}_1 \\ 1 \end{Bmatrix} = [A_{12}][A_{23}][A_{34}][A_{45}][A_{56}][A_{67}] \begin{Bmatrix} \hat{x}_7 \\ \hat{y}_7 \\ \hat{z}_7 \\ 1 \end{Bmatrix} \quad (7)$$

and

$$\begin{Bmatrix} \hat{x}_1 \\ \hat{y}_1 \\ \hat{z}_1 \\ 1 \end{Bmatrix} = [A_{12}][A_{23}][A_{34}][A_{48}][A_{89}][A_{9,10}] \begin{Bmatrix} \hat{x}_{10} \\ \hat{y}_{10} \\ \hat{z}_{10} \\ 1 \end{Bmatrix} \quad (8)$$

The position vectors \vec{r}_{p1} and \vec{r}_{p2} , expressed in terms of world coordinates, are presented in the appendix.

Body Velocities and Energies

The translational velocities of the center of mass of the upper assembly and the two pendula can be determined by differentiating their position vectors with respect to time. Using the chain rule of calculus,

$$\vec{v} = \frac{d\vec{r}}{dt} = \sum_{i=1}^7 \frac{\partial \vec{r}}{\partial q_i} \frac{dq_i}{dt} \quad (9)$$

Thus, differentiation of Eq. (6) produces

$$\begin{aligned} \vec{v}_{ua} = & \rho \left[\dot{\psi} (\cos \psi \sin \lambda_2 - \sin \psi \sin \lambda_1 \cos \lambda_2) \right. \\ & + \dot{\lambda}_1 \cos \psi \cos \lambda_1 \cos \lambda_2 \\ & \left. + \dot{\lambda}_2 (-\cos \psi \sin \lambda_1 \sin \lambda_2 + \sin \psi \cos \lambda_2) \right] \hat{x}_1 \\ & + \rho \left[\dot{\psi} (\cos \psi \sin \lambda_1 \cos \lambda_2 + \sin \psi \sin \lambda_2) \right. \\ & + \dot{\lambda}_1 \sin \psi \cos \lambda_1 \cos \lambda_2 \\ & \left. + \dot{\lambda}_2 (-\cos \psi \cos \lambda_2 - \sin \psi \sin \lambda_1 \sin \lambda_2) \right] \hat{y}_1 \\ & + \rho \left(-\dot{\lambda}_1 \sin \lambda_1 \cos \lambda_2 - \dot{\lambda}_2 \cos \lambda_1 \sin \lambda_2 \right) \hat{z}_1 \end{aligned} \quad (10)$$

Velocity vectors of the pendula are determined in an identical fashion. Due to their lengthiness, however, they are shown in the appendix rather than here.

Using the addition theorem for angular velocities, the angular velocity of the upper assembly can be expressed as a sum of simple components as

$$\vec{\omega}_{ua} = \dot{\psi} \hat{z}_1 + \dot{\lambda}_1 \hat{y}_2 - \dot{\lambda}_2 \hat{x}_3 \quad (11)$$

or expressed in terms of body fixed axes:

$$\begin{aligned}\bar{\omega}_{ua} = & (-\dot{\psi} \sin \lambda_1 + \dot{\lambda}_2) \hat{x}_4 \\ & + (\dot{\psi} \cos \lambda_1 \sin \lambda_2 + \dot{\lambda}_1 \cos \lambda_2) \hat{y}_4 \\ & + (\dot{\psi} \cos \lambda_1 \cos \lambda_2 - \dot{\lambda}_1 \sin \lambda_2) \hat{z}_4\end{aligned}\quad (12)$$

The inertia dyadic of the upper assembly, \vec{I}_{ua} can be expressed as

$$\begin{aligned}\vec{I}_{ua} = & I_{xx} \hat{x}_4 \hat{x}_4 + I_{yy} \hat{y}_4 \hat{y}_4 + I_{zz} \hat{z}_4 \hat{z}_4 \\ & + I_{xy} (\hat{x}_4 \hat{y}_4 + \hat{y}_4 \hat{x}_4) + I_{yz} (\hat{y}_4 \hat{z}_4 + \hat{z}_4 \hat{y}_4)\end{aligned}\quad (13)$$

where $I_{\xi\eta}$ is defined to be the inertia scalar of the upper assembly relative to its center of gravity for unit vectors $\hat{\xi}_4$ and $\hat{\eta}_4$. Note that the body is assumed to have zero products of inertia about its center of gravity for the \hat{x}_4 and \hat{z}_4 axes.

The angular velocity of the lower shaft is simply

$$\bar{\omega}_{ls} = \dot{\psi} \hat{z}_1 \quad (14)$$

The relevant term of the inertia dyadic for the lower shaft is the moment of inertia of the shaft about the \hat{z}_1 axis, I_{ls} . Because the pendula are assumed to be point masses, their inertia dyadics are zero.

The kinetic energy, T , of the system can now be calculated by summing the rotational and translational kinetic energies of all the bodies:

$$\begin{aligned}T = & \frac{1}{2} m_s \bar{v}_{p1} \cdot \bar{v}_{p1} + \frac{1}{2} m_s \bar{v}_{p2} \cdot \bar{v}_{p2} + \frac{1}{2} m_{ua} \bar{v}_{ua} \cdot \bar{v}_{ua} \\ & + \frac{1}{2} \bar{\omega}_{ua} \cdot \vec{I}_{ua} \cdot \bar{\omega}_{ua} + \frac{1}{2} \bar{\omega}_{ls} \cdot \vec{I}_{ls} \cdot \bar{\omega}_{ls}\end{aligned}\quad (15)$$

where m_s is the mass of a pendulum and m_{ua} is the mass of the upper assembly.

The kinetic energy is expressed in matrix form as

$$T = \frac{1}{2} \{\dot{q}\}^T [M] \{\dot{q}\} \quad (16)$$

where the matrix [M], shown in the appendix, is symmetric. The vector {q} is defined as

$$\{q\} = \begin{pmatrix} \psi \\ \lambda_1 \\ \lambda_2 \\ \theta_1 \\ \phi_1 \\ \theta_2 \\ \phi_2 \end{pmatrix} \quad (17)$$

The potential energy, V, of the system is determined from the elevation of each of the bodies. Thus,

$$\begin{aligned} V = & m_{uag} \rho \cos \lambda_1 \cos \lambda_2 + m_{pg} [l \sin \lambda_1 (\sin \theta_1 \cos \phi_1 + \sin \theta_2 \cos \phi_2) \\ & - l \cos \lambda_1 \cos \lambda_2 (\cos \theta_1 \cos \phi_1 + \cos \theta_2 \cos \phi_2) \\ & + l \cos \lambda_1 \sin \lambda_2 (\sin \phi_1 + \sin \phi_2) + 2 (cg) \cos \lambda_1 \cos \lambda_2] \end{aligned} \quad (18)$$

Lagrangian Formulation

The Lagrangian, L, for the system is defined simply as $L = T - V$. Equations of motion can be determined from Lagrange's equations of the second kind as

$$\frac{d}{dt} \left(\frac{\partial L}{\partial \dot{q}_r} \right) - \frac{\partial L}{\partial q_r} = F_{q_r} \quad r = 1, \dots, 7 \quad (19)$$

The generalized force, F_{qr} , due to viscous damping can be expressed as

$$F_{qr} = c_r \dot{q}_r \quad r = 1, \dots, 7 \quad (20)$$

where c_r is the viscous damping coefficient expressed in dimensions of torque per unit angular velocity.

Substituting $L = T - V$ into Eq. (10) and noting that V does not depend on \dot{q} we have

$$\frac{d}{dt} \left(\frac{\partial T}{\partial \dot{q}_r} \right) - \frac{\partial T}{\partial q_r} + \frac{\partial V}{\partial q_r} = F_{qr} \quad r = 1, \dots, 7 \quad (21)$$

Since $T = 0.5\{\dot{q}\}[M]\{\dot{q}\}$ where $[M]$ does not depend on \dot{q} , the first term on the left hand side of Eq. (21) is determined by

$$\frac{\partial T}{\partial \dot{q}_r} = [M] \{\dot{q}\} \quad (22)$$

and by the chain rule of calculus,

$$\frac{d}{dt} \left(\frac{\partial T}{\partial \dot{q}_r} \right) = [\dot{M}] \{\dot{q}\} + [M] \{\ddot{q}\} \quad (23)$$

For the second term on the left hand side of Eq. (21),

$$\frac{\partial T}{\partial q_r} = \frac{1}{2} \sum_{\substack{i=1 \\ j=1}}^7 \frac{\partial M_{ij}}{\partial q_r} \dot{q}_i \dot{q}_j \quad (24)$$

So that the equations of motion become

$$\sum_{i=1}^7 (\dot{M}_{ir} \dot{q}_i + M_{ir} \ddot{q}_i) - \sum_{\substack{i=1 \\ j=1}}^7 \left(\frac{\partial M_{ij}}{\partial q_r} \dot{q}_i \dot{q}_j \right) + \frac{\partial V}{\partial q_r} = F_{qr} \quad r = 1, \dots, 7 \quad (25)$$

These equations are assembled into a matrix form,

$$[\dot{M}] \{\dot{q}\} + [M] \{\ddot{q}\} - [DELM]^T \{\dot{q}\} + \left\{ \frac{\partial V}{\partial q} \right\} = \{F_q\} \quad (26)$$

where [DELM] is defined by

$$DELM_{ij} = \sum_{k=1}^7 \frac{\partial M_{ik}}{\partial q_j} \dot{q}_k \quad (27)$$

This system of equations was numerically integrated using a double precision version of DIFFEQ, a numerical integration program. The user of DIFFEQ must supply a subroutine which computes the derivatives of the state variables with respect to the independent variable, given the current values of the independent variable and the state variables.

SIMULATION RESULTS

To ensure the accuracy of the equations of motion, simulation results were compared with those from a multibody dynamics program called CAMS. Results were also compared with experimental data.

CAMS (Control Analysis for Mechanical Systems), a three-dimensional multibody program, was used to verify the accuracy of the previously derived equations of motion. To run CAMS, a user creates a data file specifying the type of connection existing between bodies, as well as the inertial

properties, initial positions, and initial orientations of all of the bodies in the system.

Because CAMS is more generic than the program tailored specifically to solve the satellite problem, it was considerably more time consuming to generate an input data file for CAMS than for SATELL, the specific program written for this study. Several runs were completed using CAMS. However, only two representative runs are displayed here for brevity.

The physical values of the test rigs used for the analyses are given in Table 1. I_s is defined as the moment of inertia of the test rig about its spin axis. I_t is defined as the moment of inertia of the test rig about a transverse axis through its center of gravity. For all runs in this section, the center of gravity of the test rig at its initial speed is located at the universal joint.

Figs. 6-12 compare the output of CAMS and SATELL for a case in which half filled, one ft. diameter spheres spin about an axis of maximum moment of inertia (specifically, $I_s/I_t = 1.6$). Fig 12 shows the half cone angle versus time for each of the programs, where the half cone angle, β , is defined to be the angle between the \hat{z}_4 and \hat{z}_2 axes. Mathematically,

$$\beta = \cos^{-1}(\cos \lambda_1 \cos \lambda_2) \quad (28)$$

Close agreement is seen in both the magnitudes and frequencies of all of the state variables.

Figs. 13-17 compare the results of CAMS and SATELL for the case of spin about an axis of minimum moment of inertia.

Comparison with Experimental Data

To determine the validity of the mathematical model, output from SATELL was compared with Anderson's [10] experimental results.

In his experiments, Anderson used six-inch plastic spheres. Physical properties of two of the test rigs used in experiments are given in Table 2. In both cases, the spheres were half full. Two transverse moments of inertia are listed, with I_{t1} the moment of inertia of the test rig about the \hat{x}_4 axis and I_{t2} the moment of inertia of the test rig about the \hat{y}_4 axis.

Figs. 18-22 show a comparison of experimental data and SATELL output for spin about an axis of minimum moment of inertia, runs 1E and 1SE. Only about ten seconds of experimental data could be acquired before the unstable upper assembly came to rest on a supporting collar.

CONCLUSIONS

This work has developed the equations of motion for a test rig designed to model a spin-stabilized satellite. The applicability of the equations of motion to the motion of a satellite is based on two assumptions. The first is that the mechanical assembly is a valid model of a satellite, and the second is that the mathematical model is a valid model of the mechanical test rig.

The major accomplishments of the study have included:

- Development of the equations of motion of a spacecraft simulator using a Lagrangian formulation
- Numerical integration of the developed equations of motion in order to simulate the motion of the test rig.
- Comparison with a multibody dynamics program to verify accuracy of the equations

Comparison with experimental results to determine the validity of the mathematical model

Basic theories were confirmed. That is, that a body containing a sloshing fluid is stable when spun about an axis of maximum moment of inertia and unstable when spun about an axis of minimum moment of inertia.

Comparison of the results of SATELL with the results of CAMS showed good agreement. The results agreed very closely. The relative ease in calculating the input values for SATELL supports its use over that of CAMS for this particular application.

Agreement between experimental data and the output of SATELL was reasonable. The results showed similar frequencies and magnitudes. Difficulty in modeling the experimental setup arose in determining values for mass moments of inertia of the test rig. These values were calculated using formulas for mass moments of inertia of basic geometric shapes. Another difficulty was encountered in determining damping coefficients at the universal joint and pendulum supports.

Now that a computer program has been developed to simulate the dynamics of a spin-stabilized structure carrying liquid stores, many additional factors can be studied. For example, different size tanks and different inertias can be considered. The absence of gravity in outer space can also be simulated by simply setting the acceleration of gravity equal to zero. Furthermore, plans call for additional development of the computer program to handle cases where the liquid tanks are not perfectly symmetric and may not even hold the same quantity of liquid.

ACKNOWLEDGMENT

This study was accomplished with the support of the Air Force Office of Scientific Research under grant AFOSR-86-0080.

REFERENCES

1. Slabinski, V. J. "INTELSAT IV In-orbit Liquid Slosh Tests and Problems in the Theoretical Analysis of the Data." COMSAT Technical Review, 8, No. 1 (Spring 1978):1-39.
2. Martin, Ernesto R. "Experimental Investigations on the Fuel Slosh of Dual-spin Spacecraft." COMSAT Technical Review, 1, No. 1 (Fall 1971): 1-19.
3. Hill, Daniel E. "Dynamics and Control of Spin-stabilized Spacecraft with Sloshing Fluid Stores," Ph.D. dissertation, Iowa State University, Ames, Iowa, 1985.
4. Miller, Miles C. "Flight Instabilities of Spinning Projectiles Having Nonrigid Payloads," Journal of Guidance and Control, 5, No. 2 (March-April 1982):151-157.
5. Agrawal, Brij N. "Stability of Spinning Spacecraft with Liquid-Filled Tanks," American Institute of Aeronautics and Astronautics, 19th Aerospace Sciences Meeting, St. Louis, Missouri, January 1981.
6. Sumner, Irving E. "Experimentally Determined Pendulum Analogy of Liquid Sloshing in Spherical and Oblate-Spheroidal Tanks," Technical Note TN D-2737. National Aeronautics and Space Administration, April 1965.
7. Sayar, Bashir A. and Baumgarten, J. R. "Linear and Nonlinear Analysis of Fluid Slosh Dampers," AIAA Journal, 20, No. 11 (November 1982): 769-772.
8. Zedd, Michael F. and Dodge, Franklin T. "Energy Dissipation of Liquids in Nutating Spherical Tanks Measured by a Forced Motion-Spin Table," NRL Report 8932, Washington D.C.: Naval Research Laboratory, October 1985.
9. Cowles, Doug S. "Design of a Spin-Stabilized Spacecraft Simulator with Liquid Fuel Stores," M.S. thesis, Iowa State University, Ames, Iowa, 1987.
10. Anderson, Michael D. "Instrumentation of a Spin-Stabilized Spacecraft Simulator with Liquid Fuel Stores." M.S. thesis, Iowa State University, Ames, Iowa, 1988.

APPENDIX

$$[A_{12}] = \begin{bmatrix} \cos \psi & -\sin \psi & 0 & 0 \\ \sin \psi & \cos \psi & 0 & 0 \\ 0 & 0 & 1 & 0 \\ 0 & 0 & 0 & 1 \end{bmatrix}$$

$$[A_{23}] = \begin{bmatrix} \cos \lambda_1 & 0 & \sin \lambda_1 & 0 \\ 0 & 1 & 0 & 0 \\ -\sin \lambda_1 & 0 & \cos \lambda_1 & 0 \\ 0 & 0 & 0 & 1 \end{bmatrix}$$

$$[A_{34}] = \begin{bmatrix} 1 & 0 & 0 & 0 \\ 0 & \cos \lambda_2 & -\sin \lambda_2 & 0 \\ 0 & \sin \lambda_2 & \cos \lambda_2 & 0 \\ 0 & 0 & 0 & 1 \end{bmatrix}$$

$$[A_{45}] = \begin{bmatrix} 1 & 0 & 0 & r \\ 0 & 1 & 0 & 0 \\ 0 & 0 & 1 & (cg) \\ 0 & 0 & 0 & 1 \end{bmatrix}$$

$$[A_{48}] = \begin{bmatrix} 1 & 0 & 0 & -r \\ 0 & 1 & 0 & 0 \\ 0 & 0 & 1 & (cg) \\ 0 & 0 & 0 & 1 \end{bmatrix}$$

$$[A_{56}] = \begin{bmatrix} \cos \theta_1 & 0 & \sin \theta_1 & 0 \\ 0 & 1 & 0 & 0 \\ -\sin \theta_1 & 0 & \cos \theta_1 & 0 \\ 0 & 0 & 0 & 1 \end{bmatrix}$$

$$[A_{89}] = \begin{bmatrix} \cos \theta_2 & 0 & \sin \theta_2 & 0 \\ 0 & 1 & 0 & 0 \\ -\sin \theta_2 & 0 & \cos \theta_2 & 0 \\ 0 & 0 & 0 & 1 \end{bmatrix}$$

$$[A_{67}] = \begin{bmatrix} 1 & 0 & 0 & 0 \\ 0 & \cos \phi_1 & -\sin \phi_1 & 0 \\ 0 & \sin \phi_1 & \cos \phi_1 & 0 \\ 0 & 0 & 0 & 1 \end{bmatrix}$$

$$[A_{9,10}] = \begin{bmatrix} 1 & 0 & 0 & 0 \\ 0 & \cos \phi_2 & -\sin \phi_2 & 0 \\ 0 & \sin \phi_2 & \cos \phi_2 & 0 \\ 0 & 0 & 0 & 1 \end{bmatrix}$$

$$\begin{aligned}
\bar{r}_{p_1} = & \{-l[\cos \psi (\cos \lambda_1 \sin \theta_1 \cos \phi_1 \\
& + \sin \lambda_1 \cos \lambda_2 \cos \theta_1 \cos \phi_1 - \sin \lambda_1 \sin \lambda_2 \sin \phi_1) \\
& + \sin \psi (\cos \lambda_2 \sin \phi_1 + \sin \lambda_2 \cos \theta_1 \cos \phi_1)] \\
& + r \cos \psi \cos \lambda_1 \\
& + (cg)(\cos \psi \sin \lambda_1 \cos \lambda_2 + \sin \psi \sin \lambda_2)\} \hat{x}_1 \\
& \{-l[\sin \psi (\cos \lambda_1 \sin \theta_1 \cos \phi_1 \\
& + \sin \lambda_1 \cos \lambda_2 \cos \theta_1 \cos \phi_1 - \sin \lambda_1 \sin \lambda_2 \sin \phi_1) \\
& - \cos \psi (\cos \lambda_2 \sin \phi_1 + \sin \lambda_2 \cos \theta_1 \cos \phi_1)] \\
& + r \sin \psi \cos \lambda_1 \\
& + (cg)(\sin \psi \sin \lambda_1 \cos \lambda_2 - \cos \psi \sin \lambda_2)\} \hat{y}_1 \\
& \{-l(-\sin \lambda_1 \sin \theta_1 \cos \phi_1 \\
& + \cos \lambda_1 \cos \lambda_2 \cos \theta_1 \cos \phi_1 - \cos \lambda_1 \sin \lambda_2 \sin \phi_1) \\
& - r \sin \lambda_1 + (cg) \cos \lambda_1 \cos \lambda_2\} \hat{z}_1
\end{aligned}$$

$$\begin{aligned}
\bar{r}_{p_2} = & \{-l[\cos \psi (\cos \lambda_1 \sin \theta_2 \cos \phi_2 \\
& + \sin \lambda_1 \cos \lambda_2 \cos \theta_2 \cos \phi_2 - \sin \lambda_1 \sin \lambda_2 \sin \phi_2) \\
& + \sin \psi (\cos \lambda_2 \sin \phi_2 + \sin \lambda_2 \cos \theta_2 \cos \phi_2)] \\
& - r \cos \psi \cos \lambda_1 \\
& + (cg)(\cos \psi \sin \lambda_1 \cos \lambda_2 + \sin \psi \sin \lambda_2)\} \hat{x}_1 \\
& \{-l[\sin \psi (\cos \lambda_1 \sin \theta_2 \cos \phi_2 \\
& + \sin \lambda_1 \cos \lambda_2 \cos \theta_2 \cos \phi_2 - \sin \lambda_1 \sin \lambda_2 \sin \phi_2) \\
& - \cos \psi (\cos \lambda_2 \sin \phi_2 + \sin \lambda_2 \cos \theta_2 \cos \phi_2)] \\
& - r \sin \psi \cos \lambda_1 \\
& + (cg)(\sin \psi \sin \lambda_1 \cos \lambda_2 - \cos \psi \sin \lambda_2)\} \hat{y}_1 \\
& + [-l(-\sin \lambda_1 \sin \theta_2 \cos \phi_2 \\
& + \cos \lambda_1 \cos \lambda_2 \cos \theta_2 \cos \phi_2 - \cos \lambda_1 \sin \lambda_2 \sin \phi_2) \\
& + r \sin \lambda_1 + (cg) \cos \lambda_1 \cos \lambda_2] \hat{z}_1
\end{aligned}$$

$$\begin{aligned}
\bar{v}_{p_1} = & \{\dot{\psi}[\cos \psi (-l \cos \lambda_2 \sin \phi_1 - l \sin \lambda_2 \cos \theta_1 \cos \phi_1 + (cg) \sin \lambda_2) \\
& + \sin \psi (l \cos \lambda_1 \sin \theta_1 \cos \phi_1 - l \sin \lambda_1 \cos \lambda_2 \cos \theta_1 \cos \phi_1 \\
& - l \sin \lambda_1 \sin \lambda_2 \sin \phi_1 + r \cos \lambda_1 - (cg) \sin \lambda_1 \cos \lambda_2)] \\
& + \dot{\lambda}_1 [\cos \psi (-l \cos \lambda_1 \cos \lambda_2 \cos \theta_1 \cos \phi_1 - l \cos \lambda_1 \sin \lambda_2 \sin \phi_1 \\
& - (cg) \cos \lambda_1 \cos \lambda_2 - l \sin \lambda_1 \sin \theta_1 \cos \phi_1 - r \sin \lambda_1 \sin \lambda_2) \\
& - \dot{\lambda}_2 [\cos \psi (l \sin \lambda_1 \cos \lambda_2 \sin \phi_1 - l \sin \lambda_1 \sin \lambda_2 \cos \theta_1 \cos \phi_1
\end{aligned}$$

$$\begin{aligned}
& - (cg) \sin \lambda_1 \sin \lambda_2) \\
& + \sin \psi (-l \cos \lambda_2 \cos \theta_1 \cos \phi_1 + (cg) \cos \lambda_2 + l \sin \lambda_2 \sin \phi_1)] \\
& + \dot{\theta}_1 [\cos \psi (-l \cos \lambda_1 \cos \theta_1 \cos \phi_1 + l \sin \lambda_1 \cos \lambda_2 \sin \theta_1 \cos \phi_1) \\
& + l \sin \psi \sin \lambda_2 \sin \theta_1 \cos \phi_1] \\
& + \dot{\phi}_1 [\cos \psi (l \sin \lambda_1 \sin \lambda_2 \cos \phi_1 + l \cos \lambda_1 \sin \theta_1 \sin \phi_1 \\
& + l \sin \lambda_1 \cos \lambda_2 \cos \theta_1 \sin \phi_1) \\
& + \sin \psi (-l \cos \lambda_2 \cos \phi_1 + l \sin \lambda_2 \cos \theta_1 \sin \phi_1)] \hat{x}_1 \\
& + \{ \dot{\psi} [\sin \psi (-l \cos \lambda_2 \sin \phi_1 - l \sin \lambda_2 \cos \theta_1 \cos \phi_1 - (cg) \sin \lambda_2) \\
& - \cos \psi (l \cos \lambda_1 \sin \theta_1 \cos \phi_1 + l \sin \lambda_1 \cos \lambda_2 \cos \theta_1 \cos \phi_1 \\
& - l \sin \lambda_1 \sin \lambda_2 \sin \phi_1 + r \cos \lambda_1 + (cg) \sin \lambda_1 \cos \lambda_2)] \\
& + \dot{\lambda}_1 [\sin \psi (-l \cos \lambda_1 \cos \lambda_2 \cos \theta_1 \cos \phi_1 + l \cos \lambda_1 \sin \lambda_2 \sin \phi_1 \\
& + (cg) \cos \lambda_1 \cos \lambda_2 + l \sin \lambda_1 \sin \theta_1 \cos \phi_1 - r \sin \lambda_2) \\
& + \dot{\lambda}_2 [\sin \psi (l \sin \lambda_1 \cos \lambda_2 \sin \phi_1 + l \sin \lambda_1 \sin \lambda_2 \cos \theta_1 \cos \phi_1 \\
& - (cg) \sin \lambda_1 \sin \lambda_2) \\
& - \cos \psi (-l \cos \lambda_2 \cos \theta_1 \cos \phi_1 - (cg) \cos \lambda_2 - l \sin \lambda_2 \sin \phi_1)] \\
& + \dot{\theta}_1 [\sin \psi (-l \cos \lambda_1 \cos \theta_1 \cos \phi_1 - l \sin \lambda_1 \cos \lambda_2 \sin \theta_1 \cos \phi_1) \\
& - l \cos \psi \sin \lambda_2 \sin \theta_1 \cos \phi_1] \\
& + \dot{\phi}_1 [\sin \psi (l \sin \lambda_1 \sin \lambda_2 \cos \phi_1 - l \cos \lambda_1 \sin \theta_1 \sin \phi_1 \\
& + l \sin \lambda_1 \cos \lambda_2 \cos \theta_1 \sin \phi_1) \\
& - \cos \psi (-l \cos \lambda_2 \cos \phi_1 - l \sin \lambda_2 \cos \theta_1 \sin \phi_1)] \hat{y}_1 \\
& - \dot{\lambda}_1 (l \cos \lambda_1 \sin \theta_1 \cos \phi_1 - r \cos \lambda_1 - l \sin \lambda_1 \cos \lambda_2 \cos \theta_1 \cos \phi_1
\end{aligned}$$

$$\begin{aligned}
& -l \sin \lambda_1 \sin \lambda_2 \sin \phi_1 - (cg) \sin \lambda_1 \cos \lambda_2) \\
& + \dot{\lambda}_2 (l \cos \lambda_1 \cos \lambda_2 \sin \phi_1 + l \cos \lambda_1 \sin \lambda_2 \cos \theta_1 \cos \phi_1 - (cg) \cos \lambda_1 \sin \lambda_2) \\
& + \dot{\theta}_1 (l \sin \lambda_1 \cos \theta_1 \cos \phi_1 + l \cos \lambda_1 \cos \lambda_2 \sin \theta_1 \cos \phi_1) \\
& + \dot{\phi}_1 (l \cos \lambda_1 \sin \lambda_2 \cos \phi_1 - l \sin \lambda_1 \sin \theta_1 \sin \phi_1 \\
& + l \cos \lambda_1 \cos \lambda_2 \cos \theta_1 \sin \phi_1) \} \hat{z}_1
\end{aligned}$$

$$\begin{aligned}
\bar{v}_{p2} = & \left\{ \dot{\psi} [\cos \psi (-l \cos \lambda_2 \sin \phi_2 - l \sin \lambda_2 \cos \theta_2 \cos \phi_2 + (cg) \sin \lambda_2) \right. \\
& + \sin \psi (l \cos \lambda_1 \sin \theta_2 \cos \phi_2 + l \sin \lambda_1 \cos \lambda_2 \cos \theta_2 \cos \phi_2 \\
& - l \sin \lambda_1 \sin \lambda_2 \sin \phi_2 + r \cos \lambda_1 + (cg) \sin \lambda_1 \cos \lambda_2)] \\
& + \dot{\lambda}_1 [\cos \psi (-l \cos \lambda_1 \cos \lambda_2 \cos \theta_2 \cos \phi_2 + l \cos \lambda_1 \sin \lambda_2 \sin \phi_2 \\
& + (cg) \cos \lambda_1 \cos \lambda_2 + l \sin \lambda_1 \sin \theta_2 \cos \phi_2 - r \sin \lambda_1 \sin \lambda_2) \\
& + \dot{\lambda}_2 [\cos \psi (l \sin \lambda_1 \cos \lambda_2 \sin \phi_2 + l \sin \lambda_1 \sin \lambda_2 \cos \theta_2 \cos \phi_2 \\
& - (cg) \sin \lambda_1 \sin \lambda_2) \\
& + \sin \psi (-l \cos \lambda_2 \cos \theta_2 \cos \phi_2 - (cg) \cos \lambda_2 - l \sin \lambda_2 \sin \phi_2)] \\
& + \dot{\theta}_2 [\cos \psi (-l \cos \lambda_1 \cos \theta_2 \cos \phi_2 - l \sin \lambda_1 \cos \lambda_2 \sin \theta_2 \cos \phi_2) \\
& - l \sin \psi \sin \lambda_2 \sin \theta_2 \cos \phi_2] \\
& - \dot{\phi}_2 [\cos \psi (l \sin \lambda_1 \sin \lambda_2 \cos \phi_2 + l \cos \lambda_1 \sin \theta_2 \sin \phi_2 \\
& - l \sin \lambda_1 \cos \lambda_2 \cos \theta_2 \sin \phi_2) \\
& - \sin \psi (-l \cos \lambda_2 \cos \phi_2 - l \sin \lambda_2 \cos \theta_2 \sin \phi_2)] \} \hat{x}_1 \\
& - \left\{ \dot{\psi} [\sin \psi (-l \cos \lambda_2 \sin \phi_2 - l \sin \lambda_2 \cos \theta_2 \cos \phi_2 - (cg) \sin \lambda_2) \right. \\
& - \cos \psi (l \cos \lambda_1 \sin \theta_2 \cos \phi_2 - l \sin \lambda_1 \cos \lambda_2 \cos \theta_2 \cos \phi_2)
\end{aligned}$$

$$\begin{aligned}
& -l \sin \lambda_1 \sin \lambda_2 \sin \phi_2 + r \cos \lambda_1 + (cg) \sin \lambda_1 \cos \lambda_2) | \\
& + \dot{\lambda}_1 [\sin \psi (-l \cos \lambda_1 \cos \lambda_2 \cos \theta_1 \cos \phi_2 + l \cos \lambda_1 \sin \lambda_2 \sin \phi_2 \\
& + (cg) \cos \lambda_1 \cos \lambda_2 + l \sin \lambda_1 \sin \theta_2 \cos \phi_2 - r \sin \lambda_2) | \\
& + \dot{\lambda}_2 [\sin \psi (l \sin \lambda_1 \cos \lambda_2 \sin \phi_2 + l \sin \lambda_1 \sin \lambda_2 \cos \theta_2 \cos \phi_2 \\
& - (cg) \sin \lambda_1 \sin \lambda_2) \\
& - \cos \psi (-l \cos \lambda_2 \cos \theta_2 \cos \phi_2 + (cg) \cos \lambda_2 + l \sin \lambda_2 \sin \phi_2) | \\
& + \dot{\theta}_2 [\sin \psi (-l \cos \lambda_1 \cos \theta_2 \cos \phi_2 + l \sin \lambda_1 \cos \lambda_2 \sin \theta_2 \cos \phi_2) \\
& - l \cos \psi \sin \lambda_2 \sin \theta_2 \cos \phi_2] \\
& + \dot{\phi}_2 [\sin \psi (l \sin \lambda_1 \sin \lambda_2 \cos \phi_2 + l \cos \lambda_1 \sin \theta_2 \sin \phi_2 \\
& + l \sin \lambda_1 \cos \lambda_2 \cos \theta_2 \sin \phi_2) \\
& - \cos \psi (-l \cos \lambda_2 \cos \phi_2 + l \sin \lambda_2 \cos \theta_2 \sin \phi_2) |] \dot{y}_1 \\
& + [\dot{\lambda}_1 (l \cos \lambda_1 \sin \theta_2 \cos \phi_2 - r \cos \lambda_1 - l \sin \lambda_1 \cos \lambda_2 \cos \theta_2 \cos \phi_2 \\
& - l \sin \lambda_1 \sin \lambda_2 \sin \phi_2 - (cg) \sin \lambda_1 \cos \lambda_2) \\
& + \dot{\lambda}_2 (l \cos \lambda_1 \cos \lambda_2 \sin \phi_2 - l \cos \lambda_1 \sin \lambda_2 \cos \theta_2 \cos \phi_2 - (cg) \cos \lambda_1 \sin \lambda_2) \\
& + \dot{\theta}_2 (l \sin \lambda_1 \cos \theta_2 \cos \phi_2 - l \cos \lambda_1 \cos \lambda_2 \sin \theta_2 \cos \phi_2) \\
& + \dot{\phi}_2 (l \cos \lambda_1 \sin \lambda_2 \cos \phi_2 - l \sin \lambda_1 \sin \theta_2 \sin \phi_2 \\
& - l \cos \lambda_1 \cos \lambda_2 \cos \theta_2 \sin \phi_2) |] \dot{z}_1
\end{aligned}$$

Because $[M]$ is symmetric, only the upper elements of the matrix are displayed here. The lower elements are determined by $M_{ij} = M_{ji}$.

$$\begin{aligned}
 M_{11} = & m_s l^2 \left[(\cos^2 \lambda_2 + \sin^2 \lambda_1 \sin^2 \lambda_2) (\sin^2 \phi_1 + \sin^2 \phi_2) \right. \\
 & + \cos^2 \lambda_1 (\sin^2 \theta_1 \cos^2 \phi_1 + \sin^2 \theta_2 \cos^2 \phi_2) \\
 & + (\sin^2 \lambda_2 + \sin^2 \lambda_1 \cos^2 \lambda_2) (\cos^2 \theta_1 \cos^2 \phi_1 + \cos^2 \theta_2 \cos^2 \phi_2) \\
 & + 2 \cos^2 \lambda_1 \cos \lambda_2 \sin \lambda_2 (\cos \theta_1 \cos \phi_1 \sin \phi_1 + \cos \theta_2 \cos \phi_2 \sin \phi_2) \\
 & + 2 \cos \lambda_1 \sin \lambda_1 \cos \lambda_2 (\cos \theta_1 \sin \theta_1 \cos^2 \phi_1 \cos \theta_2 \sin \theta_2 \cos^2 \phi_2) \\
 & \left. - 2 \cos \lambda_1 \sin \lambda_1 \sin \lambda_2 (\cos \theta_1 \cos \phi_1 \sin \phi_1 + \cos \theta_2 \cos \phi_2 \sin \phi_2) \right] \\
 & + 2m_s r^2 \cos^2 \lambda_1 \\
 & + 2m_s (cg)^2 (\sin^2 \lambda_2 + \sin^2 \lambda_1 \cos^2 \lambda_2) \\
 & + 2m_s l r \left[-\cos \lambda_1 (\sin \theta_1 \cos \phi_1 - \sin \theta_2 \cos \phi_2) \right. \\
 & - \cos \lambda_1 \sin \lambda_1 \cos \lambda_2 (\cos \theta_1 \cos \phi_1 - \cos \theta_2 \cos \phi_2) \\
 & \left. + \cos \lambda_1 \sin \lambda_1 \sin \lambda_2 (\sin \phi_1 - \sin \phi_2) \right] \\
 & + 2m_s l (cg) \left[\cos^2 \lambda_1 \cos \lambda_2 \sin \lambda_2 (\sin \phi_1 - \sin \phi_2) \right. \\
 & - (\sin^2 \lambda_2 + \sin^2 \lambda_1 \cos^2 \lambda_2) (\cos \theta_1 \cos \phi_1 - \cos \theta_2 \cos \phi_2) \\
 & \left. - \cos \lambda_1 \sin \lambda_1 \cos \lambda_2 (\sin \theta_1 \cos \phi_1 - \sin \theta_2 \cos \phi_2) \right]
 \end{aligned}$$

$$\begin{aligned}
& m_{ua}\rho^2 (\sin^2 \lambda_2 + \sin^2 \lambda_1 \sin^2 \lambda_2) \\
& + I_{xx} \sin^2 \lambda_1 + I_{yy} \cos^2 \lambda_1 \sin^2 \lambda_2 + I_{zz} \cos^2 \lambda_1 \cos^2 \lambda_2 \\
& - I_{xy} \cos \lambda_1 \sin \lambda_1 \sin \lambda_2 + I_{yz} \cos^2 \lambda_1 \cos \lambda_2 \sin \lambda_2
\end{aligned}$$

$$\begin{aligned}
M_{12} = & m_s l^2 \left[\cos \lambda_1 (\cos^2 \lambda_2 - \sin^2 \lambda_2) (\cos \theta_1 \cos \phi_1 \sin \phi_1 - \cos \theta_2 \cos \phi_2 \sin \phi_2) \right. \\
& + \cos \lambda_1 \cos \lambda_2 \sin \lambda_2 (\cos^2 \theta_1 \cos^2 \phi_1 - \sin^2 \phi_1 + \cos^2 \theta_2 \cos^2 \phi_2 - \sin^2 \phi_2) \\
& - \sin \lambda_1 \sin \lambda_2 (\cos \theta_1 \sin \theta_1 \cos^2 \phi_1 + \cos \theta_2 \sin \theta_2 \cos^2 \phi_2) \\
& \left. - \sin \lambda_1 \cos \lambda_2 (\sin \theta_1 \cos \phi_1 \sin \phi_1 + \sin \theta_2 \cos \phi_2 \sin \phi_2) \right] \\
& + 2m_s (cg)^2 \cos \lambda_1 \cos \lambda_2 \sin \lambda_2 \\
& + m_s l r [\sin \lambda_1 \cos \lambda_2 (\sin \phi_1 - \sin \phi_2) \\
& + \sin \lambda_1 \sin \lambda_2 (\cos \theta_1 \cos \phi_1 - \cos \theta_2 \cos \phi_2)] \\
& m_s l (cg) \left[-\cos \lambda_1 (\cos^2 \lambda_2 - \sin^2 \lambda_2) (\sin \phi_1 + \sin \phi_2) \right. \\
& - 2 \cos \lambda_1 \cos \lambda_2 \sin \lambda_2 (\cos \theta_1 \cos \phi_1 + \cos \theta_2 \cos \phi_2) \\
& \left. + \sin \lambda_1 \sin \lambda_2 (\sin \theta_1 \cos \phi_1 - \sin \theta_2 \cos \phi_2) \right] \\
& + m_{ua}\rho^2 \cos \lambda_1 \cos \lambda_2 \sin \lambda_2 \\
& - I_{yy} \cos \lambda_1 \cos \lambda_2 \sin \lambda_2 - I_{zz} \cos \lambda_1 \cos \lambda_2 \sin \lambda_2 \\
& - I_{xy} \cos \lambda_1 \sin \lambda_1 \sin \lambda_2 - I_{yz} \cos \lambda_1 (\cos^2 \lambda_2 - \sin^2 \lambda_2)
\end{aligned}$$

$$\begin{aligned}
M_{13} = & m_s l^2 \left[-\sin \lambda_1 (\sin^2 \phi_1 - \cos^2 \theta_1 \cos^2 \phi_1 - \sin^2 \phi_2 + \cos^2 \theta_2 \cos^2 \phi_2) \right. \\
& - \cos \lambda_1 \cos \lambda_2 (\cos \theta_1 \sin \theta_1 \cos^2 \phi_1 - \cos \theta_2 \sin \theta_2 \cos^2 \phi_2) \\
& \left. - \cos \lambda_1 \sin \lambda_2 (\sin \theta_1 \cos \phi_1 \sin \phi_1 - \sin \theta_2 \cos \phi_2 \sin \phi_2) \right]
\end{aligned}$$

$$\begin{aligned}
& -2m_s (cg)^2 \sin \lambda_1 \\
& + m_s l r [\cos \lambda_1 \cos \lambda_2 (\cos \theta_1 \cos \phi_1 - \cos \theta_2 \cos \phi_2) \\
& \cos \lambda_1 \sin \lambda_2 (\sin \phi_1 - \sin \phi_2)] \\
& + m_s l (cg) [2 \sin \lambda_1 (\cos \theta_1 \cos \phi_1 + \cos \theta_2 \cos \phi_2) \\
& + \cos \lambda_1 \cos \lambda_2 (\sin \theta_1 \cos \phi_1 + \sin \theta_2 \cos \phi_2)] \\
& - m_u a \rho^2 \sin \lambda_1 - I_{xx} \sin \lambda_1 + I_{xy} \cos \lambda_1 \sin \lambda_2
\end{aligned}$$

$$\begin{aligned}
M_{14} & = m_s l^2 (\cos \lambda_1 \cos \lambda_2 \cos \theta_1 \cos \phi_1 \sin \phi_1 \\
& \cos \lambda_1 \sin \lambda_2 \cos^2 \phi_1 - \sin \lambda_1 \sin \theta_1 \cos \phi_1 \sin \phi_1) \\
& - m_s l r \cos \lambda_1 \sin \lambda_2 \sin \theta_1 \cos \phi_1 \\
& - m_s l (cg) (-\cos \lambda_1 \sin \lambda_2 \cos \theta_1 \cos \phi_1)
\end{aligned}$$

$$\begin{aligned}
M_{15} & = -m_s l^2 (\cos \lambda_1 \cos \lambda_2 \sin \theta_1 + \sin \lambda_1 \cos \theta_1) \\
& + m_s l r (\cos \lambda_1 \cos \lambda_2 \cos \phi_1 - \cos \lambda_1 \sin \lambda_2 \cos \theta_1 \sin \phi_1) \\
& + m_s l (cg) (\sin \lambda_1 \cos \phi_1 + \cos \lambda_1 \sin \lambda_2 \sin \theta_1 \sin \phi_1)
\end{aligned}$$

$$\begin{aligned}
M_{16} & = m_s l^2 (\cos \lambda_1 \cos \lambda_2 \cos \theta_2 \cos \phi_2 \sin \phi_2 \\
& \cos \lambda_1 \sin \lambda_2 \cos^2 \phi_2 - \sin \lambda_1 \sin \theta_2 \cos \phi_2 \sin \phi_2) \\
& - m_s l r \cos \lambda_1 \sin \lambda_2 \sin \theta_2 \cos \phi_2 \\
& - m_s l (cg) (-\cos \lambda_1 \sin \lambda_2 \cos \theta_2 \cos \phi_2)
\end{aligned}$$

$$\begin{aligned}
M_{17} = & -m_s l^2 (\cos \lambda_1 \cos \lambda_2 \sin \theta_2 + \sin \lambda_1 \cos \theta_2) \\
& + m_s l r (\cos \lambda_1 \cos \lambda_2 \cos \phi_2 - \cos \lambda_1 \sin \lambda_2 \cos \theta_2 \sin \phi_2) \\
& + m_s l (cg) (\sin \lambda_1 \cos \phi_2 + \cos \lambda_1 \sin \lambda_2 \sin \theta_2 \sin \phi_2)
\end{aligned}$$

$$\begin{aligned}
M_{22} = & m_s l^2 [\cos^2 \lambda_2 (\cos^2 \theta_1 \cos \phi_1 - \cos^2 \theta_2 \cos \phi_2) \\
& \sin^2 \lambda_2 (\sin^2 \phi_1 + \sin^2 \phi_2) + (\sin^2 \theta_1 \cos^2 \phi_1 - \sin^2 \theta_2 \cos^2 \phi_2) \\
& - 2 \cos \lambda_2 \sin \lambda_2 (\cos \theta_1 \cos \phi_1 \sin \phi_1)] \\
& + 2m_s r^2 + 2m_s (cg)^2 \cos^2 \lambda_2 \\
& - 2m_s l r (\sin \theta_1 \cos \phi_1 - \sin \theta_2 \cos \phi_2) \\
& + 2m_s l (cg) [-\cos^2 \lambda_2 (\cos \theta_1 \cos \phi_1 + \cos \theta_2 \cos \phi_2) \\
& + \cos \lambda_2 \sin \lambda_2 (\sin \phi_1 + \sin \phi_2)] \\
& + m_{ua} \rho^2 \cos^2 \lambda_2 + I_{yy} \cos^2 \lambda_2 + I_{zz} \sin^2 \lambda_2 - I_{yz} \cos \lambda_2 \sin \lambda_2
\end{aligned}$$

$$\begin{aligned}
M_{23} = & m_s l^2 [\cos \lambda_2 (\sin \theta_1 \cos \phi_1 \sin \phi_1 - \sin \theta_2 \cos \phi_2 \sin \phi_2) \\
& \sin \lambda_2 (\cos \theta_1 \sin \theta_1 \cos^2 \phi_1 + \cos \theta_2 \sin \theta_2 \cos^2 \phi_2)] \\
& - m_s l r [\cos \lambda_2 (\sin \phi_1 - \sin \phi_2) - \sin \lambda_2 (\cos \theta_1 \cos \phi_1 - \cos \theta_2 \cos \phi_2)] \\
& - m_s l (cg) \sin \lambda_2 (\sin \theta_1 \cos \phi_1 - \sin \theta_2 \cos \phi_2) \\
& - I_{xy} \cos \lambda_2
\end{aligned}$$

$$\begin{aligned}
M_{24} = & m_s l^2 (\cos \lambda_2 \cos^2 \phi_1 - \sin \lambda_2 \cos \theta_1 \cos \phi_1 \sin \phi_1) \\
& - m_s l r \cos \lambda_2 \sin \theta_1 \cos \phi_1 - m_s l (cg) \cos \lambda_2 \cos \theta_1 \cos \phi_1
\end{aligned}$$

$$M_{25} = m_s l^2 \sin \lambda_2 \sin \theta_1 + m_s l (cg) \cos \lambda_2 \sin \theta_1 \sin \phi_1 \\ - m_s l r (\sin \lambda_2 \cos \phi_1 + \cos \lambda_2 \cos \theta_1 \sin \phi_1)$$

$$M_{26} = m_s l^2 (\cos \lambda_2 \cos^2 \phi_2 - \sin \lambda_2 \cos \theta_2 \cos \phi_2 \sin \phi_2) \\ + m_s l r \cos \lambda_2 \sin \theta_2 \cos \phi_2 - m_s l (cg) \cos \lambda_2 \cos \theta_2 \cos \phi_2$$

$$M_{27} = m_s l^2 \sin \lambda_2 \sin \theta_2 + m_s l (cg) \cos \lambda_2 \sin \theta_2 \sin \phi_2 \\ + m_s l r (\sin \lambda_2 \cos \phi_2 + \cos \lambda_2 \cos \theta_2 \sin \phi_2)$$

$$M_{33} = m_s l^2 \left[(\sin \phi_1 + \sin \phi_2) + (\cos^2 \theta_1 \cos^2 \phi_1 + \cos^2 \theta_2 \cos^2 \phi_2) \right] \\ + 2m_s (cg)^2 - 2m_s l (cg) (\cos \theta_1 \cos \phi_1 + \cos \theta_2 \cos \phi_2) \\ + m_{ua} \rho^2 + I_{xx}$$

$$M_{34} = m_s l^2 \sin \theta_1 \cos \phi_1 \sin \phi_1$$

$$M_{35} = m_s l^2 \cos \theta_1 - m_s l (cg) \cos \phi_1$$

$$M_{36} = m_s l^2 \sin \theta_2 \cos \phi_2 \sin \phi_2$$

$$M_{36} = m_s l^2 \cos \theta_2 - m_s l (cg) \cos \phi_2$$

$$M_{44} = m_s l^2 \cos^2 \phi_1$$

$$M_{45} = 0.$$

$$M_{46} = 0.$$

$$M_{47} = 0.$$

$$M_{55} = m_s l^2$$

$$M_{56} = 0.$$

$$M_{57} = 0.$$

$$M_{66} = m_s l^2 \cos^2 \phi_2$$

$$M_{67} = 0.$$

$$M_{77} = m_s l^2$$

TABLE 1. Test rig data for comparison with CAMS

run	total mass	sphere diam	% fill	r	(cg)	spin speed	I_s	I_t
	slug	ft		ft	ft	rpm	slug ft ²	slug ft ²
1S	2.0	1	50	1	0	100	2.22	1.39
1C	2.0	1	50	1	0	100	2.22	1.39
3S	2.0	1	50	1	0	100	2.08	3.47
3C	2.0	1	50	1	0	100	2.08	3.47

TABLE 2. Test rig data for comparison with experiment

run	total mass	height of c.g.	spin speed	I_s	I_{t_1}	I_{t_2}
	slug	ft	rpm	slug ft ²	slug ft ²	slug ft ²
1E	0.507	-0.080	-100	0.223	0.343	0.340
1SE	0.507	-0.080	-100	0.223	0.343	0.340
2E	0.431	-0.121	-70	0.324	0.280	0.289
2SE	0.431	-0.121	-70	0.324	0.280	0.289

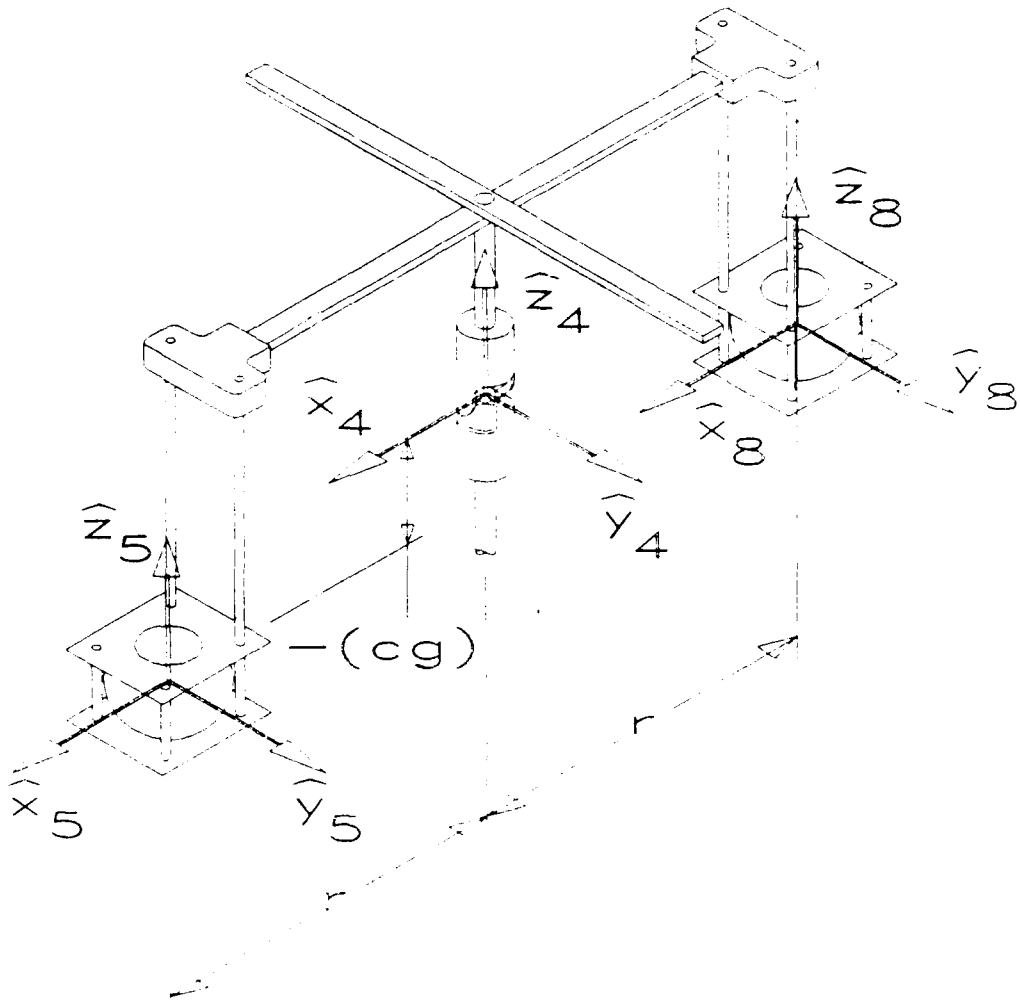


FIGURE 1. Schematic of mechanical system.

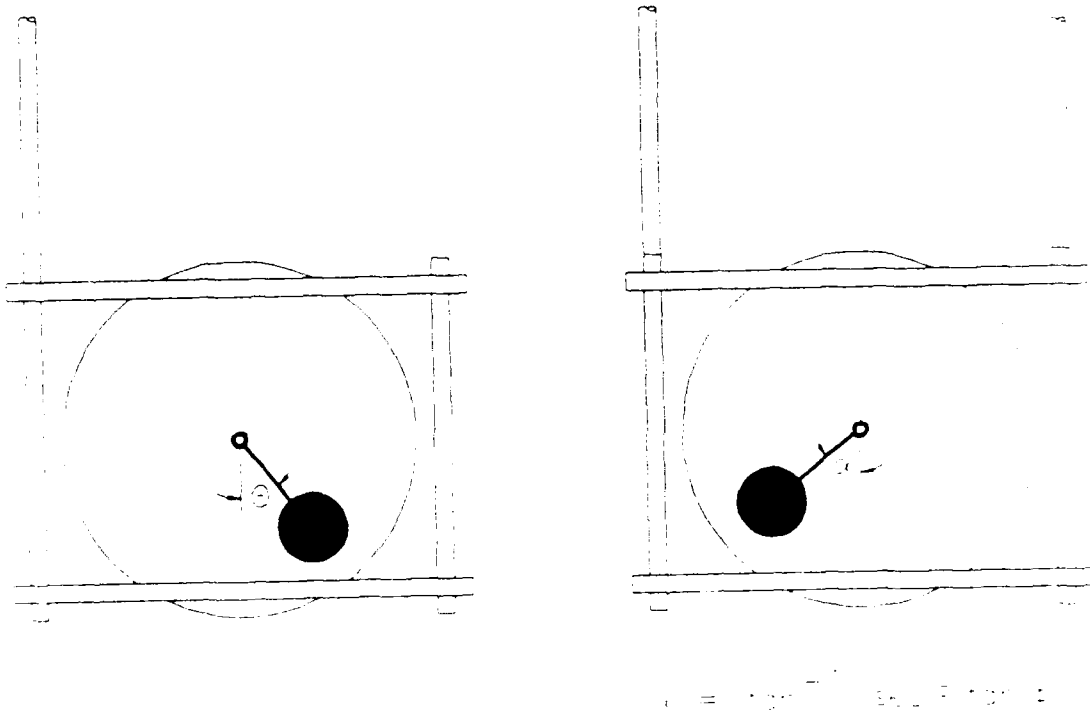


FIGURE 2. Position of pendulum with respect to test rig

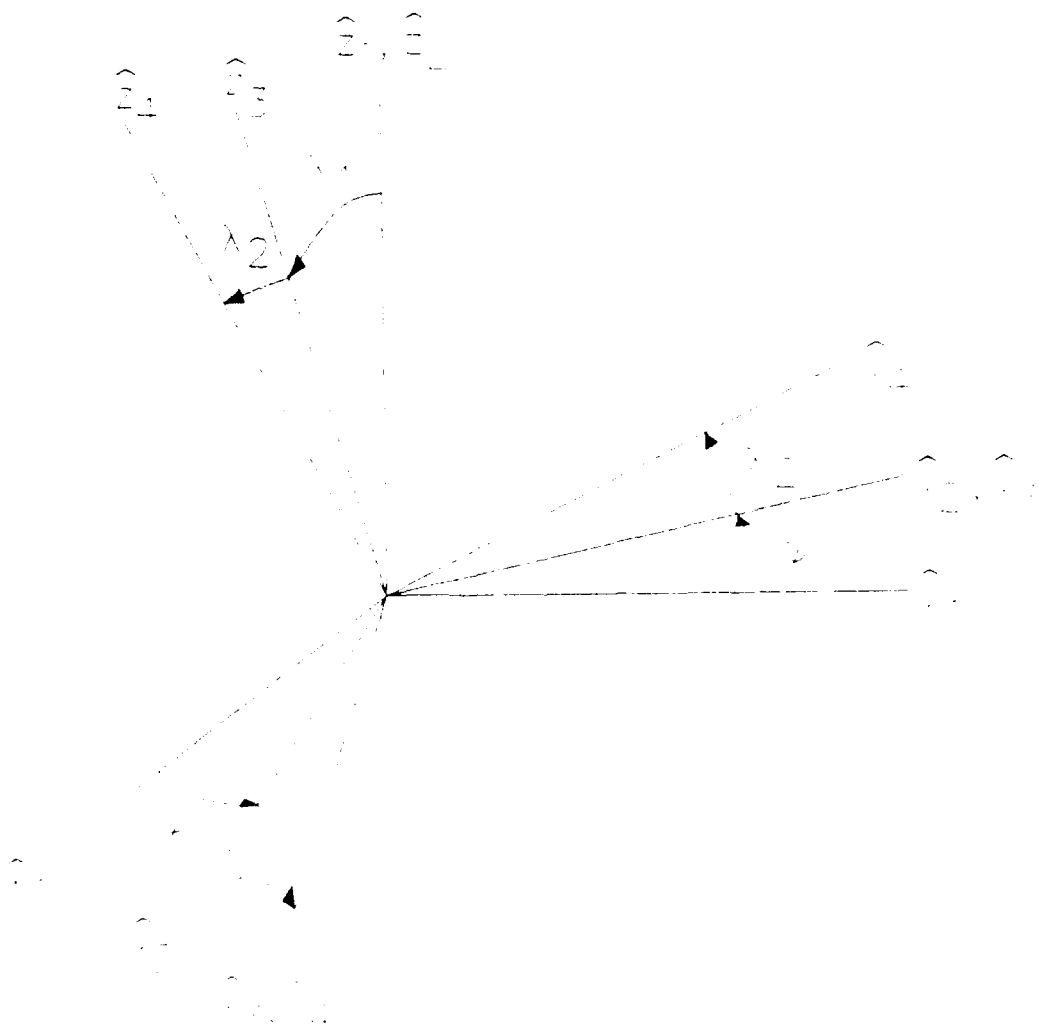


FIGURE 3. Upper limb model notation.

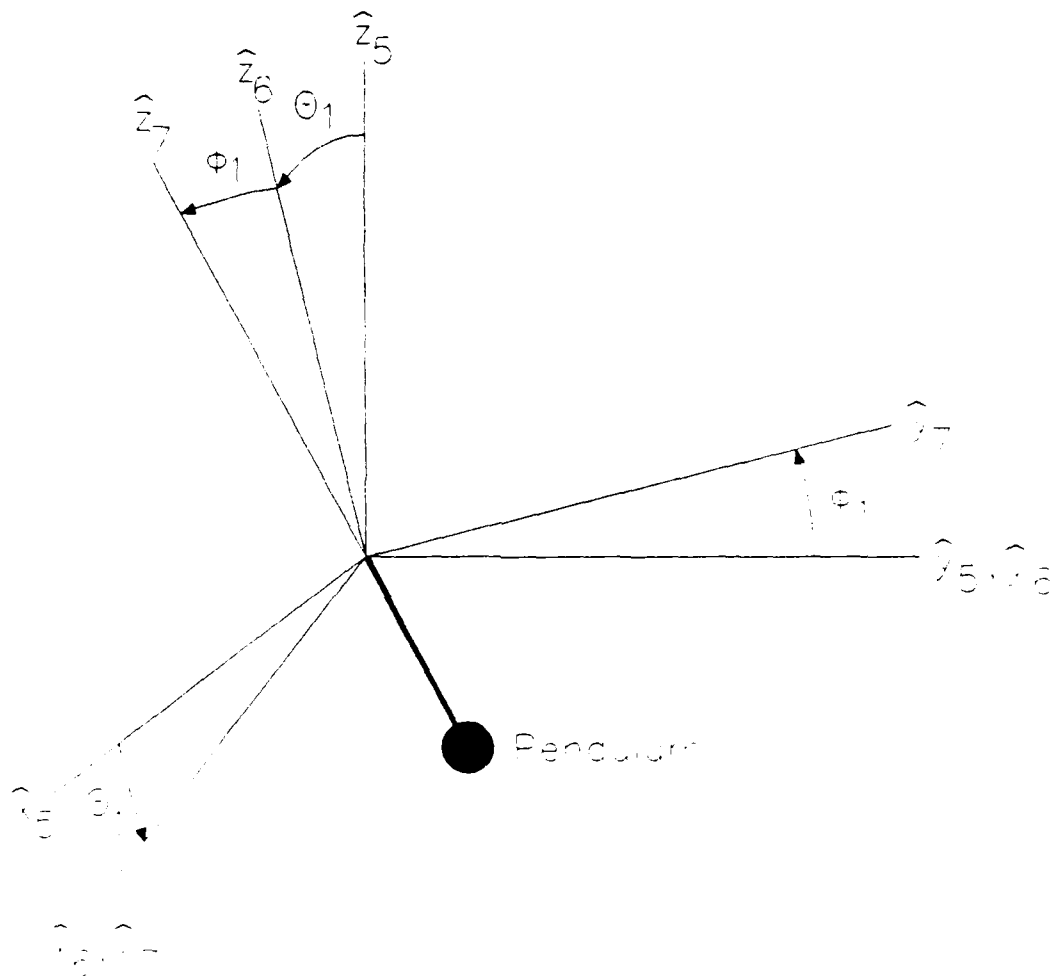


FIGURE 4. Rotation of pendulum 1

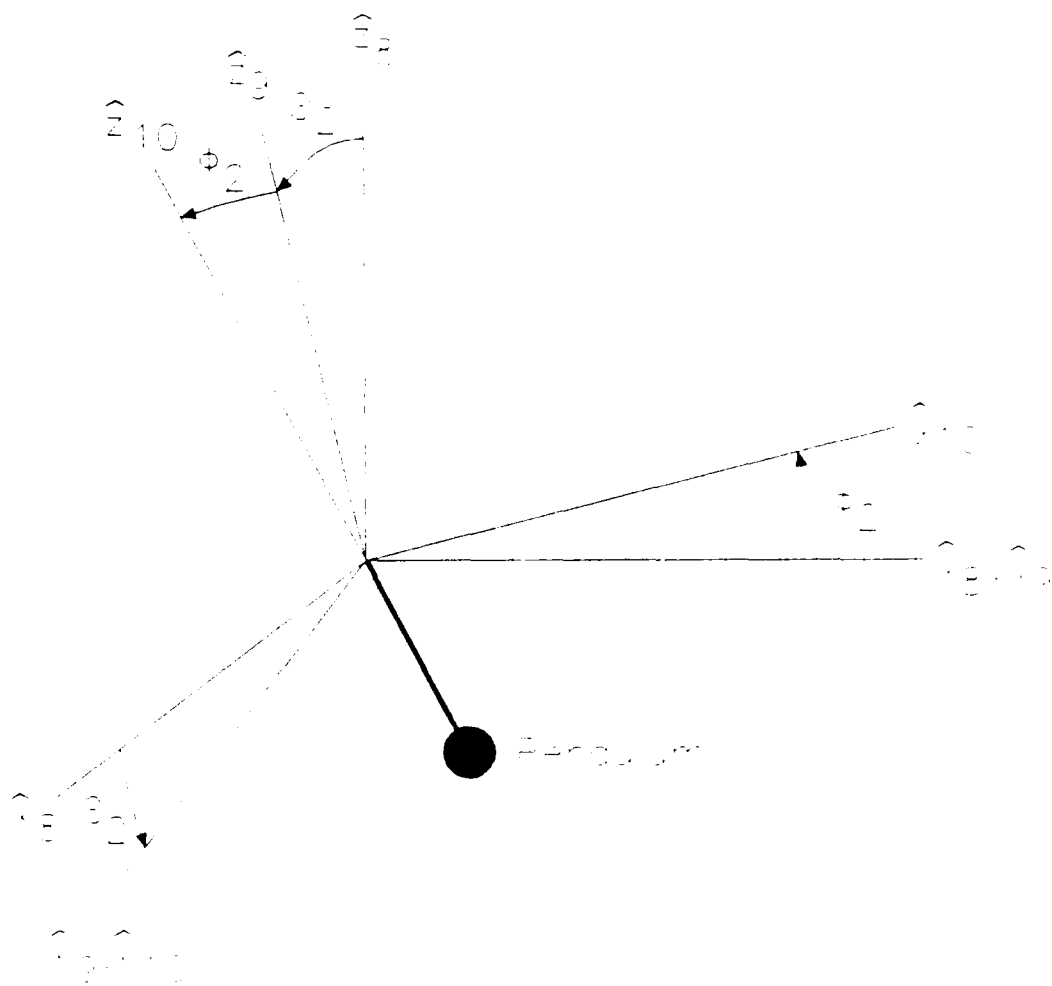


FIGURE 5. Rotation of pendulum.

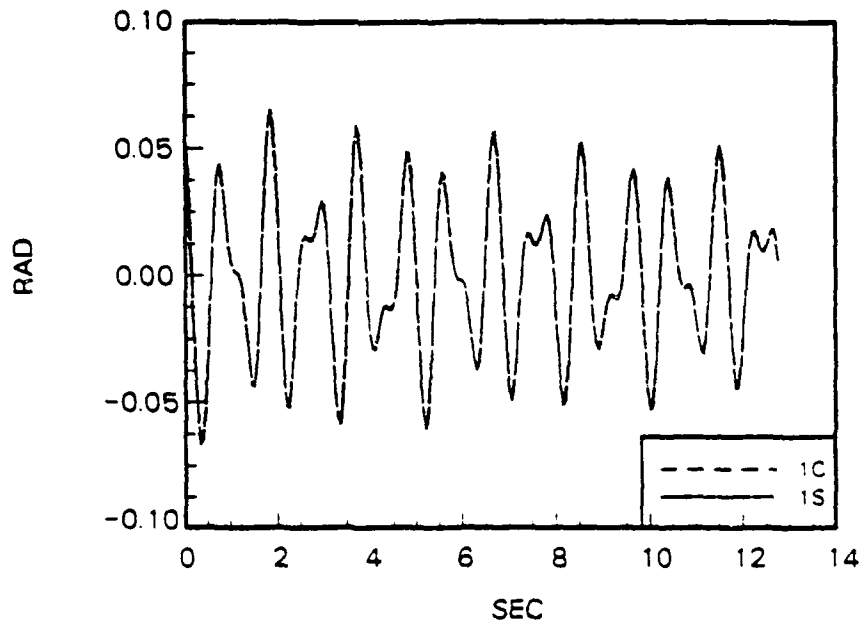


FIGURE 6. λ_1 versus time for 1C and 1S

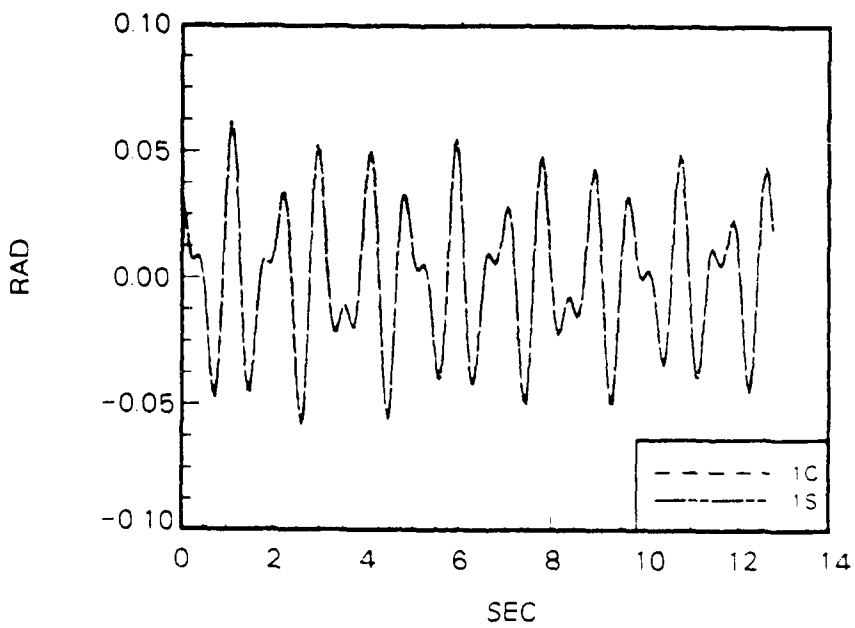


FIGURE 7. λ_2 versus time for 1C and 1S

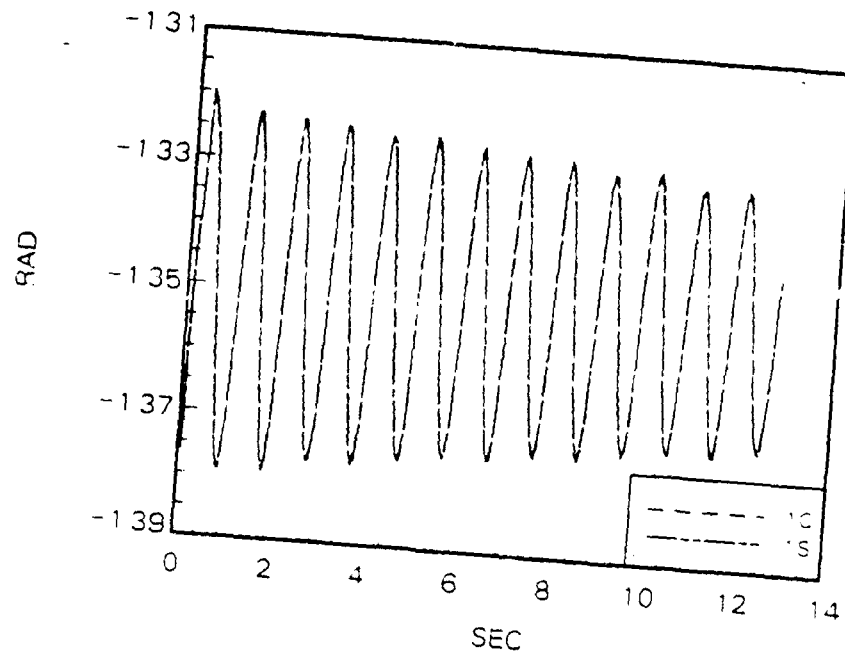


FIGURE 8. θ_1 versus time for IC and IS

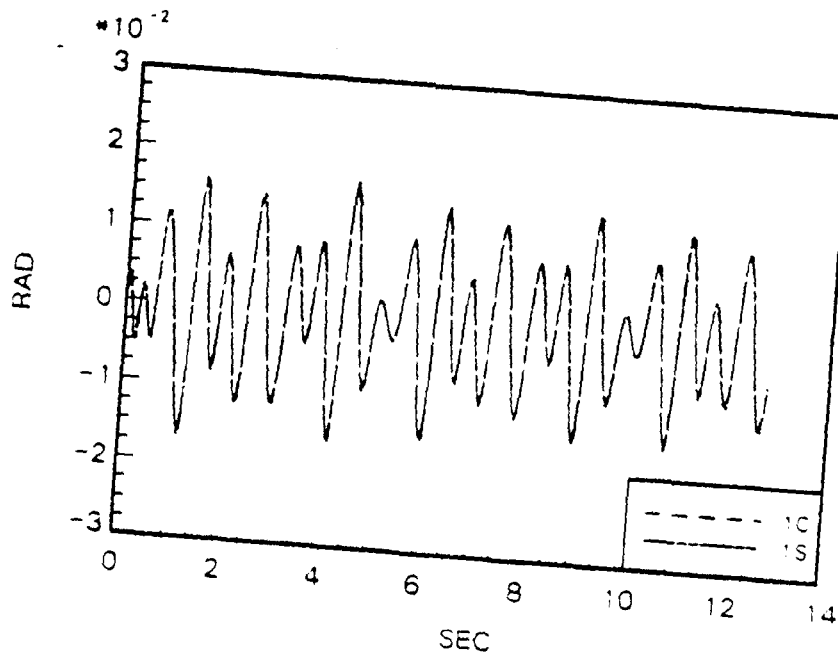


FIGURE 9. ϕ_1 versus time for IC and IS

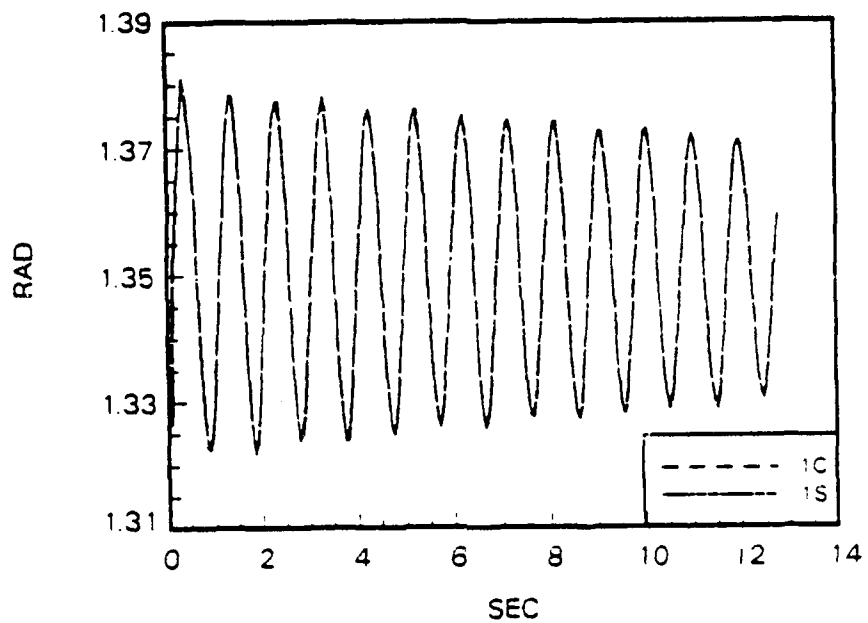


FIGURE 10. θ_2 versus time for 1C and 1S

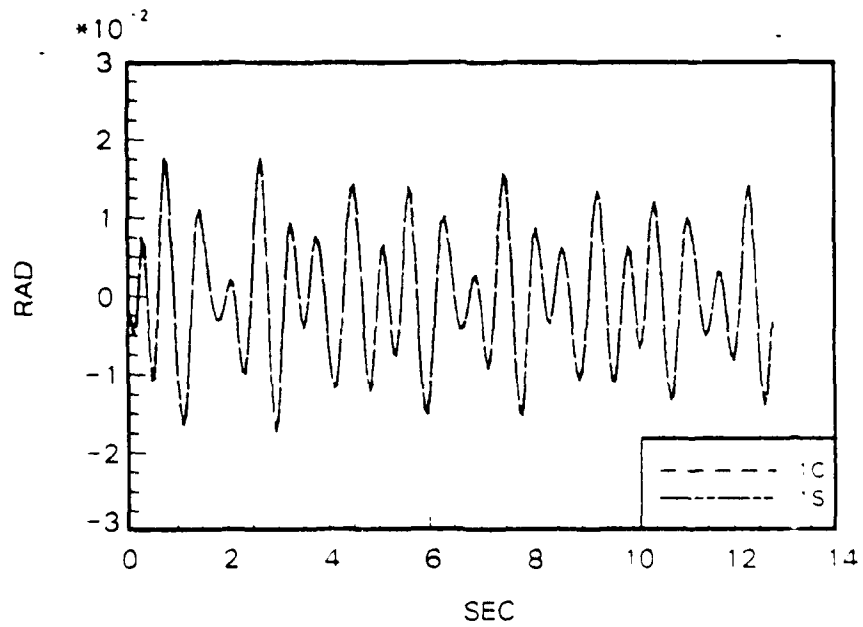


FIGURE 11. ϕ_2 versus time for 1C and 1S

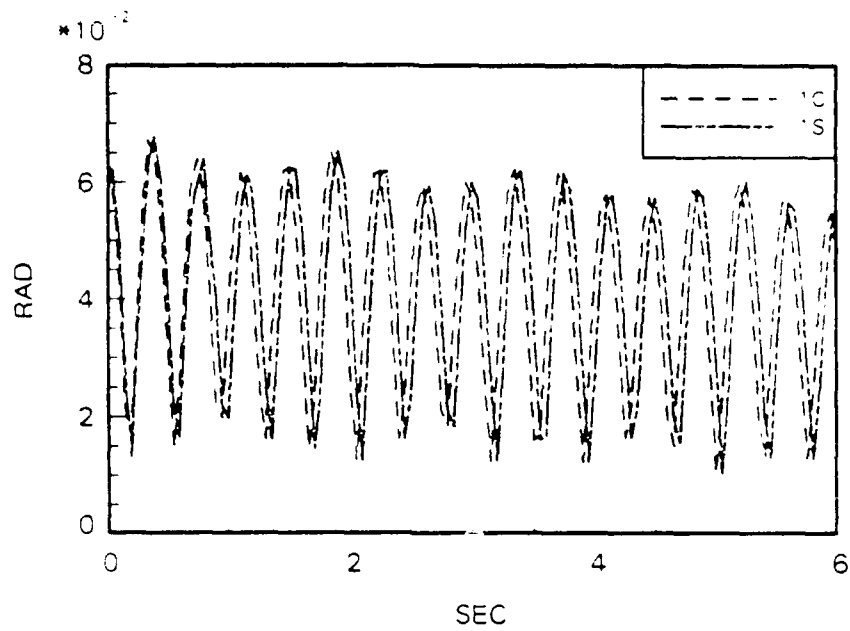


FIGURE 12. β versus time for 1C and 1S

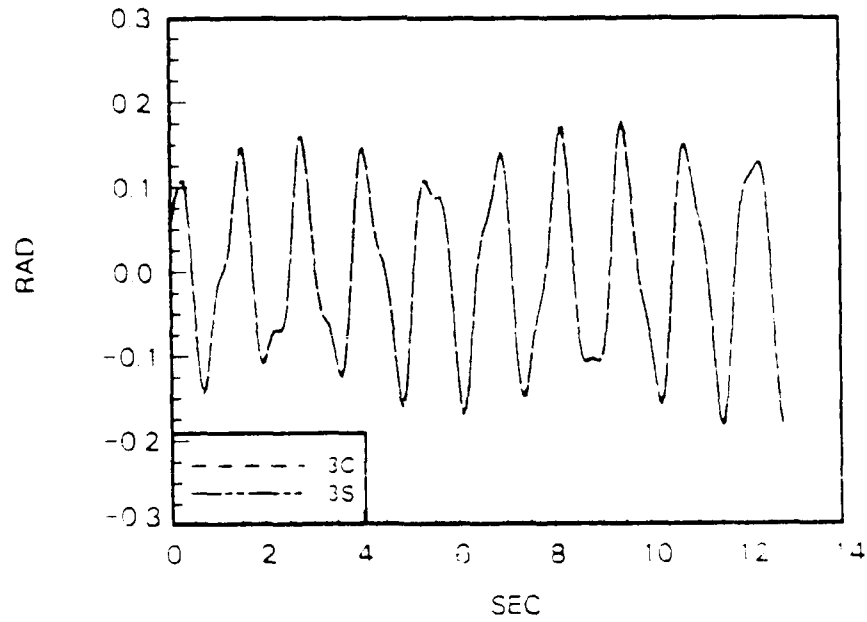


FIGURE 13. λ_1 versus time for 3C and 3S

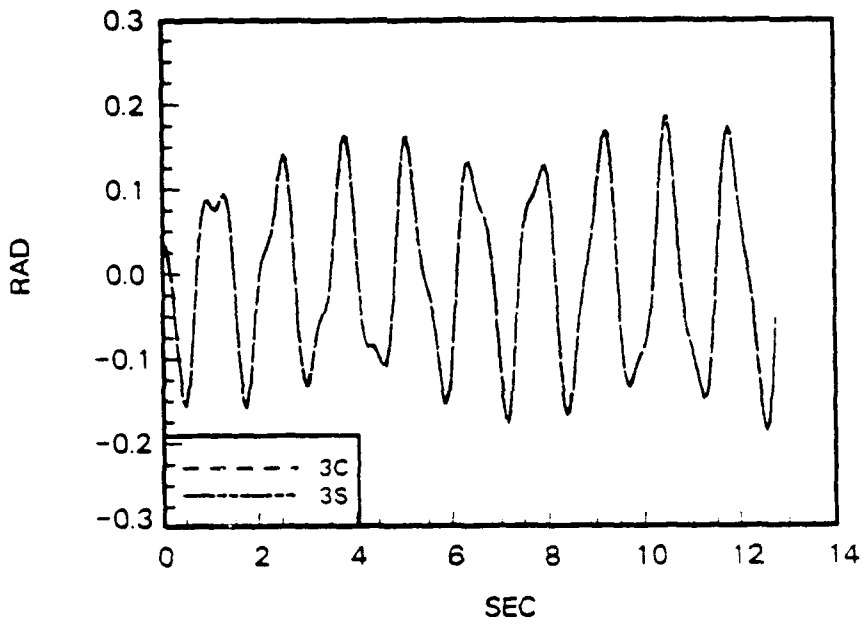


FIGURE 14. λ_2 versus time for 3C and 3S

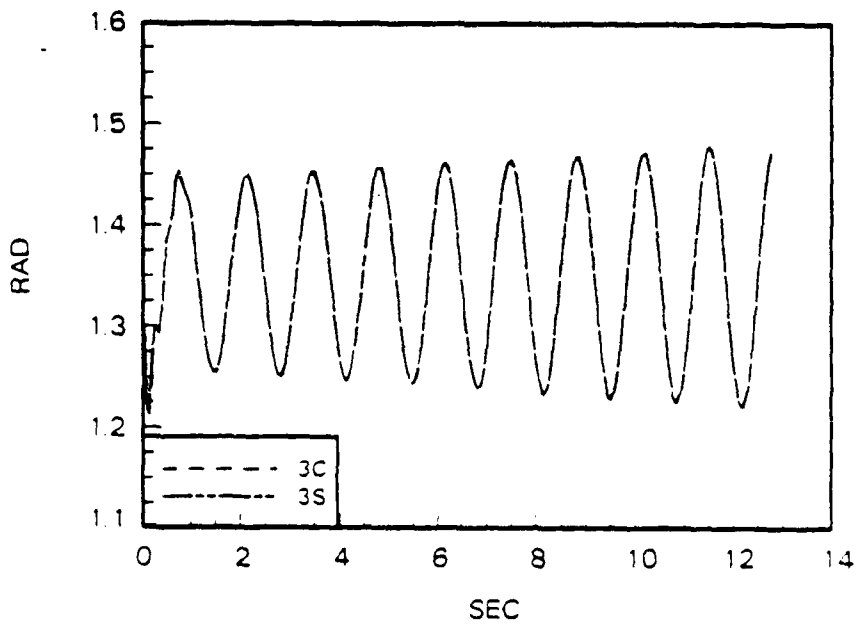


FIGURE 15. θ_2 versus time for 3C and 3S

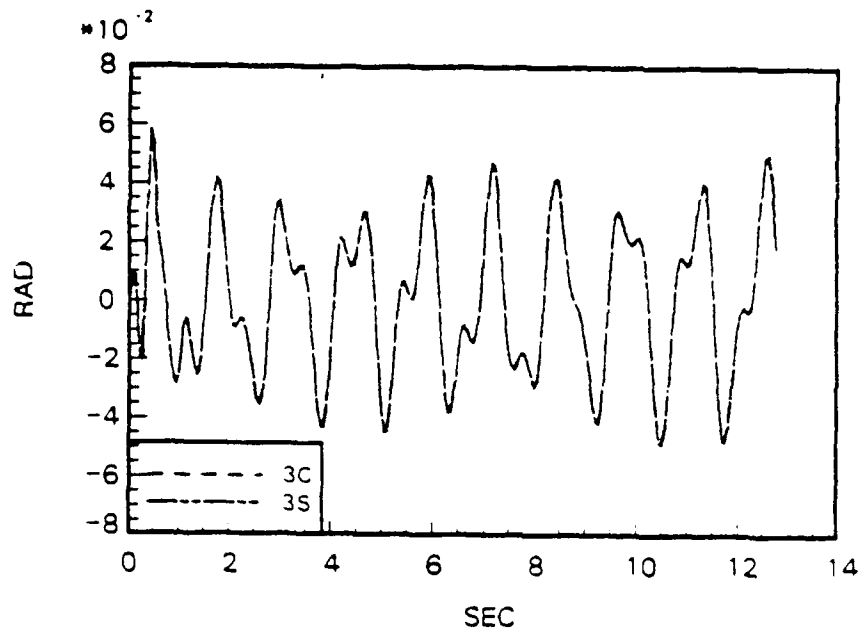


FIGURE 16. ϕ_1 versus time for 3C and 3S

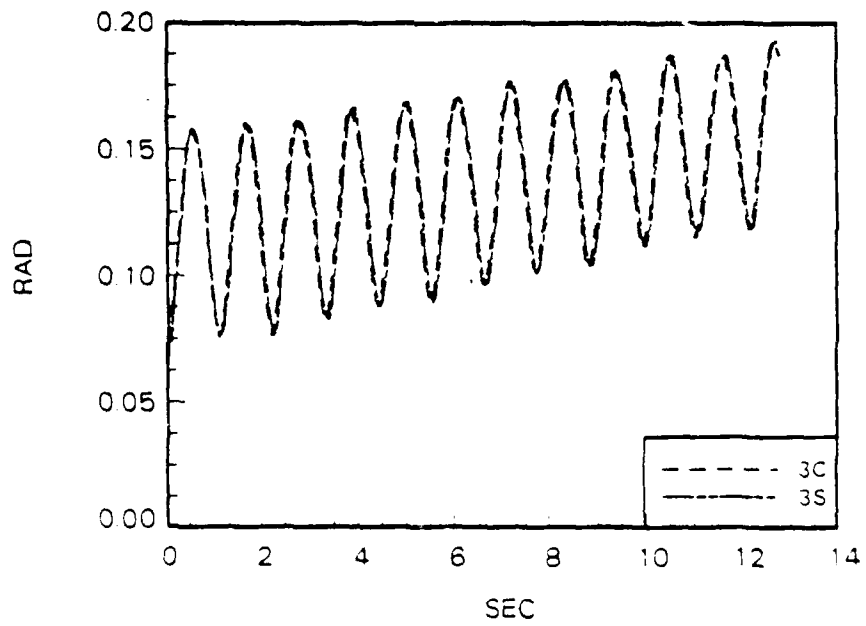


FIGURE 17. β versus time for 3C and 3S

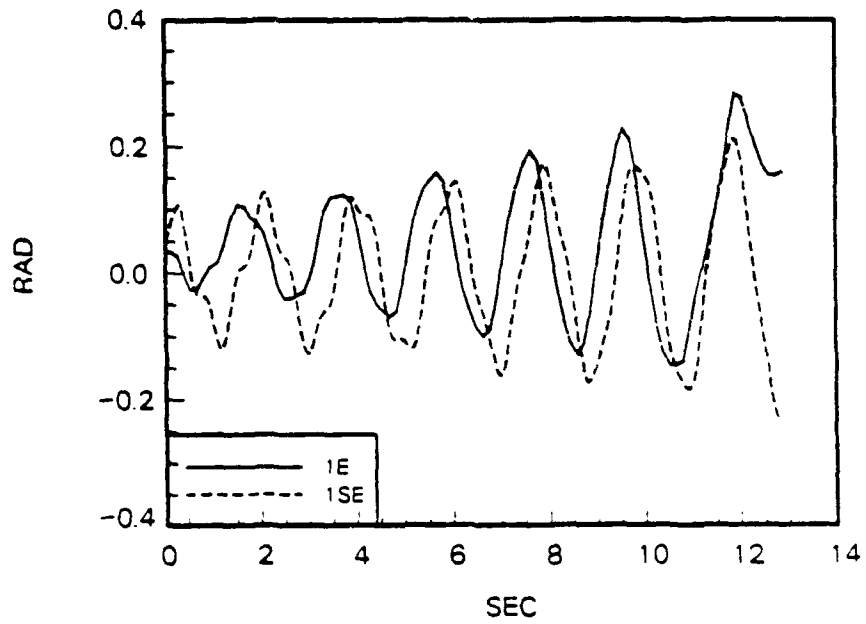


FIGURE 18. λ_1 versus time for 1E and 1SE

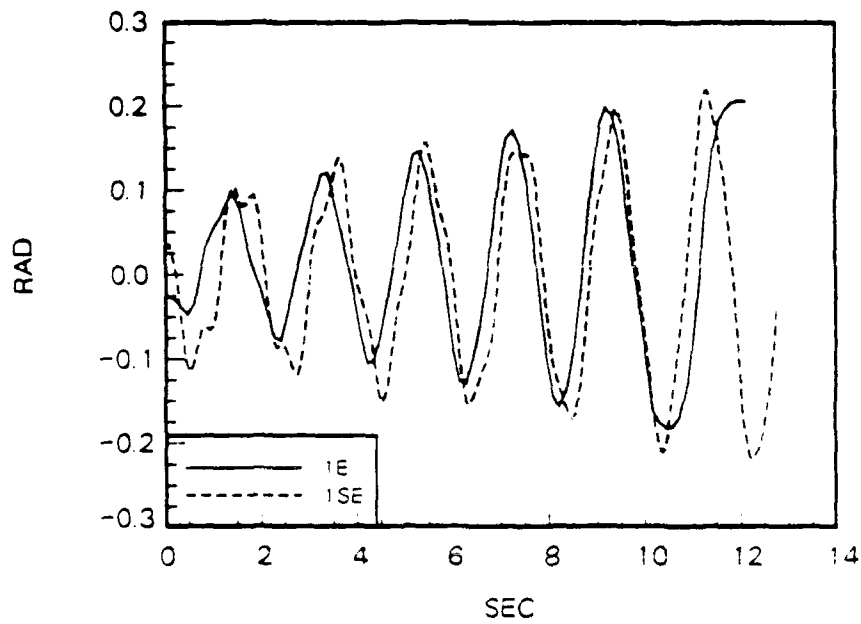


FIGURE 19. λ_2 versus time for 1E and 1SE

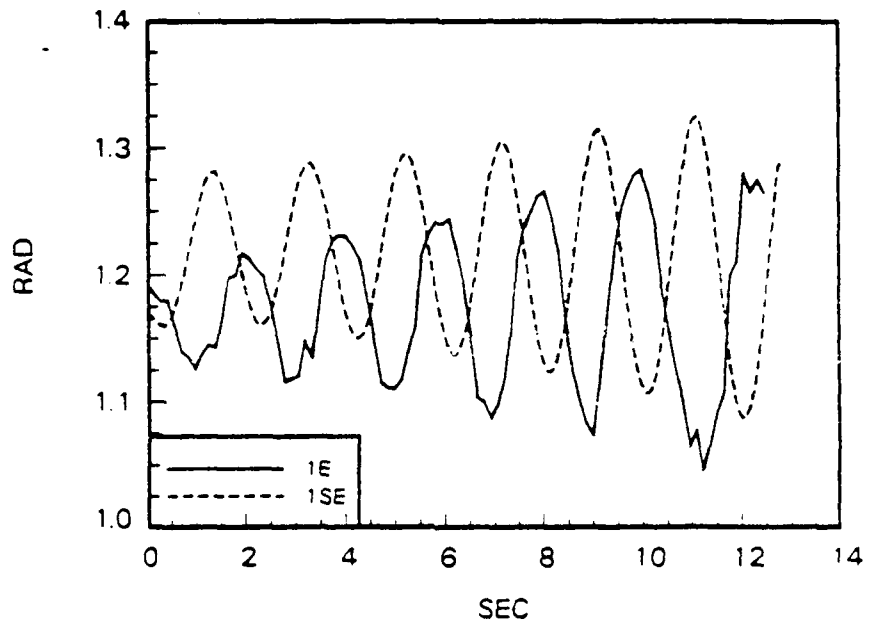


FIGURE 20. θ_2 versus time for 1E and 1SE

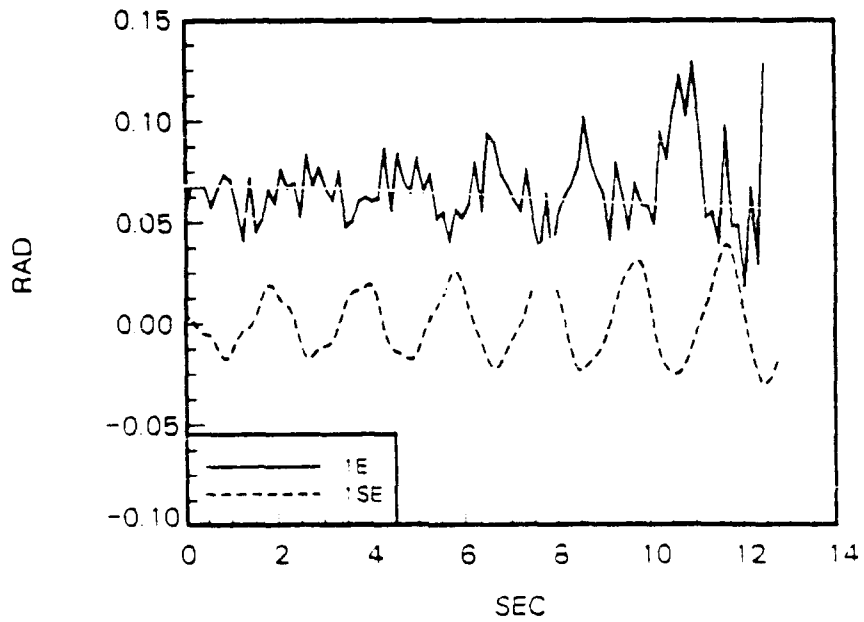


FIGURE 21. ϕ_1 versus time for 1E and 1SE

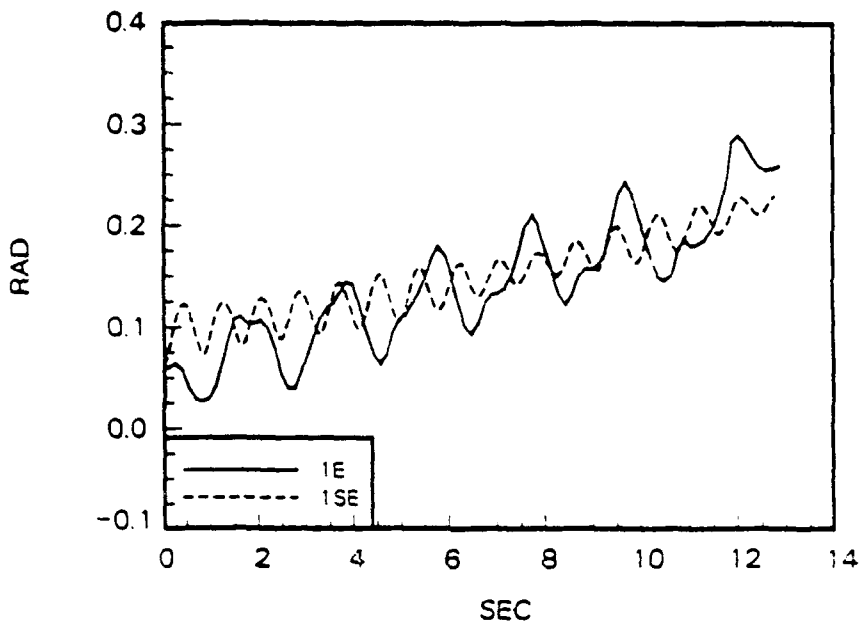


FIGURE 22. β versus time for 1E and 1SE

APPENDIX F

TWO-DIMENSIONAL VISCOUS
SLOSH ANALYSIS

A Numerical Solution for
2-D Viscous Fluid Sloshing in Rectangular
Containers of Finite Aspect Ratio

J. Prusa and A. C. Kassinos

Department of Mechanical Engineering
Iowa State University
July 1989

This paper was prepared for submission
to the Journal of Computational Physics

ABSTRACT

The sloshing of a liquid in a two-dimensional container undergoing a constant, horizontal acceleration is examined in this study. A fluid initially in a state of hydrostatic equilibrium is suddenly accelerated from rest. This sudden acceleration causes an equally sudden change in the pressure field such that the original hydrostatic pressure field no longer gives the correct initial condition. The dimensional formulation is singular at the moment the acceleration begins. By using appropriate scales for the velocity and pressure fields, a nonsingular dimensionless formulation is developed which leads to the correct initial condition for pressure. A transformation to container centered coordinates is also used. In this noninertial frame, the sudden acceleration becomes a horizontal body force. Another transformation immobilizes the wavy free surface, and maps the liquid domain into a unit square for all time. A numerical method is used to solve the resulting dimensionless formulation. Detailed information on pressure and velocity fields is given, as well as global information on sloshing frequency and viscous damping rates.

1. INTRODUCTION

The motion of waves along a gas-liquid interface poses a problem of tremendous analytical and practical interest. Examples range from the prediction of tides [1] to the sloshing of liquids in finite containers. The prediction of tides, bores, and wave induced drag all have obvious maritime applications. The sloshing of fluids is of prime concern in all types of moving vehicles (tanker trucks, railroad cars, and ships; as well as aircraft and spacecraft) since their motion may be adversely affected by the sloshing. The adverse effects may range from outright changes in vehicle orientation due to unwanted moments generated by the sloshing to substantial periodic forcing due to vehicle resonance near the natural frequency of the fluid.

1.1 Analytical Works

Theoretical studies, beginning some two hundred years ago [1] and continuing to the present day, have built up a considerable body of knowledge about wave dynamics. Although somewhat limited in scope, these studies have contributed greatly to our understanding of these types of problems. Almost all analytical work focuses upon potential flows. Two basic approximations are universally employed.

In shallow water (or long) wave theory, the wavelength of a disturbance is assumed to be much larger than the depth of the fluid. This implies that the vertical acceleration of fluid particles is negligible--that the pressure distribution is purely hydrostatic and that the horizontal components of velocity are not functions of fluid depth. In a horizontally unbounded fluid, the velocity of propagation, c (celerity), is equal to $(hg)^{1/2}$ where h is the depth of fluid below the wave and g is the acceleration of gravity. For waves of infinitesimal amplitude, the total energy of the wave is half kinetic and

half potential [1]. For waves of small, but not infinitesimal amplitude, the wave changes shape as it propagates because higher parts of the wave, corresponding to larger values of h in the preceding formula, travel faster than lower parts of the wave. In horizontally bounded fluids, for one dimensional infinitesimal waves, the oscillations are harmonic with frequency $(\sigma_n/2\pi)$ and wavelength λ_n such that $\sigma_n = n\pi c/l$ and $\lambda_n = 2l/n$ where n is integer and l is the length of the bounded horizontal region. The extension to two dimensional, infinitesimal bounded waves is straightforward; with $n\pi/l$ being replaced by $k_{m,n} = (m^2/p^2 + n^2/l^2)^{1/2}$, where m, n are integer, and p, l are the lengths of the bounded region; and $\lambda_n = 2l/n$ and $\lambda_m = 2p/m$ being the corresponding wavelengths of the disturbances in the two directions. For $p > l$, the component oscillation of largest period (smallest $\sigma_{m,n}$) is obtained by choosing $m = 1$ and $n = 0$, this disturbance is everywhere parallel to the longer side of the bounded domain [1].

In deep water (or surface) wave theory, the wavelength of a disturbance is assumed to be comparable to the depth of the fluid. Although the amplitude of the wave is assumed to be infinitesimal, vertical and horizontal accelerations are now of comparable magnitude. Unlike the case of shallow water waves, in deep water waves the magnitude of motion decreases rapidly with depth (exponentially fast, in fact, for the limiting case of infinitely deep water). In a horizontally unbounded fluid, the celerity is $c = \{(\bar{g}\lambda/2\pi) \tanh(2\pi h/\lambda)\}^{1/2}$. Thus the wave speed is dependent upon the wavelength of the disturbance (such that c increases with λ) as well as the fluid depth. In a horizontally bounded fluid, for one dimensional waves, the oscillations are again harmonic with frequency $\sigma_n/2\pi$ and wavelength $\lambda_n = 2l/n$ where $\sigma_n^2 = \bar{g}k_n \tanh(k_n h)$ and $k_n = 2\pi/\lambda_n$. As was the case for shallow waves, the total energy of a deep wave is half kinetic and half potential. The extension

to two-dimensional bounded waves merely involves replacing k_n above with $k_{m,n}$ as given by the shallow wave theory [1].

Within the framework of either shallow or deep water wave theory, a number of additional aspects of wave motion have been examined. These include the effects of variable depth, forced oscillations, small but finite amplitude waves, waves in circular basins and spherical sheets, rotation, and traveling pressure disturbances, to list a few [1]. More recently, two and three-dimensional sloshing in horizontal cylindrical and spherical containers has been investigated [2,3] with these techniques. An interesting result has been the observation that the dependence of frequency with depth is also mode dependent. For the lowest modes of oscillation, frequency simply increases with the depth of fluid in the container. For higher mode oscillations, however, the frequency first decreases and then increases with depth. Another recent study of forced vertical oscillations in a slightly non-square basin has also revealed the existence of symmetry-breaking bifurcations and chaotic free surface oscillations if the basin is sufficiently non square and/or the frequency of forcing is sufficiently detuned from the natural frequencies of oscillation [4]. This work has been confirmed experimentally [5]. The specter of chaotic sloshing leads to the disturbing thought that sloshing motions in their fullest nonlinear form may be inherently unpredictable.

In certain cases, potential flow theory may also be helpful in examining waves whose amplitudes are not small. For example, it is possible for a wave to propagate through a liquid of depth comparable to the wave amplitude without the wave changing its shape. Such a wave, which seems to defy the results of shallow wave theory, is called a soliton. The key requirement for this behavior is that the wavelength of the soliton not be so great (compared to the depth) that vertical accelerations are negligible. Thus the basic assumption

of shallow wave theory is untenable in this case [1]. As the soliton amplitude is decreased (and thus the vertical acceleration decreases), the wavelength of the soliton increases, and it approaches the shape of a shallow water wave of infinitesimal amplitude.

The effects of surface tension and fluid viscosity has been investigated theoretically using deep wave theory. If surface tension dominates gravitational effects, then the celerity increases with surface tension and decreases with disturbance wavelength. With both surface tension and gravitational effects taken into account, the frequency of oscillation is found to increase with increases in gravity, surface tension, and/or disturbance wavenumber, k . The celerity first decreases, but then reaches a minimum value and finally increases with k . For a free surface at which the gas (or vapor) density is negligible compared to the liquid density ρ , the critical wavelength corresponding to the minimum value of celerity $c_{\min}^2 = 2(\gamma\bar{g}/\rho)^{1/2}$ is $\lambda_c = 2\pi(\gamma/\rho\bar{g})^{1/2}$, where γ is the coefficient of surface tension. If $\lambda/\lambda_c > 3$, then gravitational effects dominate the wave dynamics, while for $\lambda/\lambda_c < 1/3$, surface tension effects dominate. More generally, $\sigma^2 = gk + \gamma k^3/\rho$ and $c^2 = \bar{g}/k + \gamma k/\rho$ [1]. A recent work employing a regular perturbation in terms of wave amplitude shows that surface tension acts to decrease wave amplitude and to increase the potential energy of the wave to values well beyond the level of kinetic energy. These increases in potential energy are due to the surface tension. The gravitational contribution to the potential energy first increases, and then decreases with increasing surface tension [6]. The effect of viscosity is to cause a damping of the wave such that its amplitude decays exponentially in time like $e^{-\nu k^2 t}$ where ν is the kinematic viscosity of the liquid. For the case of infinitesimal deep waves, viscosity has no effect on wavelength, frequency, or wavespeed [1].

The idealizations of potential flow and shallow water wave theory may even be used to gain realistic insight into the breaking of waves. Surface tension is found to act to keep the free surface from breaking up [7].

1.2 Numerical Works

Despite the apparent number and diversity of analytical solutions for wave problems, analysis which can reveal the full nonlinear scope of wave dynamics lies well beyond present day analytical techniques. In recent times (the past 25 years), numerical methods and solutions for wave problems have appeared which incorporate effects of viscosity, surface tension, finite enclosures (rectangles, cylinders, and spheres), and finite wave amplitude simultaneously.

Perhaps the first numerical method which could successfully be used to treat arbitrary wave problems was the Particle in Cell (PIC) method [8]. In the PIC method, a continuum model is not used, instead, the motion of a finite number of fluid particles is followed using a Lagrangian description of the dynamics. First order upwind differencing was used in the PIC method, resulting in solutions with significant numerical viscosity. Also, momentary crowding or depletion of particles could occur in a computational cell, resulting in random, high frequency oscillations of fluid properties.

The idea of tracking a finite number of fluid marker particles was used in a continuum model called the Marker and Cell (MAC) method [9,10]. The MAC method is a finite difference method which solves the governing equations for primitive variables on a staggered mesh. A Poisson equation which implicitly enforces continuity is used for pressure. The position of the free surface is deduced by the distribution of marker particles. Unlike the PIC method, however, these particles are not involved in the dynamical calculation other than that they are used to determine where the free surface is located.

Initial results with the MAC method indicated that for sloshing in containers, that the period of sloshing increases with viscosity and that the multiple modes of oscillation which occurred did not have periods which were rational multiples of each other. Thus there is a lack of perfect periodicity in the sloshing and the free surface is never flat once sloshing has commenced (until steady state is reached). While the MAC method generally can be used to make successful predictions of wave problems, the marker particles are not always distributed smoothly. This in turn, leads to a free surface and pressure field which are not smooth. Perhaps the bilinear interpolation on the velocity field which is used to determine the marker particle velocities is the root of this lack of smoothness. Another difficulty is that since the free surface will generally lie somewhere inside a computational cell (rather than the edge), that the application of the free surface (zero stress) boundary conditions is of an ad hoc "particle cell" nature. This too may contribute to the lack of smoothness in the solution. In the original MAC method, zero normal stress at the free surface is approximated by setting the pressure of the cell containing the interface equal to zero. This is correct only in the double limit of zero viscosity and zero surface tension and if the free surface runs exactly through the center of the cell. Zero tangential stress is approximated by setting $\bar{n} \cdot \bar{\nabla} \bar{U} = 0$, where \bar{n} is the outward pointed unit normal vector to the free surface and \bar{U} is the velocity vector. This expression is correct only in the double limit of vanishing surface curvature and negligible tangential gradient of the component of velocity normal to the free surface. These limitations and a more general formulation of the zero stress boundary conditions were first given in [11]. Inclusion of the more general normal stress condition in the MAC method was found to increase the accuracy of a bore calculation by a factor of 2 to 3. In a coanda ("teapot") effect calculation,

the more general condition resulted in a qualitatively correct solution, whereas the solution based upon the original free surface boundary conditions did not. In each case, the more general zero tangential stress condition was not met because that would have required the position of the free surface to a degree of accuracy greater than the MAC method could provide. Consequently, while the accuracy was considerably improved using the improved normal stress condition, noticeable errors still occurred. While [11] does provide a more general formulation for the zero stress conditions at the free surface, the results are not completely general because higher order second derivative terms in free surface position are missing, limiting the formulation in [11] to slightly curved free surfaces.

An evolutionary by-product of the MAC method was a general purpose numerical algorithm called SOLA-SURF [11]. This algorithm relied upon use of a kinematic condition rather than upon marker particles to determine the position of the free surface. As a result, the free surface was determined much more accurately than in a typical MAC method. Unlike the MAC method, the surface cell pressure was not set equal to zero. Instead, it was chosen such that a linear interpolation between it and the pressure in the first cell below yielded zero pressure at the free surface. Unfortunately like the MAC method, the vertical component of velocity at the top of the surface cell was chosen so that the surface cell is divergence free. This is unfortunate because it is only that portion of the surface cell which lies below the free surface that should be divergence free. Thus while the pressure field is accurately aligned with the free surface, the velocity field is not. Like the MAC method, SOLA-SURF is fully explicit in time, and sets the horizontal component of velocity at the free surface so that $\bar{n} \cdot \bar{\nabla} \bar{u} = 0$ there. SOLA-SURF also determines the pressure field by choosing cell pressures which result in divergence free

interior cells. Convective terms are represented by a hybrid finite difference formula which is a combination of second order centered and first order upwind differences (the original MAC method uses only centered differences). While this hybrid formula helps to keep solutions smoother, it does so at the cost of increased numerical viscosity. Solutions for several sample wave problems are illustrated in [11], including the interaction of two solitons, and the damped bobbing of a free floating body. While the solutions appear reasonable and match analytical results (where available) reasonably well, no definitive information on numerical error is given. Such a study would probably have shed some light on the soliton interaction where, for example, each soliton is found to change height slightly, and there appears high frequency, low amplitude disturbances. It is not clear that these effects are truly nonlinear effects as suggested.

While the SOLA-SURF algorithm represents a considerable advance over the MAC method in terms of being able to more accurately predict free surface position, this enhanced accuracy comes at the cost of a considerable decrease in the arbitrariness of the shape of the surface. In particular, in two dimensions the surface position as determined by the kinematic condition must remain a singly valued function of one (or two in three dimensions) of the independent spatial coordinates. Thus the surface may not fold over upon itself. Physically, this means that phenomena like breaking waves or a spray of drops cannot be modeled. Also, the free surface should not be inclined more than the diagonal of a surface cell. Neither of these limitations occurred in the original MAC method, which was quite capable of handling multiply connected fluid regions separated by free surfaces of arbitrary orientation.

The development of the SOLA-VOF algorithm (where VOF stands for Volume of Fluid method), represents an attempt to retain the fluid region tracking

ability of the MAC method while at the same time retaining increased accuracy with which the free surface location is known [12]. The key is to introduce an auxiliary function F , whose average value in a surface cell gives the volume of fluid in that cell. Since F moves with the fluid, the substantial derivative can be used to determine a simple partial differential equation for F . The differencing for F is of an extremely ad hoc nature, and reflects the fact that F is a step function. The free surface is approximated by a straight line segment in the surface cell; its slope and height can be determined from the volume of fluid function F . Solutions to several interesting wave problems are given in [12], and they all look, for the most part, qualitatively correct. Reasonable agreement with analytical results, where available, is also demonstrated.

1.3 Present Work

All of the works so far cited, while covering an extensive list of wave problems, are all for liquids which are at rest in a global sense. That is, for unbounded liquids, accelerations occur only inside the wave, whereas for sloshing in containers, the containers themselves are inertial. Difficulties in the dynamic control of spacecraft [13] dictate that wave dynamics in non-inertial frames of reference also be studied. It is this imperative which motivates the present study of sloshing in an accelerating, rectangular container. For greatest accuracy, the free surface position is calculated using a kinematic condition. This method has the advantage of being readily generalizable to three dimensions. The present work requires that the free surface remain singly valued, as discussed previously. However, the use of a function for surface position does not preclude the possibility of modeling more complex wave dynamics such as breaking. It may be practicable to divide

th. computational region up into several domains, whereby in each domain, the function for the position of the free surface is singly valued [14].

2. MATHEMATICAL FORMULATION

The basic 2-D geometry of the problem is depicted in Fig. 1. A viscous fluid, initially at rest, fills a rectangular container of width a to a depth b . The position of the free surface--denoted by R --is a function of horizontal coordinate \bar{x} , and time, \bar{t} . The remaining independent variable is the vertical coordinate, \bar{y} . The dependent hydrodynamic variables are the horizontal and vertical components of velocity, \bar{u} and \bar{v} , respectively; and the pressure \bar{p} . Since the fluid is initially at rest (with respect to a constant gravitational field which is pointed vertically down), it is in a state of hydrostatic equilibrium.

Suddenly, the container is translated to the right with a constant acceleration. As viewed from a noninertial frame of reference which is moving with the container, this motion results in an apparent uniform body acceleration of magnitude \bar{q} , directed to the left (the principle of equivalence).

A primitive variable formulation was chosen to model the problem primarily because it was felt that this was more readily generalizable to 3D (see the companion paper to this work [15]) and because information on the pressure field was one of the major types of information to be obtained from the study. We note that a streamfunction-vorticity approach could easily be used for the present 2-D study, however. In this latter type of formulation, the body forces enter into the formulation only through the boundary conditions, because the cross differentiation of the momentum equations which produces the vorticity transport equation eliminates conservative body force terms from the governing equations themselves.

Three separate variable transformations are used in this formulation. The first one is used to change the frame of reference so that the coordinate system stays fixed with respect to the container. The second transformation

maps the free surface--whatever its shape--into a straight horizontal line. The final transformation regularizes the formulation at the moment translation of the container begins.

2.1 Dimensional Formulation

We assume an incompressible, Newtonian liquid for the sloshing fluid. Since the rigid container is translated to the right, this means that the origin of any inertial frame of reference translates to the left with respect to a noninertial frame of reference which is fixed with respect to the container. Since the translation is due to constant acceleration, we define the coordinate transformation from $(\bar{x}, \bar{y}, \bar{t})$ space to (x^*, y^*, t^*) space:

$$x^* = \bar{x} - 1/2\bar{q}\bar{t}^2, \quad y^* = \bar{y}, \quad \text{and} \quad t^* = \bar{t} \quad (1a)$$

Substitution of equation (1a) into the standard forms of the continuity and momentum equations for an inertial frame of reference results in:

$$\nabla \cdot U^* = 0 \quad (1b)$$

$$\frac{\partial u^*}{\partial t^*} + U^* \cdot \nabla u^* = -\frac{1}{\rho} \frac{\partial p^*}{\partial x^*} + \nu \nabla^2 u^* - \bar{q} \quad (1c)$$

$$\frac{\partial v^*}{\partial t^*} + U^* \cdot \nabla v^* = -\frac{1}{\rho} \frac{\partial p^*}{\partial y^*} + \nu \nabla^2 v^* - \bar{g} \quad (1d)$$

where $\nabla = (\partial/\partial x^*)\bar{i} + (\partial/\partial y^*)\bar{j}$, $\nabla^2 = \nabla \cdot \nabla$, and $U^* = u^*\bar{i} + v^*\bar{j}$. Here \bar{i} and \bar{j} are the unit basis vectors in (x^*, y^*) space. Note that the dependent variables are redefined for this noninertial frame of reference.

$$u^* = \bar{u} - \bar{q}\bar{t}, \quad v^* = \bar{v}, \quad \text{and} \quad p^* = \bar{p} \quad (1e)$$

Although equations (1b-d) may be used to determine the dependent variables u^* , v^* , and p^* , they are not in a form which brings out the elliptic nature of the pressure field. We differentiate equation (1c) with respect to x^* , and

(1d) with respect to y^* , and add the results to produce a Poisson equation for pressure:

$$\nabla^2 p^* = 2\rho J(u^*, v^*) - \rho \left(\frac{\partial D^*}{\partial t} + U^* \cdot \nabla D^* \right) + \mu \nabla^2 D^* \quad (1f)$$

where $D^* = \nabla \cdot U^*$ and $J(u^*, v^*) = \frac{\partial u^*}{\partial x^*} \frac{\partial v^*}{\partial y^*} - \frac{\partial u^*}{\partial y^*} \frac{\partial v^*}{\partial x^*}$

Here μ is the absolute viscosity ($\mu = \rho\nu$) of the fluid. Note that although the dilatation D^* is identically zero by continuity (1b), these terms are retained in the pressure Poisson equation because they are important for the stability of the numerical method used to solve it [8].

A final governing equation is required to determine the position of the free surface. We use the general kinematic condition that $dR/d\bar{t} = 0$ (originally proved by Lord Kelvin [1]). Note that $d/d\bar{t}$, the total derivative, is also known as the material or substantial derivative. Physically, this condition means that if a particle is on the free surface at any time, then it must remain on it for all time (since fluid motion with respect to the free surface must be everywhere tangential to it)--provided that the motion is continuous. Substitution of $R = R(\bar{x}, \bar{t})$ into the general kinematic condition followed by the coordinate transformation (1a) into noninertial space leads to:

$$\partial R / \partial t^* = v^* - u^* \partial R / \partial x^* \quad \text{along } y^* = R \quad (1g)$$

The initial conditions for the governing equations are:

$$R = b \text{ for all } x^*, U^* = 0 \text{ for all } (x^*, y^*) \text{ at } t^* = 0; \text{ and} \quad (2a,b)$$

$$p^* - p_0 = \rho \bar{g}(b - y^*) \text{ at } t^* = 0 \quad (2c)$$

Here b is the initial height of fluid, and p_0 is the ambient pressure at the free surface.

The boundary conditions for the governing equations are:

$$U^* = 0 \text{ along } x^* = 0, a \text{ and } y^* = 0 \quad (3a,b,c)$$

$$\frac{\partial v^*}{\partial y^*} = - \frac{\partial u^*}{\partial x^*} \text{ and } \frac{\partial u_T}{\partial n} - \kappa u_T + \frac{\partial u}{\partial \bar{t}} = 0 \text{ along } y^* = R \quad (3d,e)$$

$$\frac{\partial p^*}{\partial x^*} = \mu \frac{\partial^2 u^*}{\partial x^{*2}} - \rho \bar{q} \quad \text{along } x^* = 0, a \quad (3f)$$

$$\frac{\partial p^*}{\partial y^*} = \mu \frac{\partial^2 v^*}{\partial y^{*2}} - \rho \bar{g} \quad \text{along } y^* = 0 \text{ and } p^* = p_0 \text{ along } y^* = R \quad (3g, h)$$

where

$$u_T = \frac{u^* + v^* R'}{\sqrt{1+R'^2}} \quad \text{and} \quad u_n = \frac{-R' u^* + v^*}{\sqrt{1+R'^2}}, \quad \frac{\partial}{\partial n} = \bar{n} \cdot \nabla \quad \text{and} \quad \frac{\partial}{\partial T} = \bar{T} \cdot \nabla$$

$$\text{with } \bar{n} = \frac{-R' \bar{i} + \bar{j}}{\sqrt{1+R'^2}} \quad \text{and} \quad \bar{T} = \frac{\bar{i} + R' \bar{j}}{\sqrt{1+R'^2}}, \quad \kappa = -R'' (1+R'^2)^{3/2},$$

$$\text{and } R' = \partial R / \partial x^*, \quad R'' = \partial^2 R / \partial x^{*2}$$

Here κ is the local radius of curvature of the free surface, while u_T denotes the component of velocity tangential to the free surface, and \bar{T} is the unit tangent vector to the free surface. Thus boundary condition (3e) is a zero tangential stress condition along the free surface. Boundary condition (3d) results from continuity. The pressure boundary conditions (3f-g) result from applying the momentum equations (1c,d) at the container boundaries where $U^* = 0$. The pressure boundary condition (3h) is the result of a zero normal stress condition along the free surface (assuming negligible surface tension effect).

While the use of local orthonormal coordinates (n, T) makes clear the physical basis of the zero tangential stress boundary condition (3e), the boundary condition needs to be written in (x^*, y^*) coordinates to make it useful. The final result is:

$$(1-R'^2) \left(\frac{\partial u^*}{\partial y^*} + \frac{\partial v^*}{\partial x^*} \right) - 4R' \frac{\partial u^*}{\partial x^*} - \frac{R' R'' \dot{R}}{(1+R'^2)} = 0 \quad (3i)$$

where $\dot{R} = \partial R / \partial t^*$.

Equations (1c - 3d and 3c-i) constitute a complete formulation for the

problem. The continuity equation (1b) is not explicitly used, but instead, is used indirectly later on in the numerical method when the dilatation terms are evaluated in the pressure equation (1f).

2.2 Characteristic Scales

The moving boundary which is the free surface in a sloshing problem introduces an additional nonlinearity into the problem simply because the boundary position is a function of time. If in addition, the shape of the boundary is somewhat irregular, then further complexities arise in the analysis [16].

The difficulty of tracking a moving, irregularly shaped domain is eliminated completely in this study by transforming it into a time invariant unit square. By using R as a local characteristic scale for y^* , an elementary algebraic stretching transformation can be used to accomplish this normalization.

Another major problem comes to light when one considers the momentum equations (1c,d) and what they imply about the nature of the pressure field the moment the sudden acceleration begins. Consider the x^* momentum equation (1c) along the bottom of the container (at $y^* = 0$):

$$0 = - \frac{\partial p^*}{\partial x^*} + \mu \frac{\partial^2 u^*}{\partial y^{*2}} - \rho \bar{q} \quad (4a)$$

For fluids (such as water) which have very small values of viscosity, a naive scale analysis of equation (4a) seems to indicate that:

$$\frac{\partial p^*}{\partial x^*} \sim \rho \bar{q} \gg \mu \frac{\partial^2 u^*}{\partial y^{*2}} \quad \text{and thus } \Delta p_x \sim \rho a \bar{q} \text{ along } y^* = 0 \quad (4b)$$

where Δp_x is the change in pressure from $x^* = 0$ to $x^* = a$ along the container bottom. The insignificance of the viscous term in (4b) is even more strongly supported as $t^* \rightarrow 0$, since $U^* = 0$ at $t^* = 0$. But initially the pressure field

p^* cannot be a function of x^* because it is hydrostatic (see initial condition 2c). Thus a glaring inconsistency becomes apparent. The same naive analysis on the y^* momentum equation (1d) reveals that:

$$\Delta p_y - \rho a \bar{q} \text{ along } x^* = 0, a \quad (4c)$$

Note that the values for Δp_x and Δp_y given in equations (4b,c) are in fact exact, initially--provided the viscous terms are truly negligible. Summing the pressure changes along the left, bottom, and right walls results in:

$$\Delta p_y - \Delta p_x - \Delta p_y = \Delta p_0 \text{ or } \rho a \bar{q} - \Delta p_0 \quad (4d)$$

where Δp_0 is the pressure change along the free surface. Δp_0 should be equal to zero because the pressure is constant along the free surface (boundary condition 3h). But for $\rho a \bar{q} > 0$, $\Delta p_0 \neq 0$ and the pressure field must become discontinuous along the boundary (if both $\Delta p_0 \neq 0$ and boundary condition 3h are correct)!

Clearly, the formulation is singular at $t^* = 0$. The sudden horizontal acceleration causes a sudden shift in the pressure field, from a classical hydrostatic distribution at $t^* = 0^-$ to a non-equilibrium distribution at $t^* = 0^+$ which satisfies the governing equations and boundary conditions. Consequently the initial condition for pressure (2c) is really incorrect, and it should not be used to begin a solution.

Initially, frictional effects will be confined to thin boundary layers along the sides and bottom of the container, and so the fluid core will (as a first approximation) tend to remain at rest with respect to an inertial frame of reference. With respect to the noninertial frame of reference defined by the coordinate transformation (1a), the core will appear to be a solid body accelerating at a constant rate of $-\bar{q}t^*$. Secondary local variations will be superposed upon this solid body motion, however, by the non-equilibrium pressure distribution.

Based upon this intuition, and assuming that $\bar{q} = \bar{g}$, we choose the

characteristic velocity scale for u^* to be $u_c \sim \bar{q}t^*$. By continuity, $v^* \sim u_c$ also if $a \sim b$ (order one aspect ratio). The characteristic time, t_c , for which this scaling is valid is found by scaling the unsteady and convective terms in the momentum equations. The result is that $t_c \ll \sqrt{a/g}$ for solid body motion of the core. Physically, this limit is due to the time it takes a wave to travel across the container (celerity $\sim \sqrt{ag}$).

2.3 Dimensionless Formulation

In accord with the preceding discussion, the dimensionless variables are formulated to both:

- normalize the domain of analysis.
- regularize the solution as $t^* \rightarrow 0^+$

The first point requires the employment of a coordinate transformation to produce a natural coordinate system for the domain of analysis. We choose a simple algebraic stretching:

$$x = x^*/a, \quad y = y^*/aB, \quad \text{and} \quad t = t^*/\sqrt{a/g} \quad (5a)$$

where $B(x,t) = R(x^*,t^*)/a$, called the dimensionless gap function, is simply the dimensionless free surface position.

Regularization of the formulation is achieved by transforming the dependent variables as follows:

$$u = u^*/t\sqrt{ag}, \quad v = v^*/\sqrt{ag}, \quad \text{and} \quad p = (p^* - p_0)/\rho ag \quad (5b)$$

Note the explicit factoring of t^{-1} from the dimensional velocity to produce the dimensionless velocity. This is a crucial step in developing a model which is initially nonsingular.

Substitution of equations (5a,b) into (1b-d and 1f,g) produces the dimensionless governing equations:

$$\frac{\partial u}{\partial x} - y \left(\frac{B'}{B} \right) \frac{\partial u}{\partial y} + \frac{1}{B} \frac{\partial v}{\partial y} = D \quad (5c)$$

$$\begin{aligned} \frac{\partial(tu)}{\partial t} + t^2 \left(u \frac{\partial u}{\partial x} \right) + \frac{t}{B} \left\{ t(v - yB'u) - y\dot{B} \right\} \frac{\partial u}{\partial y} \\ = - \left\{ \frac{\partial p}{\partial x} - y \left(\frac{B'}{B} \right) \frac{\partial p}{\partial y} \right\} + tGa^{-1/2} (\nabla^2 - N)u - Q \end{aligned} \quad (5d)$$

$$\begin{aligned} \frac{\partial(tv)}{\partial t} + t^2 \left(u \frac{\partial v}{\partial x} \right) + \frac{t}{B} \left\{ t(v - yB'u) - y\dot{B} \right\} \frac{\partial v}{\partial y} \\ = - \frac{1}{B} \frac{\partial p}{\partial y} + tGa^{-1/2} (\nabla^2 - N)v - 1 \end{aligned} \quad (5e)$$

$$(\nabla^2 - N)p = 2t^2 J(u, v)/B - \partial(tD)/\partial t \quad (5f)$$

$$\dot{B} = t(v - uB') \text{ along } y = 1 \quad (5g)$$

where

$$\nabla^2 = \partial^2/\partial x^2 + B^{-2} \partial^2/\partial y^2$$

$$N = \left(\frac{2yB'}{B} \right) \frac{\partial^2}{\partial x \partial y} - \left(\frac{2B'}{B^2} - \frac{B''}{B} \right) y \frac{\partial}{\partial y} - \left(\frac{yB'}{B} \right)^2 \frac{\partial^2}{\partial y^2}$$

$$J(u, v) = \frac{\partial u}{\partial x} \frac{\partial v}{\partial y} - \frac{\partial u}{\partial y} \frac{\partial v}{\partial x}, \text{ and}$$

$$B' = \partial B/\partial x, \quad B'' = \partial^2 B/\partial x^2, \text{ and } \dot{B} = \partial B/\partial t$$

and

$$Ga = a^3 \bar{g}/\nu^2 \quad (\text{Galileo number}) \quad (5h)$$

$$Q = \bar{q}/\bar{g} \quad (\text{dimensionless horizontal acceleration}) \quad (5i)$$

Equation (5c) defines the dimensionless dilatation, $D = D^*/t\sqrt{\bar{g}/a}$. Continuity requires $D \equiv 0$. Equation (5g) is the kinematic condition for the position of the free surface--it provides the governing equation for the gap function. Terms representing the convection and diffusion of dilatation, apparent in the dimensional pressure equation (1f), have been dropped from the dimensionless

version (5f). By numerical experiment, we found them to be unnecessary for numerical stability, so only the transient dilatation term has been retained in the dimensionless Poisson equation (5f). In both momentum equations (5d,e) additional convective terms of the form

$$-yt[(\dot{B}/B) - t(B'/B)u]\partial/\partial y$$

appear due to use of the coordinate transformation (5a). Information giving the motion and shape of the free surface in physical space cannot be lost. In the transformed space, since the free surface is both immobilized and normalized, this information appears in the form of additional terms in the governing equations themselves. The $(\dot{B}/B)\partial/\partial y$ term represents a convective effect due to actual movement of the free surface, while the $(B'/B)u\partial/\partial y$ term (also appearing in the continuity equation 5c and in the pressure term of 5d) represents a convective effect due to the irregular shape of the free surface. The N operator appearing in the momentum and Poisson equations (5d-f) represents a diffusive effect due to the irregular shape of the free surface. Note that B , B' , and B'' must be singly valued and well defined (one-to-one) for the coordinate transformation (5a) and its inverse to be well behaved.

Only two similarity parameters appear in the dimensionless governing equations. The Galileo number, Ga , is the ratio of gravitational to frictional force, while Q is the dimensionless body acceleration in the x momentum equations. The gravitational body acceleration in the y momentum equations is normalized by the nondimensionalization to a unit magnitude.

Substitution of equations (5a,b) into (3a-d and f-i) produces the dimensionless boundary conditions:

$$u, v = 0 \text{ along } x = 0, 1 \text{ and } y = 0 \quad (6a)$$

$$\frac{\partial v}{\partial y} = B' \frac{\partial u}{\partial y} - B \frac{\partial u}{\partial x} \text{ and } \frac{\partial u}{\partial y} = B' \frac{\partial v}{\partial y} - B \frac{\partial v}{\partial x} \text{ along } y = 1 \quad (6b, c)$$

$$\frac{\partial p}{\partial x} - y \left(\frac{B'}{B} \right) \frac{\partial p}{\partial y} = Ga^{-1/2} \cdot t \left\{ \frac{\partial^2 u}{\partial x^2} - \left(\frac{2yB'}{B} \right) \frac{\partial^2 u}{\partial x \partial y} + \left(\frac{2B'^2}{B^2} - \frac{B''}{B} \right) y \frac{\partial u}{\partial y} + \left(\frac{yB'}{B} \right)^2 \frac{\partial^2 u}{\partial y^2} \right\} - Q \text{ along } x = 0, 1 \quad (6d)$$

$$\frac{\partial p}{\partial y} = Ga^{-1/2} \cdot (t/B) \frac{\partial^2 v}{\partial y^2} - B \text{ along } y = 0$$

$$\text{and } p = 0 \text{ along } y = 1 \quad (6e, f)$$

2.4 Non-Singular Initial Conditions

Since the hydrostatic initial condition (2c) does not give the correct pressure distribution at $t = 0^+$, it is necessary to determine it. This is done by examining the limiting forms of the governing equations (5d-g) and boundary conditions (6a-f) corresponding to $t \rightarrow 0^+$. As $t \rightarrow 0^+$, the governing equations reduce to:

$$u = -\partial p / \partial x - Q \text{ and } v = - (1/\beta) \partial p / \partial y - 1 \quad (7a, b)$$

$$\nabla_0^2 p = 0 \text{ and } \dot{B} = 0 \quad (B = \beta) \quad (7c, d)$$

where $\nabla_0^2 = \partial^2 / \partial x^2 + (1/\beta^2) \partial^2 / \partial y^2$ and

$$\beta = b/a \quad (\text{initial aspect ratio}) \quad (7e)$$

while the boundary conditions (6b-e) simplify to:

$$\partial v / \partial y = -\beta \partial u / \partial x \text{ and } \partial u / \partial y = -\beta \partial v / \partial x \text{ along } y = 1 \quad (7f)$$

$$\partial p / \partial x = -Q \text{ along } x = 0, 1 \text{ and } \partial p / \partial y = -1 \text{ along } y = 0 \quad (7g, h)$$

Boundary conditions (6a, f) are retained unchanged for the initial conditions. Note the appearance of the third and last similarity parameter, β (equation 7e). This parameter gives the initial ratio of fluid height to depth, before the sloshing motion begins.

The elliptic nature of the initial pressure field is clearly shown by the

La Place equation (7c). It is subject to one Dirichlet boundary condition (6f) and three Neumann Boundary conditions (7g,h). Through the pressure field, the velocity field is also made elliptic in nature, a behavior which is not obvious from the momentum equations (7a,b). The elliptic nature of the velocity field can be made clearer by examining the streamfunction defined by $u^* = -\partial f^* / \partial y^*$ and $v^* = \partial f^* / \partial x^*$. In dimensionless form, the streamfunction definition becomes:

$$u = -\frac{1}{B} \frac{\partial f}{\partial y} \text{ and } v = \frac{\partial f}{\partial x} + yB' u \quad (7i)$$

where $f = f^* / (\alpha t \sqrt{ag})$. Cross differentiation of the momentum equations (7a,b) and adding the results to eliminate the pressure results, upon use of (7i), in a La Place equation for the streamfunction:

$$\nabla_0^2 f = 0 \quad (7j)$$

The no-slip boundary condition (6a) results in:

$$f = 0 \text{ along } x = 0,1 \text{ and } y = 0 \quad (7k)$$

The first part of boundary condition (7f) is satisfied identically by definition of the streamfunction. The second part of (7f) is more conveniently replaced by using the momentum equation (7a) itself along the free surface.

The result is:

$$\partial f / \partial y = \beta Q \text{ along } y = 1 \quad (7l)$$

The La Place equations for streamfunction (7j) and pressure (7c) subject to the boundary conditions (7k,l) and (6f,7g,h) may be solved using the classical method of separation of variables. The solution for streamfunction may be differentiated as indicated in equation (7i) to yield the velocity field. The results are:

$$f = \sum_{m=0}^{\infty} b_m \sin X_m \sinh Y_m \quad (8a)$$

$$p = \beta(1-y) + Q(1/2-x) - \sum_{m=0}^{\infty} b_m \cos X_m \cosh Y_m \quad (8b)$$

$$u = -\sum_{m=0}^{\infty} b_m (2m+1) \pi \sin X_m \cosh Y_m \quad (8c)$$

$$v = \sum_{m=0}^{\infty} b_m (2m+1) \pi \cos X_m \sinh Y_m \quad (8d)$$

where

$$b_m = 4Q / \{ \pi^2 (2m+1)^2 \cosh[(2m+1)\pi\beta] \} \text{ and}$$

$$X_m = (2m+1)\pi x, \quad Y_m = \beta(2m+1)\pi y$$

The solutions (8b-d) provide the dimensionless initial conditions for the full governing equations (5d-f). Note that (8c,d) satisfy the no-slip boundary conditions (6a).

2.5 Steady State Condition

The ultimate steady state of the system may be considered a hydrostatic state with respect to the combined body force acceleration - $(\bar{g} + \bar{q})$. It may be easily found in closed form by integrating the momentum equations directly. In dimensionless form, the result is:

$$u, v \rightarrow 0, \quad B \rightarrow \beta + Q(1/2-x) \text{ as } t \rightarrow \infty \quad (9a,b)$$

$$p \rightarrow \beta - y + Q(1/2 - x) \text{ as } t \rightarrow \infty \quad (9c)$$

These final conditions have been written as limits rather than equalities because the system approaches them asymptotically, through the mechanism of viscous damping.

3. NUMERICAL METHOD AND COMPUTATIONAL PROCEDURE

The various derivatives appearing in the governing equations (5c-g) were approximated by finite difference formulas based upon Taylor series expansions. The resulting nonlinear algebraic equations in u , v , p , D , and B were solved iteratively, using an implicit, essentially point Gauss-Seidel method. The cross derivative term arising from the N diffusion operator and all source terms were evaluated using information totally from the previous iteration (Jacobi method). All convective terms were split up into a first order upward difference plus a second order correction term. The upward difference was evaluated using the Gauss-Seidel method while the correction terms were evaluated using the Jacobi method. All diffusion terms were approximated using the standard central difference formula. A first order, forward time difference was used for the unsteady terms.

A look at the momentum equations (1c,d) reveals that there are two choices for the Neumann boundary conditions for pressure along the container walls. In particular, a tangential or a normal pressure gradient can be specified along the walls. We experimented with both types, and found that the normal gradient boundary conditions--as given in equations (3f,g)--are vastly superior to the analytically equivalent tangential gradients. Use of the tangential gradients increased the number of iterations for convergence and even often caused divergence of the iterations. We believe that this was due to poor spatial resolutions in the boundary layers which form along the walls. Apparently, use of the normal pressure gradients tends to minimize this problem. In an effort to further enhance the speed of the algorithm, we examined the role of the spatially differentiated dilatation terms in the pressure equation (5f). We found that by retaining the spatial terms that the dilatation field was marginally improved (that is, it approached a value of zero more closely).

Negligible change in the number of iterations for convergence was observed. Despite the slight increase in CPU time per iteration which resulted, we elected to retain the spatial dilatation terms in the pressure Poisson equation for most of the computations whose results are summarized in the next section.

In order to produce time accurate solutions for each timestep, all dependent variables were iterated to a convergence criterion of

$$\left| \frac{\phi^{k+1} - \phi^k}{\phi_{\max}^k} \right| < \epsilon \quad (10)$$

where $\phi = u, v, p$, or B and k refers to the iteration number. ϕ_{\max}^k is the maximum value of $|\phi^k|$ occurring anywhere in the computational domain. A convergence criterion of $\epsilon = 10^{-5}$ was used for variable increment grids with 21×21 and 41×41 nodes. This value of ϵ seemed to be the minimum value required to keep the dilatation, D , small (of order 10^{-3}). The 21×21 grid was used only for trials with the lowest Ga and Q values. The 41×41 grid was used to produce most of the data in the following section. All of the dependent variables were under-relaxed. For interior nodes, relaxation values of 0.8 to 0.9 and 0.7 were used for the pressure and velocities, respectively. For the pressure Neumann boundary conditions, a value of 0.5 was used for the relaxation parameter. Along the free surface, a relaxation parameter of 0.5 was used for the velocities.

A constant timestep of $\Delta t = 0.01$ was used in all trials. This resulted in about 350 timesteps per period. The choice of timestep size was dictated primarily by the desire to reduce overall CPU time as much as possible. Since our method was fully implicit, it was possible to use substantially larger timesteps and still obtain converged solutions. The total number of iterations (accumulated over all timesteps) could be reduced, however. In principle, it could be increased to the point where a single period was insufficiently resolved in

time. We felt that 20 to 50 timesteps per period provided a reasonable minimum time resolution. Our choice of stepsize thus represents a significant improvement over the minimum criterion, and consequently, we believe that the time truncation error in our results is negligible.

For $Ga = 10^4$ about fifty to one hundred iterations per timestep were required, on average, to produce a converged solution. More iterations were required when the wave motion neared a stationary point (point of maximum potential energy and minimum kinetic energy). Less iterations were required when the free surface was passing through the final equilibrium position given by equation (9b) (point of maximum kinetic energy and minimum potential energy). Surprisingly, less iterations were also required early in the trial, when the amplitude of the sloshing was largest. At later times even though frictional effects acted to damp out fluid motion, the number of iterations steadily increased. Finally, the number of iterations for convergence also decreased with Ga . For the $Ga = 10^4$ trials, typically 3 to 4 hours of CPU time were required on a NAS9160 (a 10-30 megaflop machine) to compute a solution to a dimensionless time of 16.

4. RESULTS AND DISCUSSION

A number of computational trials were executed, corresponding to the following twelve sets of similarity parameters:

- $Ga = 10^4$, $\beta = 0.5$, and $Q = 0.1, 0.2, 0.3$
- $Ga = 10^4$, $Q = 0.2$, $\beta = 0.75$ and 1.00
- $Q = 0.2$, $\beta = 0.5$, $Ga = 10^3, 10^5, 10^6, 10^7, 10^8, 10^9$, and 10^{10}

Since the Galileo number is inversely proportional to the square of kinematic viscosity, Ga decreases as the fluid becomes more viscous. In order to gain a feel for the value of Ga , Table 1 presents representative values of it for various fluids at 20°C, assuming $a = 0.1$ m.

TABLE 1. Representative Values of Ga for Various Fluids at 20° C assuming $a = 0.1$ m.

fluid	liquid Hg	water	air	SAE 10W oil	glycerin
Ga	10^{12}	10^{10}	10^8	10^6	10^4

We present detailed results of the solution only for the trial with $Ga = 10^4$, $q = 0.2$, and $\beta = 0.5$. This trial will be referred to as the standard case throughout the remainder of the section. Limited, global information on the rate of energy dissipation is presented for the remaining eleven trials.

4.1 Accuracy of the Solution and Verification With the Inviscid Limit

Since our formulation (and finite differencing) is non-conservative, one variable which can be monitored that immediately yields information on the accuracy of the solution is the overall fluid volume, \bar{V} . In dimensionless form it is given by:

$$V = \bar{V}/a^2 = \int_0^1 B dx \tag{11a}$$

Since the fluid is incompressible, the volume is constant. Thus equation (11a) should yield $V = \beta$ in all trials at all times, whatever the shape of the free-surface. In all trials, we have essentially observed that $V > \beta$, albeit only slightly. In the standard case ($Ga = 10^4$, $Q = 0.2$, and $\beta = 0.5$), initially V drops below β by 0.001%, and then increases above β by 1.4% at a dimensionless time of $t = 1.98$. At this moment, the fluid is near a point of greatest potential energy and least kinetic energy (these extrema occur at $t = 1.96$). Local maxima in the V error occur near successive points of energy extrema, but these errors decay in magnitude as time increases--and the total sloshing motion becomes more and more damped out. Inbetween the potential and kinetic energy extrema, the V error drops considerably from its peak values at the energy extrema. The error in fluid volume increases with increasing Ga and/or decreasing β , and/or increasing Q . For the trial with $Ga = 10^{10}$ (and $Q = 0.2$, $\beta = 0.5$), the maximum error in V was 3.8%. For the trial with $Q = 0.3$ (and $Ga = 10^4$, $\beta = 0.5$), the maximum error in V was 3.2%, while for the trial with $\beta = 1.0$ (and $Ga = 10^4$, $Q = 0.2$) the maximum error was only 0.3%.

The period of oscillation of the numerical solution may also be compared with a linearized analytical result [1] for irrotational sloshing. This analytical solution is valid in the triple limit $Ga \rightarrow \infty$, $Q \rightarrow 0$, and the sloshing \rightarrow infinitesimal magnitude. The period of oscillation for the present results is determined by examining the transient behavior of the kinetic energy of the fluid, defined by:

$$\begin{aligned} \overline{KE} &= \int_{\overline{V}} \frac{1}{2} \rho (\overline{u}^2 + \overline{v}^2) d\overline{V} \\ &= \frac{1}{2} \rho \overline{V} \overline{q}^{-2} t^{*2} + \rho \overline{q} t^* \int_{\overline{V}} u^* d\overline{V} + \frac{1}{2} \rho \int_{\overline{V}} (u^{*2} + v^{*2}) d\overline{V} \end{aligned} \quad (11b)$$

The first term on the RHS of equation (11b) is the rate of work required to

accelerate the fluid if it moved like a solid body. The dimensionless kinetic energy is found by subtracting this work from equation (11b), and then normalizing the resulting difference with respect to a gravitational kinetic energy:

$$KE = \frac{KE - \frac{1}{2} \rho \bar{v} \bar{q}^{-2} t^{*2}}{\rho a \bar{g}^{-2} t^{*2}} = \int_0^1 \int_0^1 \left\{ uQ + \frac{1}{2}(u^2 + v^2) \right\} B dx dy \quad (11c)$$

This kinetic energy equation is appropriate for a frame of reference which moves with the container. Note that as viscous damping causes the sloshing motion to dissipate, that $KE \rightarrow 0$ whereas \bar{KE} increases to infinity like $\frac{1}{2} \rho \bar{v} \bar{q}^{-2} t^{*2}$ (as $t^* \rightarrow \infty$). The results of the comparison are shown in Table 2. Despite the fairly large value of Q and the extreme viscosity of the fluid (low Ga), the numerical result compares very favorably with the analytical result [1]. For the trial with $\beta = 0.50$, it predicts a period 2.2% longer than the analytical result. With $\beta = 1.0$, the numerical result predicts a period which is 1.1% longer. In order to assess the effects of large Q and low Ga , additional trials were examined for their sloshing periods. These results are shown in Table 3. The effects of Q (for $Ga = 10^4$ and $\beta = 0.5$) are seen to be quite pronounced. When extrapolated back to $Q = 0$, these data indicate a period of 3.74, within 1.1% of the analytical result. The effect of Ga appears to be less significant. As $Ga \rightarrow \infty$ (inviscid fluid limit), the period appears to decrease slightly (less than 1%). When a correction for finite viscosity is added (on top of the zero Q correction), the predicted period for $Ga \rightarrow \infty$, $Q \rightarrow 0$, and $\beta = 0.5$ drops to 3.72, which is only 0.5% longer than the analytical result [1]. In order that the third limit condition of the analytical result be approximately satisfied, the periods listed in Tables 2 and 3 were determined from the numerical solutions only at the ends of the trials, when the sloshing motion had damped out to the maximum extent. In all cases, we

TABLE 2. Comparison of Sloshing Periods

	β		
	0.50	0.75	1.00
Analytical result [1]	3.70	3.58	3.55
Present numerical result, trial $Ga = 10^4$ and $Q = 0.2$	3.78	3.62	3.59
Percent error	+2.2%	+1.1%	+1.1%

TABLE 3. Effect of Horizontal Acceleration and Fluid Viscosity on Sloshing Period. Present Numerical Results for $\beta = 0.5$.

		Q		
		0.1	0.2	0.3
Ga	10^4	3.75	3.78	3.84
	10^7	--	3.79	--
	10^{10}	--	3.76	--

noticed a finite amplitude (of the sloshing) effect on the sloshing period. For trials with $Q = 0.2$ and $\beta = 0.5$, periods with large finite amplitudes were typically 1.0% larger than periods with very small amplitude motion, for $10^{10} \geq Ga \geq 10^4$.

The numerical result for the trial for the standard case is also compared with a potential flow solution. The potential flow solution, valid for irrotational flow ($Ga \rightarrow \infty$ limit), was determined by numerically solving the Laplace equation for velocity potential $\bar{\phi}$, where $\nabla \bar{\phi} = U^*$. Zero tangential velocity along the solid walls resulted in Neumann boundary conditions for $\bar{\phi}$ around the container wall. At the free surface, Bernoulli's equation was used

to provide an appropriate boundary condition for $\bar{\phi}$. This potential flow solution was formulated for a sudden acceleration, hence it is valid for finite Q as well as for large amplitude sloshing. Figure 2 shows the comparison using the average slope of the free surface. The slope has been normalized so that its maximum value is 2 while the steady state value is 1. The periods are again seen to be very similar. Note the viscous damping of the present numerical result for the standard case, which is rapidly approaching steady state.

4.2 Initial Conditions

Since the initial conditions (8a-d) are themselves a non-trivial part of the overall solution, an example solution for them is depicted in Fig. 3. The initial pressure field for $Q = 1$ and $\beta = 1$, Fig. 3a, is clearly quite different from the hydrostatic distribution which one is naively led to expect. The initial velocity field is shown in Fig. 3b with a plot of lines of constant streamfunction. Velocity vectors are everywhere tangential to lines of constant streamfunction; overall they point leftward.

Taken together, Figs. 3a,b indicate that as soon as the sudden acceleration is imparted to the container, there is a sudden loss of pressure in the upper right corner, a sudden increase of pressure in the lower left corner, and a net leftward migration of fluid. This overall pattern results in the free surface falling in the right half of the container and rising in the left half of the container.

4.3 Velocity and Pressure Fields

The detailed transient velocity field for the standard case is shown in Fig. 4. With the exception of Fig. 4a, the velocity vector $\vec{U} = (u\vec{i} + v\vec{j})t$ is

plotted. Since u and v are multiplied by dimensionless time, \tilde{U} is directly proportional to the physical velocity ($\tilde{U} = U^* / \sqrt{ag}$). Fig. 4a shows the initial velocity field $U = u\bar{i} + v\bar{j}$ (rather than \tilde{U}). This figure is analogous to the streamfunction plot, Fig. 3b, only now the values of Q and β are somewhat less. Fig. 4b again shows the initial velocity field, but now in terms of \tilde{U} . Since $t = 0$, the velocity field is identically a zero field. All vectors are reduced to points. Note that Fig. 4b effectively shows the node distribution of the computational grid which was used. Nonzero velocity magnitudes appear only for $t > 0$; and by $t = 0.10$, they are quite noticeable. As the velocity field continues to grow in magnitude, a slight deformation in the free surface becomes noticeable by $t = 0.20$. At a dimensionless time of $t = 0.40$, the velocity field is approaching its maximum magnitude. At $t = 0.80$, the fluid is near a maximum in kinetic energy and the deformation of the free surface is becoming significant. Up to this point in time, the velocity field has retained the same qualitative character, and looks much like the initial condition, Fig. 4a. Beyond this time, the kinetic energy decreases as the fluid approaches a state of maximum potential energy. By $t = 1.51$, small recirculating regions appear in the lower corners of the container. At $t = 2.01$, these recirculating regions have grown greatly in size, merged, and now dominate the velocity field. Only a small vestige of the initial flow pattern remains in the fluid core. The fluid is near a state of maximum potential energy and minimum kinetic energy. Figures 4i-k repeat the preceding sequence of events, only in the reverse direction. At $t = 2.51$, the fluid is again near a state of maximum kinetic energy, similar to Fig. 4e. Only now, in Fig. 4i, damping has considerably reduced the magnitude of the velocity vectors. In Fig 4j, small regions of recirculation are again seen in the lower

corners of the container. Inbetween the times corresponding to Figs. 4j and k, at $t = 3.84$, the fluid reaches a state of minimum kinetic energy--one period of the slosh has been completed. In Fig. 4k, the flow has largely changed direction again and resumed much of its initial character, as the second period of the slosh gets underway. At $t = 4.51$, the fluid is again near a state of maximum kinetic energy. The effect of viscous dissipation is even more obvious than in Fig. 4i. The sloshing motion has been damped out sufficiently by $t = 4.69$ that only 6% of the initially available kinetic energy remains. Consequently Fig. 4l, at $t = 4.51$, shows the fluid close to its final steady state, for which the free surface is a line with a slope of -0 . Although the computation was carried out to a dimensionless time of $t = 16.90$, no new flow physics is revealed for $t > 4.51$.

The transient pressure field for the standard case is shown in Fig. 5. Here, isobars with a constant dimensionless pressure increment of $\Delta p = 0.05$ are plotted. The initial pressure field is depicted in Fig. 5a. As was the case for the velocity field, note the resemblance to the initial pressure distribution depicted in Fig. 3a. In Fig. 5b, recall that the flow is near a state of maximum kinetic energy. Note the bifurcation in the zero pressure isobar (the free surface is at zero pressure) at the extreme right of the diagram. The small triangular region defined by the two branches of the zero isobar is a region of very slight negative pressure. We note that such a region is physically possible so long as it is an interior region (which it is) and so long as the physical pressure in this region does not drop below the cavitation pressure. If the free surface pressure is somewhat greater than the cavitation pressure, then this region of negative pressure does not pose any special problems. It is of interest to recognize that the pressure initial condition, equation (8b), also predicts a tiny region of negative pressure in

this corner of the flow field, if Q is large enough. Although the sloshing has really just started, the pressure field has largely adjusted itself so that qualitatively it now looks very much like the final steady state field, which is given in Fig. 5e (the kinetic energy has been dissipated by a factor of about 10^5 at $t = 16.90$). The relatively minor adjustments to the pressure field which do occur are confined to the vicinity of the free surface. Note the persistence of the negative pressure region to Fig. 5c. Here, the fluid is near a point of maximum potential energy. As in Fig. 5b, the right side of the surface is falling (note that viscous drag along the right wall acts to retard the motion of the surface locally). At $t = 3.51$, the edge of the free surface along the right side of the container is now rising--and there is no region of negative pressure. Curiously, no region of negative pressure develops along the left ledge of the free surface, which is now falling. By $t = 4.51$, the flow has reversed itself again (beginning of second period of sloshing), and the free surface along the right wall is again falling. At this time, the fluid is again near a point of maximum kinetic energy. The region of negative pressure has reappeared, albeit much smaller.

4.4 Parametric Effects on Sloshing

From the earlier section on verification, the effects of Ga , Q , and β on the sloshing period have already been noted (see Tables 2 and 3). In summary, the period increases very slightly with decreasing Ga ; increases slightly with increasing Q ; and increases somewhat more significantly with decreasing values of β . In this section the effects of the three similarity parameters on the rate of viscous damping of the sloshing motion is examined.

Figure 6 presents results on the damping rate for three trials, each with the same values of Ga and Q , but with different values of β . The figure

presents the envelope of maximum kinetic energy KE_{\max} as a function of time. The states of KE_{\max} are states in which the free surface approximates its final steady state shape. Thus the fluid potential energy is minimized. For the standard case, the first KE_{\max} occur at dimensionless times of $t = 0.87, 2.80,$ and 4.69 (see Fig. 4). The most striking feature of Fig. 6 is that the damping rate is exponential in time.

Despite the complexity of the fluid motions, in terms of the dissipation of energy, a sloshing fluid behaves much like a simple damped pendulum. This exponential decay has also been shown to be correct by an analytical solution for viscous, infinitesimal, deep water waves [1]. The other important point to recognize from Fig. 6 is that while β has the most significant effect on the period (causing the points of KE_{\max} to spread out as time increases), it has very little effect on the slope of the KE_{\max} envelope. Data from the standard case represents the other two trials very well.

The effect of Q on the envelope of KE_{\max} is presented in Figure 7. The figure is very similar to Fig. 6 and again shows the exponential decay of the KE_{\max} . While the value of Q does lead to some spreading in the times of KE_{\max} , it is seen that the standard case represents the other two trials well. Thus the value of Q also has only a minor effect on the rate of viscous damping.

Figure 8 presents the effect of Ga , and hence fluid viscosity, on the rate of damping. As expected, the value of Ga has a tremendous effect, with the rate of damping increasing as Ga decreases. Regression analysis was used to determine the modulus of decay τ , defined by the relation:

$$KE_{\max} = 10^{-\tau t} \quad (11d)$$

The results of the regression analysis are summarized in Table 4. Note the differences in significant figures in the τ values for various Ga . They reflect actual differences in the precision with which the τ values were

determined. These differences in precision are due in part to the differences in the duration of dimensionless time for which a trial was executed.

Although the four trials for $Ga \geq 10^7$ show a nice exponential type of

Table 4: Modulus of Decay, τ , as a Function of Ga . Regression Analysis of Present Numerical Results for $Q = 0.2$ and $\beta = 0.5$

Ga	10^3	10^4	10^5	10^6	10^7	10^8	10^9	10^{10}
τ	0.62	0.255	0.126	0.061	0.0352	0.023	0.018	0.0177

damping relationship for $KE_{\max}(t)$, we believe that the τ values for $Ga > 10^7$, as given in Table 4, may be far less accurate than they are precise (although this is uncertain at present). This suspicion is based upon the long time ($t > 30$) behavior of KE_{\max} for the $Ga = 10^7$ and 10^{10} trials. In particular, the numerical solution begins to show oscillation in the value of KE_{\max} as the time increases. These oscillations became pronounced sooner (in time) as Ga increases. The magnitude of the oscillations increase exponentially fast with time for a given trial, leading us to believe that they are due to a numerical error. These oscillations may be discerned in the envelope for the $Ga = 10^{10}$ trial in Fig. 8. They also exist in the $Ga = 10^7$ trial but are much more subtle. As time increases beyond $t = 30$, the oscillations increase so much in magnitude that the results obviously became physically incorrect--increases in KE_{\max} appear in the numerical results. At first, these increases occur in an alternating pattern. From a given KE_{\max} to the next, the value is seen to decrease (normal behavior). Upon going to the next value of local maximum, however, KE_{\max} is seen to increase in value beyond the preceding one. The next KE_{\max} then again decreases in value, followed by an increase, and so on. This has the effect of making the KE_{\max} envelope "bumpy". When the alternating

pattern in energy maximums first establishes itself, the oscillations are very small and the KE_{\max} still decrease, on average. But as the oscillations grow, a point is reached where the KE_{\max} grow very rapidly. Divergence of the iterations follows shortly afterwards. For the $Ga = 10^7$ trial, the first increase in KE_{\max} does not occur until $t = 59.83$, well beyond the domain of Fig. 8. For the $Ga = 10^{10}$ trial, the time at which this occurs is $t = 19.89$. For $t > 30$, the oscillations in KE_{\max} grow so large that the iterations diverge at $t = 58.49$.

Since $\tau = \tau(Ga)$ only can be inferred from the information displayed in Fig.'s 6-8, a plot of $\log \tau$ vs. $\log Ga$ can be used to deduce the functional relationship $\tau(Ga)$. A simple linear relationship was observed -- but only for the trials with $Ga < 10^7$. The $Ga = 10^7$ result was somewhat off the line, while the $Ga = 10^{10}$ result was quite distant. The $Ga = 10^8$ and 10^9 trials produced results at intermediate distances from the linear relationship. For the reasons given above, these four points were discarded, and the remaining points were used for a linear regression analysis with the following result:

$$\tau = 5.6Ga^{-0.33} \quad (11e)$$

Because the modulus of decay for the standard case is the most precise (and ostensibly, most accurate) value listed in Table 4, it was double weighted in the determination of $\tau(Ga)$. Equation (11e) gives values of τ which are in error by about 5%, at most. It should be valid for the parameter range $Ga \geq 10^3$, $Q \leq 1$, and $\beta = 1$.

It is of interest to note the analytical solution for viscous, infinitesimal, deep water waves presented in [1]. predicts an exponential damping in time for the displacement, η , of the free surface from its steady-state (equilibrium) position. In dimensional form, the modulus of decay for η is found to be proportional to the viscosity, $\tau_{\eta} \sim \nu$. Since the fluid potential energy is proportional to η^2 and $KE \sim$ potential energy (via an energy balance).

one is led to the result that $\bar{\tau}_\eta \sim \nu$ also. In terms of Galileo number, this requires $\tau_\eta \sim Ga^{-1/2}$.

5. SUMMARY AND CONCLUSIONS

The problem of viscous sloshing in a rectangular container induced by a sudden, constant horizontal acceleration is examined and solved using a numerical finite difference method. Initially, the fluid is in a state of hydrostatic equilibrium. The problem is characterized by a moving, irregularly shaped free surface, and an initial singularity caused by a sudden change in the pressure field from time $t = 0^-$ to $t = 0^+$. A coordinate transformation is used to fix the container in a noninertial reference space. This transformation causes the translation in physical space due to the acceleration to appear as an additional body force term in the governing equations (principle of equivalence). A second coordinate transformation maps the free surface, whatever its shape at any given moment of time, into a horizontal line. The domain of analysis thus becomes the unit square. A third transformation of the dependent variables regularizes the formulation as $t \rightarrow 0^+$. An analytical solution is then presented which uniquely defines the initial condition. Three similarity parameters are found to govern the nature of solutions for the problem. The Galileo number, Ga , is a measure of the ratio of gravitational to frictional forces acting on the fluid. The dimensionless horizontal acceleration, Q , gives the ratio of horizontal to gravitational accelerations. The final parameter, β , is the initial aspect ratio of the fluid ($\beta \rightarrow 0$ implying container width \gg initial depth of fluid when it was in a state of hydrostatic equilibrium). Ga does not enter into the initial condition.

The present results indicate that the period of sloshing is least

sensitive to the value of Ga , and depends most strongly upon the value of β . The β effect is, however, mild, with the sloshing period decreasing somewhat as β increases. Results from an analytical solution (valid for triple limit; $Ga \rightarrow \infty$, $Q \rightarrow 0$, waves are infinitesimal in size) for the sloshing period agree with the present numerical results to the order of one percent.

The rate of viscous damping is fairly insensitive to the values of Q and β . The fluid kinetic energy is found to decay exponentially fast in time, with a modulus of decay which is proportional to $Ga^{-0.33}$. The present results are expected to be valid in the parameter range $Ga \geq 10^3$, $Q \lesssim 1$, and $\beta \sim 1$. The qualitative nature of exponential decay agrees with an analytical solution for viscous, deep water waves of infinitesimal magnitude. The analytical solution, which is valid for the limits $Ga \gg 1$, $Q \rightarrow 0$, and $\beta \rightarrow 0$ (with $\beta \gg$ wave amplitude); predicts a viscous dependency in which the modulus of decay for the displacement of the free surface from its final equilibrium position is proportional to $Ga^{-1/2}$.

Detailed analysis of the transient pressure field indicates that regions of low pressure may form just below the free surface, along the container walls. If the free surface pressure is sufficiently close to the fluid's vapor pressure, cavitation may occur. This event becomes more likely as Q is increased.

ACKNOWLEDGMENTS

The Authors would like to acknowledge the support obtained from the Air Force Office of Scientific Research through Grant #AFOSR-86-0080 for conducting this study. Computation time was supported with a block grant from the Iowa State University Computation Center. Additional support and computational time were made available by the National Science Foundation Presidential Young Investigator Award of Dr. Prusa through Grant #CBT-8451145.

REFERENCES

1. H. Lamb, "Hydrodynamics," 6th ed. (Cambridge University Press/Dover Publications, Inc., New York, 1945), pp. 7, 254, 264, 282, 423, 447, 459, and 623.
2. P. McIver, J. Fluid Mech. 201, 243 (1989).
3. P. McIver and S. R. Smith, J. Engng. Maths. 21, 139 (1987).
4. Z. C. Feng and P. R. Sethna, J. Fluid Mech. 199, 495 (1989).
5. F. Simonelli and J. P. Gollub, J. Fluid Mech. 199, 471 (1989).
6. S. J. Hogan, J. Fluid Mech. 96, 417 (1980).
7. D. H. Peregrine, "Annual Review of Fluid Mechanics," (Annual Reviews, Inc., 1983), p. 149.
8. P. Roache, "Computational Fluid Dynamics," (Hermosa Publishers, Albuquerque, 1976), p. 194, 240.
9. F. H. Harlow and J. E. Welch, Phys. Fluids 8, 2182 (1965).
10. F. H. Harlow and J. E. Welch, Phys. Fluids 9, 842 (1966).
11. C. W. Hirt, B. D. Nichols, and N. C. Romero, Los Alamos Scientific Laboratory, Tech. Rep. LA-5852 (1975).
12. C. W. Hirt and B. D. Nichols, J. Comput. Phys. 39, (1981), 201.
13. V. J. Slabinski, Comsat Tech. Review 8, (1978), 1.
14. J. Prusa and L. S. VandeKamp, Tech. Paper ASME 85-HT-12, (1985).
15. A. C. Kassinos and J. Prusa, to be submitted for publication, Iowa State University Tech. Report, 1989.
16. L. S. Yao and J. Prusa, "Advances in Heat Transfer 19," (Academic Press, Inc., San Diego, 1989), p. 1.

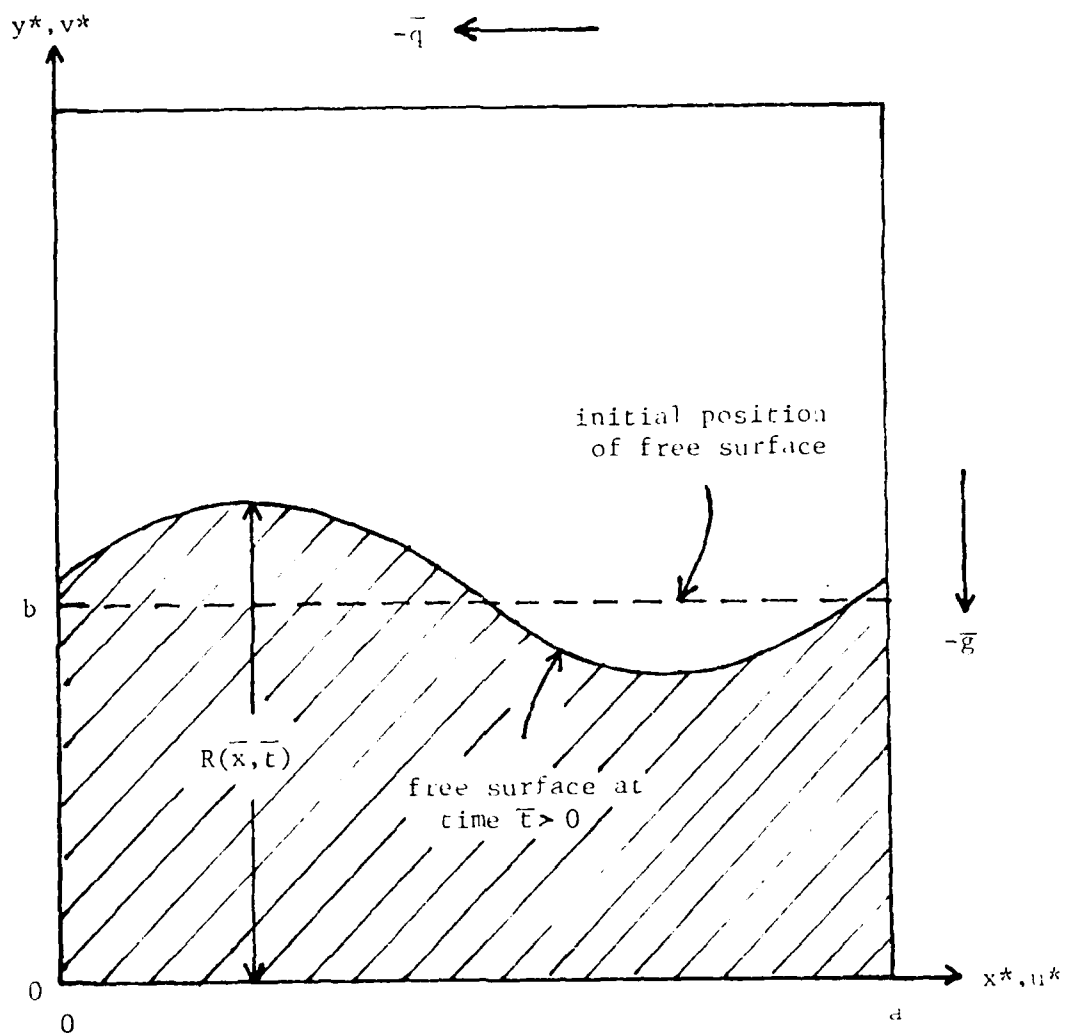


Figure 1. Geometry of the two-dimensional viscous sloshing model.

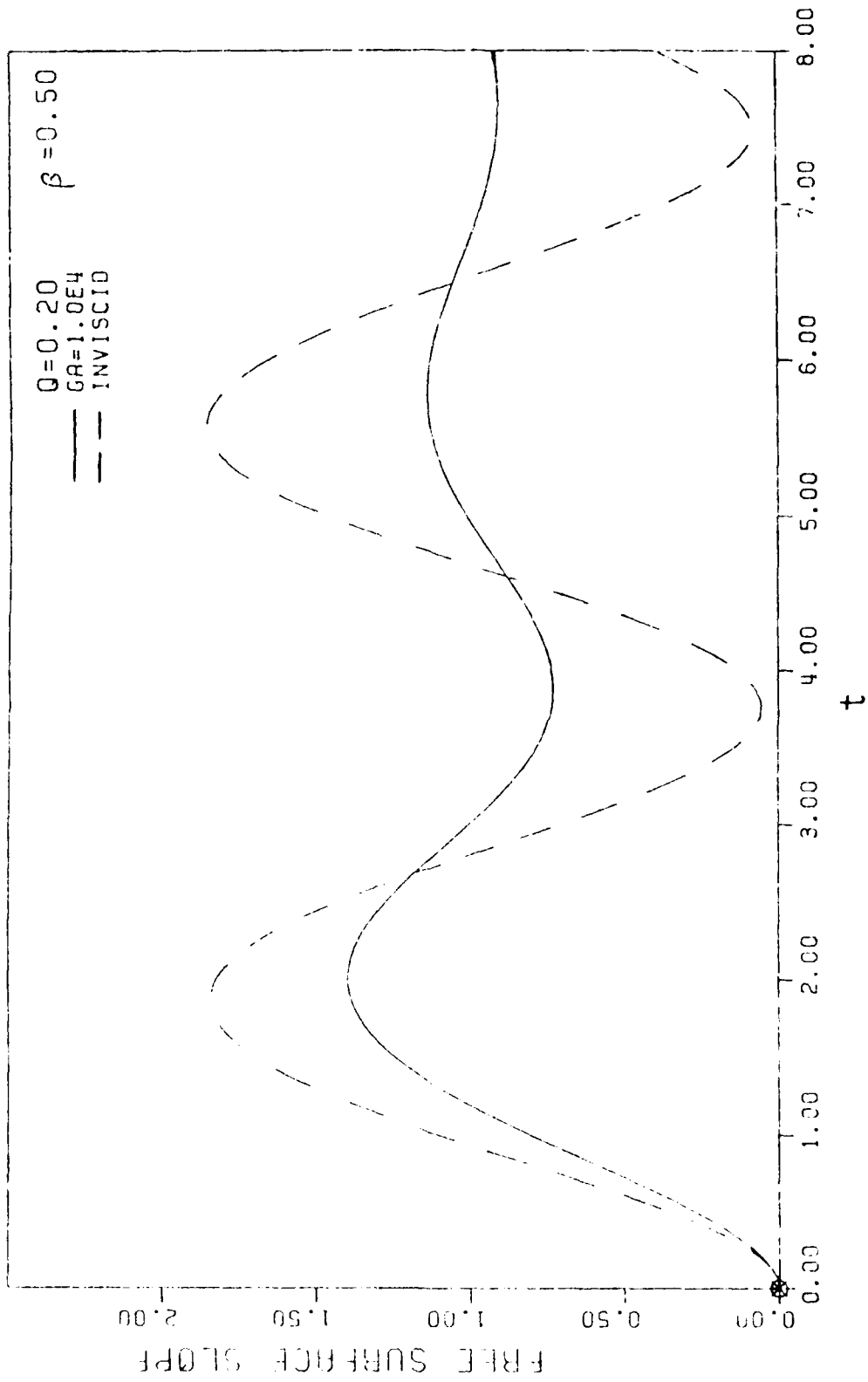


Figure 2. Comparison of the potential and viscous flow models for slope of the free surface as a function of time $Q = 0.2$ and $\beta = 0.5$.

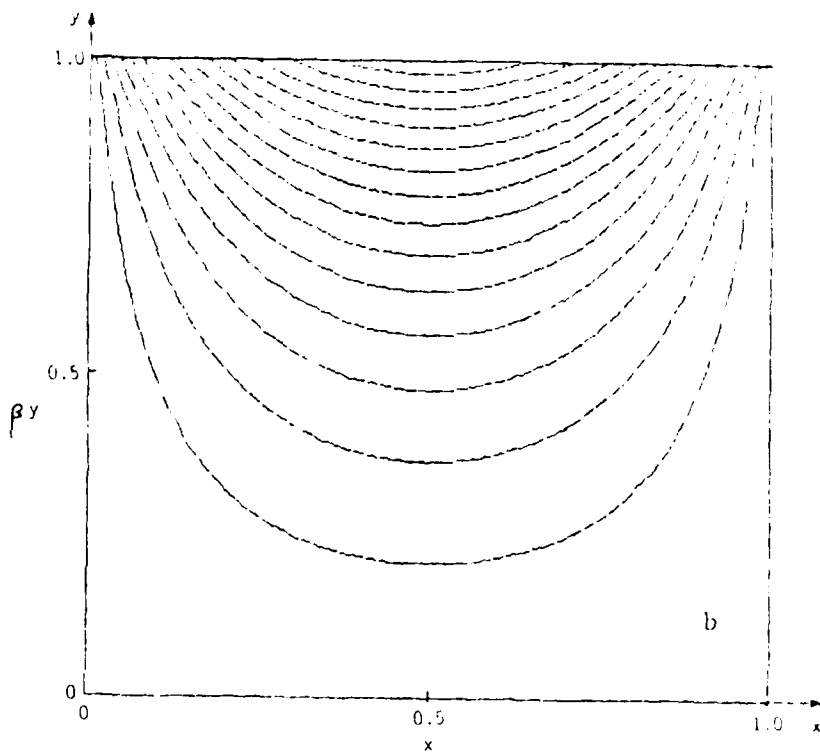
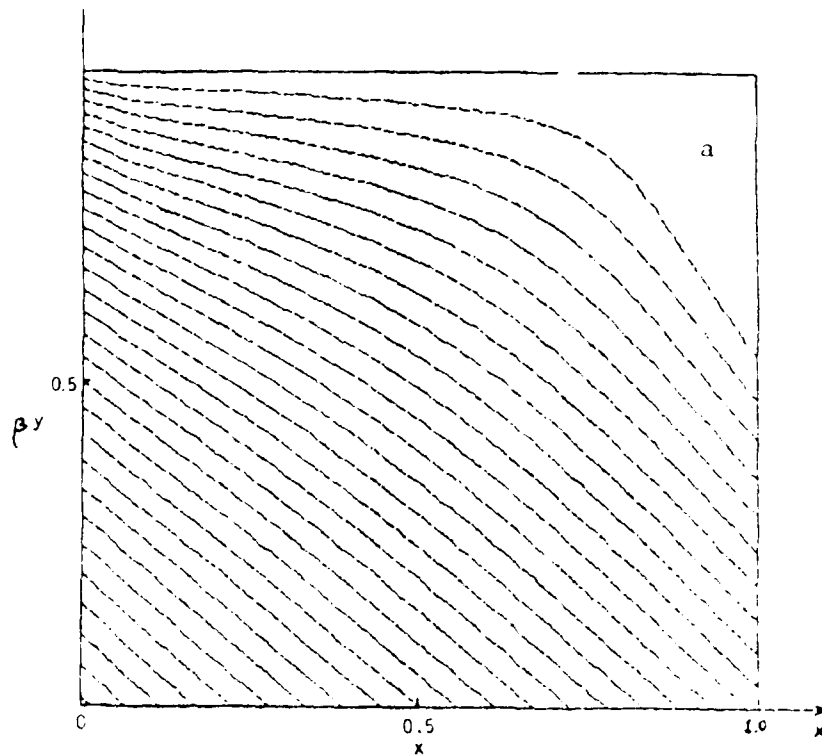


Figure 3. Initial conditions for $Q = 1$ and $\beta = 1$. (a) pressure field, $\Delta p = 0.05$, (b) streamfunction field, $\Delta f = 0.025$.

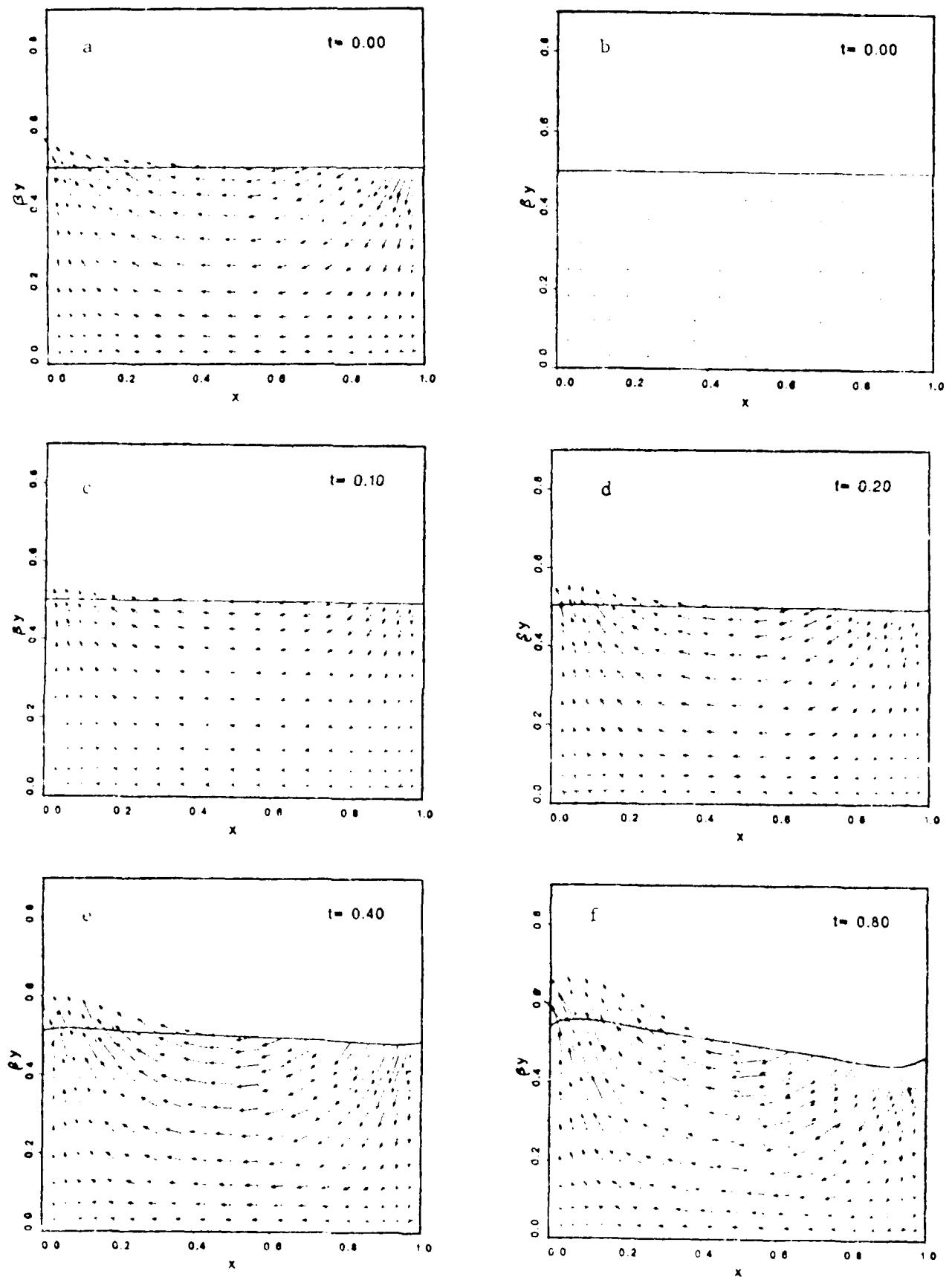


Figure 4. Transient development of the velocity field for $Ga = 10^4$, $Q = 0.2$, and $\beta = 0.5$. (a) initial velocity field as given by equations (8c,d). (b-1) velocity field $\vec{U} = (u\vec{i} + v\vec{j})t$.

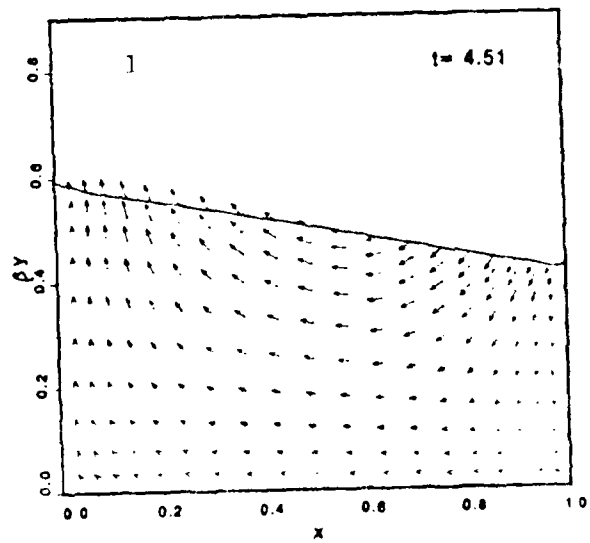
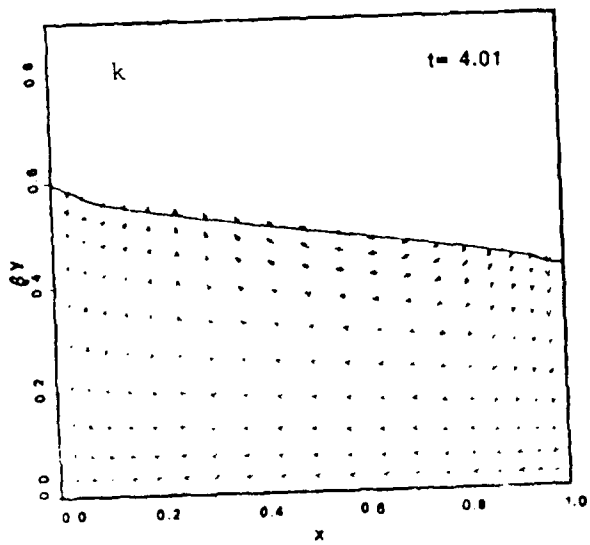
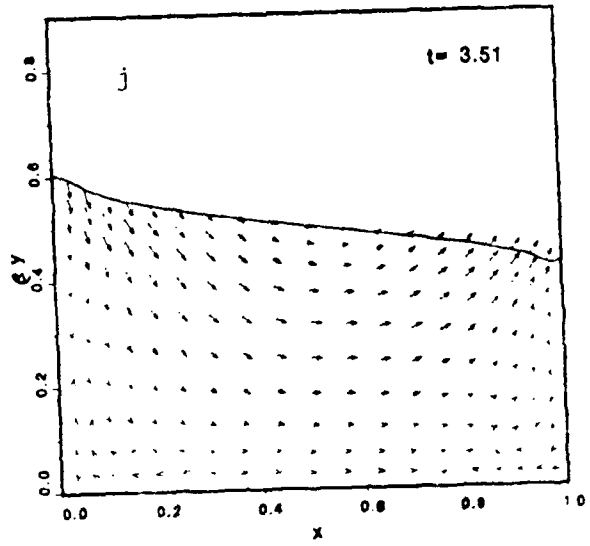
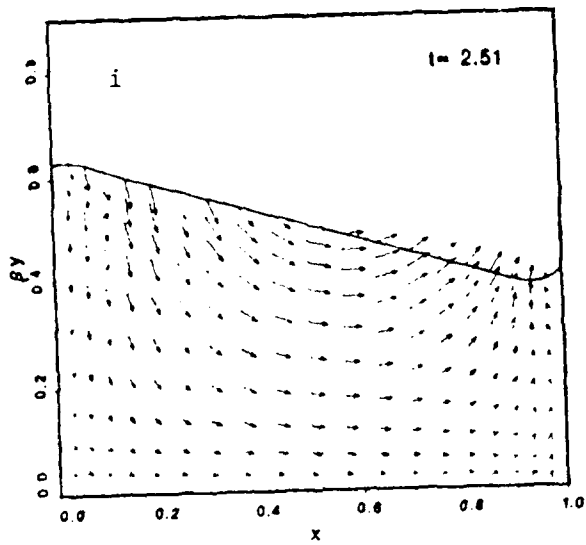
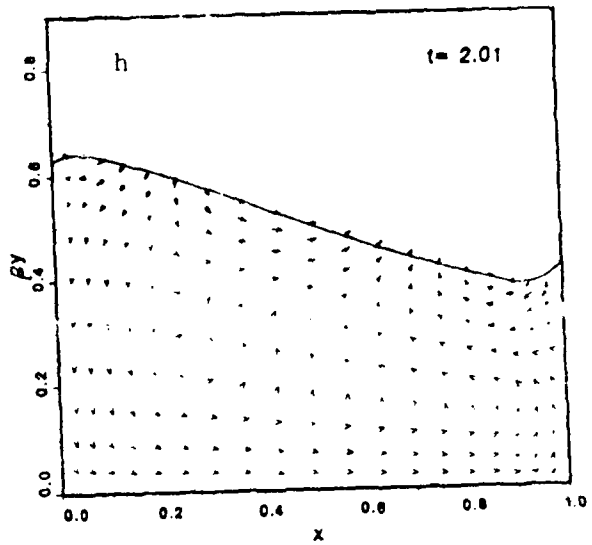
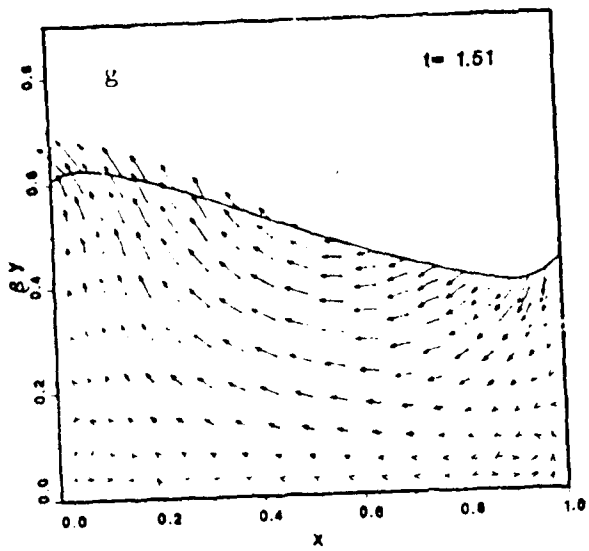


Figure 4. Transient development of the velocity field for $Ga = 10^4$, $Q = 0.2$, and $\beta = 0.5$. (a) initial velocity field as given by equations (8c,d). (b-l) velocity field $\vec{U} = (u\vec{i} + v\vec{j})t$.

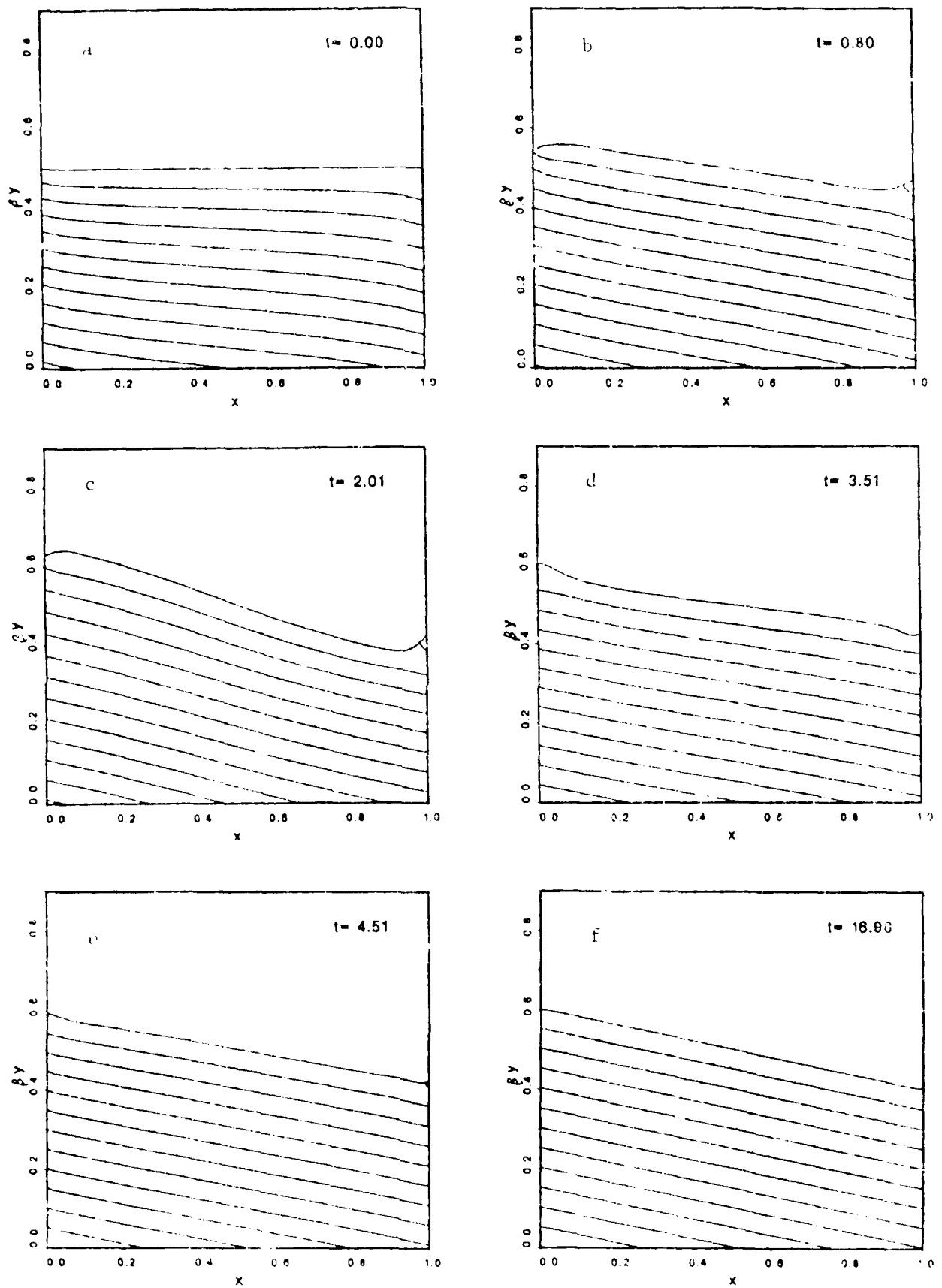


Figure 5. Transient development of the pressure field for $Ga = 10^4$, $Q = 0.2$, and $\beta = 0.5$.

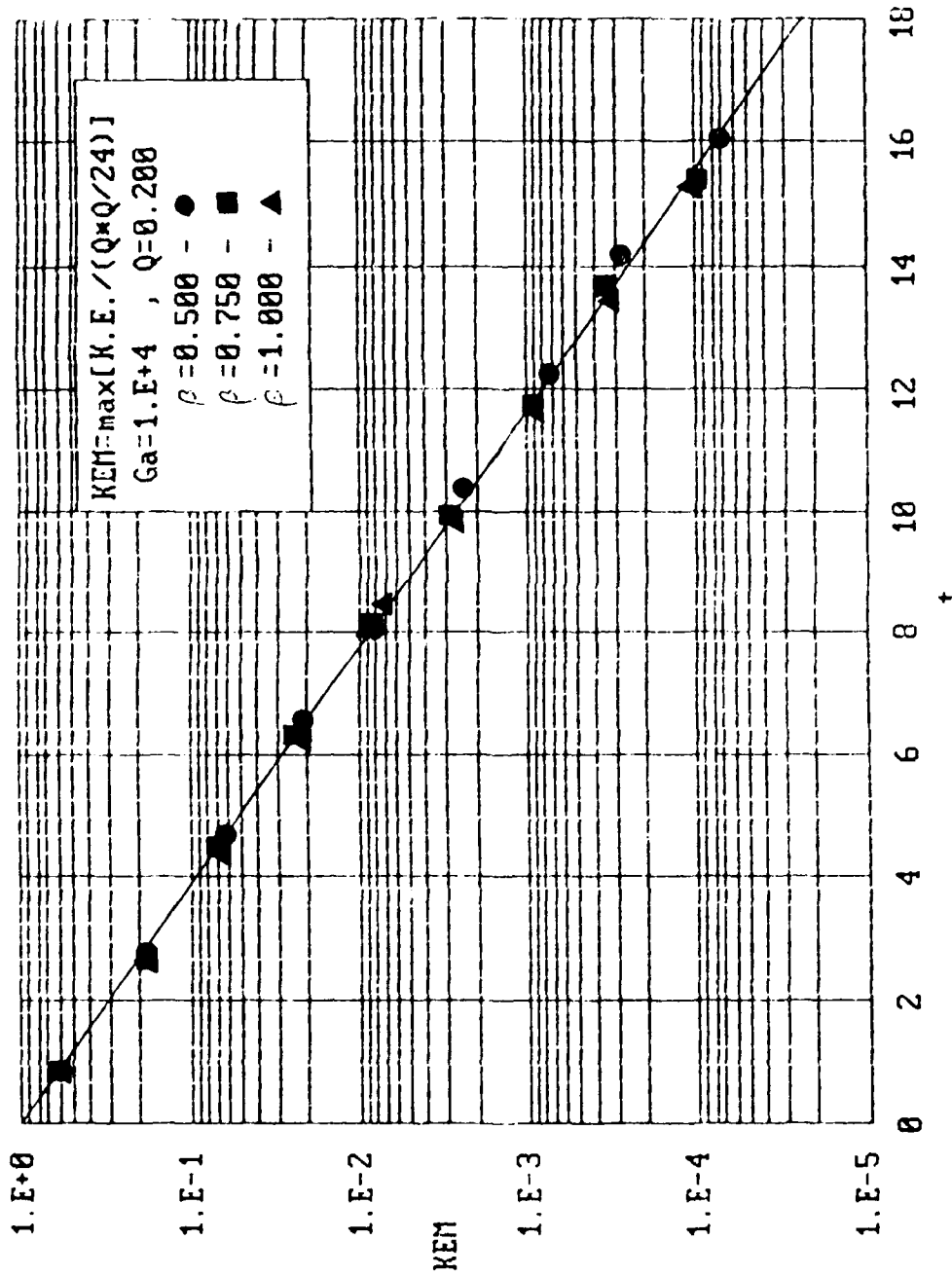


Figure 6. Effect of initial liquid aspect ratio on the rate-of viscous damping. $Ga = 10^4$ and $Q = 0.2$.

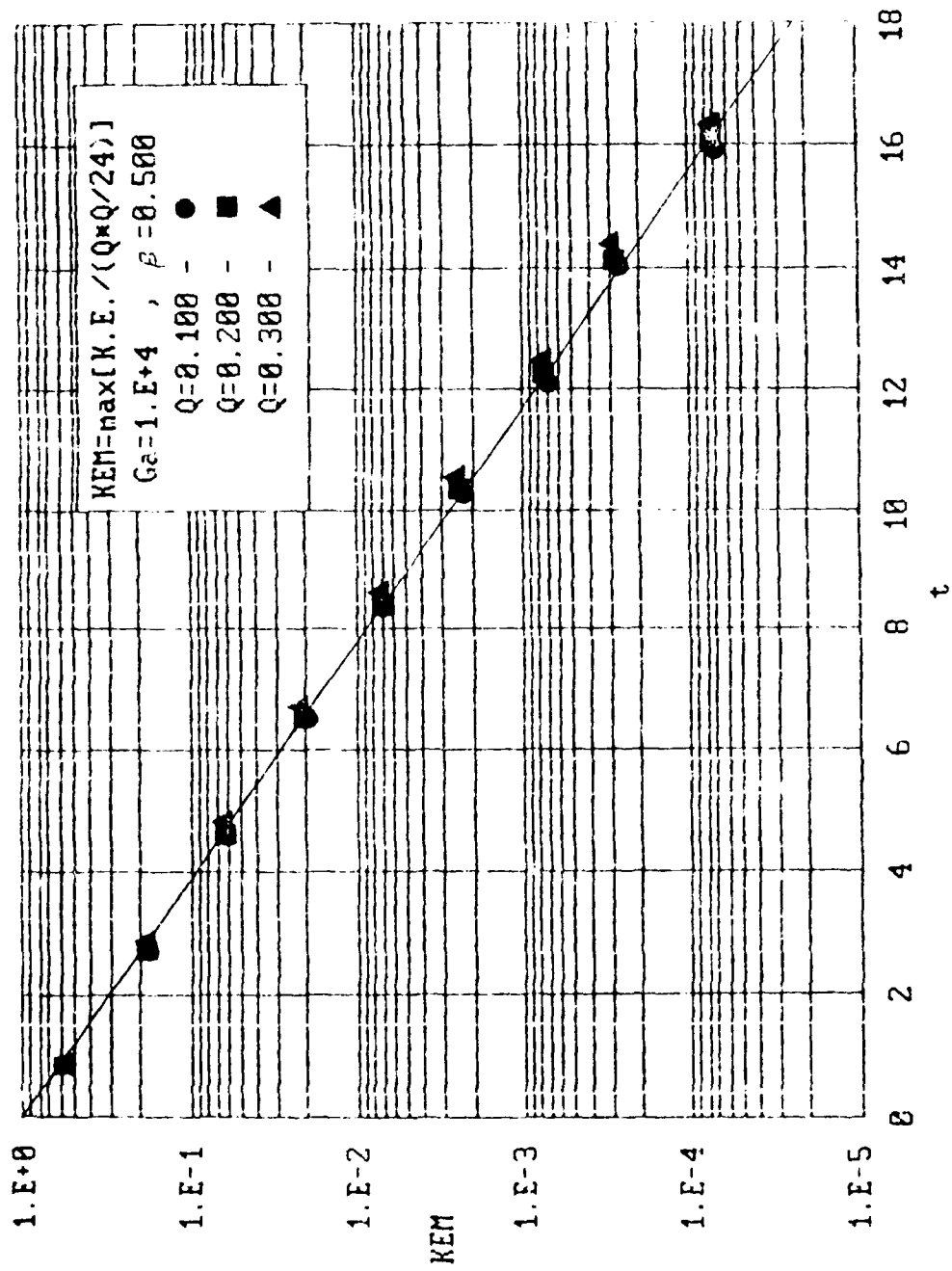


Figure 7. Effect of horizontal acceleration on the rate of viscous damping.
 $Ga = 10^4$ and $\beta = 0.5$.

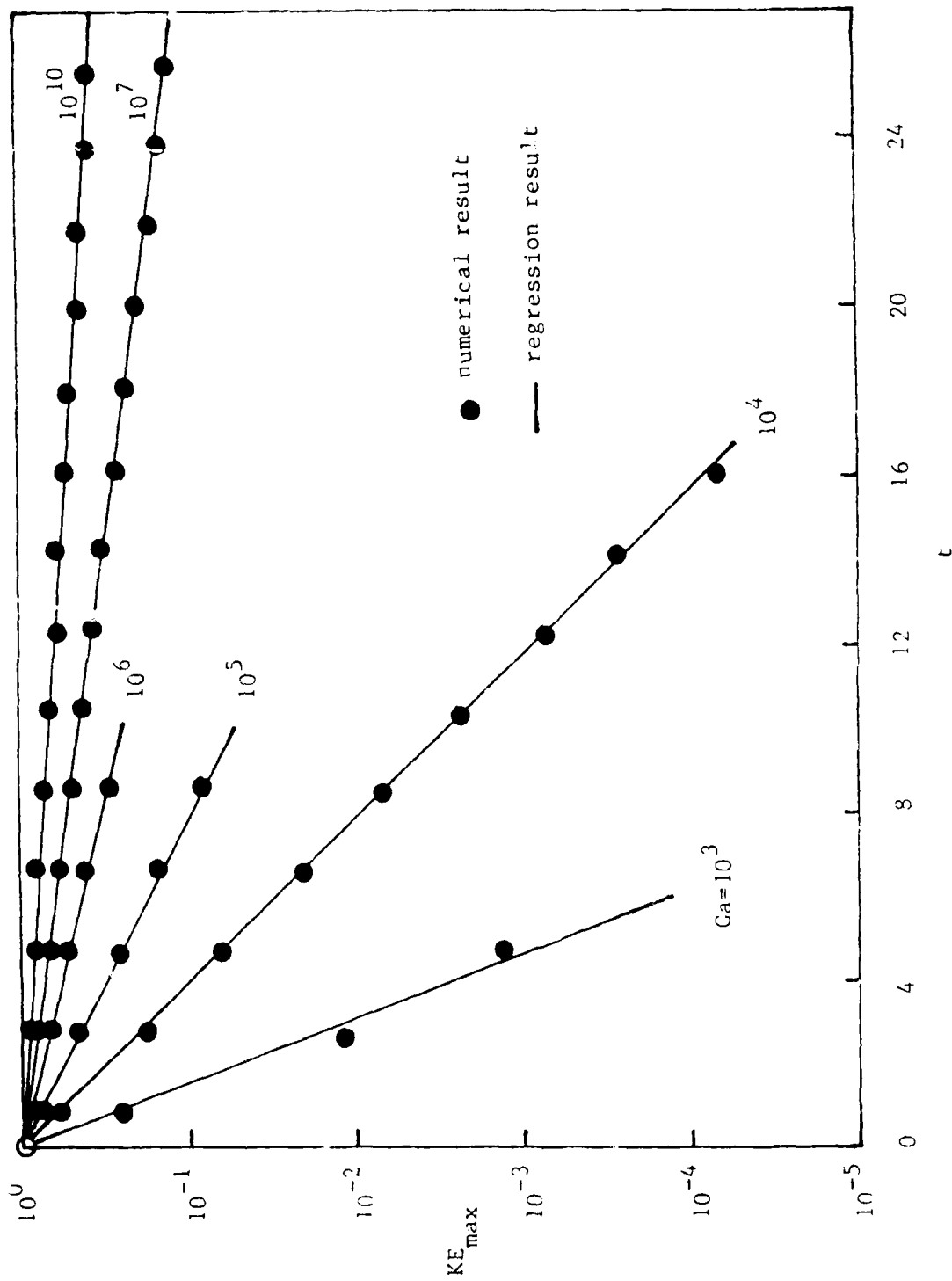


Figure 8. Effect of Galileo number on the rate of viscous damping. $\Omega = 0.2$ and $\beta = 0.5$.

APPENDIX G

THREE-DIMENSIONAL VISCOUS
SLOSH ANALYSIS

Study of 3-D Viscous Sloshing in Spherical Containers

A. C. Kassinos J. M. Prusa

18 Sept 1989

Abstract

A model is developed to describe the motion of a viscous fluid within a partially filled moving spherical container. The container is undergoing a motion characteristic of that experienced by spin-stabilized space vehicles. The incompressible three dimensional Navier-Stokes equations are cast into a frame appropriate for the description of the fluid motion and solved using a numerical technique. The model is presented in detail and sample calculations are given.

1 INTRODUCTION

The sloshing of a viscous incompressible fluid within a partially filled moving spherical container is being considered here. The fluid sloshing is induced by changes that occur in the equilibrium pressure field within the fluid as a result of the motion of the container. The container is assumed to be undergoing a general motion, characteristic of that experienced by spin-stabilized space vehicles.

The present work is motivated by the need to describe the complex motion that occurs in liquid stores that are carried aboard spin-stabilized spacecraft. Certain configurations of the STAR-48 series of communication satellites have consistently demonstrated a nutational instability during the perigee burn. After launching from the space shuttle the satellite's power assist module fires its thruster to move the satellite out to a geosynchronous orbit. Sinusoidal oscillations about the pitch and yaw axis of the spacecraft, which have the same frequency but are out of phase by 90 degrees, have been observed to occur shortly after the application of this sudden thrust. The vector combination of these two vibrations gives rise to a nutating motion about the spin axis of the spacecraft which results in the destabilization of the vehicle. It is believed that the nutating motion is initiated and sustained by the sloshing that occurs in the liquid stores in response to the sudden axial thrust. The immediate problem has been traditionally resolved by severely restricting the motion of the fluid through the use of baffles. However, the cause of the problem has remained obscure because the internal fluid motion is very difficult to analyze.

The analysis of the dynamic behavior of fluids in moving containers presents a difficult task. In general the modelling of the fluid motion requires the use of non-inertial coordinate systems, thus resulting in a complicated set of governing equations. The presence of a free surface, another non-linearity, introduces additional modelling complications. The domain on which the governing equations are solved, which is determined by the position of the free surface, is not known a priori and has to be determined as part of the solution. In 1881 Stearne [1]¹ published a theoretical result for the irrotational spin-up of an infinitely deep liquid. Lamb [2], in 1945, used a linearized analytical method to determine the mode shapes and characteristic frequencies associated with the small amplitude irrotational sloshing of a liquid in a rectangular container. The rapid developments in the space and missile technologies that took place in the early 1960's spurred an explosive interest in understanding sloshing phenomena which lasted for approximately a decade. Numerous papers were published during this era, the majority of which expanded on the analytical work by Lamb to include other geometries [3,4,5], or non-linear effects [6,7,8]. The effects of viscous damping were studied experimentally for cylindrical and spherical containers [8,9], although the use of baffles as damping devices dominated the majority of the experimental work at the time. A comprehensive summary of most of this early work can be found in [9].

More recently, in 1983, a report published by Sandia National Laboratories [10] deals with the solution of the three dimensional Navier-Stokes equations for a cylindri

¹Numbers in brackets designate References at the end of the paper.

cal canister filled with fluid and undergoing spinning and nutating motions. The model is simplified due to the absence of a free surface. In addition, only steady state solutions of highly viscous fluids in an aeroballistic frame of reference are considered.

A general model is presented here which may be used to study sloshing phenomena under a variety of conditions. It allows for general translational and rotational motions of the container as well as superimposed small amplitude vibrations. A free surface tracking coordinate transformation technique is presented which allows the free surface to be modelled under a variety of sloshing conditions without any modifications in the model.

2 MATHEMATICAL MODEL

The sloshing of a viscous fluid inside a moving spherical container is modelled using first principles. Equations describing the conservation of mass and linear momentum are formulated in a coordinate system that is moving along with the container. The selection of a body fixed coordinate system to describe the fluid motion was based on the simplicity of the resulting form of the boundary conditions and on the straightforward interpretation of the numerical solution.

The motion of a fluid particle in an inertial frame of reference can be described by the Navier-Stokes equations. The incompressible three dimensional form of these equations can be written using index notation as

$$\frac{\partial u_n}{\partial t} + u_i \frac{\partial u_n}{\partial x_i} = -\frac{1}{\rho} \frac{\partial p}{\partial x_n} - g_n + \nu \delta_{ij} \frac{\partial^2 u_n}{\partial x_i \partial x_j} \quad (1)$$

$$\frac{\partial u_i}{\partial x_i} = 0 \quad (2)$$

where u_i is the absolute velocity of a fluid particle.

g_i is the acceleration due to gravity.

p is the static pressure.

ρ is the fluid density.

and ν is the kinematic viscosity of the fluid.

In a body fixed coordinate system, information pertaining to the motion of the container is transferred from the boundary conditions to the governing equations as extra terms. These terms are to be determined by considering the motion of the

container, which is assumed to be attached to a moving spacecraft, with respect to the inertial coordinate frame x .

2.1 Linearly Accelerating Coordinate System

The effects of the spacecraft acceleration on the fluid particles within the container are introduced into the governing equations by considering the following transformation. Let x_0 denote a coordinate system that is moving with the spacecraft (see figure 1) and ℓ denote its position with respect to the inertial coordinate system x . Introducing new coordinates and a new velocity defined as,

$$x_{0i} = x_i - \ell_i, \quad (3)$$

$$u_{0i} = u_i - \dot{\ell}_i, \quad (4)$$

into equations (1) and (2), where dotted quantities represent time derivatives, the following set of equations results.

$$\frac{\partial u_{0n}}{\partial t} + u_{0i} \frac{\partial u_{0n}}{\partial x_{0i}} = -\frac{1}{\rho} \frac{\partial p}{\partial x_{0n}} - g_{0n} - \nu \delta_{ij} \frac{\partial^2 u_{0n}}{\partial x_{0i} \partial x_{0j}} \quad (5)$$

$$\frac{\partial u_{0i}}{\partial x_{0i}} = 0 \quad (6)$$

where $g_{0i} = g_i - \ddot{\ell}_i$.

Therefore, with the velocity defined with respect to the non-inertial frame, the effect of linear acceleration is to introduce extra terms into the governing equations. These terms act to modify the body force terms such that g_{0i} now represents the net body force as a result of the spacecraft acceleration and the acceleration due to gravity.

2.2 Spinning Nutating Coordinate System.

The effects of spin stabilization and nutation can be captured by the following transformation. Consider a coordinate system x_1 that is fixed on the spacecraft and thus is spinning and nutating with respect to coordinate system x_0 . The instantaneous angular orientation of the coordinate system x_1 with respect to x_0 can be envisioned to be the result of three successive rotations. The three angles of rotation α_i , $i = 1, 2, 3$, corresponding to the three successive rotations are known as the Euler angles. In a right-hand coordinate system there are a total of twelve possible sequences of rotations that can be used to define the given orientation of the x_1 coordinate system. The zyx convention used here defines the following sequence. The x_0 coordinate system is rotated counterclockwise by an angle α_3 about the $x_{0,3}$ axis as shown in figure (2). The resulting intermediate coordinate system \bar{x}_1 is then rotated counterclockwise by an angle α_2 about the $\bar{x}_{1,2}$ axis to yield the coordinate system labelled \bar{x}_1 . A third counterclockwise rotation by an angle α_1 about the $\bar{x}_{1,1}$ axis yields the desired x_1 system.

The coordinates of any point in x_1 can then be related to its respective coordinates in x_0 by

$$x_{1j} = \alpha_{ij} x_{0j} \quad (7)$$

where α_{ij} represents the transformation tensor containing the metrics and is given in the Appendix. The metrics are obtained from the geometry of figure (2) and are generally products of simple trigonometric functions in terms of the Euler angles α_i .

Introducing a new velocity measured relative to the nutating coordinate system x_1 .

$$u_{1i} = \alpha_{ji} u_{0j} - \dot{\alpha}_{ji} \alpha_{jk} x_{1k} \quad (8)$$

into the governing equations (5.6) yields.

$$\frac{\partial u_{1n}}{\partial t} + u_{1i} \frac{\partial u_{1n}}{\partial x_{1i}} - 2\beta_{rni} u_{1i} - \beta_{t ni} x_{1i} - \beta_{f ni} x_{1i} = -\frac{1}{\rho} \frac{\partial p}{\partial x_{1n}} - g_{1n} - \nu \delta_{ij} \frac{\partial^2 u_{1i}}{\partial x_{1i} \partial x_{1j}} \quad (9)$$

$$\frac{\partial u_{1i}}{\partial x_{1i}} = 0 \quad (10)$$

where $\beta_{r ij} = \dot{\alpha}_{ki} \alpha_{kj}$,

$$\beta_{t ij} = \ddot{\alpha}_{ki} \alpha_{kj}$$

$$\beta_{f ij} = \dot{\alpha}_{ki} \dot{\alpha}_{kj} - \dot{\alpha}_{ki} \dot{\alpha}_{im} \alpha_{km} \alpha_{nj}$$

and $g_{1i} = \alpha_{ij} g_{0j}$.

Consequently, the rotation of the coordinate system x_1 with respect to x_0 results in the appearance of three new types of terms in the governing equations. The term $\beta_{r ni} u_{1i}$ represents the Coriolis acceleration effects experienced by fluid particles as a result of the rotation of the axis. The term $\beta_{f ni} x_{1i}$ represents centrifugal accelerations effects induced by the the axial rotation. The term $\beta_{t ni} x_{1i}$ can be separated into tangential acceleration terms and additional centrifugal acceleration terms.

2.3 Body Fixed Coordinate System

The spherical container enclosing the fluid is assumed to be attached to the flexible frame of a moving spacecraft. Let h_i denote the position vector from the origin of the nutating coordinate system x_1 to the origin of the body fixed coordinate system x_2 which coincides with the center of the spherical container (see figure 2). Since there is no relative rotation between coordinate systems x_1 and x_2 , any changes in the magnitude of h_i are caused by the elasticity of the spacecraft frame. The governing equations in the body fixed coordinate system are obtained by replacing x_1 and u_1 by,

$$x_{2i} = x_{1i} - h_i \quad (11)$$

and,

$$u_{2i} = u_{1i} - \dot{h}_i \quad (12)$$

in equations (9,10) to yield,

$$\frac{\partial u_{2n}}{\partial t} - u_{2i} \frac{\partial u_{2n}}{\partial x_{2i}} - 2\beta_{r_m} u_{2i} - \beta_{t_m}(x_{2i} - h_i) - \beta_{f_m}(x_{2i} - h_i) = -\frac{1}{\rho} \frac{\partial p}{\partial x_{2n}} - g_{2n} + \nu \delta_{ij} \frac{\partial^2 u_{2n}}{\partial x_{2i} \partial x_{2j}} \quad (13)$$

$$\frac{\partial u_{2i}}{\partial x_{2i}} = 0 \quad (14)$$

where $g_{2i} = g_{1i} - \ddot{h}_i$.

As a result of this transformation, the body force term g_{2i} is modified to reflect the acceleration experienced by a fluid particle within the container as a result of the motion induced by the elastic spacecraft frame.

2.4 Self Adjusting Body Fixed Coordinate System.

All the physical principles needed to describe the motion of a fluid particle within the container are embodied in equations (13,14). However, the presence of a free fluid surface introduces a nonlinearity into the model since it represents a boundary of unknown shape and position that has to be determined as part of the solution. In order to describe the motion of the free surface by a kinematic condition, its position F needs to be expressed as a function of time, t , as well as two of the three independent spatial coordinates x_2 . The choice of such a pair of spatial coordinates must be carefully considered to ensure that F remains single valued everywhere.

Since the initial value of u_3 is somewhat arbitrary, h_2 can be taken to be equal to zero without any loss in generality. This would imply that the center of the spherical container lies in the $x_{11} - x_{13}$ plane. For a container that is rotating about the x_{13} axis the direction of the motion of the bulk of the fluid will be along the $x_{21} - x_{23}$ plane. However, neither of the two likely choices, $F(t, x_{21}, x_{22})$ or $F(t, x_{22}, x_{23})$, can ensure that F will remain single valued. Consequently, a self adjusting body fixed coordinate system, labelled x_3 in figure (3), is introduced. The coordinate system x_3 is defined by a single clockwise rotation by an angle ϕ about the x_{22} axis. With the position of the free surface described by $F(t, x_{22}, x_{23})$ the value of ϕ is adjusted to ensure that F remains single valued.

The coordinates of a point with respect to the self adjusting frame x_3 can be determined from its coordinates with respect to frame x_2 from,

$$x_{3i} = s_{ji} x_{2j} \quad (15)$$

where s_{ij} is the transformation tensor given in the Appendix.

Replacing x_2 in the governing equations and introducing a new velocity,

$$u_{3i} = s_{ji} u_{2j} \quad (16)$$

yields the following set of governing equations in the self adjusting frame.

$$\frac{\partial u_{3n}}{\partial t} - (u_{3i} - f_{ik} x_{3k}) \frac{\partial u_{3n}}{\partial x_{3i}} - (2\lambda_{rni} - f_{ni}) u_{3i} - \lambda_{1ni} x_{3i} - \lambda_{2ni} h_i = - \frac{1}{\rho} \frac{\partial p}{\partial x_{3n}} - g_{3n} - \nu \delta_{ij} \frac{\partial^2 u_{3n}}{\partial x_{3i} \partial x_{3j}} \quad (17)$$

$$\frac{\partial u_{3i}}{\partial x_{3i}} = 0 \quad (18)$$

where $f_{ij} = \dot{s}_{ni} s_{nj}$.

$$\lambda_{r1j} = \mathcal{J}_{rnm} s_{ni} s_{mj}$$

$$\lambda_{1ij} = (\mathcal{J}_{fnm} - \mathcal{J}_{tnm}) s_{ni} s_{mj}$$

$$\lambda_{2ij} = (\mathcal{J}_{fnj} - \mathcal{J}_{tnj}) s_{ni}$$

and $g_{3i} = s_{ji} g_{2j}$.

The new terms appearing in the governing equations are due to the rotation of the axis. The x_3 coordinate system is rotating with respect to the x_2 system but the velocity u_3 is still measured with respect to x_2 . Thus, the Coriolis and the convection terms are modified to reflect this.

2.5 Poisson Equation for Pressure.

The pressure distribution within the fluid can be determined by the solution of a Poisson equation which is derived from the momentum equations. Differentiating

equation (17) with respect to x_{3n} and contracting on n yields.

$$\frac{1}{\rho} \delta_{ij} \frac{\partial^2 p}{\partial x_{3i} \partial x_{3j}} = 2 [J_{12}(u_{31}, u_{32}) - J_{13}(u_{31}, u_{33}) - J_{22}(u_{32}, u_{33})] \\ - \left[2\lambda_{r_{ni}} \frac{\partial u_{3i}}{\partial x_{3n}} - \delta_{ni} \lambda_{1_{ni}} \right] \\ - \left[\frac{\partial D}{\partial t} - D^2 - (u_{3i} - f_{ik} x_{3k}) \frac{\partial D}{\partial x_{3i}} - \nu \delta_{ij} \frac{\partial^2 D}{\partial x_{3i} \partial x_{3j}} \right] \quad (19)$$

where D represents the dilatation and is defined by

$$D = \frac{\partial u_{3i}}{\partial x_{3i}} \quad (20)$$

and the two dimensional Jacobians $J_{ij}(A, B)$ are defined by

$$J_{ij}(A, B) = \left(\frac{\partial A}{\partial x_{3i}} \frac{\partial B}{\partial x_{3j}} - \frac{\partial B}{\partial x_{3i}} \frac{\partial A}{\partial x_{3j}} \right)$$

The dilatation terms in equation (19) which are ideally zero for an incompressible fluid are retained in the above derivation because they are used to ensure the stability of the numerical method.

2.6 Free Surface Conditions

The motion of the free surface is determined by a kinematic condition. This condition, which was first introduced by Lamb [11], is based on the assumption that fluid particles that lie on the free surface must remain there. For the geometry of the present problem the position of the free surface $F(t, x_{32}, x_{33})$ can be calculated from,

$$\frac{\partial F}{\partial t} = (u_{32} - f_{2k} x_{3k}) - (u_{32} - f_{2k} x_{3k}) \frac{\partial F}{\partial x_{32}} - (u_{33} - f_{3k} x_{3k}) \frac{\partial F}{\partial x_{33}} \quad (21)$$

However, the kinematic condition as formulated above is inviscid in nature. Consequently, its use is inappropriate in the highly viscous region adjacent to the container walls. The motion of the free surface along the container wall is determined by a local momentum balance which incorporates viscous and surface tension effects (see [12] for details).

The dynamic conditions at the free surface are obtained by requiring that the normal and tangential stress components be continuous across the liquid-vapor interface. The viscous stress components in the vapor phase are several orders of magnitude smaller than those in the liquid phase. Consequently, these terms are ignored, and the resulting dynamic conditions at the free surface are expressed in terms of a local curvilinear coordinate system as,

normal stress:

$$p - p_o = 2\mu \frac{\partial U_n}{\partial n} \quad (22)$$

tangential stresses:

$$\frac{\partial U_n}{\partial \tau_2} - \frac{\partial U_{\tau_2}}{\partial n} - \kappa_2 U_{\tau_2} = 0 \quad (23)$$

$$\frac{\partial U_n}{\partial \tau_3} - \frac{\partial U_{\tau_3}}{\partial n} - \kappa_3 U_{\tau_3} = 0 \quad (24)$$

where U_n denotes the velocity component normal to the free surface and U_{τ_2} and U_{τ_3} the two velocity components tangent to the surface. The normal, n , and tangential coordinates, τ_2 and τ_3 along the free surface are based on the following set of unit vectors, which are defined in terms of the unit vectors of the x_3 coordinate system, \bar{e}_i , as,

$$\bar{n} = \frac{\bar{e}_{31} - F_2 \bar{e}_{32} - F_3 \bar{e}_{33}}{\sqrt{1 - F_2^2 - F_3^2}} \quad (25)$$

$$\bar{\tau}_2 = \frac{F_2 \bar{e}_{31} - \bar{e}_{32}}{\sqrt{1 - F_2^2}} \quad (26)$$

$$\bar{\tau}_3 = \frac{F_3 \bar{e}_{31} - F_2 F_3 \bar{e}_{32} - (1 - F_2^2) \bar{e}_{33}}{\sqrt{1 - F_2^2 - F_3^2} \sqrt{1 - F_2^2}} \quad (27)$$

The κ_i represents the local curvatures of the free surface which are defined by

$$\kappa_i = \frac{F_i}{(1 - F_i^2)^{3/2}} \quad (28)$$

with.

$$F_i = \frac{\partial F}{\partial x_{3i}} \quad \text{and} \quad F_{ii} = \frac{\partial^2 F}{\partial x_{3i}^2}.$$

The dynamic free surface conditions and the continuity equation are used to provide boundary conditions for the pressure and the three velocity components along the free surface.

2.7 Initial and Boundary Conditions

One of the advantages of the body fixed coordinate system is that the appropriate boundary conditions can be easily determined. The velocity, u_{3i} , has been defined so that the no-slip condition for a viscous fluid along a wall retains its familiar form.

$$u_{3i} = 0 \quad (\text{along the container wall}). \quad (29)$$

The pressure boundary conditions along the container wall are obtained by forming an expression for the normal gradient along the wall from the momentum equations.

The normal stress condition along the free surface is further simplified by neglecting the viscous terms. Thus at the free surface,

$$p - p_o = 0 \quad (30)$$

where p_o represents the pressure of the vapor phase.

Initially, at time $t = 0^-$, the fluid is motionless and the pressure is in equilibrium with the net body force experienced by the fluid as a result of the acceleration due to gravity and linear and centrifugal acceleration components resulting from the motion of the container. The initial condition equations are obtained by setting,

$$u_{3i} = 0$$

in the governing equations (17,18,19) to yield

$$\frac{1}{\rho} \frac{\partial p}{\partial x_{3n}} = -g_{3n} - \lambda_{1n} x_{3i} - \lambda_{2n} h_i \quad (31)$$

$$\frac{1}{\rho} \delta_{ij} \frac{\partial^2 p}{\partial x_{3i} \partial x_{3j}} = \delta_{ij} \lambda_{1ij} \quad (32)$$

The above equations can be solved to determine the pressure distribution within the fluid under static conditions.

At time $t = 0$, the motion of the container is altered such that the net body force experienced by the fluid as a result of the container motion is different than that present at time $t = 0^-$. Since the fluid is modelled as incompressible the pressure field adjusts to the new conditions instantaneously. Thus, at time $t = 0^+$, a new pressure distribution exists within the fluid. Equations (31,32) can be used to determine the pressure field at $t = 0^+$ since the fluid is still motionless.

2.8 Nondimensionalization of the Governing Equations

The governing equations are nondimensionalized according to the following characteristic scales:

- length $L \sim a$
- time $\tau \sim \sqrt{a/g}$
- velocity $\mathcal{U} \sim \sqrt{ag}$

where a represents the radius of the spherical container and g the acceleration due to gravity. The characteristic velocity scale, \mathcal{U} , is equivalent to the propagation speed determined from shallow water wave theory. A nondimensional pressure is defined by,

$$p = \frac{\bar{p} - \bar{p}_0}{\rho a g} \quad (33)$$

The dimensionless group that emerges from the nondimensionalization is the Galileo number, Ga , defined as,

$$Ga = \frac{a^3 g}{\nu^2}$$

which represents a ratio of the gravitational to the viscous effects. The dimensionless Galileo number can also be viewed as being analogous to the square of a Reynolds number based on the characteristic velocity scale, \mathcal{U} .

3 Numerical Method

The three dimensional equations of motion developed in the previous section are solved using a numerical method to determine the motion of the fluid within the spherical container. An elliptic grid is used that conforms to the irregular, time dependent shape of the fluid region. The governing equations are expressed in terms of the generalized grid coordinates and solved using a second order accurate finite difference method. An outline of the numerical method and the computational procedure is given.

3.1 Generalized Grid Coordinates

The accuracy of a numerical solution is strongly dependent on the selection of the computational grid. This is particularly critical for moving boundary problems where the shape and position of the free boundary are generally unknown and are determined as part of the solution.

Generalized grid coordinates, ξ_i , are generated using the elliptic system of equations proposed by Shanks and Thompson [13] and independently by Thomas and Middlecoff [14],

$$\nabla^2 \xi_i = Q_i(\xi_1, \xi_2, \xi_3) \quad \nabla \xi_i^2 = 0 \quad \text{for } i=1,2,3 \quad (3.1)$$

where the functions Q_i are adjusted to obtain the desired grid point distribution.

The irregularly shaped fluid region is mapped on to a cube, the dimensions of which, $\xi_{1, \max}$, $\xi_{2, \max}$, and $\xi_{3, \max}$, are selected so that the distance between any two

adjacent grid points in the computational domain is equal to unity. This is done to simplify the finite difference representations.

The mapping of the physical region onto the computational domain is depicted in figure (4). The point defined by the intersection of the x_{31} axis with the free surface is mapped onto the face of the cuboid defined by $\xi_1 = 0$. The boundary along the container wall is mapped onto the opposite face of the cuboid at $\xi_1 = \xi_{1,max}$. The x_{31} axis is mapped onto the $\xi_2 = 0$ plane while the free surface onto the $\xi_2 = \xi_{2,max}$ plane. Finally, a cut is taken along the plane defined by the x_{31} and the positive x_{32} axis and this section is mapped onto the $\xi_3 = 0$ and the $\xi_3 = \xi_{3,max}$ faces of the cuboid.

The procedure followed in solving these equations is similar to the one described in 14. Equations (34) are transformed into the computational domain by interchanging the role of dependent and independent coordinates and solved using a finite difference method. The only significant deviation from the procedure described in 14 is that an algebraic equation is first used to approximate the grid to the desired degree of orthogonality along the boundaries. The control functions Q are then determined explicitly from the approximated grid values. This is done to save computational effort by taking advantage of the known geometrical features of the physical region.

Governing Equations

The governing equations are transformed in terms of the generalized coordinates ξ to take the following form:

momentum equations:

$$\begin{aligned} \frac{\partial u_{3n}}{\partial t} - (\dot{\eta}_i - \eta_{i,j} u_{3j} - \eta_{i,j} f_{jk} x_{3k}) \frac{\partial u_{3n}}{\partial \xi_i} \\ - (2\lambda_{r,m} + f_{nr}) u_{3i} - \lambda_{1,ni} x_{3i} - \lambda_{2,ni} h_i = \\ - \eta_{i,n} \frac{\partial p}{\partial \xi_i} - g_{3n} - \frac{1}{\sqrt{Gd}} \left(\gamma_{ij} \frac{\partial^2 u_{3n}}{\partial \xi_i \partial \xi_j} - \Gamma_i \frac{\partial u_{3n}}{\partial \xi_i} \right) \end{aligned} \quad (35)$$

continuity:

$$\eta_{j,i} \frac{\partial u_{3i}}{\partial \xi_j} = 0 \quad (36)$$

pressure equation:

$$\begin{aligned} \eta_{k,i} \eta_{n,j} \delta_{ij} \frac{\partial^2 p}{\partial x_{ik} \partial x_{ln}} - \eta_{n,i,j} \delta_{ij} \frac{\partial p}{\partial \xi_n} = 2\eta_{n,1} \eta_{m,2} \dot{J}_{nm} (u_{31}, u_{32}) \\ + 2\eta_{n,2} \eta_{m,3} \dot{J}_{nm} (u_{31}, u_{33}) + 2\eta_{n,2} \eta_{m,3} \dot{J}_{nm} (u_{32}, u_{33}) \\ + \left(2\eta_{i,n} \lambda_{r,m} \frac{\partial u_{3i}}{\partial \xi_j} - \lambda_{i,n} \delta_{ij} \right) \left(\frac{\partial p}{\partial t} - S_p \right) \end{aligned} \quad (37)$$

where,

$$\dot{J}_{nm} = \delta_{nm} \dot{\eta}_i + \eta_{i,m} \dot{\eta}_n$$

$$\Gamma_i = \delta_{i,m} \eta_{i,m}$$

the pressure equation spatial dilatation source term, S_p , is given by,

$$S_p = D^2 - (\dot{\eta}_i - \eta_{i,j}u_{3j} - \eta_{i,j}f_{jk}x_{3k}) \frac{\partial D}{\partial \xi_i} \quad (38)$$

$$- \frac{1}{\sqrt{Ga}} \left(\gamma_{ij} \frac{\partial^2 D}{\partial \xi_i \partial \xi_j} - \Gamma_i \frac{\partial D}{\partial \xi_i} \right) \quad (39)$$

with the dilatation, D , given by,

$$D = \eta_{j,3} \frac{\partial u_{3j}}{\partial \xi_j} \quad (40)$$

the two dimensional Jacobians in terms of ξ_i defined by,

$$J_{i,j}(A, B) = \left(\frac{\partial A}{\partial \xi_i} \frac{\partial B}{\partial \xi_j} - \frac{\partial B}{\partial \xi_i} \frac{\partial A}{\partial \xi_j} \right)$$

and the grid transformation metrics given by,

$$\dot{\eta}_i = \frac{\partial \eta_i}{\partial t}$$

$$\eta_{i,j} = \frac{\partial \eta_i}{\partial \xi_j}$$

$$\eta_{k,ij} = \frac{\partial^2 \eta_k}{\partial \xi_i \partial \xi_j}$$

The kinematic condition at the free surface, $\xi_2 = \xi_{2,max}$, can be written in terms of the generalized coordinates as,

$$\begin{aligned} \frac{\partial F}{\partial t} &= u_{32} - f_{2k}x_{3k} \\ &- \dot{\eta}_2 - \eta_{2,2}(u_{32} - f_{2k}x_{3k}) - \eta_{2,3}(u_{33} - f_{3k}x_{3k}) \frac{\partial F}{\partial \xi_2} \\ &- \dot{\eta}_3 - \eta_{3,2}(u_{32} - f_{2k}x_{3k}) - \eta_{3,3}(u_{33} - f_{3k}x_{3k}) \frac{\partial F}{\partial \xi_3} \end{aligned} \quad (41)$$

The pressure boundary condition along the container wall, at $\xi_1 = \xi_{1,max}$, is obtained by using the chain-rule to form an expression for the ξ_1 -gradient from the momentum equations. Thus,

at $\xi_1 = \xi_{1 \max}$:

$$\frac{\partial p}{\partial \xi_1} = \left[\lambda_{1 n i} x_{3 i} - \lambda_{2 n i} h_i - g_{3 n} - f_{i k} x_{3 k} \eta_{1 i} \frac{\partial u_{3 n}}{\partial \xi_1} \right] \frac{\partial x_{3 n}}{\partial \xi_1} - \frac{1}{\nu G u} \left[\gamma_{11} \frac{\partial^2 u_{3 i}}{\partial \xi_1^2} - 2\gamma_{12} \frac{\partial^2 u_{3 i}}{\partial \xi_1 \partial \xi_2} - 2\gamma_{13} \frac{\partial^2 u_{3 i}}{\partial \xi_1 \partial \xi_3} - \Gamma_1 \frac{\partial u_{3 n}}{\partial \xi_1} \right] \frac{\partial x_{3 n}}{\partial \xi_1} \quad (42)$$

3.2 Finite Difference Method

The governing equations are approximated using an implicit second order accurate finite difference scheme. Sample difference approximations are given below for some of the terms in the governing equations. The time level is denoted by superscript n while superscript m is used to denote the iteration level. Subscripts i , j , and k , are used to denote the position of a grid point in the ξ_1 , ξ_2 , and ξ_3 directions respectively.

Time derivatives are differenced using a forward difference as in,

$$\frac{\partial u}{\partial t}_{i,j,k}^{n-1,m-1} = \left(\frac{u_{i,j,k}^{n-1,m-1} - u_{i,j,k}^{n,m-1}}{\Delta t} \right) + \mathcal{O}(\Delta t) \quad (43)$$

the diffusion terms are differenced using centered differences of the form,

$$\frac{\partial^2 u}{\partial \xi_1^2}_{i,j,k}^{n-1,m-1} = \left(u_{i-1,j,k}^{n-1,m-1} - 2u_{i,j,k}^{n-1,m-1} + u_{i+1,j,k}^{n-1,m-1} \right) + \mathcal{O}(\Delta L)^2 \quad (44)$$

and the convective terms are differenced using a two-step finite difference of the form,

$$\begin{aligned} A \frac{\partial u}{\partial \xi_1}_{i,j,k}^{n-1,m-1} &= \frac{A}{2} \frac{1}{2} \left[\left(u_{i,j,k}^{n-1,m-1} - u_{i-1,j,k}^{n-1,m-1} \right) + \mathcal{E}_i' \right] \\ &+ \frac{A}{2} \frac{1}{2} \left[\left(u_{i,j,k}^{n,m-1} - u_{i-1,j,k}^{n,m-1} \right) + \mathcal{E}_i'' \right] + \mathcal{O}(\Delta L)^2 \quad (45) \end{aligned}$$

where \mathcal{E}_{fc} and \mathcal{E}_{bc} represent second order correction terms that are added to the upwind differences to obtain centered, second order accurate difference approximations. They are defined by,

$$\mathcal{E}_{fc} = -\frac{u_{i,j,k-1}^{n+1,m} - 2u_{i,j,k}^{n+1,m} + u_{i,j,k+1}^{n+1,m}}{2}$$

$$\mathcal{E}_{bc} = \frac{u_{i,j,k-1}^{n+1,m} - 2u_{i,j,k}^{n+1,m} + u_{i,j,k+1}^{n+1,m}}{2}.$$

It has been demonstrated that by evaluating the second order correction terms at the previous iteration level, m , the second order accuracy of a centered difference is retained while the resulting system of finite difference equations becomes more diagonally dominant (see [12] for details).

The Jacobian of the generalized grid transformation vanishes along the x_{31} axis. This corresponds to a singularity in the governing equations and it requires the special treatment of the equations along the x_{31} axis. As a result, two different procedures were identified for obtaining the values of the dependent variables along the x_{31} axis. These involve the use of a locally rectangular system of coordinates or matching. Although both procedures appeared to work equally well, the matching procedure was selected because of its simplicity. Consequently, the dependent variables along the x_{31} axis are solved by requiring that the variable and its first derivative remain continuous across the x_{31} axis. This can be accomplished by the use of the following pseudo-boundary conditions,

$$A_{i,j,k}^{n+1,m-1} = A_{i,j,k}^{n+1,m} \quad \text{for } 0 \leq \theta < \pi \quad (16)$$

$$\frac{\partial A^{n+1,m-1}}{\partial \xi_2^{i,j,k}} = \frac{\partial A^{n-1,m}}{\partial \xi_2^{i,j,k_e}} \quad \text{for } \pi + \vartheta \leq 2\pi \quad (47)$$

where A denotes any of the dependent variables, u_{31} , u_{32} , u_{33} , p , or F , and ϑ is used to denote the circumferential angle corresponding to the grid section identified by k along which ξ_3 is constant. Note that k_e is used to denote the grid section which is displaced by 180 degrees in the circumferential direction from the section denoted by k .

3.3 Computational Procedure

The resulting set of finite difference equations is solved iteratively using the Gauss-Siedel procedure. An outline of the computational procedure is given. With the solution converged at time t , identified as time level n , the following sequence of steps is taken to advance the solution to the next time level, $n + 1$:

1. The value of time is adjusted to the $n + 1$ level such that $t^{n+1} = t^n + \Delta t$.
2. Using the converged solution at time level n the kinematic condition equation (41) is solved explicitly to obtain the new free surface position, F^{n+1} .
3. The values of the various parameters describing the position of the container, t_1 , u_1 , and h_1 , are updated. Coefficients β_1 , β_2 , β_3 , and g_2 , are then also updated.
4. Based on the new position of the free surface, F^{n+1} , the value of the surface tracking angle ϕ is adjusted such that the coordinate system x_3 rotates to

follow the center of gravity of the fluid. Coefficients f , λ_1 , λ_2 , and g_2 that depend on ϕ are updated.

5. A new computational grid that conforms to the shape of the fluid defined by F^{n+1} is obtained by solving equations (34). The generalized coordinate metrics, η , are updated.
6. The velocities at the wall are set equal to zero according to the no slip condition (29). Velocity values at all interior points are calculated from the finite difference representation of equations (35). The dynamic conditions and continuity are used to calculate the velocity values along the free surface. Values along the x_{31} axis are calculated according to the matching conditions (46,47).
7. The dilatation, D , is calculated at all grid points using equation (40).
8. The pressure is set equal to zero along the free surface according to condition (30). Pressure values at all the interior points are calculated using the finite difference representation of the pressure equation (37). The pressure values along the container wall are calculated by boundary condition (42). Using the matching conditions new pressure values are calculated along the x_{31} axis.
9. Steps 6 to 8 are repeated until the solution for the velocities, u_i , and the pressure, p , meets the convergence criterion.

$$\frac{A^{n+1,m} - A^{n,m}}{A^{n,m}} < \epsilon \quad \text{for all } i, k$$

A typical value of ϵ used during the computations was $\epsilon = 10^{-5}$.

4 Sample Results and Discussion.

The model described in the previous sections was used to generate results for two cases which will be presented here. The first case, case-A, involved the simulation of the resulting fluid flow in a spherical container of radius $a = 7.41$ cm, and half-filled with liquid glycerin at 21.1 degrees Celsius, when the container is impulsively spun about its axis of symmetry. The second case, case-B, involved the simulation of the flow that results within the same container when the spin axis is located 24.10 cm away from the container axis of symmetry. Both of these cases were selected as a first step in evaluating the model because of the relatively uncomplicated flow regimes that result under these conditions. The first case allows for the evaluation of the three dimensional model under conditions for which the resulting flow is essentially two dimensional. The geometry of the second case was selected to allow for future comparisons with experimental data from a test rig.

Case A: Two Dimensional Spin-up.

The flow of glycerin in a half-filled spherical container is considered here. Initially, at time $t = 0^-$, the container is motionless and the glycerin is in a state of hydrostatic equilibrium. At time $t = 0$, the container begins to rotate about its axis of symmetry, x_{23} , such that,

$$\omega_{23} = \begin{cases} 0 & \text{for } t < 0 \\ \Omega t & \text{for } t \geq 0 \end{cases}$$

where the dimensionless angular velocity is equal to $\Omega = 0.49636$, which corresponds to approximately 54.5 rpm. Instantaneously, at time $t = 0^+$, the pressure distribution within the fluid adjusts itself to reflect the centrifugal acceleration experienced by fluid particles as a result of the sudden rotation. The change in the pressure field causes the fluid to begin to oscillate about the new equilibrium position until it is brought to rest by viscous dissipation.

The governing equations were solved to determine the resulting fluid motion with the values of the following parameters set equal to:

$$t_i = 0 \quad \text{for } i = 1, 2, 3$$

$$v_1 = v_2 = 0$$

$$h_i = 0 \quad \text{for } i = 1, 2, 3$$

and the value of the surface tracking angle equal to:

$$\psi = -\pi/2$$

The value of the dimensionless Galileo number corresponding to these conditions is equal to:

$$Ga = 3922$$

The centrifugal acceleration experienced by fluid particles is proportional to $r\Omega^2$, where r represents the radial distance from the spin axis. Consequently, circumferential symmetry exists, and the resulting flow field is two dimensional. The two

dimensional nature of the flow field was demonstrated very well by the numerical solution. Less than one percent variation with circumferential position was detected in any of the values of the dependent variables.

The resulting flow within the container is depicted in figure (5). The velocity field along the $x_{21} - x_{23}$ plane is plotted for five different values of dimensionless time, t . At time $t = 0^-$, the fluid is still motionless. This is depicted in figure (5a) where the solid line at $x_{23} = 0$ represents the initial position of the free surface given by:

$$F(0^-, x_{32}, x_{33}) = 0$$

and the dashed line represents the equilibrium position of the free surface, which is a paraboloid given by:

$$F(\infty, x_{32}, x_{33}) = C_0 + \frac{1}{2}\Omega^2 (x_{32}^2 + x_{33}^2)$$

where C_0 is a constant determined analytically from a global mass constraint.

The sudden rotation of the container causes the pressure distribution within the fluid to drop to levels below those determined by the hydrostatic balance near the spin axis, and to levels exceeding the hydrostatic values for points located away from the spin axis. In response to these changes, the fluid begins to fall near the center of the container and to rise near the wall. This is depicted by the velocity field shown for $t = 0.80$ in figure (5b). The fluid flow is strongest near the free surface with fluid particles near the center of the container moving downwards and outwards and fluid particles rising along the wall. The fluid motion near the bottom of the container

is significantly weaker. The fluid continues to move past the equilibrium position and by time $t = 1.60$ it has slowed down and the flow pattern begins to reverse itself. This is shown in figure (5c) and more clearly in figure (5d), where at $t = 2.40$ the fluid is moving back toward the center of the container. The most significant flow remains along the free surface with the fluid near the bottom of the container undergoing a weak recirculating motion. At time $t = 3.20$, figure (5e), the fluid has nearly completed one full cycle as it moves back toward its initial position. The actual dimensionless period exhibited by the fluid was approximately equal to 3.24.

The fluid oscillations decay as a result of the viscous dissipation, the effects of which are shown in figure (6). Here, D_{rms} , which is defined by,

$$D_{rms}(t) = \frac{\sqrt{\int_{r_{min}}^{r_{max}} (F(t, x_{32}, x_{33}) - F(\infty, x_{32}, x_{33}))^2 dA}}{\sqrt{\int_{r_{min}}^{r_{max}} (F(0, x_{32}, x_{33}) - F(\infty, x_{32}, x_{33}))^2 dA}}$$

and it represents a measure of the root mean square deviation of the free surface position from the equilibrium position plotted versus time. Initially, at time $t = 0$, D_{rms} is equal to one. This represents the maximum deviation of the free surface from its equilibrium position. As time increases the fluid begins to move toward the equilibrium position, and consequently D_{rms} decreases. Its value goes through a local minimum as the free surface passes through the equilibrium position, at approximately $t = 1.2$, and it begins to increase as the equilibrium position is being over-shot. After approximately two full cycles, at $t = 4.85$, the maximum value of D_{rms} decreased to less than seven percent of the initial value.

Case B: Three Dimensional Spin-up.

A second case was computed using the same parameters as in case-A with the exception of h_1 . For this case, the value of the dimensionless parameter h_1 was set equal to.

$$h_1 = 3.252 .$$

This indicates that the center of the spherical container is located away from the spin axis, x_{13} , at $x_{11} = h_1$.

The centrifugal acceleration experienced by fluid particles as a result of the sudden rotation of the container is now proportional to

$$x_{32}\Omega^2 - (x_{33} - h_1)\Omega^2 .$$

The centrifugal acceleration effects are stronger for this case due to the position of the container relative to the spin axis. Consequently, the resulting flow field is no longer symmetrical about the x_{31} axis. The equilibrium position of the free surface is given by,

$$F(\infty, x_{32}, x_{33}) = C_1 - \frac{1}{2}\Omega^2 (x_{32}^2 - x_{33}^2) - \Omega^2 h_1 x_{33}$$

where once again C_1 is a constant determined analytically from a global mass balance.

The motion of the fluid within the container is depicted in figure 7. Figure 7 is a three dimensional graphical representation of the motion of the free surface. The shape of the free surface is depicted by the circular net defined by the solid

lines. The x_{21} coordinate system and the initial position of the free surface along the container wall are shown in dashed lines. The spherical container is outlined by the dotted lines. The three dimensional shape of the free surface is drawn as it would be seen by an observer rotating along with the spherical container such that its position remains along a line 45 degrees above the horizontal $x_{21} - x_{22}$ plane, and 45 degrees between the negative x_{21} axis and the positive x_{22} axis. The position of the container relative to the stationary x_1 coordinate system is shown in the captions on top of figure (7). The direction of observation is also indicated by the arrow. The initial position of the free surface, at time $t = 0^+$ is shown in figure (7a). The fluid, in response to the sudden centrifugal acceleration resulting from the motion of the container, begins to move away from the spin axis. Thus the free surface rises along the portion of the container wall that is the farthest away from the spin axis, and begins to drop along the portion of the wall that is closer to the spin axis. This is clearly depicted in figure (7b), where the position of the free surface is shown for $t = 0.10$. Figure (7c) shows the position of the free surface at a later value of time, $t = 0.80$, where the fluid has moved even closer to the equilibrium position.

The direction of the motion of the bulk of the fluid is along the $x_{21} - x_{22}$ plane. This is due to the absence of any tangential acceleration effects, since the motion of the container was assumed to have been started impulsively. The velocity field along the $x_{21} - x_{22}$ plane is shown in figure (8) for the same values of dimensionless time as the ones used in figure (7). Here, the motion of the fluid particles can be envisioned more clearly. The asymmetry that results from the difference in the

magnitude of the centrifugal acceleration at the two sides of the container is clearly shown in terms of the position of the free surface and the direction of the velocity vectors.

The results presented here were generated using a computational grid with 11 nodes in the radial direction, 11 nodes in the azimuthal direction, and 21 nodes in the circumferential direction. Case-A required a total of 3.52 hours of CPU time on a NAS AS 9180, an IBM compatible mainframe computer with a computing speed of approximately 10 Mflops, to be solved to a dimensionless time of $t = 6.14$ using a time step of $\Delta t = 0.02$. Case-B, required a total of 6.32 hours of CPU time to reach a value of $t = 1.04$ using the same time step size.

Acknowledgments:

The Authors would like to acknowledge the support obtained from the Air Force Office of Scientific Research through Grant AFSOR-86-0080 for conducting this study. Computation time was supported with a block grant from the Iowa State University Computation Center. Additional support and computational time were made available by the National Science Foundation Presidential Young Investigator Award of Dr. Pusa through Grant CBT-8451145.

REFERENCES:

1. Stearne, J., "Quarterly Journal of Mathematic", V. XVII, 1881, p. 90.
2. Lamb, H., Hydrodynamics, Sixth ed., Dover publ., 1945, sec 257.
3. Cooper, R. M., "Dynamics of Liquids in Moving Containers", ARS J., V 30, no 8, Aug 1960, pp 725-729.
4. Chu, Wen-Hwa, "Fuel Sloshing in a Spherical Tank Filled to an Arbitrary Depth", AIAA J., V 2, no. 11, Nov. 1964, pp 1972-1979.
5. Abramson, H. N., "Liquid Sloshing in Compartmented Cylindrical Tanks", ARS J., V 32, no. 6, June 1962, pp 978-990.
6. Penney, W. G., and Price, A. T., "Some Gravity Wave Problems in the Motion of Perfect Liquids", Phil. Trans. Roy. Soc. (London), V. A218, 1952, pp 44-59.
7. Summer, I. E., and Stofan, A. J., "Experimental Investigation of Viscous Damping of Liquid Sloshing in Spherical Tanks", NASA TN D-1991, 1963.
8. Case, K. M., and Parkinson, W. C., "Damping of Surface Waves in an Incompressible Liquid", J. Fluid Mech., V 2, part 2, Mar 1957, pp 172-184.
9. Abramson, H. N., "The Dynamic Behavior of Liquids in Moving Containers", Southwest Research Institute, NASA SP-106, 1966.
10. Vaughn, B. H., and Oberkampf, L. W., and Wolfe, P. W., "Numerical Solution for a Spinning Nutating, Fluid Filled Cylinder", Sandia National Laboratories, SAND83-1789, 1983.
11. Lamb, H., Hydrodynamics, Sixth ed., Dover publ., 1945, sec 270.
12. Kassinos, A., Viscous Sloshing in Three Dimensional Moving Containers, Ph. D. Dissertation, Iowa State University, (in preparation).
13. Shanks, S. P., and Thompson, J. E., "Numerical Solution of the Navier-Stokes Equations for 2D Hydrofoils in or Below a Free Surface", Proc. 2nd Int. Conf. on Numer. Ship Hydro., University of California, Extension Publ., 1987.
14. Thomas, P. D., and Middlecoff, J. E., "Direct Control of the Control Point Distribution in Meshes Generated by Elliptic Equations", AIAA J., V. 18, 1980, pp 650-655.

APPENDIX:

The position of a given point in the nutating coordinate system x_1 can be related to its respective coordinates in the x_0 coordinate system by,

$$x_{1i} = \alpha_{ij} x_{0j}$$

where the metrics of the transformation in terms of the three Euler angles u_i are given by,

$$\alpha_{ij} = \begin{pmatrix} C_3 C_2 - C_3 S_2 S_1 - S_3 C_1 & C_3 S_2 C_1 + S_3 S_1 \\ S_3 C_2 - S_3 S_2 S_1 - C_3 C_1 & S_3 S_2 C_1 - C_3 S_1 \\ -S_2 & C_2 S_1 & C_2 C_1 \end{pmatrix}$$

where here $S_i = \sin(u_i)$ and $C_i = \cos(u_i)$.

The transformation from the x_2 to the x_3 coordinate systems is described by,

$$x_{3i} = s_{ij} x_{2j}$$

where the metrics s_{ij} are defined by,

$$s_{ij} = \begin{pmatrix} \cos \phi & 0 & -\sin \phi \\ 0 & 1 & 0 \\ \sin \phi & 0 & \cos \phi \end{pmatrix}$$

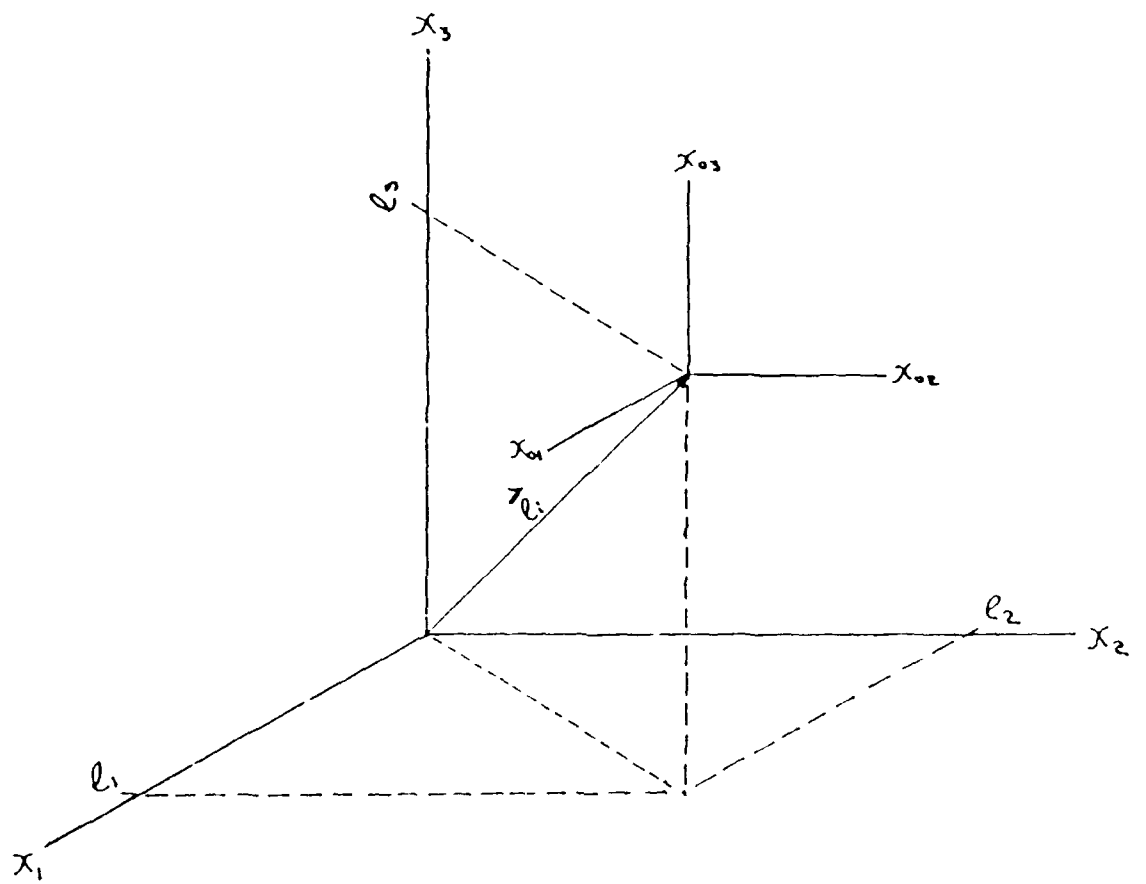


Figure 1: Linearly accelerating coordinate system.

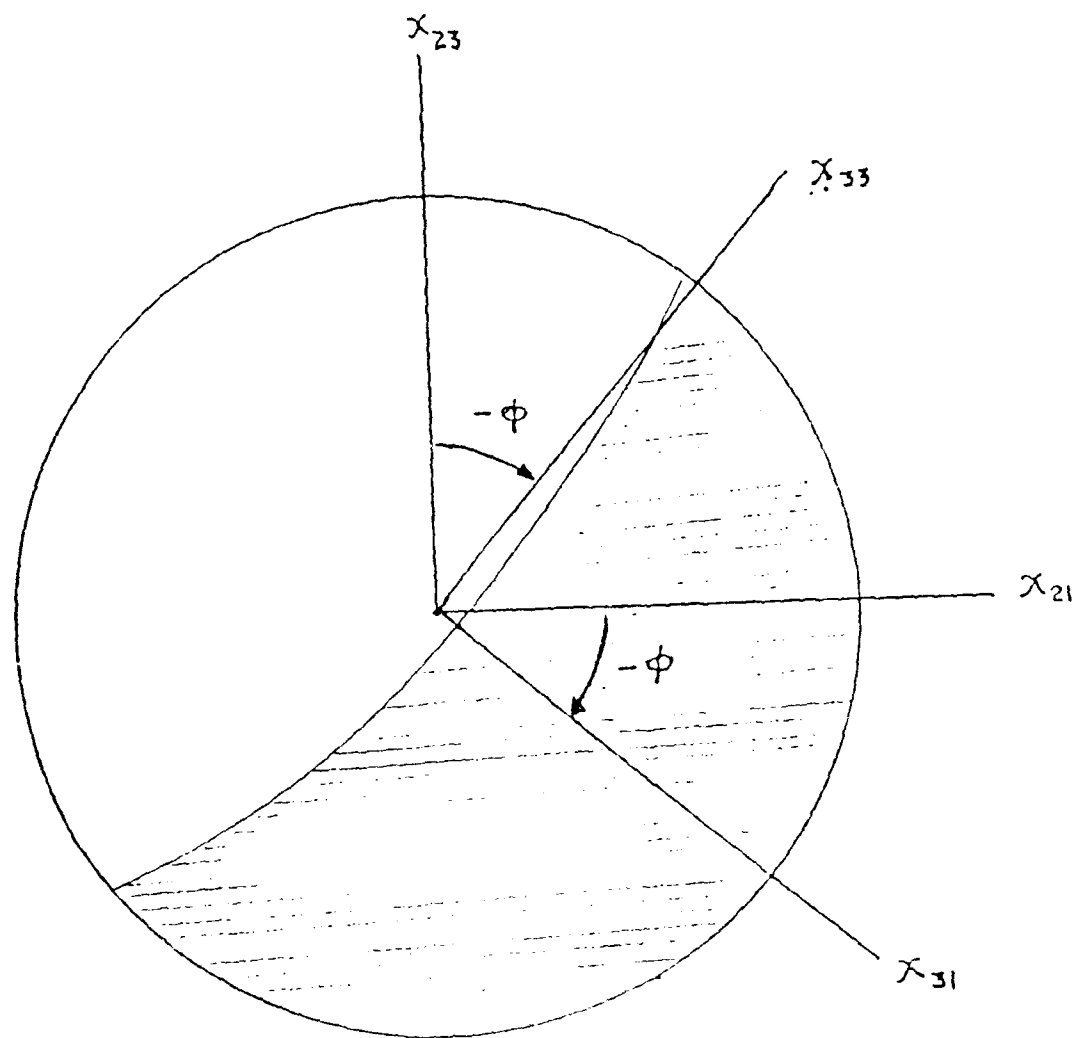


Figure 3: Self adjusting coordinate system.

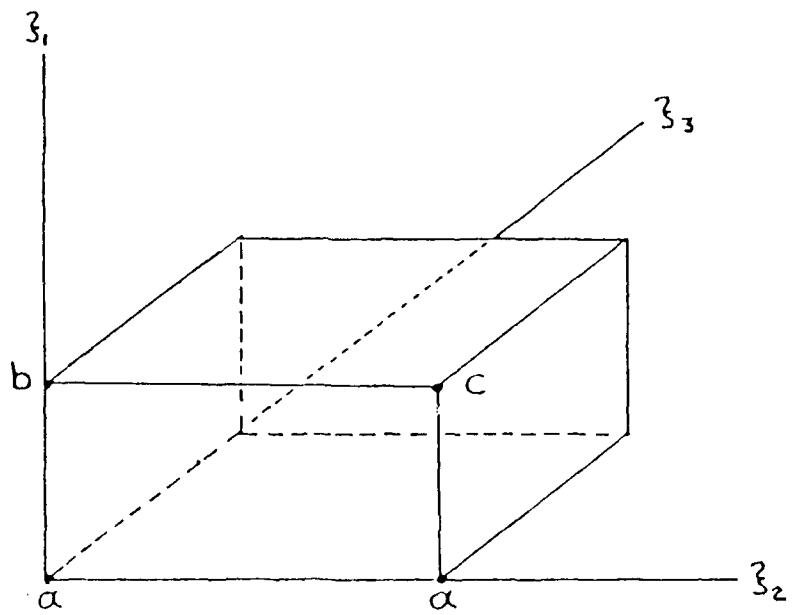
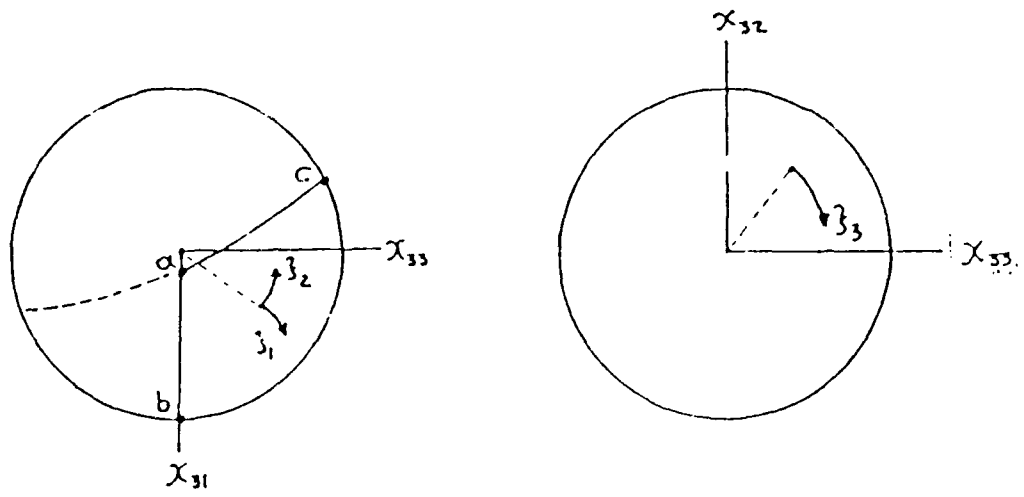


Figure 4: Generalized grid coordinate system.

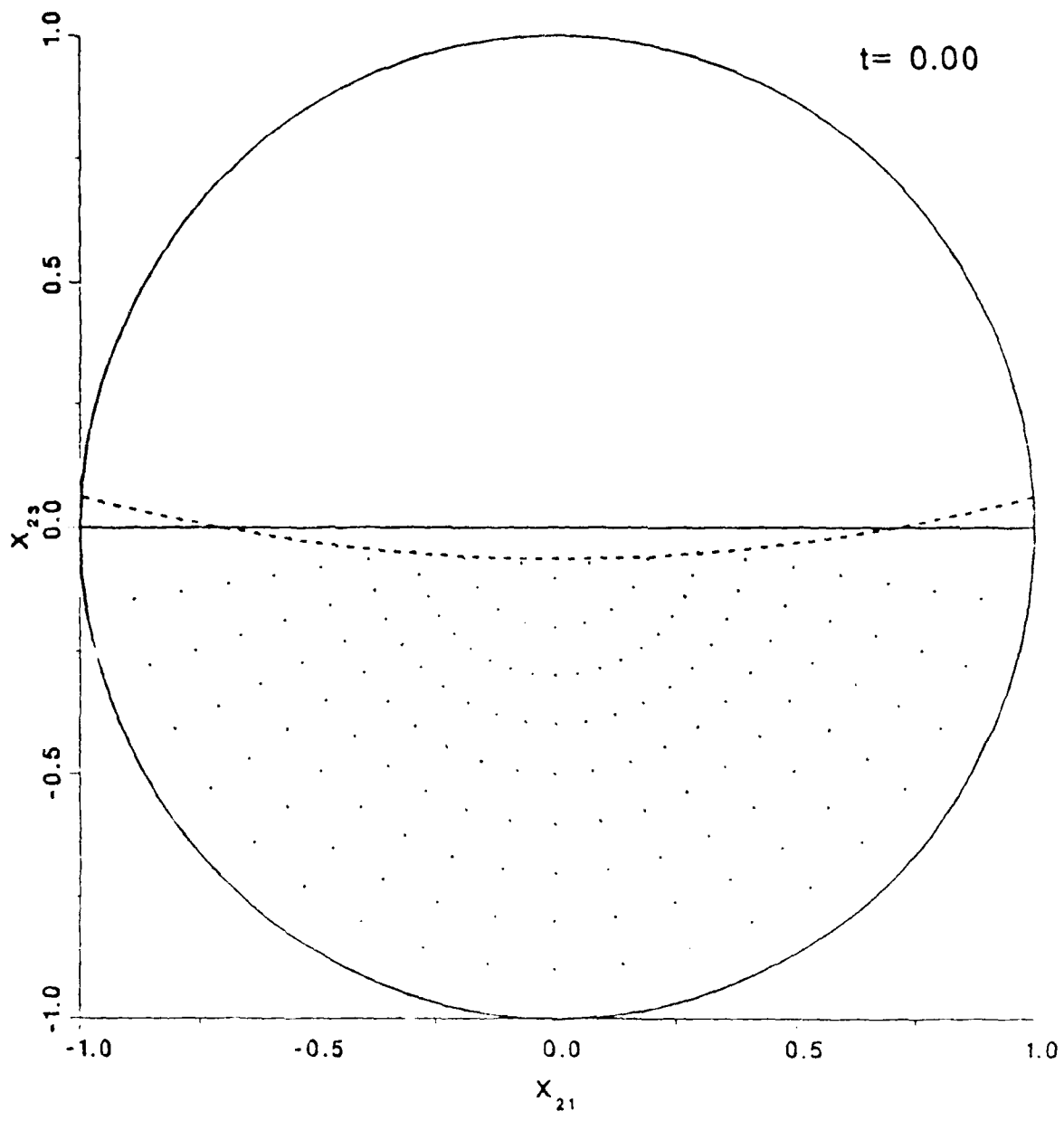


Figure 5a: Velocity field for the 2-D spin-up at $t = 0.0$

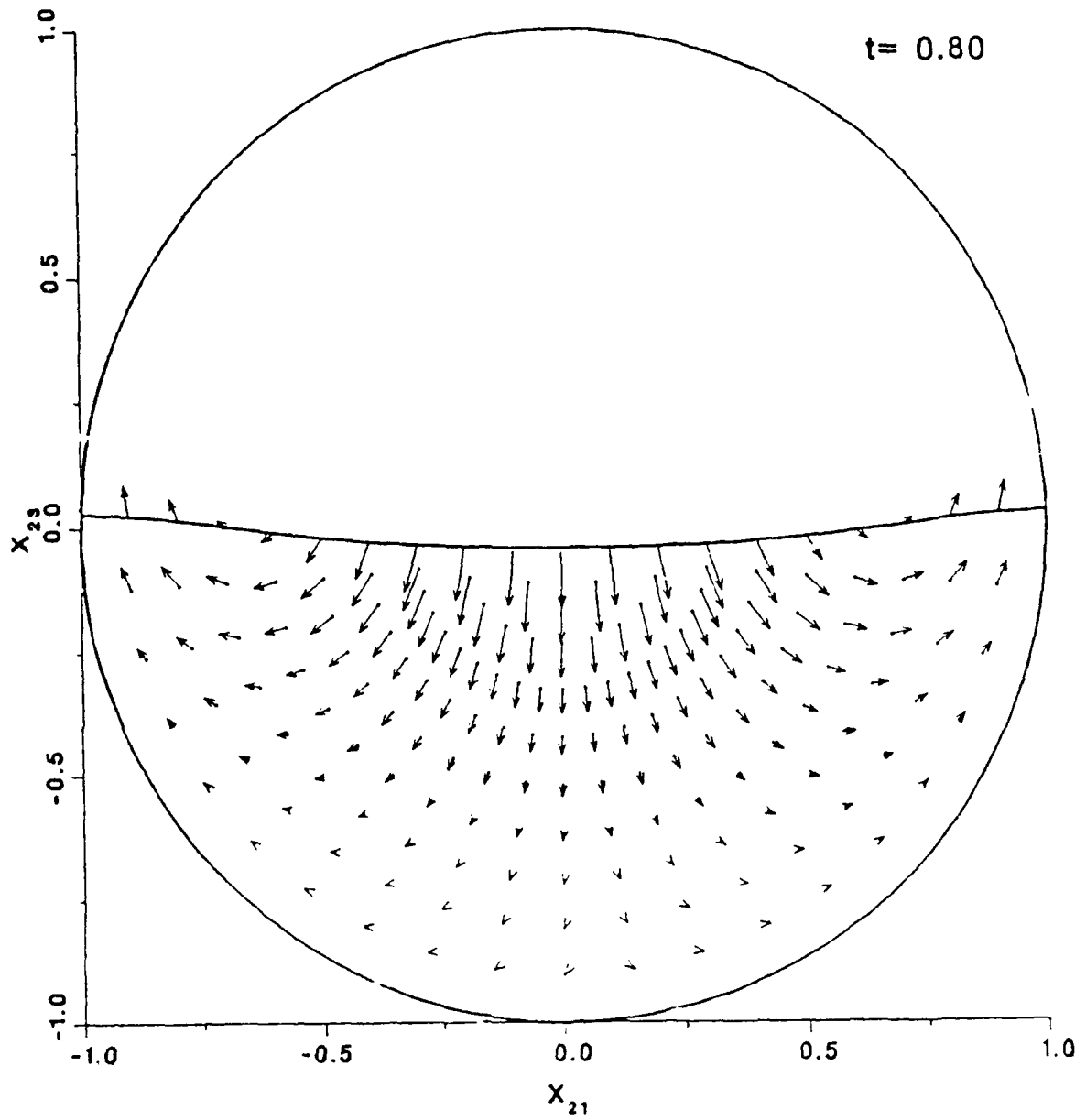


Figure 5b: Velocity field for the 2 D spin-up at $t = 0.8$

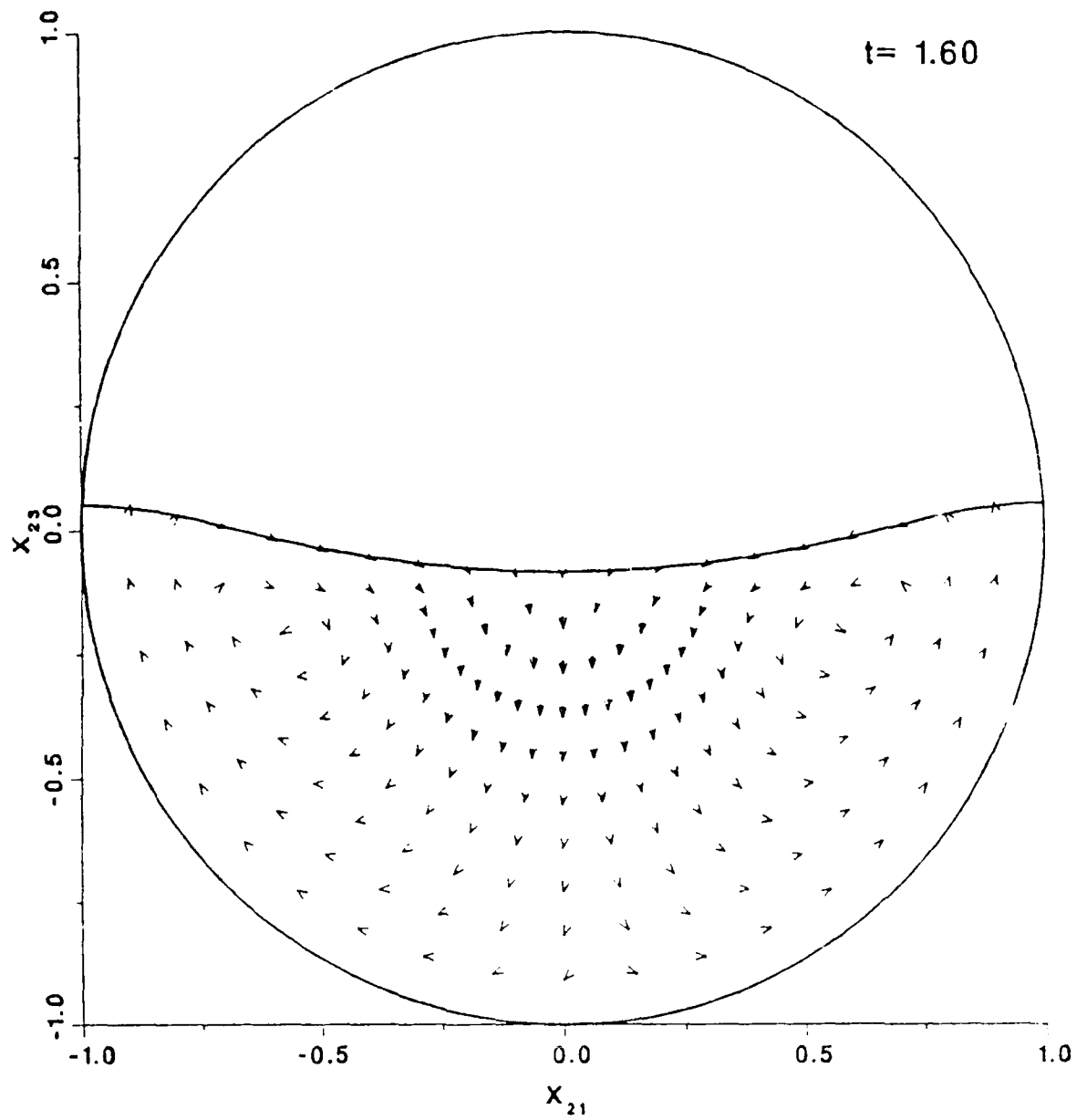


Figure 5c: Velocity field for the 2-D spin-up at $t = 1.6$

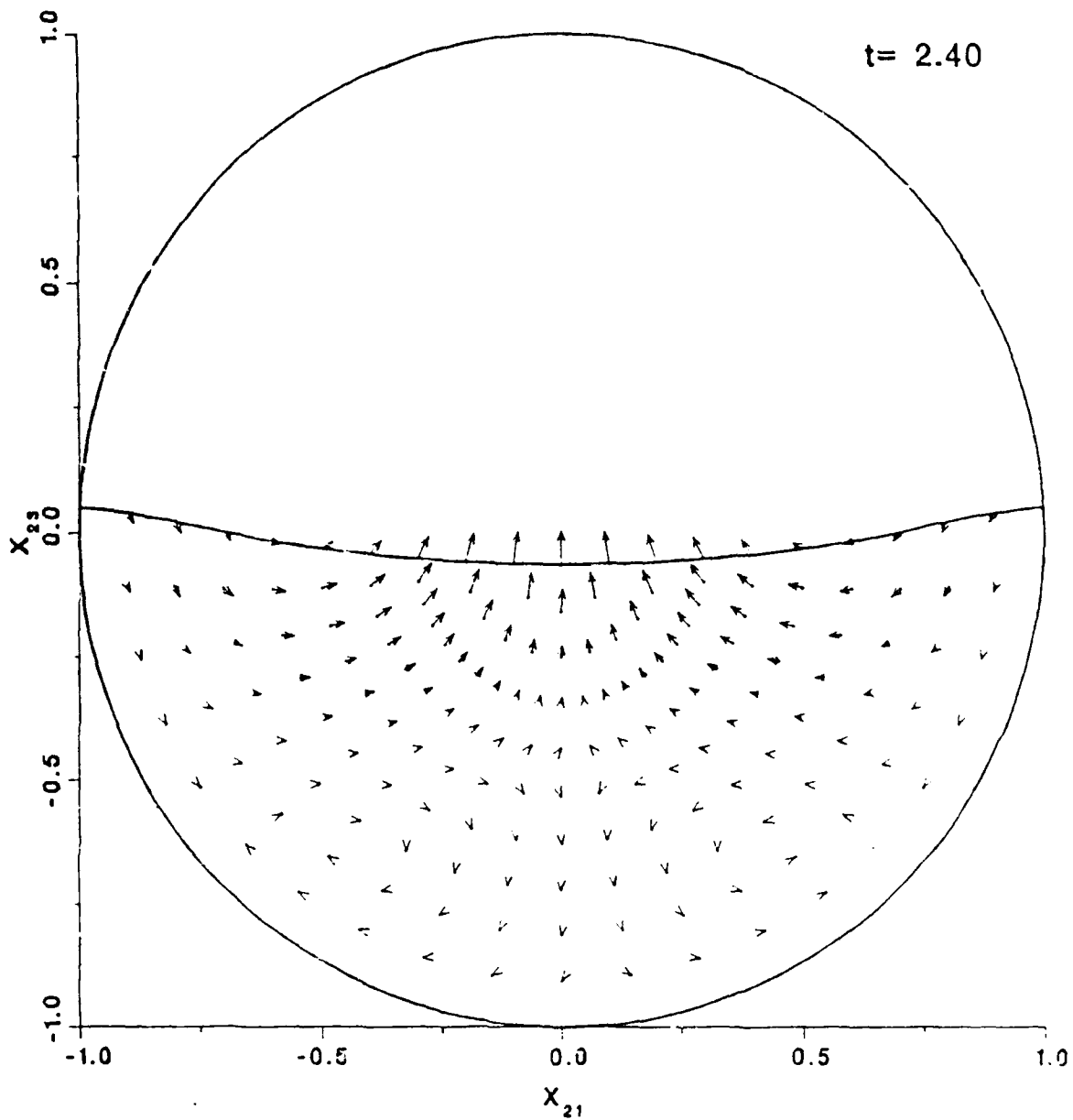


Figure 5d: Velocity field for the 2-D spin-up at $t = 2.4$

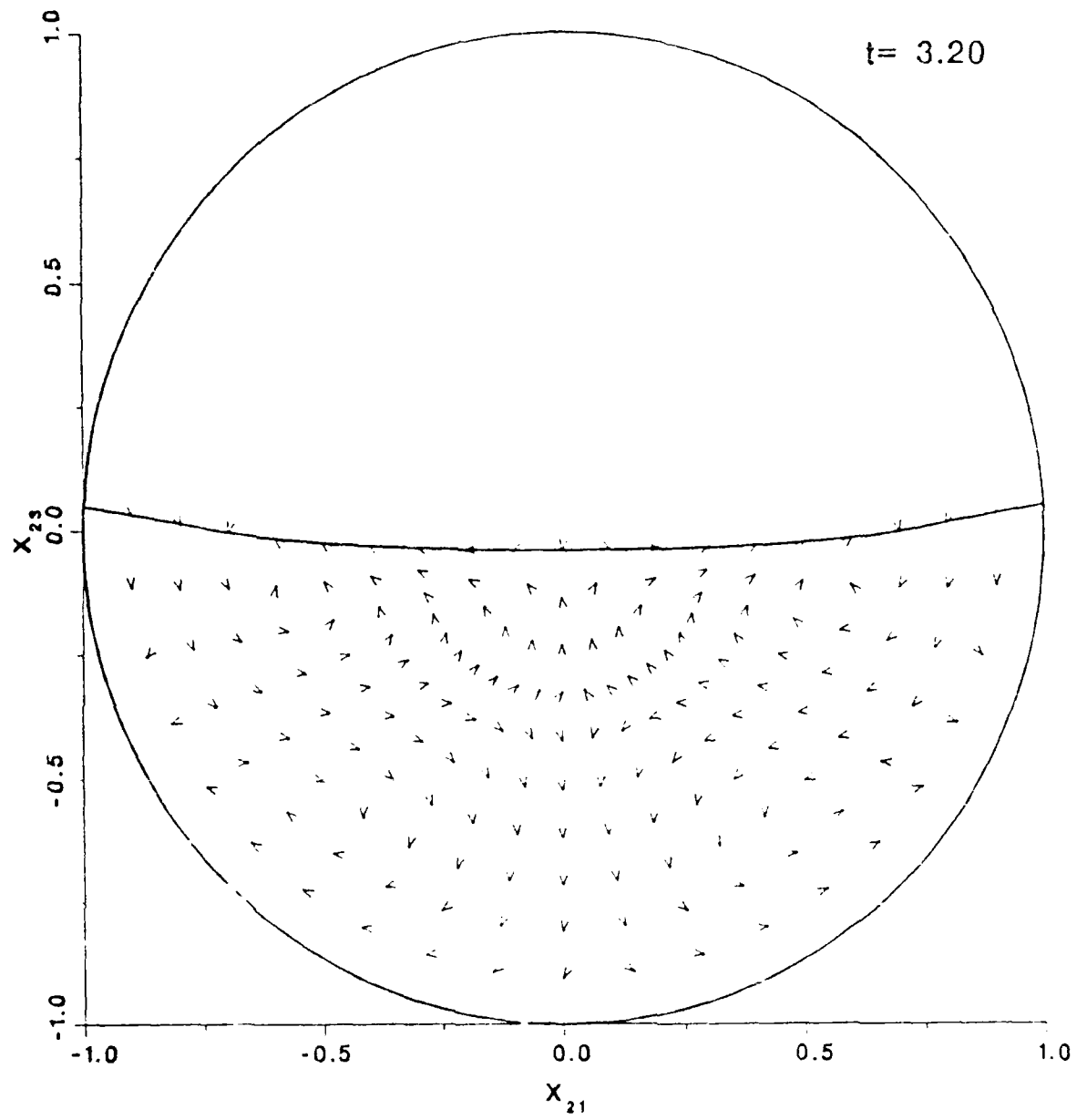


Figure 5c: Velocity field for the 2-D spin-up at $t = 3.2$

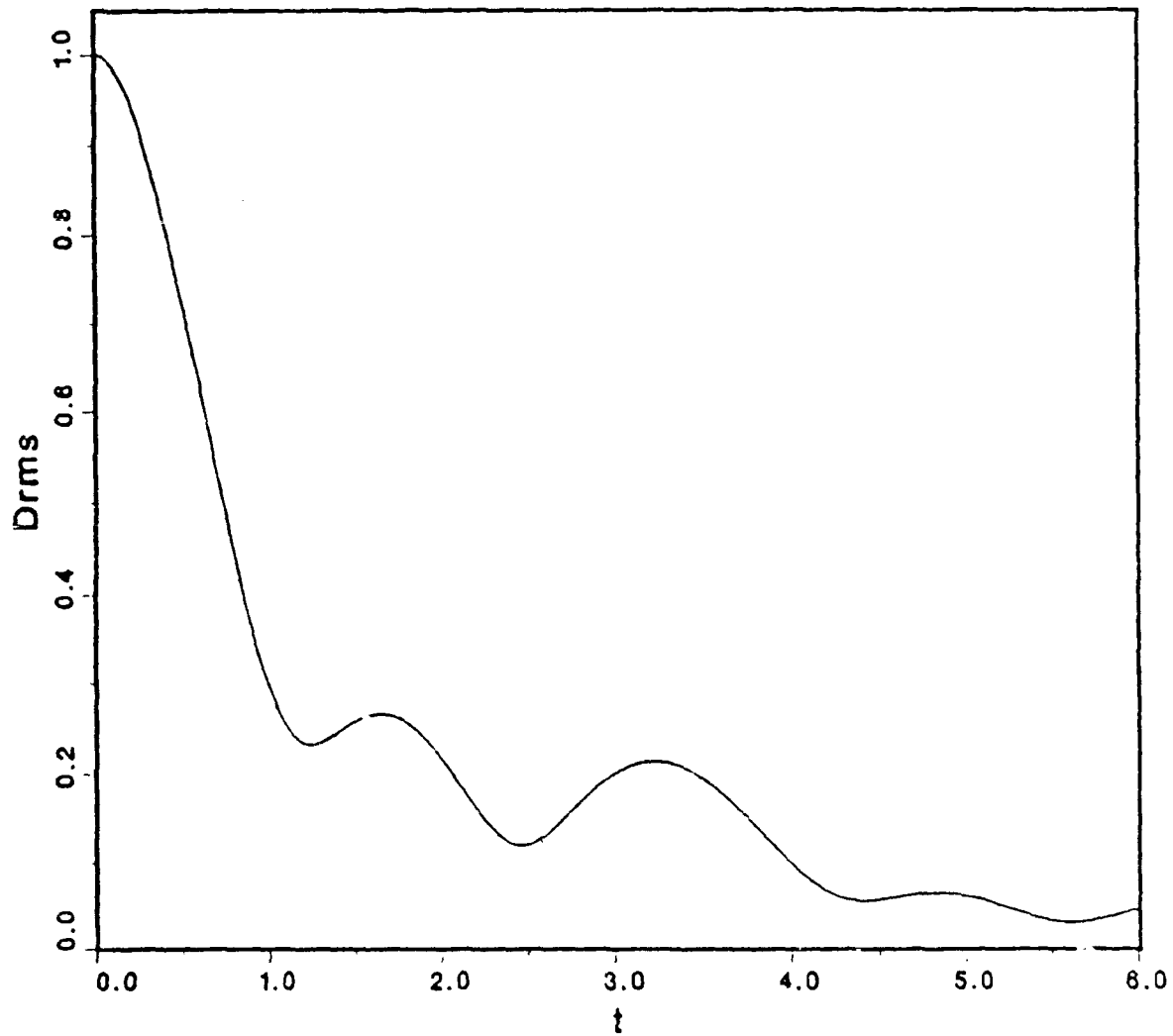


Figure 6: Viscous dissipation for the 2-D spin up.

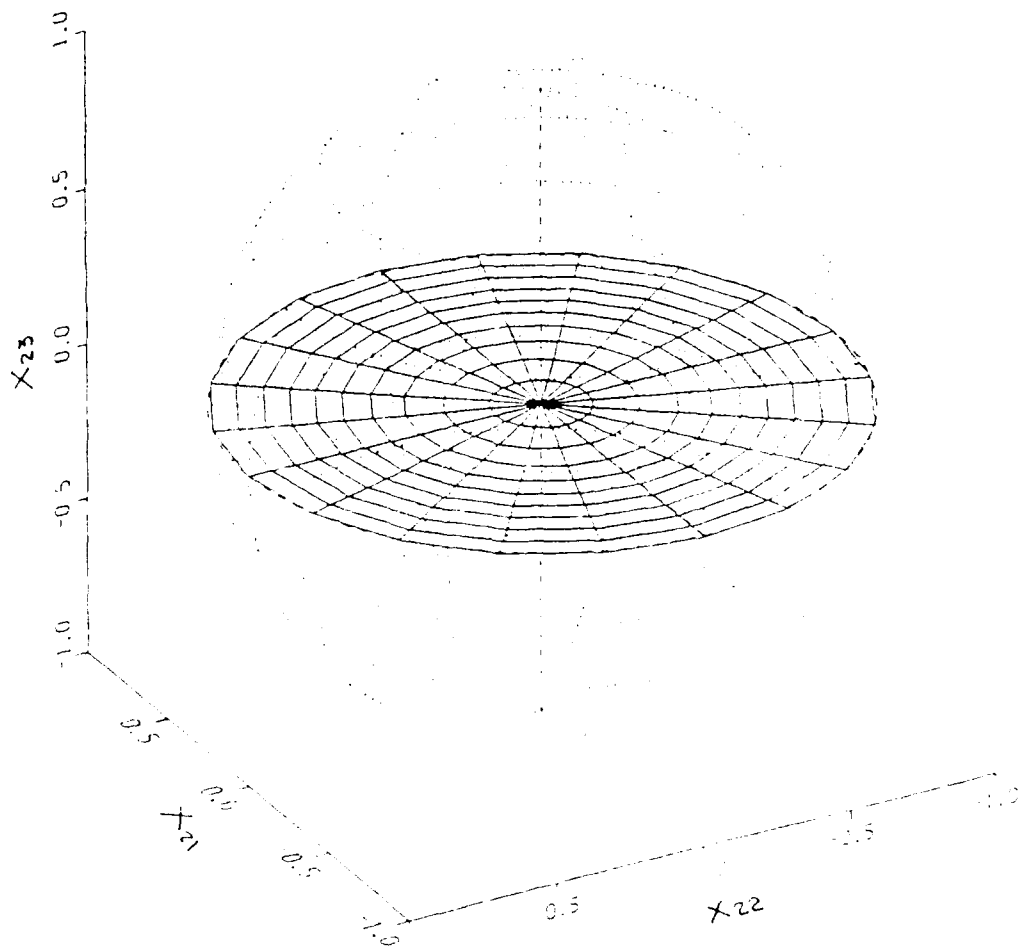
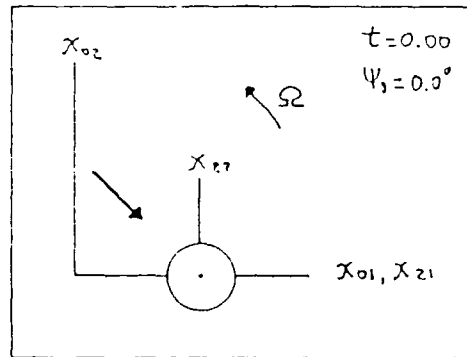


Figure 7a: Free surface position for the 3-D spin-up at $t = 0.00$

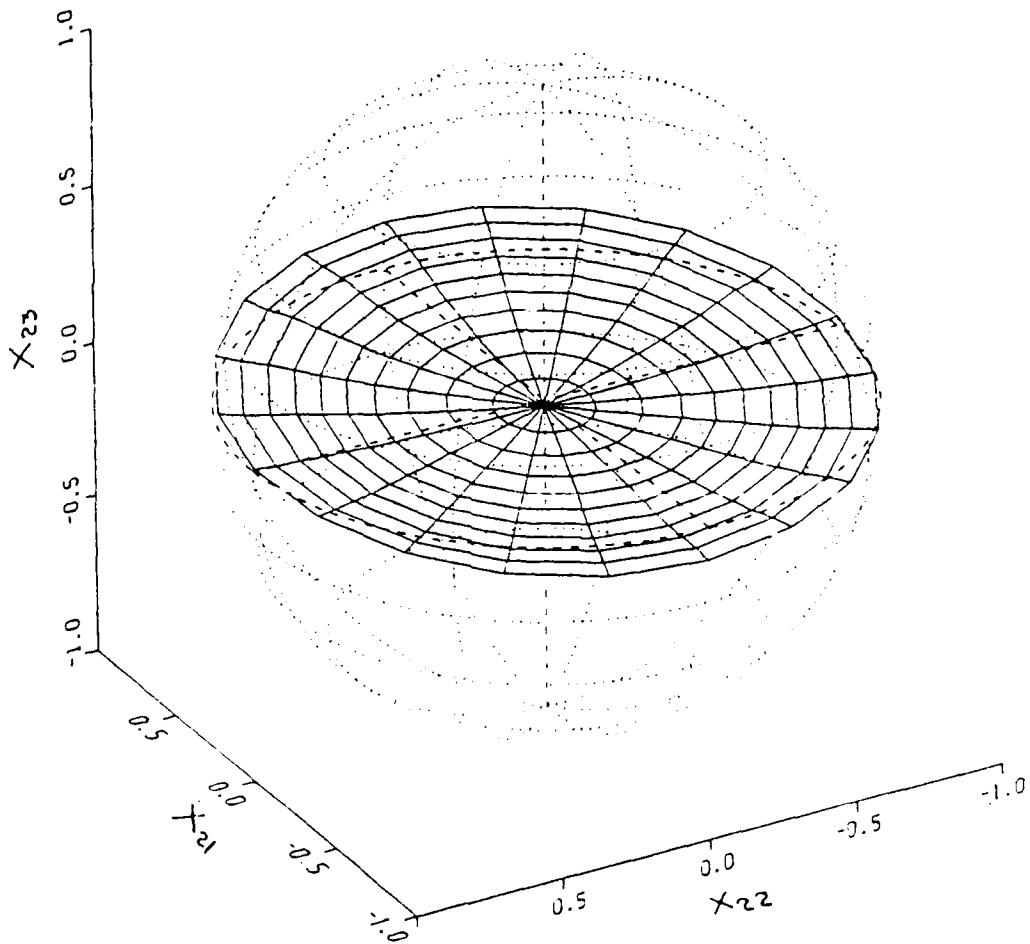
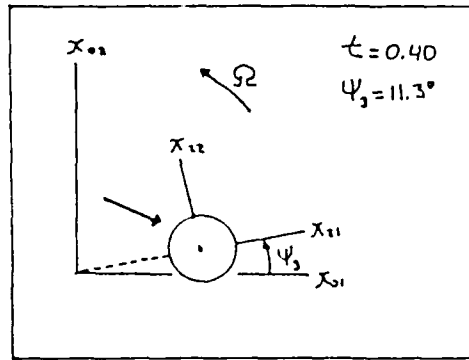


Figure 7b: Free surface position for the 3-D spin-up at $t = 0.4$

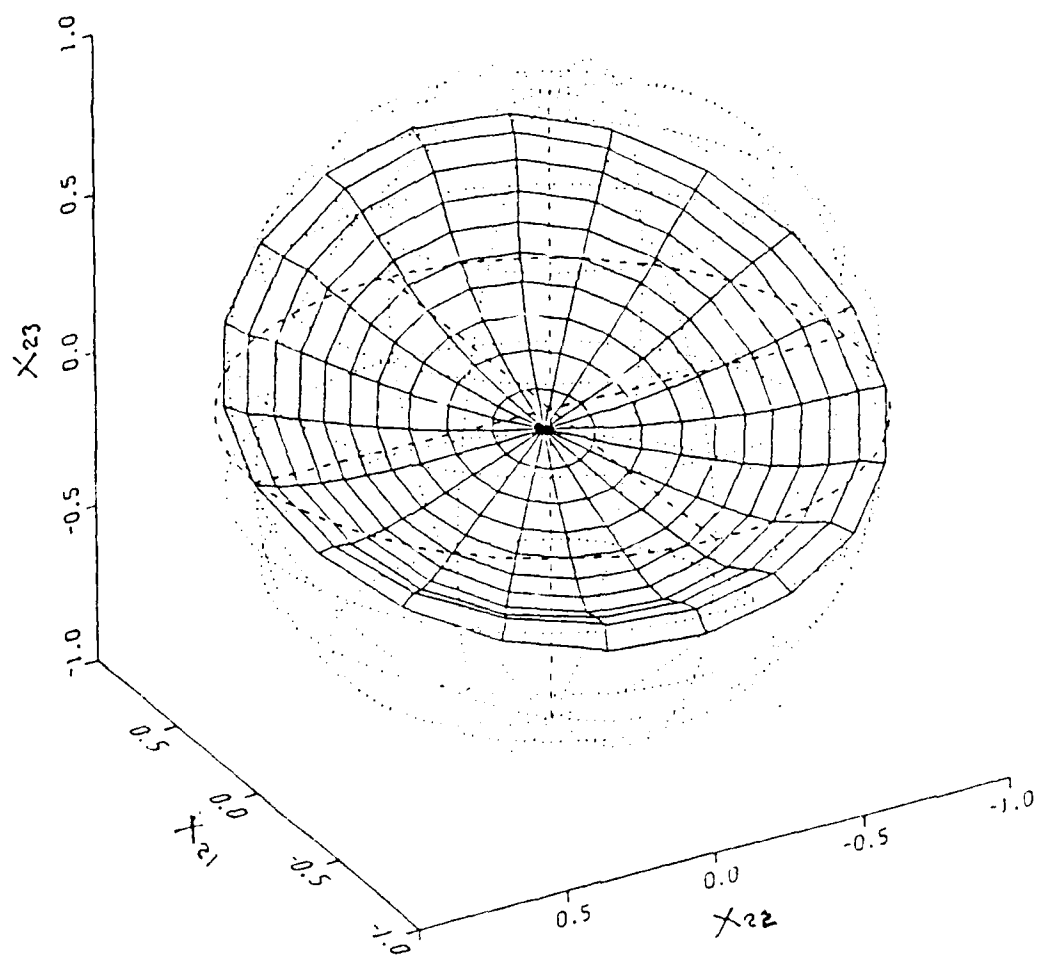
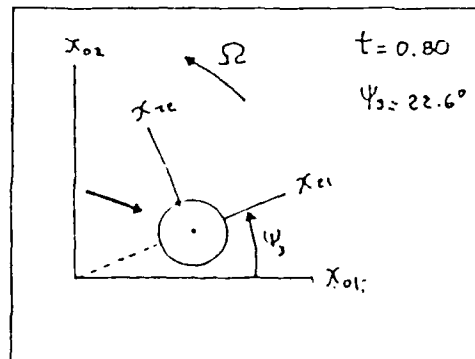


Figure 7c: Free surface position for the 3-D spin-up at $t = 0.8$